Study of Exchange Bias and Interfacial Coupling Effects in a Micromagnetic Thin Film Bilayer.

by

John Anthony Thibault

A thesis submitted in partial fulfillment of the requirements for the degree of

Master of Science

Department of Physics

University of Alberta

Abstract

Exchange bias and interfacial coupling effects in thin-film bilayers of magnetic materials were investigated during the period July, 2018, to Sep, 2021. Thin films of permalloy and cobalt oxide were deposited, in the form of micrometer size bilayer disks, on doubly-clamped nanomechanical resonators that were fabricated at the University of Alberta NanoFAB facility. The samples were mounted in an evacuated cryostat and were studied by observing their AC torque response to externally applied DC and RF magnetic fields. The apparatus was a three-axis AC torque magnetometer developed at the University of Alberta by our research group. Preliminary experimental data from ambient and field-cooled linear hysteresis loops showed a shift of the coercive field points thus providing the traditional signature of exchange bias behaviour and demonstrating that the samples and measurement techniques were suitable for further study of exchange bias effects. The original intent of previous researchers in our group was to investigate the effect of exchange bias on magnetic vortex behaviour, but that endeavor evolved toward a more fundamental study of exchange bias and interfacial coupling effects, the findings of which are reported herein. After modification to some of the samples to increase their torque response and improvements to the apparatus to enhance thermal and mechanical stability, the work continued by collecting and examining data from both linear and rotating hysteresis loops at ambient and cryogenic temperatures. The data were compared to predictions obtained from a phenomenological energy equation and macrospin model. Results from micromagnetic simulations were used to augment the investigative process.

Data from the linear hysteresis loops indicated exchange bias behaviour much in agreement with currently held views, but the findings from the rotating hysteresis loops suggested that exchange bias effects were not the dominant contributor to hysteretic behaviour in the rotating loops and that at least one additional interfacial coupling mechanism was involved. An additional task was to search for an exchange bias signature that did not require collecting data from a complete hysteresis loop. It was hoped that such a signature could be found by examining the torque response as a function of temperature. An experiment to this end was conducted wherein the findings indicated a progressive increase in torque as the temperature was lowered. The results were consistent with the view that exchange bias effects become observable as the sample temperature is decreased below the Néel temperature and that the strength of the effect increases as the temperature is further decreased.

Preface

Some of the content in Chapter 6 of this thesis was taken from a manuscript and supplementary materials section that were published together in AIP Advances in Mar, 2022. The contributing authors were M.G. Dunsmore, J.A. Thibault, K.R. Fast, V.T.K. Sauer, J.E. Losby, Z. Diao, M. Belov, and M.R. Freeman. The entire manuscript and supplementary materials section, as published, do not appear in Chapter 6. Instead, only those parts specifically related to the experimental results, analysis, and discussion are presented.

Preliminary versions of the manuscript and supplementary materials section were prepared by M.G. Dunsmore and J.A. Thibault with both authors contributing approximately equally. The final versions were more of a group collaboration with contributions of approximately 35% from M.G. Dunsmore, 35% from J.A. Thibault, 5% from K.R. Fast, 5% for Z. Diao, and 20% from our supervisor, M.R. Freeman. The contributions from V.T.K. Sauer, J.E. Losby, and M. Belov were from preliminary work relating to sample preparation. V.T.K. Sauer also collected data for preliminary investigations conducted prior to collection of the data that were reported on in the manuscript and supplementary materials section.

The content in Chapter 6 comes by way of a collaborative effort from M.G. Dunsmore and myself, J.A. Thibault. M.G. Dunsmore undertook writing of software for solving the Landau-Lifshitz-Gilbert equation, writing of modeling and computational software for thermomechanical calibration of the data, generation of fits to the data, and preparation of figures. M.G. Dunsmore also generated computer models for resonator behaviour and RF magnetic field distribution. I, J.A. Thibault, maintained the apparatus, cryogenic, and vacuum systems, performed the experiments, collected the data, conducted calibrations of the DC magnetic fields, and collected data relating to the strengths of the RF magnetic fields.

Dedications

I dedicate this work to my parents who have provided endless encouragement and support for my entire life. The passing of my mother in the spring of 2021 will prevent her attendance at convocation, but I know that she will be there in spirit.

I dedicate any success that may come from my efforts to all of the soldiers I served with that either did not make it home or that were so irreversibly changed that their lives are, everyday, a painful struggle.

Acknowledgments

In 2014, I decided that I should make an attempt to obtain a graduate degree in physics, but I was 52 years old and thought that the time for undertaking such an endeavour had passed. I presented the idea to my good friend Dr. Geoff Steeves, University of Victoria, Department of Physics, and to my former mentors Dr. Jim Rogers and Dr. Walter Jones both retired from the University of Alberta, Department of Physics. Each of them were supportive and encouraged me to make the attempt. I worked for Dr. Rogers and Dr. Jones as a technician in the mid to late 1980's and learned much about science, physics, and life in general from both of them. Letters of recommendation for entry into a graduate program were provided by Dr. Rogers and Dr. Jones. I am grateful and thank them for their support. I also thank my friend, Geoff Steeves, for his encouragement.

I would not have been able to complete my studies and lab work without the help of many people. My supervisor, Dr. Mark Freeman, was particularly helpful and was always patient and tolerant. All of the members of the supervisory committee were helpful. I never left a committee meeting without knowing more than when I had walked in. One of the committee members provided much time, help, assistance, and guidance during the entire academic process that began in January of 2015.

The office staff provided help whenever I asked. The machinists, technicians, and the Undergraduate Laboratories staff were always willing to lend a hand. I do not take the assistance from any of these people for granted and am much appreciative of their positive attitude toward helping every student with whatever problem they may have had. There was also a very positive attitude among the academic staff. I was never turned away and am appreciative for all of the help they provided since I started the program.

All of the members of our research group, some still serving and some not, were pleasant, positive, and helpful. I thank them all for their kindness.

The project could not have been undertaken without support from the Natural Sciences and Engineering Research Council of Canada (RGPINS 04239 and 2021-02762), the Canada Foundation for Innovation (34028), and the Canada Research Chairs (230377). Technical support for fabrication of the nanomechanical torque devices was provided by the University of Alberta nanoFAB and the National Research Council Nanotechnology Research Centre. Deposition of the bilayer materials was conducted by Dr. Erik Luber.

Table of Contents

List of Figures

Chapter 1

Introduction

1.0) Thesis presentation.

The thesis is presented in chapter format. A brief description of the contents in each of the chapters is,

1.0.1) Chapter 1. Introduction.

A project overview, providing basic details of the work, is presented first so that the reader can become familiar with the scope of work and the results as early as possible. Chronology of the project is given next followed by a short historical account of the original discovery of exchange bias and a brief discussion of the motivation for studying exchange bias and interfacial coupling. A commercial application that relies on the exchange bias effect is described. Some of the interesting historical aspects of magnetism from original discovery to modern times is presented.

1.0.2) Chapter 2. Theory and Experimental Methods.

Theoretical considerations are presented. There is no attempt made to provide an exhaustive account of all theoretical and experimental work regarding magnetism. Instead, the content is restricted to a description of those parts of magnetic theory that are directly relevant to the project. A phenomenological model describing the observed exchange bias and interfacial coupling behaviours is presented. In the

Experimental Methods section, several measurement techniques suitable for experimental investigation of exchange bias are discussed. Computational methods as investigative tools are also discussed. A detailed description of three-axis AC torque magnetometry is given since it was this apparatus configuration that was used for the project reported on herein. The chapter closes with a short, general, discussion regarding calibration followed by description of the specific procedures used for calibration of the three-axis AC torque magnetometer by a thermomechanical method.

1.0.3) Chapter 3. Sample.

Details regarding sample design and fabrication are presented. A modification to improve the torque response of some of the samples is described.

1.0.4) Chapter 4. Apparatus.

The apparatus components, their functions, and improvements to temperature and mechanical stability are described. Procedures for calibration of the DC magnetic fields and determination of the RF currents in the excitation coil are given.

1.0.5) Chapter 5. Experimental work.

Work performed previous to that presented in this thesis is briefly reviewed. Training of personnel for apparatus operation and data collection is outlined. Raster images of several samples were obtained. Data from linear, rotated, and rotating hysteresis loops were collected at ambient and cryogenic temperatures. The torque response as a function of temperature was also recorded. Thermomechanical calibration data were collected and used to convert the measured voltage signals to torque. A description of the various types of data that were collected is provided.

1.0.6) Chapter 6. Results, Analysis, and Discussion.

The results from linear and rotating hysteresis loops obtained at ambient and cryogenic temperatures are given. The results from data collected while the temperature was decreased incrementally are also presented. Comments and a discussion of the results are provided. In the analysis section the data are fit to phenomenological models. Comments and interpretations regarding the influences and effects of the model terms are given.

Much of the content for the results, analysis, and discussion was taken from a manuscript and supplementary materials section that were published together in AIP Advances in March of 2022.[1] Note that the method of analysis, the fits, and the figures were the work of Michael Dunsmore, a currently serving member in our research group.

1.0.7) Chapter 7. Conclusions and future work.

The experiment, results, and final interpretations are summarized. Suggestions for directions that might be taken to make further contributions to the study of exchange bias and interfacial coupling effects are made.

Chapter 1. Introduction.

1.1) Project Overview.

The primary focus of the research was to study exchange bias and interfacial coupling effects in thin-film, bilayer, micromagnetic samples. The measurement methodology differed substantially from much of previously published work. In contrast to DC or AC torque measurements made on a single axis, a three-axis AC torque magnetometer, developed by our research group, was used throughout the investigation.

Excitation from externally applied DC and RF magnetic fields induced torques on the bilayer deposits of magnetic material. Since the deposits and the resonator paddle can be considered as a single structure, torque components in the deposits are transferred to the resonator paddle thus generating detectable motion. The three-axis AC torque magnetometer was used to measure the oscillatory responses of the resonator as a function of the applied DC and RF magnetic fields. Thermomechanical calibration permitted conversion of the raw data to absolute torque (here, “absolute” means reporting of torque in the native units of Nm as opposed to relative or normalized torque).

The samples to be studied were prepared by depositing thin-film layers of cobalt oxide (antiferromagnetic) and permalloy (ferromagnetic) on the moveable paddle of a nanomechanical resonator (the cobalt oxide was deposited first, followed by the permalloy). An additional capping layer, such as tantalum, was not deposited over the top, permalloy, layer. It is possible that an oxide layer (likely Nickel Oxide) formed, or was forming, on top of the permalloy layer during conduct of the experiment from 2018 to 2021. Evidence for oxidation and a consequent reduction in the effective thickness of the permalloy layer was found by other members of our group and is discussed in Chapter 6, Results, Analysis, and Discussion.

A total of 240 samples were made. The fabrication process is not perfect. Some, possibly very many, of the 240 samples would be expected to have mechanical and/or magnetic deficiencies rendering them unsuitable for study. To increase the probability of creating as many useful samples as possible, lithography patterns for several different resonator geometries and deposit sizes were generated. The experiment began by searching for suitably responsive samples. Many such samples were found and preliminary investigations were conducted by examining the data from linear hysteresis loops at ambient and cryogenic temperatures.

Preliminary data indicated that the mechanical response along two of the resonator axes was inadequate. The sample wafer was returned to the NanoFAB where one of the two resonator torsion arms of several samples was severed using a focused ion beam (FIB) process. The modification was successful. The previously inadequate responses were much improved and the resulting signals were well above the apparatus noise floor.

Data were collected from linear and rotating hysteresis loops at ambient and cryogenic temperatures. The torque response in a linear loop is a function of the DC magnetic field strength. Typically, the DC field is swept from a high positive value, decreased through zero to a negative value approximately equal in magnitude to the high positive value and then increased through zero until returning to the original high positive value. For rotating loops, the torque response is a function of the DC field angle with respect to a fixed reference. (The most convenient fixed reference is the apparatus x axis, but can also be the direction along which the DC field was applied during cooling from ambient to cryogenic temperature.) The DC field is rotated clockwise followed by a counterclockwise rotation (counterclockwise followed by clockwise can also be done).

The data were reduced and then analyzed by way of comparison to fits that were generated by considering a macrospin model and an appropriate phenomenological

energy equation. The fits were derived from macrospin solutions to the Landau-Lifshitz-Gilbert (LLG) equation. The energy terms in the phenomenological model included contributions from uniaxial, unidirectional, and rotatable anisotropies. The influence of a spin-flop coupling term was also included. The experimental data showed exchange bias, interfacial coupling, and training effects that were consistent with the model predictions.

The observed features in the linear hysteresis loops corresponded substantially with observations made by others,[2-5] but data from the rotating hysteresis loops suggested that exchange bias was neither the sole or dominant contributor to observed features in the rotating hysteresis loops. Interfacial coupling effects, other than exchange bias, were primarily responsible for the features in the rotating hysteresis loops. This finding is not contrary to the prevailing thoughts regarding exchange bias, but it does suggest that studies of exchange bias should include examination of data from both linear and rotating hysteresis loops. (Meiklejohn, one of the original discoverers of the exchange bias effect, comments on the relevance and importance of rotating data in a review article.[6] Refer to section 1.3, Discovery of Exchange Bias.)

1.2) Project Chronology.

In early 2018, our research group began work toward an experiment to study a magnetic effect referred to as exchange bias (sometimes referred to as exchange anisotropy; both terms appear in published works and are used somewhat interchangeably). The effect is both interesting and curious and has been the subject of both experimental and theoretical research since its discovery by W.H. Meiklejohn and C.P. Bean in 1956.[2]

Under the supervision and direction of our group leader, Dr. Mark Freeman, postdoctoral researchers J.E. Losby and V.T.K. Sauer prepared nanoscale, thin-film, bilayer samples at facilities located on the University of Alberta main campus. The samples were prepared specifically for the purpose of investigating exchange bias phenomena. In mid 2018, the samples were mounted in an apparatus that had been previously designed for other research work conducted by our group.

Studies of vortex behaviour[7] in nanoscale samples were conducted by other members of our research group prior to the work on exchange bias. The effect of exchange bias on vortex behaviour was the groups' original interest when the exchange bias experiment began. Exchange bias behaviour in the samples was observed in late 2018/early 2019. In April of 2019, several of the samples were modified to improve their mechanical response along two of three measurement axes.

I joined the exchange bias project in January of 2019, and became fully involved in May of that year. By this time, the original interest of studying the influence of exchange bias on vortex behaviour had become secondary to a simpler, more general, study of exchange bias and interfacial coupling effects in nanoscale, thin-film, samples.

1.3) Discovery of Exchange Bias.

Exchange bias refers to effects originally observed by W. H. Meiklejohn and C. P. Bean in 1956.[2] The authors were investigating magnetic behaviours in a sample of fine particles of cobalt, (ferromagnetic), that were coated with cobalt oxide, (antiferromagnetic). The particle size was given as 100 to 1000 angstroms. The Néel temperature of the cobaltous oxide was given as 293° C. They reported observations of linear hysteresis loops that, when cooled to liquid nitrogen temperature while in a saturating magnetic field, showed a shift of the coercive points as compared to data obtained at room temperature or when cooled to liquid nitrogen temperature in the absence of a field. Additionally, torque curves showed that the field-cooled data had a one-fold angular symmetry with a positive, vertical, offset from zero. The room temperature and zero-field-cooled data showed a two-fold angular symmetry with no offset. The rotational hysteresis loss of the field-cooled particles was substantial and notably different than the zero, or low, rotational hysteresis loss in normal ferromagnetic materials. The claim in the article was that "*A new type of magnetic anisotropy has been discovered which is best described as an exchange anisotropy. This anisotropy is the result of an interaction between an antiferromagnetic material and a ferromagnetic material.*" On page 906 of the article, the authors introduce a unidirectional anisotropy term into a free energy equation in an attempt to establish a theoretical basis for their newly discovered exchange bias effect. An interesting historical fact is that they referred to the introduction of the unidirectional anisotropy term as *ad-hoc* which may seem surprising today since, presently, this term is still in widespread use as the fundamental source of exchange bias behaviour.

In a 1962 review article,[6] Meiklejohn points out that shifted linear hysteresis loops can be obtained from models that can account for the one-fold symmetry of the angular torque dependence and argues that the two observations are, thus, evidence of the same

effect. He further argues that the exchange anisotropy observed in the torque curves is, specifically, a unidirectional anisotropy, and that the rotational hysteresis loss in high field is "...a more general characteristic of the effect than is a shifted hysteresis loop."

Since Meiklejohn and Bean's discovery, exchange bias systems have been the topic of numerous experimental and theoretical research articles[3-5, 8-11] wherein attempts have been made to develop theoretical models to account for observed effects. A review of many such articles seems to indicate that, in spite of considerable advances, there appears to be no single, generalized, theoretical model that can account for all observed effects in all types of exchange bias systems. It is possible that a generalized model does not exist or that it may not be forthcoming since some observations may be dependent on various uncontrollable factors such as the specific molecular formulas for the ferromagnetic and antiferromagnetic substances, the physical and magnetic properties of the ferromagnetic/antiferromagnetic interface, and, for similarly prepared samples, a variation in magnetic behaviour that may be due to sample chemistry, thickness, placement, or other such parameters that may cause sample to sample variations.

1.4) Motivation.

Since discovery of the exchange bias effect, researchers have had the task of developing a complete theory that provides a satisfactory explanation for the observations of exchange bias behaviour. While there have been many advancements, there still appears to be considerable difficulty in accomplishing the goal of obtaining an all-encompassing theory. In a 2001 review article,[12] Kiwi identifies seven requirements necessary for "...proper theoretical description and understanding of EB."[13] All of his requirements are relevant and important, but the first requirement, that formulation of a mechanism capable of explaining the cause of unidirectional anisotropy that is "...free of ad hoc assumptions on the interface structure..."[14] is the one that draws the most attention since it implies that at least some aspects of existing theories are founded more in qualitative assumption than in demonstrable fact.

In a series of papers[3, 10, 15, 16] from 1999 to 2006 a group of researchers at Stanford used X-Ray and photoelectron emission microscopy techniques to generate considerable data regarding exchange bias systems and were able to provide much information relating to the cause of exchange bias behaviour. The authors provide a review of their work in a web article. The title is "X-Rays Unravel the Puzzle of Exchange Bias".[17] The first sentence reads "...x-rays have helped to solve a longstanding scientific problem in magnetism."[17] The article leaves one with an apparent notion that there is nothing left to do with regard to exchange bias since the problem has already been solved, but in a more recent article[18] published in 2021, an update of the work with thin-film samples is provided. The article concludes with a suggestion for future research which, according to the authors, should include development of "...new models to understand the exchange bias effect...and investigate new systems and effects to enable a deeper knowledge of exchange bias systems".[19]

Whether or not the group at Stanford[3, 10, 15-17] are of the opinion that exchange bias has been "solved" is not entirely clear in spite of the unfortunate title of their web article. It seems more likely that they, like most researchers, would be content to continue their work in hope of deeper understanding or new discovery.

A time may come when all the aspects of exchange bias have been thoroughly explained to everyone's satisfaction, but this would not mean that further progress in other areas could not benefit from continued study of the effect. Having become familiar with the sound of a violin or the plot in a play by Shakespeare does not mean that there is nothing to be gained from further such experience and, so, it is with these thoughts in mind that we are motivated to continue our endeavours and to advance the knowledge regarding exchange bias systems and magnetism in general.

1.5) Applications.

An all-encompassing theoretical model has not prevented successful commercial application of exchange bias systems. Their use as spin valves in the read/write recording heads of magnetic memory devices (e.g. computer hard drives) is a perfect example of engineering and technical development that has not been hampered by delays in the formulation of precise theoretical explanation.

1.6) History of magnetism.

A) Discovery of magnetism. Ancient China and Greece, Thales of Miletus, Zheng Gongliang, and Shen Kua.

Observations of magnetism seem to have begun in ancient times approximately two millennia in the past. The word "seem" is used since a review of many sources[20] did not reveal any specific date of discovery or specific person to whom credit should be given for having made the original discovery of magnetic behaviour. There does appear to be, however, a general consensus that magnetism was discovered independently in China c. 100 B.C.[21] and possibly as early as 2000 B.C.,[22] in Greece as early as 700 B.C.[23] and in pre-Columban America, (dates unknown).[24] The observation was that a certain type of stone and iron were attracted to each other. These special stones contained magnetite (iron oxide, Fe_3O_4) and are referred to in the literature as lodestones. The stones are formed by natural processes and become magnetized not in the Earth's field, since it is too weak, but by high current discharges normally associated with lightning.[25] Giancoli remarks that the special stones, lodestones, were at some point called magnets owing to their discovery in Magnesia, a region in Asia Minor.[26] The "natural magic" of lodestones[27] caused many of the ancient peoples to imagine that there was some sort of spirituality to be associated with magnets. Thales of Miletus, c. 625 – 545 B.C., "...had thought that a lodestone possesses a soul because it could move a piece of iron...".[28]

The historical record may not be able to provide an account of the earliest known application of magnetism, but a notable device was the Chinese "South Pointer",[29] a spoon-shaped device carved from lodestone, that was "...possibly used to order and harmonize buildings by the geomantic principles of *feng shui*".[30] Invention of the device would have been in China during the Han period, c. 100 B.C., upon discovering "...the orientating effect of the magnet...".[31] Coey also mentions the South Pointer, its discovery in China during the same period, and its use for geomancy.[32]

We often think of the compass as the first technical application of magnetism. In 1064, Zheng Gongliang discovered "...that iron could acquire a thermoremanent magnetization when quenched from red heat".[33] Processes for making steel had been discovered during the Han Dynasty, (206 B.C. - 25 A.D),[34] and steel needles "...magnetized in the Earth's field were the first artificial permanent magnets".[35] In approximately 1088, during the Song Dynasty, Shen Kua described a navigational compass[36] which, presumably, was developed to practical form soon thereafter. The navigational compass did not appear in Europe until its reinvention a century after Shen Kua.[37]

B) Magnetism, AD 1200 to 1900. From Peregrinus to Gilbert, Brahe, Copernicus, Kepler, Descartes, Bernoulli, Galvani, Volta, Mesmer, Louis XVI, Franklin, Oersted, Ampère, Faraday, Maxwell, Fitzgerald, and Hertz.

The search for a perpetual motion machine has probably occupied many minds from ancient to modern times. In 1269, such a machine, a "*perpetuum mobile*" that relied on magnetic behaviour for its function, was described by Petrus Peregrinus in the first European text on magnetism.[38] Much after Peregrinus, in 1600, and in a more scientific, experimental, approach to the study of magnetism, William Gilbert's monograph, *De Magnete*, identified the Earth as the source of magnetic force tending to align a compass needle which was contrary to the previously held view that magnetic forces originated from the Stars.[39] Gilbert "...inferred that the Earth itself was a great magnet".[40] He expands his ideas by suggesting that "...gravity was the magnetic force exercised by the giant lodestone of the Earth upon surrounding objects..." and "...that all of the bodies in the solar system mutually influenced each other's movements through the interaction of their magnetic forces".[41]

Gilbert was aware of the solar system models proposed by Brahe and Copernicus and agreed with Copernicus that the stars were fixed and stationary and that the Earth rotated on its axis daily.[42] Gilbert held that "As the earth, sun, moon, and planets were all magnetic bodies, they oriented themselves in space, just as compasses oriented themselves on earth, so that all the bodies of the solar system moved in the same plane with their axes parallel...".[43] Later, Kepler used Gilbert's ideas to explain the ellipticity of the planetary orbits and attributed planetary movements to magnetism by supposing "...that the sun sent out magnetic effluvia which rotated like the spokes of a wheel with the spin of the sun in the plane of rotation of the planets."[44]

It may be that Gilbert retained an ancient view that magnetic objects have a soul. According to Coey, this idea "...was finally laid to rest by Descartes",[45] but Coey does not provide any detail regarding Descartes' comments. Schuster[46] says that Descartes, in *Principles of Philosophy*, argues that magnetism can be explained mechanistically. (The Latin version of Descartes' book, *Principia Philosophiae*, was published in 1644. A French version, *Les Principes de la Philosophie*, was published in 1647.[47])

The period following Descartes was likely filled with both scientific and philosophical debate concerning magnetism, but progress was not entirely in the domain of conjecture since there was at least one important technical advance when, in 1743, Daniel Bernoulli invented the horseshoe magnet.[48] (There appears to be no shortage of confusion from web sources. A Wikipedia page[49] credits William Sturgeon for invention of the horseshoe magnet in 1825. It seems, however, that Sturgeon invented the *electro*magnet, in the shape of a horseshoe, but not the horseshoe magnet which is a permanent magnet, able to withstand its own demagnetizing field without destroying itself,[50] and not requiring current carrying windings. Coey has Bernoulli as inventor of the horseshoe magnet in 1743 and Sturgeon as inventor of the iron-cored electromagnet in 1824.)

Studies of magnetism and electricity were most certainly intertwined. In the 1780's, Galvani used the term *animal electricity* to account for muscle contractions of frog's legs when stimulated by an electric currrent.[51, 52] Volta, a contemporary of Galvani, continued the work and suggested a mechanism of muscle contraction different from that of Galvani's.[53, 54] In 1775, Franz Anton Mesmer brought magnetism to medicine by arguing that the human body contained an invisible fluid and that "...the invisible fluid in the body acted according to the laws of magnetism".[55] Mesmer called his theory *animal magnetism*.[55] (Coey[56] loosely suggests that Mesmer was inspired by the work of Galvani and Volta, but this was not verified.) Mesmer's doctrine of *animal magnetism* was "enthusiastically embraced in Parisian salons for some years...",[57] but was discredited in a 1784 report that followed a Royal Commission appointed by Louis XVI and chaired by Benjamin Franklin.[58]

Oersted's 1820 discovery, that a current carrying wire rotated around a magnetic pole and the converse observation that a magnet tended to rotate around a stationary current carrying wire, provided evidence for a rotatory force.[59] The existence of a rotatory force was in contradiction with current thought, particularly at the French school of Newtonian physicists, which held that "...all actions were the result of push-and-pull forces operating over a distance according to the inverse square law."[60]

By the end of 1820, Ampère had shown that a coil of wire, carrying a current, behaved like a magnet.[61] Later, in 1825, Ampère explained this observation by suggesting that magnetism resulted from "...resistance-free circular electric currents in the particles of magnetic bodies".[62]

A magnet induces magnetism in a piece of iron when the two are in near proximity and a body carrying a static electric charge introduces the appearance of charge on a nearby body. Faraday was aware of these magnetic and electric behaviours and, in 1822, began a

search for similar such effects in the behaviour of electric currents.[63] By 1831, Faraday's researches led him to the discovery of electromagnetic induction whereby varying an electric current in one coil of wire induces a current in a second, nearby, coil of wire and, similarly, moving the first coil of wire, whilst carrying a constant current, also induces a current in the second coil of wire.[64] Interestingly, Faraday rejected the atomic theory of matter and, also, the notion that forces acted at a distance over empty space.[65] He held that opposite electric charges and opposite magnetic poles were connected by lines of force that were contained in an ether filling all of space.[66] A unit of magnetism, or of electric charge, was associated with each line of force. For Faraday, the lines of force "...had a real physical significance".[67] (Giancoli, comments on the notion of a *field*, as developed by Faraday and says "Whether the electric field is *real* and really exists, is a philosophical, even metaphysical, question. In physics it is a very useful idea, in fact a great invention of the human mind."[68])

Faraday continued his work and, in 1845, while searching for a connection between light, magnetism, and electricity, discovered that introducing a magnetic field, in the propagation direction of linear polarized light incident on a piece of glass, caused a rotation of the plane of polarization.[69] In 1846, he suggested that the interaction of magnetism and light indicates that light may be "...wave vibrations along the lines of force."[70]

An electromagnetic theory of light was proposed by Maxwell in 1862.[71] He adopted an ether model wherein Faraday's lines of force were "...tubes of ether rotating on their axes."[72] and said that "...light consists in the transverse undulations of the same medium which is the cause of electric and magnetic phenomenon."[73] Maxwell eventually abandoned his ether model, but others, notably Kelvin and MacCullagh, developed their own ether models in the period 1867 to 1884.[74]

In 1883, Fitzgerald proposed that if Maxwell's electromagnetic theory of light was correct then electromagnetic radiations might be generated by periodic variation of an electric current in a circuit.[75] Hertz, in the period 1886 to 1888, was successful in generating and detecting electromagnetic waves and showed that the waves had properties similar to light in that they could be reflected, refracted, diffracted and polarized and that they traveled in straight lines at a velocity comparable to that of light.[76]

Electricity and magnetism come together not only in the theory of electromagnetic waves, but also in a way that gives rise to a measurable force. The Lorentz force law, remarkably simple in form, equates the force on a charged particle with terms including the charge, its velocity, and the electric and magnetic fields in which the charged particle is immersed.[77] (There appears to be somewhat of a story regarding determination of this law and how it was arrived at. Apparently, contributions from Maxwell's work, from J.J. Thompson in 1881, and from Oliver Heaviside in 1889 were all considered in the developments that ultimately led to the form derived by Lorentz in 1895.[78])

C) <u>Magnetism and Quantum Mechanics. Recent and present.</u>

Coey remarks that Gilbert's North and South magnetic poles have "...no physical reality..."[79] and that Ampère's approach, that the source of magnetic fields is electric currents, provides a better physical explanation for magnetic behaviour.[80] According to Coey, "...the real building blocks of electricity and magnetism are *electric charges* and *magnetic dipoles*; the dipoles are equivalent to electric current loops."[81]

By the late 19th and early 20th centuries, technical advances in the application of electricity and magnetism had already led to electric motors and generators, artificial lighting powered by electricity-carrying distribution networks, electric trams, and telegraph cables spanning the Earth.[82]

Chapter 1. Introduction.

There are some interesting historical facts surrounding telegraph cables and the development of permalloy. (This thesis is a report on the magnetic behaviour of bilayer samples of permalloy and cobalt oxide). Permalloy was invented in 1914 by Gustav Elman, at Bell Telephone Laboratories, as part of an effort to increase the rate at which telegraphic data could be transmitted over a cable and, in 1921, permalloy was patented by Western Electric, a subsidiary of Bell. Previously, in 1885, Oliver Heaviside worked out a theory for distortionless transmission of signals through cables by way of inductive compensation. The Telegraph Construction and Maintenance Company (Telcon), at Enderby's Wharf in Greenwich, SE London, used permalloy tape, provided by Western Electric, in the construction of a telegraph cable that was laid between New York and the Azores. In 1923, Telcon patented an alternative material, mumetal, that had desirable properties lacking in permalloy.[83]

In the early 1900's, theoretical advances had not yet led to a satisfactory explanation of ferromagnetism in solids. The molecular field theory of Weiss, approximately 1907, indicated that, for iron, there was "...an internal magnetic field parallel to, but some three orders of magnitude great than, the magnetization."[84] According to Maxwell, the magnetic field should be continuous, but the external field of a magnetized piece of iron is much lower than predicted by the molecular field theory.[85]

Classical physics was not able to provide a sufficiently accurate theory of magnetism. Identifying the underlying mechanism responsible for magnetism was not accomplished until a new physics, quantum mechanics, was developed. Continuing the discussion of magnetism, then, will have to be preceded by an introduction to quantum mechanics, a theory which provided explanation for many observations, made in the late 19th and early 20th centuries, that classical physics was unable to account for.

The theory of quantum mechanics had its beginnings in the search for an adequate explanation of blackbody radiation. An early attempt in 1896 by Wien was not successful, but the problem was solved in 1900 by Planck when he suggested that blackbody radiation is emitted in the form of energy quanta such that the radiation is discontinuous.[86] ('Energy quanta', and 'quantization' of the continuous parameters of classical physics are examples of the distinction between quantum and classical physics.)

Discovery of the electron by Thomson in 1897[87] and the nuclear atom by Rutherford in 1910[88] eventually led to Bohr's 1913 model of the atom wherein the atomic angular momentum was quantized and the electron orbits were characterized by so called *stationary states* that prevented radiation of electromagnetic energy thus preventing decay and eventual collapse of the orbits.[89] (Bohr had been working with Rutherford and suggested that Rutherford's atomic model could be rescued by introducing electron orbits that were in non-radiating stationary states.[90]) The wave properties of matter, a theory introduced by deBroglie in 1924,[91] was consistent with and provided support for Bohr's model. The foregoing are only a few examples of the many contributions to early quantum theory.

The development of quantum theory relied heavily on experimental observations obtained from spectroscopy. "Of all the tools that have been applied to the study of the detailed structure of matter, it can fairly be said that *spectroscopy* has been applied in more ways to more problems , and has produced more fundamental information, than any other."[92] Observations of atomic spectra provided experimental data that served as a guide to the early theoretical development of atomic models.

Bohr's model of the atom had a single quantum number, the *principal quantum number*, that specified the energy of the atomic state.[93] Bohr was able to give a quantitative account of the atomic spectra of hydrogen available at the time,[94] but, as the

resolving power of spectrographic instruments continued to improve, a finer structure in the spectra of hydrogen was revealed that Bohr's model was not able to explain.[95] The fine structure in the spectra of hydrogen was addressed by Sommerfeld who, in 1915, supposed that, in addition to Bohr's circular electron orbits, one should consider secondary, elliptical, orbits to which Sommerfeld assigned a second quantum number, the *orbital quantum number*, to specify the magnitude of the angular momentum of the electron.[96, 97] Sommerfeld also introduced a third quantum number, the *magnetic quantum number*. This third quantum number is assigned to the direction of the electron's angular momentum and allows for the energy levels to be split thus accounting for Zeeman's 1896 observation of the splitting of spectral lines when an atom is in a magnetic field.[98, 99]

With the work of Sommerfeld, the early quantum theory had three quantum numbers describing electron orbits, but the list of quantum numbers was not yet complete. In 1922, Stern and Gerlach conducted an experiment "...to measure the possible orientations in space of the magnetic moments of silver atoms."[100] The results indicated that "...the component of angular momentum in a certain direction is quantized...",[101] but no satisfactory manipulation of the three known quantum numbers could explain why two lines of silver atoms appeared on the collecting target when there should have been either one or three lines.[102] Specifically, the results suggested an orbital quantum number of 1/2 which was considered as unacceptable since it was not an integer value.[103]

In the 1920's, spectroscopists had "...found that some energy states appeared to require *half-integral quantum numbers* for their description."[104] In 1925, Uhlenbeck and Goudsmit suggested that, in addition to the angular momentum and magnetic moment resulting from orbital motion of the electrons, "...the observed energy shifts could be obtained by assuming that electrons possess angular momentum and a magnetic moment which would interact with the field of the nucleus...".[105] Uhlenbeck and Goudsmit introduced the idea that there are two sources of atomic angular momentum and magnetic

moment the first of which was the known contributions from electron orbital motion and the second being the result of an *intrinsic angular momentum* and an *intrinsic magnetic moment* associated with the electron itself.[106] These new properties of the electron were, at some point, described by the word *spin* although the notion of the electron "spinning" on its own axis does not seem to be correct.[107] A fourth quantum number, the *spin quantum number*, characterizes the new properties. For the electron, the spin quantum number can have values of either +1/2 or -1/2. The spin quantum number is particle specific and both integral or half-integral values are allowed. Pauli had suggested, also in 1925, the existence of a fourth quantum number, but he thought that it "...would be associated with the time coordinate in a relativistic theory...".[108] A substantial contribution did come from Pauli, again in 1925, when he "...formulated the principle that no two electrons in a given atom could have the same set of quantum numbers, a restriction which limited and defined the possible electronic structures of the elementary atoms."[109] (This is the *Pauli exclusion principle*.)

Chemists found Bohr's atomic model useful as a tool for interpretation of molecular structure and chemical combination.[110] Physicists, however, found Bohr's model to be inadequate since it provided explanation for only the hydrogen class of atoms and was unable to predict the relative intensities of spectral lines.[111] This problem was addressed in 1925 by Heisenberg when he suggested that mechanical models of the atom should be abandoned and that measurable parameters, such as spectral frequency and intensity, be used as the input to mathematical equations the output of which would provide the correct predictions.[112] Using this method, Heisenberg was able to explain the Zeeman effect which was problematic for the Bohr model.[113]

The theories of Bohr, Sommerfeld, and others of the time, are now referred to as the *old quantum theory* which was replaced by the theory of *quantum mechanics* that was developed during the period 1925 to 1930 by Heisenberg, Schrödinger, Dirac and others

"...following the ideas of de Broglie."[114] Two forms of the theory appeared at approximately the same time. The first, in 1925 and 1926, was that due to Heisenberg, Born, and Jordan which is described as *matrix mechanics* and the second, in 1925, was the *wave mechanics* from Schrödinger who, apparently, began by expanding on de Broglie's ideas regarding matter waves.[115] In 1926, Schrödinger was able to demonstrate an equivalency between matrix and wave mechanics both of which are now considered as "...particular forms of a general formulation of quantum mechanics, which was developed by P. A. M. Dirac in 1930."[116]

Schrödinger's wave mechanics suggested a vastly different atomic model than that of Bohr. The electron orbits in Bohr's model depended on quantization of the electron angular momenta for their stationary, non-radiating, character. Additionally, according to de Broglie, the circumference of a specific orbit should be an integral number of wavelengths where the wavelength is determined from the matter wave that is associated with an electron in that orbit.[117] These features of the Bohr electron orbits are not retained in Schrödinger's model since Schrödinger's electrons "...no longer moved in definite orbits."[118] This new atomic theory "...showed that the density of electric charge in the atom alternated in a wavelike form outwards from the nucleus, the peaks of the waves corresponding to what had been the orbits of the earlier Bohr atom."[119] Schrödinger's wave mechanics were, and still are, "...most fruitful..."[120], but his theory, while being able to account for three of the quantum numbers, did not predict the fourth quantum number (due to spin) and, since the dimension of time was not considered, the theory is a non-relativistic one.[121] Dirac's 1928 relativistic form of quantum mechanics contained terms accounting for the spin quantum number.[122] Dirac's theory also predicted the existence of a positively charged electron, the *positron,* which was discovered later, in the cosmic radiation, by Anderson in 1932.[123] (Note that Mason gives the date for Dirac's work as 1928 whereas Bransden and Jochain give it as 1930.)

An important development in quantum mechanics came from Born and Heisenberg. In 1926, Born suggested that "...the height of the wave at any point should be taken as a measure of the probability of finding an electron in that position."[124] Born's suggestion "...indicated that an electron could not be located with complete accuracy; only the probability of finding an electron at a particular point could be determined."[124] Similarly, Heisenberg showed, in 1927, that the product of an electron's momentum and its energy produced a result that could not be expressed with complete accuracy since the result would always be "...uncertain to a degree that could never be less than $h/2\pi$ where h was Planck's constant."[125] The inherent, unavoidable, and inescapable inability to specify a result with complete accuracy is embodied in *the principle of uncertainty* which "...follows from the wave-particle duality of matter and radiation..."[126] and is one of the defining, however curious, aspects of quantum mechanics.

Theories of magnetism, that are consistent with quantum mechanics, saw continued development during the years following Heisenberg, Schrödinger, and Dirac and continue to do so as new theoretical and experimental findings are made. A very short list of the contributions to magnetic theory after the mid 1800's is the study of spontaneous magnetization and hysteresis by James Ewing in approximately 1881,[127] Curie's Law by Pierre Curie in approximately 1895,[128] invention of the induction motor independently by Ferraris in 1885 and Tesla in 1887,[129, 130] Larmor precession by Larmor in 1897,[131] the discovery of ferromagnetic resonance phenomena by Arkad'yev in 1911,[132] the Ising model for magnetic systems by Ising in 1924,[133] introduction of the spin-orbit interaction possibly by Thomas or Dirac in approximately 1927,[134] the Heisenberg or Heisenberg-Dirac Hamiltonian, in 1929, representing the interaction between two neighbouring atoms,[135, 136] discovery of the Meissner effect by Meissner and Ochsenfeld in 1933,[137] discovery of antiferromagnetism by Louis Néel in 1936,[138] the Landau-Lifshitz equation by Landau and Lifshitz in 1935 and the contribution to it from Gilbert in 1955,[139] the

discovery of exchange bias by Meiklejohn and Bean in 1956,[2] and the continuing development of magnetic resonance imaging (MRI) that started in the 1970's.[140]

The list of contributions is by no means complete nor does it accurately identify what may have been the most important theoretical, experimental, or technical advances. Also, the study of magnetism is not confined to the minds and laboratories of physicists. Geology, geophysics, biology, chemistry, medicine, engineering, and other disciplines benefit from the accumulating knowledge regarding magnetism. The purpose of presenting the list was simply to demonstrate that the work has a long history and that new discoveries are likely to be made.

D) Ampère's molecular currents. Richardson, Einstein and de Haas, Barnett, Stewart, and Chattock.

The connection between magnetism and electron motion had been established, theoretically at least, well before 1900. (Recall that nearly a century earlier, Ampère, in 1825, suggested a connection between magnetism and circulating currents in the particles of magnetic bodies.) The contributions to atomic and quantum theory from Rutherford in 1910, Bohr in 1913, Sommerfeld in 1915, and others of the time, were not required to demonstrate, experimentally, the existence of Ampère's molecular currents. The opening sentence of a 1908 paper by Richardson indicates that the connection between magnetism and electron motion was already well known when he comments that "...the magnetic properties of bodies arise from the motion of the constituent electrons of their atoms."[141] Richardson's paper addressed the question of whether or not atomic magnetism, caused by the motions of electrons in an atom, could be compared, or equated, to the macroscale magnetism observed by Ampère in a current carrying coil of wire thus providing supporting evidence for Ampère's 1825 suggestion regarding molecular currents.

An interesting historical point regarding the atomic model available to Richardson is that he refers to both negative *and* positive electrons and to two types of atoms. In 1908, there were both chemical and magnetic atoms. Richardson points out that "...in many cases the magnetic atoms are the same as the chemical atoms, in other cases possibly not."[142] He describes the electron motions as being orbital, but does not indicate what might be, if anything, at the centre of the electron orbits. Further, he suggests that the positive electrons are not in motion. "The most usual form of the electron theory of matter assumes that the negative electrons alone are in motion and most of the experimental facts seem to be in favor of this conclusion."[143] It appears that developments in atomic theory proceeded quite quickly during the period 1908 to 1915.

Richardson adopts the view that atomic magnetic fields arise from the orbital motions of electrons[144] in the same way that Ampère's macroscopic magnetic field arises from electric currents circulating in a coil of wire. He then gives an expression for the atomic magnetic moment that can be assigned to the motion of an electron in its orbit and notes that when there is no preferential alignment of the magnetic moments the total magnetic moment will be zero and the body will not be magnetized.[145] If an external magnetic field is introduced, the atomic moments will align in the direction of the external field thus giving rise to a magnetization which Richardson gives as a combination of the moments generated by both positive and negative electrons.[146] The angular momentum of the orbiting electrons is deduced using the methods of classical mechanics. On the assumption that the motions of the positive electrons are not orbital, Richardson arrives at an expression for the summed effects of the negative electrons where the ratio of the angular momentum per unit volume to the magnetization is "...equal to twice the inverse of the specific charge (e/m_e) of the negative electrons."[147] (A value for the specific charge was available from Thomson's work in 1897, but Richardson does not comment on which value was being used or from whence it came. He just has e/m_e with no value.)

At some point, Richardson's ratio of the angular momentum per unit volume to the magnetization became more commonly used in its reciprocal form, i.e. the ratio of magnetic moment to angular momentum. The new form of the term is called the gyromagnetic ratio, γ, which, for orbital electron motion, has the value $(-e/2m_e)$. The negative sign accounts for the result that the magnetic moment and the angular momentum are oppositely directed owing to the negative charge of the electron.[148]

Finally, Richardson presents an experimental scheme whereby the existence of angular momentum, due to motions of negative electrons in atomic orbits, could be verified. He was at Princeton University at the time and says that such experiments were being conducted there, but that, as of 1908, success had not been realized "...owing to the difficulty of eliminating disturbing effects".[149]

Einstein and de Haas took up the same investigation as Richardson. In a 1915 paper, *Experimental proof of the existence of Ampère's molecular currents*,[150] Einstein and de Haas arrived at the same expression for the ratio of angular momentum to magnetic moment as did Richardson seven years previous. They used essentially the same arguments as Richardson, but note that they were not aware of his work until their paper was finished. Like Richardson in 1908, Einstein and de Haas admit the possibility of there being both positive and negative electrons. They go on to describe their apparatus and measurement technique both of which were quite elaborate and would be recognized as such even today. They reported a value for the proportionality constant, $(2m_e/e)$, that was approximately 30% different than expected, and note that some time later "...it came out that a mistake had been made in the application of the method, so that we must consider as a failure this part of our investigation."[151] They also report that their findings suggest a negative charge for the participating electrons. The work was continued at a later date. Some improvements were made to the apparatus and new experiments were conducted. The data were analyzed with a somewhat more detailed procedure than had

been used previously. This time, the value of the proportionality constant was found to agree with the expected value to within approximately 2.7% with a measurement uncertainty of up to 10%. Their closing comment is that "...within these limits the theoretical conclusions have been fairly confirmed by our observations".[152]

It seems that Einstein and de Haas regarded both their own and Richardson's theoretical treatments as unquestionably correct and that having obtained an experimental result in agreement with the theoretical prediction meant that the theory had been confirmed and that there was little or nothing left to do, however, the findings of Barnett,[153] published in 1915, the same year as the Einstein-de Haas paper, showed that the proportionality constant was only half the value predicted by Richardson. Barnett's scheme to measure the proportionality constant was quite different from that of Einstein and de Haas. Instead of measuring rotation caused by magnetization, Barnett measured the opposite effect (i.e. that of magnetization caused by rotation). The magnetization mechanism, as described by Barnett in his 1915 paper, is "...a sort of molecular gyroscopic process..." whereby a substance, when rotating, "...becomes the seat of a uniform intrinsic magnetic intensity parallel to the axis of rotation...".[154] If the substance is magnetic then it will become magnetized.

The values of the gyromagnetic ratio reported by Einstein and de Haas and those reported by Barnett differ by a factor of approximately two. In 1918, Stewart,[155] using a method similar to that of Einstein and de Haas, reported a result that was in agreement with that of Barnett's, but concluded that the measured value, only half of the expected value, resulted from motion of negative electrons about the nucleus combined with rotation of the positively charged nucleus in the opposite direction (no one knew about spin at this time). Chattock, in 1922,[156] using the method of Stewart, but with some modification, reported results for iron and nickel that were all within approximately one

percent of 0.5 meaning that he, as did Barnett and Stewart, also obtained a value of only half of what was expected.

The moment due to electron spin was not recognized until after it was suggested by Uhlenbeck and Goudsmit in 1925 and demonstrated in Dirac's 1928 theory. Upon including this additional moment, the value for the gyromagnetic ratio becomes one half of the value predicted by Richardson so that the observations of Barnett, Stewart, and Chattock turn out to be essentially correct.

Sometime after the discovery of ferromagnetic resonance, a discrepancy between values of the gyromagnetic ratio obtained from magnetomechanical methods (those of Einstein and de Haas, Barnett, Stewart, and Chattock) and those obtained from ferromagnetic resonance methods had been observed. The discrepancy is discussed in a 1962 review paper by Scott,[157] where he points out that the problem was explained by Kittel in 1949.[158] Sometime prior to Kittel's 1949 paper, it had become customary to multiply the gyromagnetic ratio, γ, by a *g-factor*, g (an electron g-factor was introduced by Alfred Landé as early as 1921). The gyromagnetic ratio for an orbital moment, $\gamma = -e/2m_e$, is used as a reference value and the form of the new term is either $g\gamma$ for gyromagnetic ratios obtained from ferromagnetic resonance methods or $g'\gamma$ for gyromagnetic ratios obtained from magnetomechanical methods. Kittel showed that a discrepancy between g and g' should exist and that, for values near the true value of g (both g and g' are nearly two for spin moments) the relation $1/g' + 1/g = 1$ holds.

Note that the g-factor for an orbital moment is precisely one whereas the g-factor for a spin moment, though usually taken as two, is slightly greater than two (refer to Chapter 2, subsection 2.1.5, ii). The spin moment, having both g and g' nearly two, not the orbital moment having g' = one, is responsible for the effects observed in ferromagnetic resonance and magnetomechanical experiments.

The conclusion to be drawn from measurements of the gyromechanical ratio is that the electron has two components of angular momentum and, therefore, two components of magnetic moment. One of these components results from orbital motion of the electron about a nucleus and is consistent with the notion of a classical Ampèrian current loop. The other component results from the intrinsic, or spin, property associated with the electron itself (i.e. an electron has this property even in the absence of any other particles and in the absence of any field). The spin property of the electron is not a classical one and, in fact, cannot be accounted for in the context of classical physics. "The mysterious built-in angular momentum emerges as a consequence of relativistic quantum mechanics."[159]

The historical account of magnetism given in this section is by no means exhaustive, however, the fundamental source of magnetism, that of the electron and the magnetic moment associated with it, has been identified. Protons and neutrons also have intrinsic spin, angular momentum, and a magnetic moment, but, as a result of the much higher masses of nucleons compared to that of electrons, the primary source of magnetism in solids is the magnetic moments of electrons.[160]

Magnetism most certainly has a long and eventful history with many interesting contributors and with many interesting developments, but further elaboration of historical context should not be necessary for adequate presentation of the experimental work, results, and conclusions that comprise the important aspects of this thesis.

Chapter 2

Theory and Experimental Methods.

2.0) Chapter introduction.

There are four sections in this chapter. The first section presents theoretical aspects and includes discussions regarding the requirement for theoretical considerations, assumptions, classification of materials, types of magnetic behaviour, fundamental magnetic theory, and the phenomenological model that was used for analysis of the data. Some of the experimental methods used to facilitate studies of exchange bias are presented in the second section. The third section is devoted to a detailed description of three-axis AC torque magnetometry and is directly relevant to the conducted experiment. Calibration is discussed in the final section. The subject of calibration is introduced followed by a description of the thermomechanical method that was used to calibrate the apparatus.

2.1) Theory.

2.1.0) Section introduction.

The section begins by explaining why it is necessary to introduce theoretical considerations. Assumptions, classification of materials, types of magnetic behaviour, and fundamental magnetic theory follow. The presentation of fundamentals will be

limited to those parts of magnetic theory that are necessary for identifying the underlying mechanism responsible for the magnetic effects observed in the experiment. Transduction of magnetic activity in the studied samples to a parameter that can be measured will be explained. The section closes with a description of the phenomenological model that was used to describe the observed exchange bias and interfacial coupling effects. The topics and their order of presentation are,

2.1.1) Requirement for theoretical considerations.
2.1.2) Assumptions.
2.1.3) Classification of materials.
2.1.4) Types of magnetic behaviour.
2.1.5) Fundamental magnetic theory.
2.1.6) Exchange bias phenomenological model.

2.1.1) Requirement for theoretical considerations.

The experiment was conducted by collecting measurements of voltage and the strengths of externally applied DC and AC magnetic fields. Specifically, voltage as a function of magnetic fields was the required parameter. How was the voltage produced? How did the magnetic fields affect the voltage? How can information regarding magnetic properties of the sample be deduced from voltage and field measurements? A review of some basic aspects of magnetic theory will aid in answering these questions.

2.1.2) Assumptions.

The underlying assumption adopted in this thesis is that the presently held *physical and theoretical constructs* are correct, or are sufficiently adequate, to account for the magnetic properties of substances. Here, *physical construct* simply refers to the atomic theory of matter wherein matter is composed of atoms that are themselves composed of electrons, protons and neutrons (the subatomic particles). The *physical construct* includes

all of what has been determined from previous experimental evidence, obtained by others, regarding the physical properties of subatomic particles such as mass, charge, and, specifically relevant to magnetism, the intrinsic magnetic moment and angular momentum carried by each. The *theoretical construct* refers to those theories, pertaining to atomic and molecular structure as well as to magnetic properties, that were developed during and since the time of Ampère, Maxwell, Faraday, Thomson, Rutherford, Bohr, Planck, Schrödinger, Heisenberg, Stern, Gerlach, Uhlenbeck, Goudsmit, Pauli, Dirac, and others. The *theoretical construct* also includes those contributions to condensed matter physics and chemistry that are relevant to the study of magnetism. These contributions include, but are not limited to, all that has been learned regarding the arrangement, motions, and various interactions between electrons and other particles or fields within an atom or molecule. Also included is what has been learned regarding interactions between conduction electrons.

The point being made in the above paragraph is that no new theories, or modifications to existing theories, will be presented in this thesis. The results from the experiment that was conducted do not indicate any requirement for new or additional theory for their explanation. To be specific, the required *physical and theoretical constructs* that are being assumed as correct are,

a) "The magnetic moments in solids are associated with electrons.",[161]

b) "The elementary quantity in solid-state magnetism is the magnetic moment...",[162]

c) "...intrinsic magnetic moments are associated with the spin of each electron and a further contribution is associated with its orbital motion around the nucleus.",[163]

d) for a magnetic moment, m, in a magnetic field, B, the moment experiences a torque given by the cross product of the moment with the field, $\vec{\tau} = \vec{m} \times \vec{B}$.[164]

Item (d) above is the most relevant to the experiment since the torque on a nanomechanical resonator is what generates the measured signal.

It may seem that the assumptions being made do not require justification since they are all well founded in the present paradigm of magnetism. It was necessary to accept them and their validity in order to provide a framework in which the results from the experiment could be considered, but one should be reminded that the present paradigm does not provide precise explanation for all magnetic phenomenon. For example, Ashcroft and Mermin point out that "The theory of the origin of magnetic interactions is one of the less well developed of the fundamental areas of solid state physics."[165] They further comment that,

> "Indeed, the development of a tractable model of a magnetic metal, capable of describing both the characteristic electron spin correlations as well as the electronic transport properties predicted by simple band theory, remains one of the major unsolved problems of modern solid state theory."[166]

(Electron spin correlations refer to the tendency toward parallel spin alignment resulting from electron–electron interactions.[167] Electron transport refers to "...the response of the electrons to applied fields or temperature gradients."[168] Band theory refers to "...the distribution of energy levels available to an electron which moves under the influence of the atomic nuclei and the other electrons inside a crystal...".[169] Band theory addresses some of the difficulties encountered in the free-electron model "...which can largely be attributed to the fact that the electrons of a metal are not really completely free but are acted upon by the atoms of the crystal lattice of the metal and by the other electrons."[170])

In discussing the magnetic ordering of solids, where the average magnetic moment of individual magnetic ions is non-zero below a substance specific critical temperature, Ashcroft and Mermin bring our attention to the fact that "No systematic solution has been found..." to describe magnetic properties as a function of temperature and applied magnetic field[171] and that "...a correct (currently nonexistent) general theory of magnetism in metals..." has yet to be developed.[172]

The comments from Ashcroft and Mermin are from their 1976 textbook. Are they still relevant? Have all questions been answered? Is there anything left to do? Marder, 2010, says that our work is unfinished. "If magnetism is the oldest great mysteries of solids, it has also remained one of the most difficult to explain."[173] "Some of the very simplest questions one can possibly pose in the subject of magnetism are still unsolved."[173]

Feynman reminds us of the shift from classical to quantum paradigms (early 1900's). If the fundamental source of magnetism is the angular momentum and magnetic moment of electrons then the classical Ampèrian current loop becomes rather problematic in spite of its remarkable ability to account for electron angular momentum and magnetic moment by considering orbital motion of an electron around a nucleus (the result derives from classical physics). Specifically, Feynman says that "...it would be dishonest to describe the magnetic properties of materials without mentioning the fact that the classical description of magnetism – of angular momentum and magnetic moments – is incorrect."[174] He continues by demonstrating that spin properties, which have their origin in quantum mechanics and not classical physics, are responsible for angular momentum and magnetic moment. What is retained is that magnetism is due to magnetic moments with the stipulation that the moments do not derive from the classical picture of microscopic Ampèrian current loops, but from quantum mechanical spin properties.

The inability of classical electrons (electrons not having spin properties) to account for magnetic properties is indicated by a result from classical statistical mechanics whereby it can be shown that "...*at any finite temperature and in all finite electric and magnetic fields, the net magnetization of a collection of electrons in thermal equilibrium vanishes identically*."[175] This result is known as the Bohr - van Leeuwen theorem. Bohr presented it in his 1911 doctoral thesis (note that this precedes Bohr's 1913 atomic model that had electron orbits with quantized angular momentum). The result was independently discovered by van Leeuwen and was presented in her 1919 doctoral thesis. The theorem

went somewhat unnoticed until it was reviewed by Van Vleck in his 1932 book, *The Theory of Electric and Magnetic Susceptibilities*, wherein he discusses and confirms the validity of the theorem.[176] The result of the theorem indicates that a classical description of magnetism is inadequate. "Every sort of magnetism is impossible for electrons in classical physics!"[177], "...a quantum theory is required from the start to explain any magnetic phenomenon."[178]

The foregoing discussion regarding assumptions and some of the inadequacies of the present paradigm of magnetism were presented as a cautionary reminder that the assumptions being adopted herein, though seemingly reasonable, may not be valid in future theoretical developments. There is always a possibility that some sort of new experimental evidence will force a rethinking of the present explanations for magnetic behaviours. No such evidence was found during conduct of the experiment, but it is important to acknowledge that the theoretical framework, being assumed herein as correct, may evolve and, given sufficient time, may change considerably.

2.1.3) Classification of materials.

Classification of materials according to their response to a magnetic field began as early as 1778 when Anton Brugmans discovered that bismuth was repelled by both poles of a magnet.[179] This work was continued in the early 1800's by Le Bailiff, Saigey, Seebeck, Coulomb, and Becquerel.[180] In 1845, Faraday, seemingly unaware of the previous investigations conducted by Brugmans, rediscovered the phenomenon and used the term *dimagnetic* to describe substances that showed the behaviour.[181] He later used the word *diamagnetism* which is the term that appears in his 1845 paper, published in the Philosophical Transactions of the Royal Society,[182] where he acknowledges the works of Le Baillif, Coulomb, and Becquerel concerning diamagnetism. Faraday classified a substance as diamagnetic if it moved from a region of higher to lower field strength.

Substances that were attracted toward higher field strength were called *magnetic*. In this paper, Faraday does not use the terms *paramagnetic* or *ferromagnetic* as is loosely suggested by Coey.[183] Faraday does suggest, however, that nickel, iron, and cobalt, substances that are now recognized as elements having ferromagnetic properties, "...would stand in a distinct class...".[184]

Note that the classification of materials according to magnetic behaviour began well before the development of any sort of modern atomic model. Thomson's discovery of the electron in 1897, Rutherford's discovery of the nucleus in 1911, Bohr's model of the atom from 1913, and the notion of intrinsic electron angular momentum and magnetic moment suggested by Uhlenbeck and Goudsmit in 1925, came long after Faraday's 1845 work. Interestingly, Faraday rejected the idea of atomic matter and held that "...matter is everywhere present, and there is no intervening space unoccupied by it."[185] These facts are important since they provide an example of how progress (material classification in this case) can be made by way of experiments that are conducted well in advance of any suggestive or supporting theory. In the paper that describes his experimental work regarding magnetic properties of substances, Faraday does not present any theory, but does use the words *magnetic field*, *lines of magnetic force*, and *induced magneto-electric currents*. He refers to Ampère and seems to be aware of his work, but makes no reference to current loops or dipole moments. The paper is descriptive, not theoretical. (Had Faraday been concerned with theoretical aspects, he may have made reference to the working theory of the time which may have included molecular current loops, dipole moments, and torques on macroscale current loops.)

Faraday provided a method by which substances can be identified as diamagnetic or magnetic, but, in the decades following Faraday, other types of magnetism were found. A review of many papers and textbooks revealed that there is considerable variation in the number of distinct types of magnetism. Hurd's 1982 paper[186] presents a figure showing

fourteen types of magnetism. Coey reorganized Hurd's figure into what he (Coey) refers to as a *magnetic family tree*[187] in which 10 of Hurd's magnetic types are used. According to Coey, diamagnetism and paramagnetism are the two fundamental categories of magnetism and are the terms used to classify materials depending on their magnetic properties. In Coey's magnetic family tree, diamagnetism stands alone while paramagnetism is at the top of a long list of other distinct magnetic sub-categories including superparamagnetism, ferromagnetism, antiferromagnetism, ferrimagnetism, helimagnetism, asperomagnetism, sperimagnetism, and speromagnetism.

Hurd begins by discussing solids and lists five basic categories of magnetism: diamagnetism, paramagnetism, ferromagnetism, antiferromagnetism, and ferrimagnetism. With regard to magnetic behaviours he comments, on page 469 of the paper, that,

> "...apart from closed shell diamagnetism, and the diamagnetism and paramagnetism of conduction electrons, the behaviour comes from permanent, microscopic moments possessed by some or all of the ions in the solid; the difference between the behaviours lies in the internal arrangement of these moments."

(Closed shell means that the electronic configuration of an atom is such that there are no unpaired electrons. Conduction electrons are those that are not fixed to an atom and that are "...allowed to wander far away from their parent atoms".[188])

Hurd is quickly summarizing what had been established by the investigations conducted by Brugmans, Oersted, Ampère, Maxwell, Faraday, Thomson, Rutherford, Bohr, Planck, Schrödinger, Heisenberg, Stern, Gerlach, Uhlenbeck, Goudsmit, Pauli, and Dirac during the period 1778 to 1928 which, when assembled into a single coherent theory, led to the conclusion that magnetism results from the magnetic moments of electrons. By the mid 1920's, this had become the accepted view and it is held to this day.

(Nuclear magnetism, due to the magnetic moments of protons and neutrons, can usually be ignored since the effects are inversely proportional to mass.[189] The mass ratio of an electron to a nucleon is approximately 1/1836.)

2.1.4) Types of magnetic behaviour.

The classification of substances according to their magnetic behaviours began with Brugmans in 1778 (well before discovery of the electron and its magnetic properties) and is a continuing research endeavor in present times. Hurd[186] provides brief descriptions of the five most fundamental magnetic behaviours as do Cullity and Graham[190]. A shortened summary of their descriptions is,

a) Diamagnetism.

A diamagnetic substance is one which is repelled by an external magnetic field. The substance is attracted toward a region of lower field strength. In the absence of an external magnetic field, the atoms in diamagnetic materials have no net magnetic moment (note that all atoms show a diamagnetic effect even if the atoms do have a net moment[191]). An external field reduces the current associated with each electron orbit in an atom thus generating a net magnetic moment that opposes the external field. The total moment is the sum of the individual, field induced, atomic moments. The atoms are considered as non-interacting. The magnetic susceptibility is negative and is not temperature dependent. "Diamagnetism is a property of all magnetic states, but it is usually negligible compared with the magnetism arising from any spontaneous moments in the system."[192] Conduction electrons, those not tied to a particular atom, also contribute to diamagnetism since, in an external field, the electrons follow a curved path analogous to an orbital path.[193]

b) Paramagnetism.

If the orbital and spin moments of an atom or molecule do not cancel then each atom or molecule will have a net magnetic moment. In the absence of an external field, the direction of the moments is random as a result of thermal agitation (k_BT energy). When a field is applied, the moments tend to align in the direction of the field. An overall net moment results from a balance between the tendency toward thermally randomized alignment and the tendency for alignment with the field. The alignment is only partial and depends on the temperature and applied field strength. A measure of the magnetization gives a time-averaged, seemingly constant, value that does not reflect the fact that the individual moments are not fixed in direction, but have a rapid continuously varying deviation about some average direction.

Paramagnetic susceptibility is positive and is inversely proportional to the temperature. For atoms or molecules that can be considered as non-interacting, the susceptibility follows the Curie Law, $\chi = C/T$, where C is the material-dependent Curie constant and T is the temperature. For a system of atoms or molecules, each of which has a net magnetic moment and where there is coupling between the atoms or molecules, the susceptibility follows the Curie-Weiss Law, $\chi = C/(T - \theta)$, where θ is a material-dependent parameter with dimensions of temperature. (The coupling referred to in the Curies-Weiss Law is an exchange interaction "...which reflects the Coulomb repulsion of two nearby electrons, usually on neighbouring atoms, acting in conjunction with the Pauli principle..."[194]) At room temperature and in fields as high as several Tesla, alignment of the magnetic moments in paramagnetic materials is only partial and small since thermal disordering dominates.

In metals, the paramagnetism of conduction electrons (Pauli Paramagnetism) is weak since "...the conduction electrons of a metal occupy energy levels in such a way that an

applied field can reorient the spins of only a very small fraction of the total number of electrons."[195] The susceptibility in this case is less dependent on temperature than is the paramagnetic susceptibility of atoms or molecules.

c) Ferromagnetism.

Ferromagnetic materials are those that have magnetic ordering on a microscopic scale wherein the magnetic moments are aligned even in the absence of an external field (spontaneous magnetization). The magnetostatic energy of a ferromagnetic substance is minimized by the formation of many, small, micrometer scale, magnetic domains each of which is magnetized at, or near to, a substance specific saturation magnetization. The directions of the magnetizations in different domains is such that the overall magnetostatic energy is minimized which results in no net magnetization of the sample. The number, sizes, and arrangements of the domains and, thus, the directions of their spontaneous magnetizations, can be altered by an externally applied field such that an overall net magnetization of the sample is induced. "A ferromagnet is an example of magnetism where an external field is just an agent to make evident on a macroscopic scale the ordering that exists microscopically."[196]

Ferromagnetic substances have a characteristic temperature (the Curie temperature) below which the magnetism is ferromagnetic and above which the magnetism is paramagnetic. The spontaneous magnetization is a maximum at T = 0 and decreases with increasing temperature. Once the Curie temperature is reached, the spontaneous magnetization is zero. Above the Curie temperature, the substance has a susceptibility that follows the Curie-Weiss law.

Theories that attempt to account for ferromagnetism fall into categories that have "...at least two rather divergent viewpoints: (1) the localized moment theory, and (2) the band theory."[197]

i) Localized moments. In the localized moment theory, "...the electrons responsible for ferromagnetism are attached to the atoms and cannot move about in the crystal."[198] A net magnetic moment is localized at each atom. The theory put forth by Pierre Weiss, 1906, introduces a molecular field, internal to the substance, that is responsible for alignment of the atomic magnetic moments and provides a mechanism for the spontaneous magnetization of ferromagnets. Domain structure, a concept also due to Weiss, results in an overall net magnetization of zero for the sample. The theory accounts for, at least approximately, the temperature dependence of the saturation magnetism and the Curie-Weiss law behaviour of the susceptibility above the Curie temperature, but, due to the assumption of localized moments, predicts an integral magnetic moment per atom for metals that cannot be reconciled with the nonintegral moments that have been confirmed from experimental observations. Coey comments that the theory is "preposterous", and notes that it requires "...an internal magnetic field parallel to, but some three orders of magnitude greater than, the magnetization."[199]

The Heisenberg model, wherein an energy (an exchange energy) is generated by an interaction of the atomic spins, S_1 and S_2, of two neighbouring atoms, is also a localized moment theory since the moments are attached to the atoms and are not shared between them. Heisenberg's Hamiltonian, $H = -2JS_1 \cdot S_2$ where J is a material-dependent exchange coupling constant having units of energy, provides an alignment mechanism for the atomic moments. When J is positive, the system energy tends toward a minimum as the spin configuration of S_1 and S_2 tends toward parallel alignment in the same direction and, thus, positive J gives ferromagnetic behaviour. Conversely, negative J causes the spins to tend toward an anti-parallel alignment thus giving antiferromagnetic behaviour.

The Heisenberg Hamiltonian can be generalized to give a sum of exchange energies over all pairs of atoms in a lattice and, if the exchange coupling constant, J, is appropriately chosen, the sum can include atom pairs that are not nearest neighbours. The exchange coupling constant is given by $J = E_s - E_t$ where E_s and E_t are the energy eigenvalues obtained from solutions to the orbital Schrödinger equation that describes a two-electron system. E_s is obtained from solutions that do not change sign under interchange of the position vectors r_1 and r_2. These are the symmetric solutions and they require a singlet spin state (a state for which the total spin of the two-electron system is zero). E_t is obtained from solutions that do change sign under interchange of the position vectors. These are the antisymmetric solutions and they require one of the three triplet spin states (those states that have a total spin of one).[200]

Interestingly, "...underlying the exchange interaction are nothing but electrostatic interaction energies, and the Pauli exclusion principle."[201] The relative directions of magnetic moments affect the energy associated with them, but the "...energy dependence is usually electrostatic rather than magnetic in origin."[202] Magnetic dipole-dipole interactions and the spin-orbit interaction (the coupling of the spin and orbital angular momenta of an electron) "...are not often the dominant magnetic interaction. By far the most important source of magnetic interaction is the ordinary *electrostatic* electron-electron interaction."[203] However, Coey notes that "The spin-orbit interaction is the origin of many of the most interesting phenomenon in magnetism, including magnetocrystalline anisotropy, magnetostriction, anisotropic magnetoresistance and the anomalous planar and spin Hall effect."[204]

Brief descriptions of the phenomena mentioned in the previous paragraph are,

1) Magnetocrystalline anisotropy: the magnetization process depends on which crystallographic direction is chosen along which to apply an external field.[205]

2) Magnetostriction: the volume of an isotropic crystal changes in an applied field due to magnetic orderering.[206]

3) Anisotropic magnetoresistance: the electrical resistance of a sample depends on the relative directions of an induced current and the magnetization.[207]

4) Anomalous planar Hall effect: A resistivity term, in addition to the one describing the normal Hall effect, that is a function of the macroscopic average magnetization.[208]

5) Spin Hall effect: Spin-up and spin-down electrons accumulate on opposite edges of a current carrying slab.[209]

ii) Band theory. In the band theory of ferromagnetism, referred to also as the collective-electron or itinerant-electron theory, "...the electrons responsible for ferromagnetism are considered to belong to the crystal as a whole and to be capable of moving from one atom to another, rather than localized at the positions of the atoms."[210] Unlike the molecular field theory, wherein the moments are localized, band theory assumes that the moments are delocalized. Band theory is able to account for nonintegral values of the moment per atom whereas molecular field theory gives only integral values (a result contrary to observation). Cullity and Graham argue that molecular field theory "...is simply not valid for metals. Instead, band theory is a more useful approach."[211] An inadequacy of band theory is that it does not predict the correct number of moments per atom for some of the ferromagnetic alloys.[212]

Qualitative understanding of the magnetic properties of metals can be obtained by "...application of the Fermi-Dirac statistics to a gas of perfectly free electrons...",[213] but this approach is unable to provide sufficiently precise quantitative results. The difficulty encountered in the free-electron model can be "...attributed to the fact that the electrons

of a metal are not really completely free but are acted upon by the atoms of the crystal lattice of the metal and by the other electrons."[214] Electron motion within the crystal is subject to interactions with the atomic nuclei and the other electrons in the crystal. The atoms in the crystal are located at lattice sites which form a spatially periodic array and, thus, the potential energy function of the crystal is also periodic. Electron motion in the crystal is, then, subject to a periodic potential.

Band theory describes "...the distribution of energy levels available to an electron which moves under the influence of the atomic nuclei and the other electrons *inside a crystal*...".[215] A qualitative description of the energy levels is arrived at by first considering a very large atomic spacing followed by a decrease in spacing that represents the structure of the actual crystal. For very large spacing, the electron energy levels will be those of a single atom, but each will have an enormous degeneracy since the total number of any one level is obtained after multiplying by the total number of atoms. As the interatomic spacing is reduced, the degeneracy "...is *removed by the mutual interactions of the atoms*, with the result that *each highly degenerate level is split into a huge number of distinct levels*."[216] The number of levels is very large and the differences in energy between them is very small so that the distribution can be described as continuous thus permitting introduction of a *density of levels* "...over an energy range which extends from the lowest to the uppermost level of a given group."[217] The result of reducing the atomic spacing is that each of the original levels associated with the large spacing become organized into a narrow energy band with each band becoming broader as the interactions become greater.[218] The wave functions that describe the energy levels give distributions having the same symmetry and periodic nature as the crystal lattice so that "...an electron in a given energy eigenstate *is equally likely to be found in the neighborhood of any of the atoms of the crystal and cannot be regarded as being associated with any individual atom*."[219]

Solutions to the Schrödinger equation for an electron moving in the periodic potential of a crystal lattice are in the form of *Bloch functions*. A Bloch function is the product of a single electron wave function (given as a plane wave) and a function that has the same periodicity as the lattice.[220] There are ranges of energies for which there are no solutions. These energies are forbidden and cause *band gaps*, the origins of which are Bragg reflections that occur at zone boundaries where the wave vector, k, is equal to +/- nπ/a. (n is an integer referring to the band index and a is the lattice constant which gives the spacing between atoms.) "Bragg reflection of electron waves in crystals is the cause of energy gaps."[221]

The allowed energies form *energy bands* that are separated by the band gaps. Each value of n gives a range of allowed energies that form an energy band and a range of forbidden energies, at k = +/- nπ/a, that form a band gap (a one-dimensional treatment has been presented, but the arguments extend to, and are valid in, three dimensions). An important point is that, contrary to the case for *free* electrons, the wave vector, $\vec{k}$, in the Bloch functions, "...is not proportional to the electronic momentum."[222] Also, the quantity $\hbar\vec{k}$ that would normally give the momentum of a free electron is, for Bloch electrons, "...the *crystal momentum*..., but one should not be misled by the name into thinking that $\hbar\vec{k}$ is a momentum, for it is not".[223]

The wave function solutions to the Schrödinger equation describe the allowed electron *states* (sometimes referred to as *orbitals*). Filling of the electron states begins in the lowest energy band (i.e. with the lowest energy electrons) and continues until all of the electrons have been accounted for. The number of electron states in a given band is equal to twice the number of primitive cells in the crystal (the number of primitive cells is the same as the number of lattice points).[224] The factor of two comes from the Pauli exclusion principle whereby "...each level specified by n and $\vec{k}$ can accommodate two electrons of opposite spin."[225]

Filling of the energy bands results in one of several possible outcomes;

1) The electrons completely fill the lower energy bands. The next higher energy band is completely empty as are all other higher energy bands. The crystal is an electrical insulator since the electrons are not able to move in the presence of an electric field. Note, however, that the size of the energy gap between the highest filled band and the next higher, empty, band determines just how good of an insulator the substance is since, for very narrow gaps, additional energy (e.g. thermal or from AC fields of sufficiently high frequency[226]) may cause some of the electrons to jump across the energy gap. This process leads to a non-zero conductivity.

2) The electrons completely fill the lower energy bands, but the next higher energy band is only partially full. Higher energy bands are empty. The partially filled band has filled states that are adjacent to unoccupied states. The difference in energy between the highest occupied state and the next higher energy state is small. The situation leads to significant conductivity, the mechanism for which is far from obvious. Leighton provides an explanation as follows,

> "In order to have metallic conduction, it is necessary to have available a large number of unoccupied states which can be combined with one another to form *wave packets* which represent the motion of electrons in prescribed directions and with various momenta. The application of an electric field will then cause the phases and amplitudes of the various states contributing to a wave packet to change in a manner which corresponds to a change in direction and/or magnitude of the momentum under the action of the field, and the changes in the various possible wave packets will combine to represent an average convection of charge in the direction of the applied field."[227]

Conduction is also possible if there is an overlap in energy bands. Overlap occurs when there are available energy states near the bottom of a band that are lower in energy than states near the top of the next lower band. The filling order is always such that the lower energy states are filled first so that, in regions of overlap, the top of a band is not filled while the bottom of the next higher band is. Stokes gives an example of overlap in Barium metal where the overlap is due to a difference in band energy depending on crystallographic direction.[228]

3) As in (1) above, the electrons completely fill the lower energy bands and the next higher energy band is empty, but the energy gap is sufficiently small to allow for a significant number of electrons to be thermally excited from energies at the top of the filled band to the slightly higher energies at the bottom of the unoccupied band. The process results in a conductivity higher than that in insulators, but lower than that in metals. Such materials are called semiconductors. The temperature-dependence of the conductivity is opposite to that of metals. The conductivity decreases with increasing temperature for metals, but increases in semiconductors.[229] Materials that contain no impurities and that have the properties of a semiconductor are called *intrinsic* semiconductors. The mechanism for semiconducting behaviour is due to the narrow width of the energy gap as described. Note that the energy gap must be small, but considerably larger than k_BT.[230]

Another class of materials, which in their pure form are insulators, but have had small quantities of impurity atoms added to them, can also have semiconducting properties and are called *impurity* semiconductors. The impurity atoms are called *donor* atoms if "...they have *more* electrons than are needed to maintain saturated valence bonds with the surrounding normal atoms...", and are called *acceptor* atoms if "...they have *too few* electrons to maintain normal valence relationships

with neighboring atoms."[231] The process of adding impurities is often called *doping*. Donor impurities result in *n-type* semiconductors where the conductivity is due to migration of the surplus electrons. Acceptor impurities result in *p-type* semiconductors where conductivity is due to the migration of *holes* (holes represent a lack of electrons).[232]

The band theory accounts for ferromagnetism in iron, cobalt, and nickel. In nickel, for example, an exchange interaction affects the energies and filling of the 3d band. The 3d band is divided into two sub-bands one of which contains only spin-up electrons while the other contains only spin-down electrons. The 4s band is partially occupied as a result of overlap with the 3d band. The partially filled 4s sub-bands have equal numbers of spin-up and spin-down electrons thus giving a net moment of zero. There are ten electrons per atom in the 3d band. An exchange interaction is discussed by Ashcroft and Mermin[233] and by Kittel[234] wherein the interaction introduces a positive energy offset in the spin-down 3d sub-band so that instead of having 5 spin-down electrons it has only 4.4. The top of the spin-down sub-band is unoccupied. The spin-up 3d sub-band contains 5 electrons. A surplus of 0.6 electrons per atom (5 spin-up – 4.4 spin down) results in a net magnetic moment. All ten electrons are accounted for if "...the missing 0.6 electron per atom resides in a free electron band, with randomly oriented spins."[235] Ferromagnetism in iron and cobalt follows from similar filling and overlap behaviour of the 3s and 4s bands. (The exchange interaction mentioned here is not given explicitly by Kittel. He does say that "After allowance for the magnetic moment contribution of orbital electronic motion, nickel has an excess of 0.54 electron per atom having spin preferentially oriented in one direction."[236] Ashcroft and Mermin do not use the words "exchange interaction", but, instead, describe a procedure wherein "...one allows for a self-consistent exchange field...that can differ for electrons of opposite spins when the two spin populations differ."[237])

Ashcroft and Mermin provide a useful note regarding band theory,

> "To explain magnetic ordering in solids, in the great majority of cases it is necessary to go well beyond the independent electron approximation, upon which band theory, with its impressive successes in accounting for nonmagnetic properties, is based. It is rarely enough merely to introduce electron-electron interactions into band theory in the form of self-consistent fields."[238]

The localized electron theory does not account for all magnetic properties, but neither does the delocalized theory. Coey points out that magnetic behaviours of some elements and compounds are best described using the localized theory while the delocalized theory is more appropriate for others.[239] It would seem that both theories are required.

d) <u>Antiferromagnetism.</u>

Antiferromagnetism results from an atomic arrangement wherein a crystal is composed of two or more sublattices that are oriented such that the net magnetization is zero.[240] The existence of two oppositely oriented sublattices was proposed by Louis Néel in 1936. (According to Cullity and Graham this should be 1932 when Néel began development of his theory of antiferromagnetism.[241]) An interesting historical fact is that Néel was a student of Pierre Weiss, founder of the Weiss molecular theory.[242]

Above a material-dependent ordering temperature (the Néel temperature) the sublattice magnetizations are both zero and the material is paramagnetic. The susceptibility follows a Curie-Weiss law similar to that of a ferromagnetic except that "...the paramagnetic Curie temperature is usually negative."[243] The paramagnetic Curie temperature is deduced by extrapolating a plot of inverse susceptibility versus temperature to the point on the temperature axis where the inverse susceptibility is zero.

Antiferromagnetic ordering begins at the Néel temperature which can be identified by a small peak in the susceptibility. Below the Néel temperature, T_N, the susceptibility behaves differently depending on the direction of an externally applied field with respect to the antiferromagnetic axis. (Magnetocrystalline anisotropy determines the direction of the sublattice magnetizations and it is this direction that is taken as the antiferromagnetic axis.[244]) The parallel susceptibility, obtained when the external field is applied parallel to the antiferromagnetic axis, is zero when the temperature is zero and rises as the temperature is increased until it equals the paramagnetic value at $T = T_N$. When the field is applied in a direction perpendicular to the antiferromagnetic axis the susceptibility remains constant at the paramagnetic value from $T = 0$ to $T = T_N$.[245]

In the Heisenberg model, the exchange coupling constant, J, is negative for antiferromagnetic substances. A negative value of J implies anti-parallel spin alignment. The moment of an atom in one sublattice is oriented opposite to a neighbouring atom in the other sublattice. Below the Néel temperature, and in zero applied field, each of the sublattices has a non-zero spontaneous magnetization. The orientations of the sublattice magnetizations are opposite to one another so that the net magnetization is zero.

Néel used the molecular theory of Weiss to describe antiferromagnetic behaviour.[246] The theory is able to account for the spontaneous magnetizations and the behaviours of the parallel and perpendicular susceptibilities both below and above the Néel temperature.[247] Cullity and Graham point out that antiferromagnets "...contain essentially no free electrons and that the electrons responsible for their magnetic properties are localized to particular ions."[248] According to Cullity and Graham, band theory, having delocalized moments, would be less successful than the molecular field theory in accounting for antiferromagnetism,[249] however, in the case of certain alloys of manganese with copper, gold, or chromium, they say, regarding the molecular field theory, that "...it would be difficult to understand how any long range magnetic order could result." and that "...the behaviour is understandable on the basis of band theory."[250]

Antiferromagnets are much more common than ferromagnets. Ionic compounds (e.g. oxides, sulphides, chlorides) account for the constituencies of most of the antiferromagnetic compounds. The positive ions have a magnetic moment whereas the negative ions do not. The distances between positive ions is too great for there to be any significant effects due to *direct exchange*. (Direct exchange refers to the interaction between two neighbouring ions and "...arises from the direct Coulomb interaction among electrons from the two ions."[251] The form of the Heisenberg Hamiltonian, for example, implies direct exchange). The exchange interactions between magnetic moments in an ionic antiferromagnet take place by way of *superexchange* wherein the interactions between the moments of the positive ions are mediated by the electrons in the magnetically neutral negative ions.[252, 253] (Note that Cullity and Graham consider the terms *superexchange* and *indirect exchange* to be synonymous whereas Ashcroft and Mermin describe indirect exchange as being due to the coupling of f-shell electrons with conduction electrons and give the rare earth metals as an example. Ashcroft and Mermin describe the exchange interaction in antiferromagnets as one of superexchange. They also describe the exchange interaction between conduction electrons as being one of *itinerant exchange*.)

e) <u>Ferrimagnetism.</u>

Ferrimagnets are similar to ferromagnets in that both have spontaneous magnetizations at room temperature. Both also have domain structure and hysteretic effects in an externally applied field.[254] As in ferromagnets, the spontaneous magnetization of ferrimagnets decreases with temperature and is zero at a substance specific Curie temperature. Above the Curie temperature, ferromagnets and ferrimagnets are paramagnetic (antiferromagnets are also paramagnetic above a substance specific temperature, but this temperature is given as the Néel temperature). Commercial development of ferrimagnetic materials, undertaken by Snoek and his co-researchers at

the Phillips Research Laboratories in the Netherlands, occurred during the period 1933 to 1945, but a theory capable of providing an account of ferrimagnetism was absent until it appeared in a 1948 paper by Néel[255] (the same Louis Néel that provided a theory for antiferromagnetism in 1932, and who, according to Cullity and Graham, was the originator of the word "ferrimagnetism"[256]).

Like antiferromagnets, ferrimagnets are ionic compounds. Ferrimagnets are effectively insulators in which there is no overlap of the electron energy levels and in which the electrons, with their magnetic moments, are localized at each ion.[257] Since the moments are localized, the molecular field theory seems applicable to ferrimagnets and, in fact, this is the theory that Néel used.[258]

If a positive exchange force aligns all of the available moments in a ferrimagnet then the moment per molecule would be higher than observed, so it must be that, unlike ferromagnets, the alignment in ferrimagnets cannot be parallel.[259] The decrease in saturation magnetization as the temperature is increased from zero to the Curie temperature is more rapid in ferrimagnets than in ferromagnets. Also, the inverse susceptibility of a ferrimagnet is a nonlinear function of temperature and, thus, does not follow a Curie-Weiss law[260] as it does for a ferromagnet.

The observed magnetic moment per molecule and the behaviours of the spontaneous magnetization and inverse susceptibility led Néel to conclude that the magnetic structure of ferrimagnetic substances was different than any other previously observed structure.[261] Néel made the assumption that the exchange constant, J, was negative as in antiferromagnets and that, also as in antiferromagnets, there were two spontaneously magnetized sublattices. Ferrimagnets differ from antiferromagnets in that the sublattice magnetizations are not equal so that a net spontaneous magnetization is present below the Curie temperature.[262]

The spontaneous magnetizations at low temperatures near zero can be calculated for several ferrimagnetic substances and then compared to observed values. The calculated values assume interactions between ions, in two sublattices, at all sites A and B where the A sites are in one sublattice, the B sites are in the other, and the moments at the A sites are aligned antiparallel to the moments at the B sites. According to Cullity and Graham[263], the interactions are between ion pairs AA, AB, and BB (BA included in AB, apparently, but not mentioned specifically by Cullity and Graham). The exchange constants, J, "...all tend to be negative, but they cannot all be negative simultaneously.[263] As in antiferromagnets, the exchange interactions are those of superexchange that are mediated by oxygen ions that have no magnetic moment. The calculated values for the spontaneous magnetizations agree reasonably well with the observed values, thus providing support for the ideas put forth by Néel. Further evidence for antiparallel alignment of the A and B moments came from neutron diffraction.[264]

2.1.5) Fundamental magnetic theory.

Theoretical considerations directly relevant to the experiment concern the response of the magnetic moments in a bilayer sample of ferromagnetic and antiferromagnetic materials during application of external DC and AC magnetic fields. More specifically, it was the response of the moments in the immediate vicinity of the interface between the two materials that was of interest since it is in this region that the effects of exchange bias are thought to originate.[265]

i) General.

Exchange bias refers to the the effect first observed in 1956 by Meiklejohn and Bean[2] wherein, after cooling the sample from a temperature above to one lower than the Néel temperature of the antiferromagnetic material while applying, during the cooling period,

a constant DC bias field of sufficient strength to saturate the ferromagnetic layer, the coercive points of a linear hysteresis loop are shifted as compared to those of a linear hysteresis loop obtained from the sample when it is above the Néel temperature (a prerequisite is that the Curie temperature of the ferromagnetic material must be higher than the Néel temperature of the antiferromagnetic material). The shifted linear hysteresis loop results from an anisotropy (a unidirectional anisotropy) that was not present in the sample while above the Néel temperature of the antiferromagnetic material, but that was induced as a result of field- cooling to a point below the Néel temperature during which time the moments of the ferromagnetic layer were aligned by the external DC bias field.[266]

The ferromagnetic and antiferromagnetic materials are in contact at the interface between them so that there is a coupling between the moments of both layers resulting in an anisotropy that has a preferred direction (thus unidirectional) and that is determined by the direction of the DC bias field that is applied during cooling. Cooling from above the Néel temperature to a lower temperature causes the moments in the antiferromagnetic layer to transition from their initially paramagnetic state to an antiferromagnetically ordered state. As a result of the interfacial coupling between the ferromagnetic and antiferromagnetic layers, the sublattice magnetizations of the antiferromagnetic layer will be in the direction of the moments in the ferromagnetic layer which, themselves, are in the direction of the DC bias field that is applied during cooling. The moments of the antiferromagnetic sublattice that is immediately adjacent to the ferromagnetic layer will be in the same direction as the moments in the ferromagnetic layer. The moments in the other sublattice will be oppositely directed so that an antiparallel alignment of the sublattice moments is maintained. The process of field-cooling results in an arrangement of moments at the interface that are coupled and that remain so even after the DC bias field is removed.[267]

A requirement for a shifted linear hysteresis loop is that there must be "...strong crystal anisotropy in the antiferromagnetic."[268] The shift in the linear hysteresis loop occurs since, although the interfacial moments are coupled, the ferromagnetic moments rotate relatively freely during reversal of the external field, while the antiferromagnetic moments rotate less because of the strong anisotropy in the antiferromagnetic layer.[269]

Two additional exchange bias effects observed by Meiklejohn and Bean[2] are: 1) the shape of the torque curve, obtained while rotating the field about the sample, changes from a $\sin(2\theta)$ behaviour for temperatures above the Néel temperature (i.e. the sample is not exchange biased) to a $\sin(\theta)$ behaviour if the sample is exchange biased by the field-cooling procedure, and 2) the field-cooling procedure causes rotational hysteresis in the torque curve.[2] Rotational hysteresis in the torque curves appears as a torque offset such that the net area between the curve and the horizontal axis is not zero.[270] The cause of the rotational hysteresis, sometimes called rotational hysteresis loss, is due to "...irreversible processes of spin rotation or domain wall motion..." that occur during rotation of the field.[271]

With regard to the rotational hysteresis mentioned above, note that it is a DC effect and that it is observable in a DC torque curve. An AC torque measurement, obtained by applying a small AC dither field to the DC field, will not be sensitive to a DC offset and, therefore, the torque curve so obtained will not show rotational hysteresis as described. The torques generated in the experiment were of the AC dither type and, so, rotational hysteresis in the form of a DC offset was not observable, however, rotational hysteresis in the form of differences between the torques obtained during a 360 degree clockwise rotation of the field and those obtained, immediately thereafter, during a 360 degree counterclockwise rotation were observed and are presented in Chapter 6.

ii) Theory for the experiment.

The experiment was conducted by collecting measurements of voltage and the strengths of externally applied DC and AC magnetic fields. The apparatus can be thought of as a "motion to voltage" transducer whereby the movement of a nanomechanical resonator, to which a magnetic sample is attached, is converted to voltage by the combination of an optical interferometer with an optical receiver, the output of which is a voltage that is proportional to the resonator motion.

To obtain an output from the apparatus, there must be an interaction between the magnetic moments in the sample and an externally applied field that causes the resonator to move. That there is such an interaction can be deduced from what has been discovered regarding magnetism, magnetic moments, and the behaviour of magnetic moments in external magnetic fields.

a) For a magnetic moment, m, in a magnetic field, B, the moment experiences a torque given by the cross product of the moment with the field, $\vec{\tau} = \vec{m} \times \vec{B}$.[272]

b) "Magnetism is intimately connected with angular momentum of elementary particles...".[273]

c) The relation between magnetic moment, m, elementary charge, e, electron mass, m_e, and angular momentum, $\boldsymbol{\ell}$, is $m = -(e/2m_e)\boldsymbol{\ell}$ where the quantity, $-e/2m_e$, is the gyromagnetic ratio, γ. A g-factor is commonly introduced to obtain the quantity $g\gamma$. The electron orbital moment has a g-factor of precisely one. For the electron spin moment, the g-factor is usually taken as two, but more precise values obtained from QED (quantum electrodynamics) are 2.002319314 [274] from 1989 and 2.00231930436256(35) [275] from 2019. Dirac's theory produces a value

of precisely two, but the value obtained from QED, referred to as the anomalous magnetic moment, agrees with the experimentally determined value to "...exquisite precision..." and both the calculation and measurement, are "...among the greatest achievements of twentieth-century physics."[276] The orbital angular momentum, $\boldsymbol{\ell}$, is quantized in units of ħ so that the component of m along some direction, usually taken as the z direction, is $m_z = -(e/2m_e)m_\ell\hbar$ where m_ℓ is the *orbital magnetic quantum number* having integer values. The quantity, $e\hbar/2m_e$, is a convenient unit and is called the Bohr magneton with notation μ_B and a 2019 value of $9.2740100783(28) \times 10^{-24}$ J/T.[275]

d) By integrating the torque in (a), the potential energy associated with the angular position of the moment with respect to the field is $E = -m \cdot B$.[277]

e) Application of an external field generates a torque on an orbiting electron through the relation in (a), $\vec{\tau} = \vec{m} \times \vec{B}$. The torque is also given by the time rate of change of angular momentum, $\tau = dl/dt$, which results in Larmor precession where the moment precesses around the direction of the applied field at an angular frequency of $\omega = \gamma B$. γ is the gyromagnetic ratio and is given as $-e/2m_e$ for an orbital magnetic moment or twice that value, $-e/m_e$, for a spin magnetic moment.[278]

Point (a) above is the sought after interaction. An externally applied field will interact with the magnetic moments in the sample with the result that a torque on the moments will be generated. The torque on the moments must somehow be transferred to the sample which means that there must be some form of coupling between the moments and the crystal lattice in which they reside. The precise nature of this moment-to-lattice coupling may not be entirely understood, but the result is nonetheless observable as was made evident in the Einstein-de Haas[150] and Barnett[153] experiments. Points (b) and (c)

show that magnetic moment and angular momentum are connected through the relation given in (c), $m = -(e/2m_e)\boldsymbol{\ell}$. Coey explains that "Spin-orbit interaction is the mechanism by which the spin system couples to the lattice phonon bath."[279] The spin-orbit interaction results from a viewpoint wherein the nucleus revolves around an electron. A current loop is associated with the revolving nucleus and, thus, there is a magnetic field at the location of the electron. Interaction of this field with the intrinsic (spin) magnetic moment of the electron results in an interaction energy through the relation $E = -m \cdot B$.[280]

Fortunately, for the experiment conducted, it was not necessary to know precisely how the torque was transferred from the moments to the lattice. The relation between moment, field, and torque held and applied to the sample. The torque was transferred to the resonator by way of direct physical attachment of the sample to the resonator. It can be inferred, then, that motion of the resonator was tied directly to the response of the moments in the sample to the external field.

Point (d) above is necessary since it provides a means by which to connect the torque to energy. A phenomenological energy equation containing several terms was used as a tool to investigate certain material constants relevant to exchange bias and interfacial coupling.

Point (e) above is relevant since precession of the magnetic moments, or, to be more precise, *damped* precession, is included in the Landau-Lifshitz-Gilbert (LLG) equation that was used to reduce the data. The LLG equation has a phenomenological damping term that causes the otherwise free precession of the moments to eventually stop so that the moments will be aligned with the field.[281]

2.1.6) Exchange bias phenomenological model.

Phenomenological energy equations provide a suitable platform for investigating the anisotropies found in magnetic systems. Such equations were used by Meiklejohn[6] and, in more recent times, by others.[8, 9, 282] It was this type of equation that was used to investigate the exchange bias and interfacial coupling effects observed in the experiment. The form of the equation was not introduced by our group, but, instead, follows from the forms used by Stiles and McMichael,[8] da Silva et al.,[9] and Müglich et al.[282]

The equation that was used was assembled by Michael Dunsmore of our research group and is expressed by writing the total energy density, ε_T, as the sum of the densities for the anisotropy energy, ε_A, the demagnetization energy, ε_D, and the Zeeman energy, ε_Z.

i) Anisotropy energy density.

The expression for the anisotropy energy density, ε_A, is,

$$\varepsilon_A = -K_{SF}\sin^2(\theta)\cos^2(\Phi - \Phi_{SF}) - K_{EB}\sin(\theta)\cos(\Phi - \Phi_{EB}) - K_{Rot}\cos(\Delta\Phi_{Rot} - \Delta\Phi_m). \quad (2\text{-}1)$$

The anisotropy constants and angles in the equation above are,

1) θ and Φ are the polar and azimuthal angles in a standard spherical coordinate system that was used to approximate the geometry of the sample. These angles give the orientation of a macrospin moment that describes the magnetization of the sample as a whole. Φ is in the x-y plane of the sample and can have values ranging from 0 to 2π with 0 corresponding to the apparatus x direction. θ is measured from the apparatus z direction which is the out-of-plane direction for the sample. As a

result of the thin-disc geometry, the magnetization in the out-of-plane direction is very small compared to the in-plane magnetization and, therefore, the values for θ are considerably less than the full range of 0 to π. In fact, θ is always very near $\pi/2$.

The magnetization magnitude and orientation are considered as being in a steady state condition since the effect of the externally applied AC field introduces only a very small perturbation to this condition. The macrospin moment is an aggregate of the smaller moments that exist at a much smaller scale throughout the body of the sample including those moments located at the interface between the ferromagnetic and antiferromagnetic layers. Specific steady state values of θ and Φ are obtained from solutions to the LLG equation by ensuring that sufficient time is given for the damping term to arrest the free precessions of the individual, small scale, moments, thus providing an orientation of the macrospin moment that can be considered as steady state. The external DC bias field is applied in the plane of the sample. Reversals of the external field as would be done for generating linear hysteresis loops, or 360 degree rotations of the field in the x-y plane as would be done for generating rotating hysteresis loops, force full rotation of the macrospin moment thus probing the in-plane coupling effects over full rotations of the magnetization.

2) Spin-flop coupling, K_{SF}. θ and Φ are as given in (1). The spin-flop coupling is uniaxial and results from canting of the antiferromagnetic sublattices with respect to their natural, equilibrium, orientations. Deviation of the sublattice orientations is caused by interaction with the ferromagnetic magnetization. A minimized energy state occurs when the ferromagnetic magnetization is perpendicular to the unperturbed orientations of the antiferromagnetic sublattice moments and, since this minimized energy state is the most favourable, the orientation of the canted configuration gives the orientation of an easy axis.[283]

Φ_{SF} is the angle between the direction of the spin-flop field and the zero reference. The magnitude and orientation of the spin-flop field are set during field-cooling from above to below the Néel temperature of the antiferromagnetic layer. The orientation of the spin-flop field is not required to be in the same direction as that of the external DC bias field that is applied immediately before and during cooling. The spin-flop field orientation will be in a direction that results in the lowest energy. Once set, the magnitude and orientation of the spin-flop field remain fixed even during rotation of the external DC bias field and rotation of the ferromagnetic magnetization that results therefrom (our understanding is that the spin-flop field is fixed during field-cooling and remains fixed thereafter, but this could not be determined from the literature that was reviewed).

3) Unidirectional anisotropy due to exchange bias, K_{EB}. θ and Φ are as given in (1). The spins in the antiferromagnetic layer that are immediately adjacent to the ferromagnetic layer (i.e. at the interface) are uncompensated, thus creating an interfacial monolayer of spins that have a net magnetization.[283, 284] The uncompensated spins resist rotation owing to the high anisotropy in the antiferromagnetic layer. The overall effect is unidirectional anisotropy at the interface.

Φ_{EB} is the angle between the exchange bias field and the zero reference. Φ_{EB} is established by the cooling-field direction and is usually considered to coincide with that direction, but tendency toward energy minimization is the controlling factor so that orientation of the unidirectional anisotropy is not necessarily required to be in exactly the same direction as the cooling-field. As for the spin-flop field, the magnitude and orientation of the unidirectional anisotropy remain fixed once set.

4) Rotatable anisotropy, K_{Rot}. A rotatable anisotropy axis exists due to the compensated antiferromagnetic spins that are near, and coupled to, the ferromagnetic spins at the interface. The compensated antiferromagnetic spins are free to rotate with the ferromagnetic magnetization, but, as a result of anisotropy, the compensated antiferromagnetic spins are not in precisely the same direction as the ferromagnetic spins. The anisotropy is represented by the anisotropy constant, K_{Rot}, while the angle between the spins that participate in this interaction is given by a small angle, $\Delta\Phi_{Rot}$.[283, 285] Once set, $\Delta\Phi_{Rot}$ remains constant.

$\Delta\Phi_M$ is the dither in the direction of the ferromagnetic magnetization. The dither is induced by the externally applied AC fields. Note that $\Delta\Phi_M$ is part of the argument in the cosine term for the rotatable anisotropy. The torque depends on the magnetization through $\vec{\tau} = \mu_o \vec{m} \times \vec{H}$ so that AC dithering of the magnetization generates an AC torque.

ii) <u>Demagnetization energy density.</u>

The expression for the demagnetization energy density, ε_D, is,

$$\varepsilon_D = \frac{1}{2}\mu_0 M_S^2\left[N_x \cos^2(\Phi)\sin^2(\theta) + N_y \sin^2(\Phi)\sin^2(\theta) + N_z \cos^2(\theta)\right]. \quad (2\text{-}2)$$

The constants and angles in the equation above are,

1) μ_o is the free space permeability.

2) M_S is the saturation magnetization of the ferromagnetic layer.

3) N_x, N_y, and N_z are the demagnetization factors in the x, y, and z directions. These directions coincide with the x, y, and z reference directions of the apparatus. Values for these constants were obtained by Michael Dunsmore using software tools to solve the elliptic integrals presented in a paper by Joseph[286] for calculating cylindrical demagnetization factors.

4) θ and ϕ are as given for equation (2-1). The form of the equation follows from the demagnetization energy given by the dot product of the demagnetizing field components, H_{Di} (i = x, y, z), and the saturation magnetization, M_s. The equation is described and discussed in papers by Rowlands[287] and Goode et al.[288]

iii) <u>Zeeman energy density.</u>

The expression for the Zeeman energy density, ε_Z, is,

$$\varepsilon_Z = -\mu_o \vec{m}_{FM} \cdot \vec{H}_{ext}^{DC} = -\mu_o m_{FM} H_{ext}^{DC} \cos(\Phi_{DC} - \Phi_m), \qquad (2\text{-}3)$$

where m_{FM} is the magnetization of the ferromagnetic layer, H_{ext}^{DC} is the externally applied DC bias field, Φ_M is the angle between the ferromagnetic magnetization and the zero reference, and Φ_{DC} is the angle between the externally applied DC bias field and the zero reference.

iv) <u>Total energy density.</u>

The total energy density, ε_T, is given by the sum of the individual energy terms,

$$\varepsilon_T = \varepsilon_A + \varepsilon_D + \varepsilon_Z. \qquad (2\text{-}4)$$

The phenomenological energy equation and the LLG equation are in forms that are ideal for iterative computation. Michael Dunsmore prepared a suitable program. Inputs to the program were the anisotropy constants, the axis orientations, the demagnetization factors, the saturation magnetization, and the externally applied DC and AC field strengths and their orientations. Simulated data generated by the program were compared to the observed data. Best fits to the data were obtained by suitable refinement of the anisotropy constants and angles.

2.2) Experimental Methods

2.2.0) Section introduction.

Several experimental methods have been used to study exchange bias. Though not an exhaustive list, some of the common methods rely on measurements and analysis of data obtained from,

2.2.1) DC torque magnetometry.
2.2.2) Anisotropic magnetoresistance, (AMR).
2.2.3) Transverse AC susceptibility.
2.2.4) Ferromagnetic resonance, (FMR).
2.2.5) X-Ray diffraction, (XMLD and XMCD).
2.2.6) AC torque magnetometry. (This was the method used for the experiment.)
2.2.7) Computational methods.

Experimental methods 1 to 7 will be described briefly in subsections 2.2.1 to 2.2.7. A three-axis AC torque magnetometer will be discussed in section 2.3. (This was the apparatus that was used to obtain data for our work.) Section 2.3 also gives the procedures that were used to obtain the experimental data. The method of thermomechanical calibration of the data is presented in section 2.4, subsections 2.4.5 to 2.4.7.

2.2.1) DC torque magnetometry.

The original discovery of exchange bias was made by Meiklejohn and Bean.[2] A DC torque magnetometer was used to obtain linear hysteresis loops as a function of applied DC magnetic field.[2, 9] Torque curves as a function of the angle between a fixed applied DC field and the easy axis of the sample were also obtained.

Linear hysteresis loops that show a shift of the coercive points after the sample has been field-cooled from above to below its Néel temperature are taken as evidence for exchange bias. A change from two-fold, non-hysteretic, to single-fold, hysteretic, angular behaviour in torque curves is also taken as evidence for exchange bias. (Meiklejohn and Bean[2] also observed considerable rotational hysteresis loss in the torque curves.)

2.2.2) Anisotropic magnetoresistance, (AMR).

Anisotropic magnetoresistance, (AMR), refers to the effect whereby a change in the relative directions of an induced current and the magnetization in the sample causes a change in the resistances between the contacts of a four wire, van der Pauw, arrangement of the leads attached to the sample. The van der Pauw formula is used to calculate the resistances from which the magnetization direction can be deduced.

Resistance measurements obtained from linear and rotating hysteresis loops show behaviours similar to those obtained from torque magnetometry (shifted linear loops and rotational hysteresis). AMR was used by da Silva et al.[9] and McMichael et al.[289]

2.2.3) Transverse AC susceptibility.

The fields associated with uniaxial and unidirectional anisotropies can be determined from measurements of the transverse AC susceptibility wherein a low frequency AC magnetic field, ($f_{AC} << f_{FMR}$), is applied perpendicular to a saturating DC magnetic field. The magnetization oscillations, induced by the AC field, can be detected using the magneto-optical Kerr effect, (MOKE). Both parallel and perpendicular AC components of the magnetization can be obtained. The data can be used to generate plots of the linear hysteresis from which the influence of the uniaxial and unidirectional anisotropies may be deduced. The technique is presented in a paper by Mitrofanov.[11]

2.2.4) Ferromagnetic resonance, (FMR).

Subjecting a sample to a fixed DC magnetic field and an RF field, perpendicular to the DC field, establishes the configuration for ferromagnetic resonance, (FMR), studies. Precession of the magnetization is driven by the RF field. When the frequency of the RF field coincides with the Larmor frequency, a resonance condition occurs causing the sample to absorb energy from the RF field. The absorption can be measured from the response of a receiving coil in close proximity to the drive coil. Since the Larmor frequency depends on the strength of the DC field, the absorption measurement can be obtained by either varying the DC field strength or the frequency of the RF drive field.

FMR provides information regarding the saturation magnetization, magnetic anisotropies, and the gyromagnetic ratio, γ, and is thus suited for studies of exchange bias. Specifically, the resonance frequency of a sample changes when the sample is exchange biased. The resonance frequency also has a dependence on the direction of the fixed DC field and shows angular variation similar to that observed with a torque apparatus. FMR was used by McMichael et al.[289] for a study of exchange bias.

2.2.5) X-Ray diffraction, (XMLD and XMCD).

X-ray magnetic linear dichroism, (XMLD), and X-Ray magnetic circular dichroism, (XMCD), have both been used to investigate exchange bias. The sample is immersed in a DC magnetic field while exposed to an incident beam of X-rays. For XMLD, measurements of reflected X-rays show a difference in absorption of a horizontally polarized incident beam compared to the absorption of a vertically polarized beam. XMCD shows a similar differential absorption effect when the incident beam is either left or right circularly polarized. Photo-electrons are ejected from the sample when exposed to X-rays. The number of photo-electrons as a function of incident photon energy and polarization provides an X-ray spectrum of the sample.

The direction and strength of the DC magnetic field and magnetic anisotropies affect the response of the sample to incident X-rays. Spin and orbital moments, spin structure, and the effects of exchange bias can be studied. The XMLD and XMCD techniques were used by Ohldag et al.[10, 16]

2.2.6) AC torque magnetometry.

AC torque magnetometry uses methods similar to those used for measurements of DC torque except that oscillatory motion of a mechanical resonator is induced by exciting the magnetization of a sample, placed on the resonator, with external DC and AC magnetic fields. Magnetization of the sample is established by the DC field. The AC field dithers the magnetization thus generating an AC torque on the sample/resonator combination through the cross product of the magnetization and the externally applied DC and AC magnetic fields. The AC torque method is used by our research group.[1, 7, 290, 291]

If the frequency of the AC field corresponds to the natural mechanical frequency of the resonator then a resonant response will result and the amplitude of the oscillatory motion will be maximized at the resonant frequency. A high Q, (low loss, narrow bandwidth), resonator is necessary since the motion is exceedingly small for readily obtainable fields.

Detection of the resonator motion provides a measurement of the amplitude response. Laser interferometry combined with synchronous, (lock-in), detection is required since the motions to be detected are often well under the wideband background noise of the apparatus. The AC magnetic field must be derived from the reference output of the synchronous detector. The scheme also requires a laser spot size sufficiently less than the size of the resonator, but large enough to illuminate a resonator edge while also illuminating a reference surface larger than and below the resonator. If the resonator material is semi-transparent at the laser wavelength then a Fabry-Perot optical cavity will

be formed between the resonator and the reference surface below the resonator thus enhancing the phase difference between the reflected beams and providing an *optical pre-amplification* of the signal.

If the mechanical constants of the resonator, the DC and AC magnetic field strengths, and the optical transduction of the interferometry system are known then the AC torque on the sample can be deduced. Measurements of the AC torque plotted against the strength of the DC bias field give linear hysteresis plots. If the DC bias field is rotated about the sample then plots of AC torque as a function of applied field angle can be produced. The data can be used to extract information regarding the anisotropy constants of the sample and the influence of exchange coupling.

2.2.7) Computational methods.

One may argue that computational methods are not in the domain of experimental science since an apparatus is apparently absent. Alternatively, one may argue that a digital machine and some problem solving algorithm are, in fact, components of an apparatus or sorts and, thus, are deserving of treatment as useful experimental tools.

Putting the debate above aside, and observing what is actually happening, one sees that computational methods have become an invaluable resource for investigating and solving many types of problems. Aerodynamics, structural dynamics, fluid dynamics, magneto dynamics, and many other disciplines all benefit from computational analysis.

Computational analysis is required when a system cannot be adequately described by a simple analytical form. Even if an accurate and perfectly descriptive analytic form is available, computational methods provide a remarkably time and cost efficient means to study the effects of changes in parameter values.

With respect to experimental science, computational methods can be used in preliminary studies that precede the actual experimental work. For example, design and characterization of the resonators that are used in the work conducted by our group begins with computational modeling of the mechanical response. The resonator designs are not advanced to the fabrication stage until it has been confirmed that the design and response parameters are as desired.

In order to know what the resonator design and response parameters should be it is necessary to determine what type of resonator, what magnetic materials, and what method of driving the resonator are required so that a transducer capable of responding, in a predetermined way, to some magnetic property of interest can be produced. Modeling using micromagnetic simulation tools provides considerable guidance toward determining the final design parameters of the resonators.

Computational methods can be implemented only if the problem to be studied can be reduced to an algorithmic form that is suitable for translation to software instructions for a digital machine. For systems that are described by a complex mathematical form, the finite element analysis (FEA) method can be used. A most basic description of the method is that it relies on a *meshing* procedure whereby the system is divided into many, many, regions (cells). Local solutions within each region are obtained while maintaining continuity along the region boundaries. The results are made, by some method, to converge to a solution for the entire system. One such method to force convergence is energy minimization. This technique is used in the micromagnetic simulation software package, mumax3.[292]

There are many sources for and types of FEA packages. Some of the packages used for micromagnetic simulation are mumax3,[292] COMSOL,[293] OOMMF,[294] nmag,[295] and MagTense.[296] This is by no means a complete list. Our group uses mumax3 for micromagnetic simulation and COMSOL for mechanical and RF simulation.

2.3) Three-axis AC torque magnetometer.

2.3.0) Section introduction.

A doubly-clamped resonator design was used for single axis AC torque measurements for work conducted by our research group on other projects.[7, 290] These projects preceded the exchange bias experiment reported on herein.

The exchange bias project used a three-axis AC torque magnetometer that was developed by our group at the University of Alberta, Department of Physics, during the period 2017 to 2020. The apparatus was designed to investigate the magnetic properties of nanoscale samples. A permalloy/cobalt oxide sample was studied from 2018 to 2021. Sample design and fabrication are presented in Chapter 3. Details of the apparatus design and function are given in Chapter 4. Investigations of exchange bias and interfacial coupling were conducted. A summary of the work is given in Chapter 5. The results are presented in Chapter 6.

The purpose of this section is to present the scheme by which AC torque about all three resonator axes can be generated and measured simultaneously.

2.3.1) Modification to resonators.

Refer to the SEM images in figures 2.3.1 and 2.3.2. The images show one of 240 resonators fabricated on a single wafer in 2018. (Refer to section 3.1 for sample details). All of the resonators were doubly-clamped, i.e. the moveable paddle is suspended by two torsion arms. One end of each torsion arm is connected to an outer edge of the structure and the other end is fixed to the moveable resonator paddle.

The image in figure 2.3.1 shows a typical doubly-clamped resonator. The most responsive mode is for torques along the y axis. Torque responses along the x and z axes are much lower since motion of the resonator paddle in these directions is restricted by the clamping arrangement. Previous experience with doubly-clamped resonators indicated that the y torque signal would be adequate. It was hoped that the torque signals from the x and z modes would also be adequate, but they were much smaller than desired.

The samples were returned to the NanoFAB in 2019 to have one torsion arm severed by a focused ion beam , (FIB), process. The image in figure 2.3.2 shows the same resonator after the modification. The result was successful. The signals from all three torque modes were well above the system noise floor.

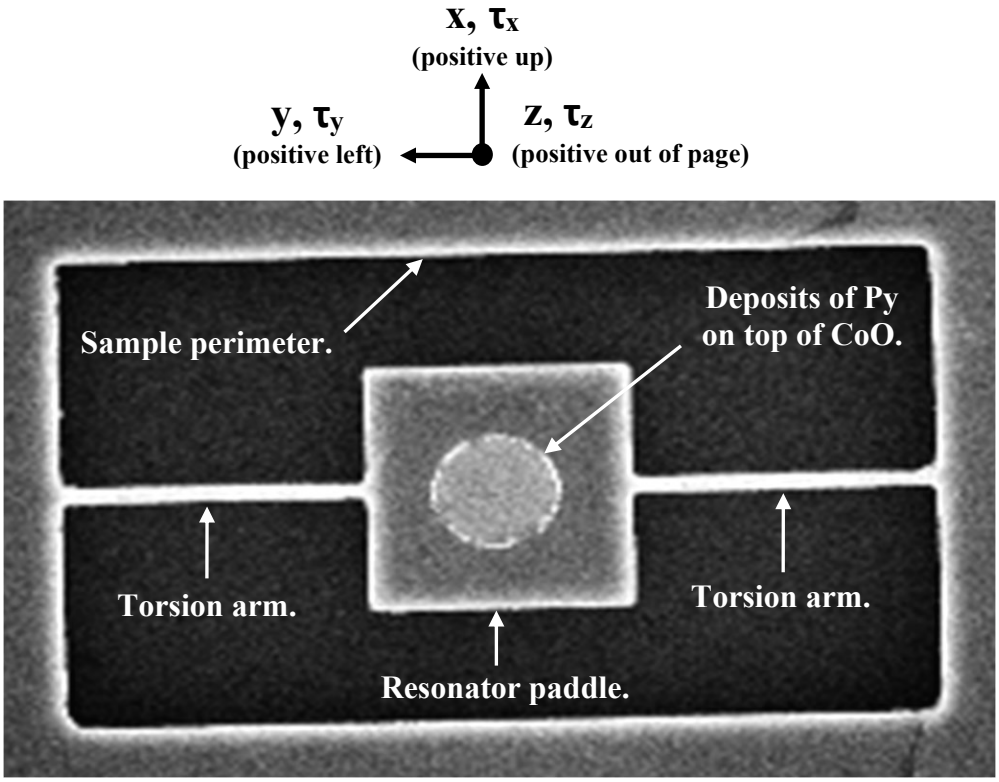

Figure 2.3.1. Typical doubly-clamped resonator. The sample perimeter is 10 x 5 um, the resonator paddle is 3 x 3 um x 0.3 um thick, the torsion arms are 0.15 x 0.3 um, and the deposits are 1.36 um diameter. The Py and CoO layer thicknesses are 20 nm each, (40 nm total thickness).

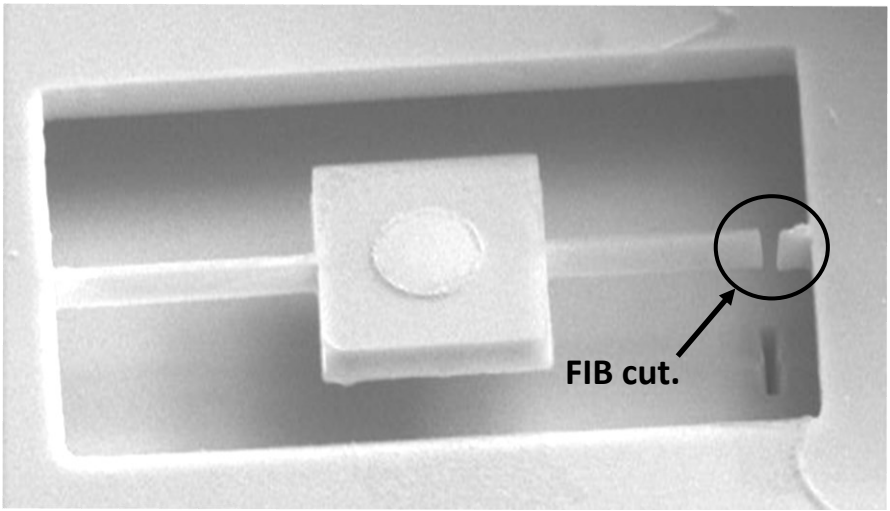

Figure 2.3.2. The same resonator after the right side torsion arm was cut.

2.3.2) Axis and torque orientations.

The SEM image in figure 2.3.3 shows the same resonator as in figures 2.3.1 and 2.3.2. The axis and torque orientations are shown.

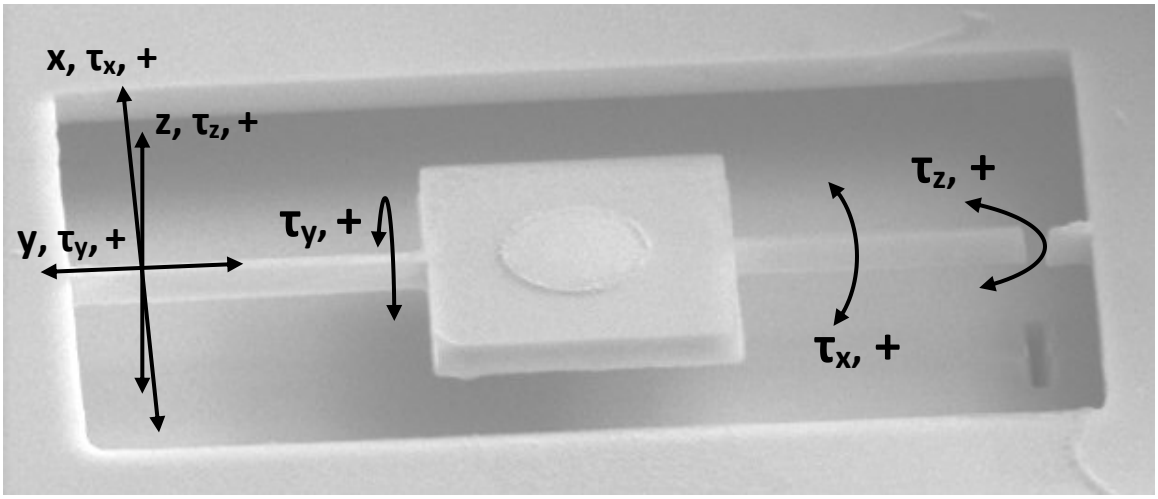

Figure 2.3.3. Axis and torque orientations.
The sample dimensions are the same as in figure 2.3.1.

2.3.3) DC and AC magnetic field orientations.

The SEM image in figure 2.3.4 shows the orientations of the DC and AC magnetic fields. The circular region on the resonator paddle is the magnetically active deposit. Cobalt oxide was deposited on the resonator paddle. Permalloy was deposited on top of the cobalt oxide. Both layers were approximately 20 nm thick. The deposit on the sample in the figure is approximately 1.36 um in diameter.

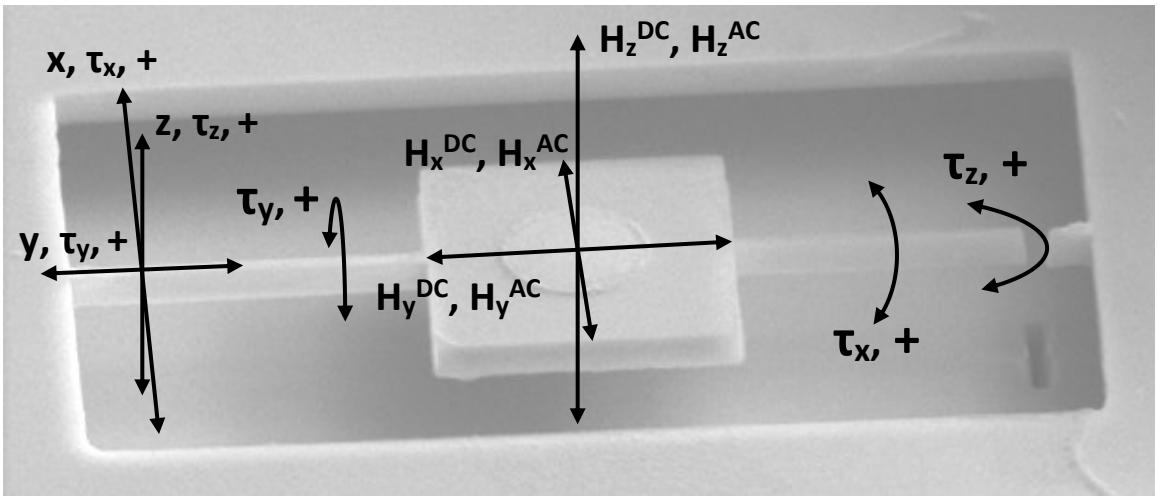

Figure 2.3.4. Orientations of DC and AC magnetic fields.
The sample dimensions are the same as in figure 2.3.1.

2.3.4) DC magnetic field.

The DC magnetic field was generated by a permanent magnet that can be translated along the apparatus x axis and rotated about the apparatus z axis by processor controlled stepper motors. Three cube magnets, 2" x 2" x 2" (5.08 x 5.08 x 5.08 cm), NdFeB material, N42 alloy, were stacked together to form a single magnet, 2" x 2" x 6" (5.08 x 5.08 x 15.24 cm). Figure 2.3.5 shows the magnet, translation stage, rotation stepper motor, and cryostat. The translation stepper motor is at the far left (not shown).

The DC magnetic field at the sample was approximately 3,000 Gauss in the x direction when the magnet was positioned immediately adjacent to the cryostat and at an angle of zero degrees with respect to the x axis.

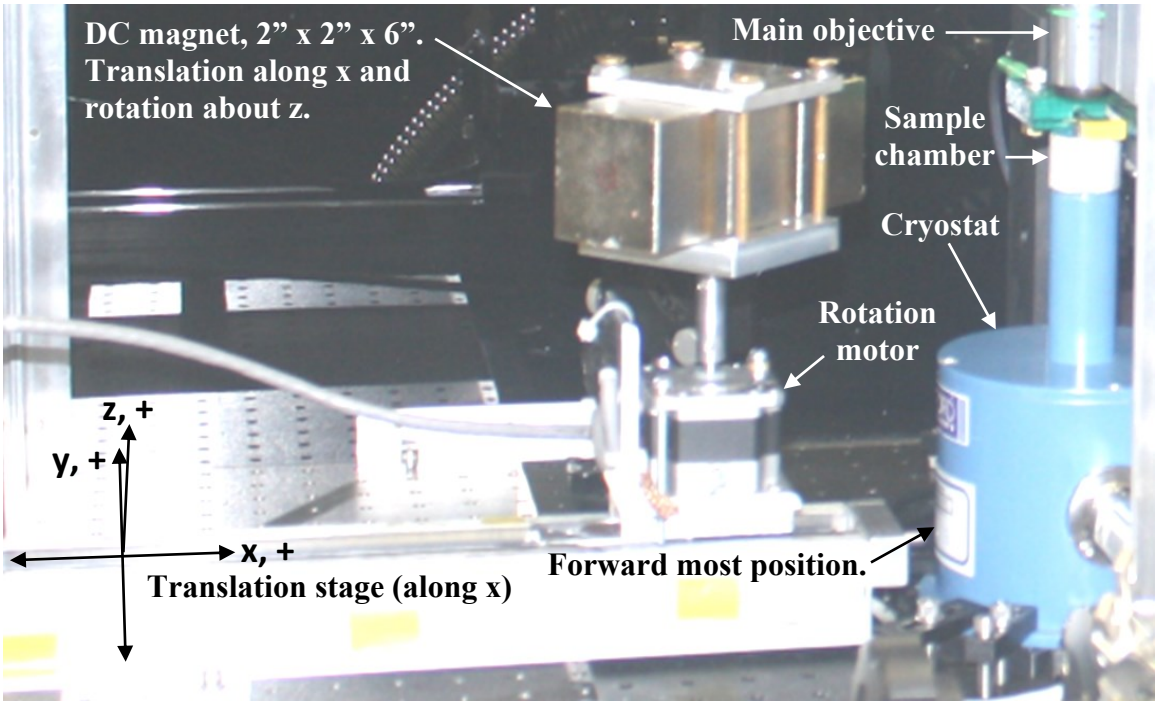

Figure 2.3.5. DC magnet, translation stage, rotation motor, cryostat, and main objective.

The DC magnet is shown in a position that is approximately 2” (5.08 cm) to the left of the cryostat at an angle of approximately 30° counterclockwise with respect to the apparatus x axis. Refer to figures 4.4.2 and 4.4.3 for other photos. The magnet can translate from the forward most position (immediately adjacent to the cryostat) to a position 22.5” (57.15 cm) left of the cryostat. It can also rotate 360° clockwise or counterclockwise about the apparatus z axis. The translation resolution is +/- 0.25 mils (+/- 6.35 um) with a repeatability of approximately 5 mils (127 um). The rotation resolution is 0.05625° with a repeatability of approximately +/- 0.1125°. Refer to figures 5.4.3 and 5.4.9 for plots of the field vs. translation position and rotation angle.

A magnetic field calibration was conducted in the summer of 2020 to determine the x, y, and z components of the DC field as functions of translation position and rotation angle. Details of the field calibration are provided in subsection 2.4.4.

2.3.5) AC magnetic fields.

The AC magnetic fields were generated by an air core RF excitation coil that was mounted on the top surface of the sample wafer (refer to figure 2.3.6). The coil was driven, simultaneously, with RF currents at the x, y, and z resonant frequencies of the resonator paddle. The directions of the AC fields were primarily along the coil axis (apparatus z axis). The AC fields in the x and y directions resulted from the spreading behaviour of the primary z components of the fields for regions outside of the coil and not on the coil axis.

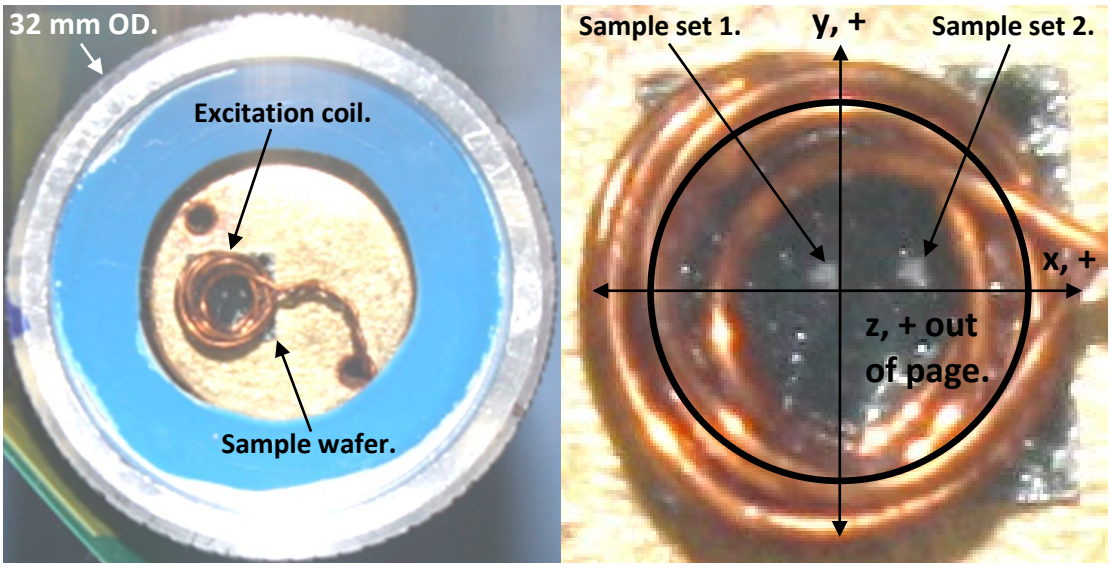

Figure 2.3.6. Sample wafer and RF excitation coil in cryostat. Left) The OD at the top of the cryostat is 32 mm. The sample wafer is 5 x 5 x 0.5 mm. Right) The two small, nearly square, shapes in the approximate centre of the wafer are the sample sets (120 samples in each set). The image on the right shows the approximate positions of the sample sets with respect to the coil axis.

The excitation coil was mounted so that the sample arrays were displaced from the coil axis as shown in figure 2.3.6, right image. The strength of the AC fields was highest in the z direction. The field strengths in the x direction would be higher at Sample set 2 than at Sample set 1. The field strengths in the y direction were comparatively small for both sample sets since they were positioned near the x axis along which there is a null in the y field components.

A COMSOL[293] model was used to estimate the AC field strengths in the x, y, and z directions. Inputs to the model were the coil geometry and RF currents. Refer to figure 2.3.6. The sample wafer was mounted on top of the cryostat cold-finger and the excitation coil was mounted on top of the sample wafer. The model accounted for screening effects resulting from the close proximity of the cold-finger to the sample wafer and excitation coil. The simulation work was conducted in late 2021 by Michael Dunsmore of our research group (the results are presented in Chapter 2, subsection 2.4.4).

2.3.6) Optics.

Motion of the resonator paddle is detected by interferometry. A laser beam is positioned and focused on the edge of the paddle so that a portion of the beam is directly reflected from the substrate base. This portion of the beam is the interferometric reference since its phase, after reflecting from the substrate base, is constant and does not depend on the resonator motion. The remaining portion of the beam undergoes multiple, recombining, reflections from the top surface of the paddle, from the Fabry-Perot optical cavity formed between the upper and lower surfaces of the paddle, and from the Fabry-Perot optical cavity formed between the lower paddle surface and the substrate base. This portion of the beam is phase modulated by the resonator motion. Recombination of the beams at a photo receiver results in a voltage signal that is intensity modulated by the resonator motion.

The optical transduction depends on the surface reflectivities and the finesse of the Fabry-Perot cavities. These were investigated by Michael Dunsmore in 2020 by modeling in COMSOL.[293] Inputs to the model were the laser wavelength, optical constants of silicon and silicon oxide, the resonator dimensions, and the height of the resonator above the substrate base. The model provided an estimate of the total reflected intensity and the phase difference between the portion of the beam reflected directly from the substrate base and the portions reflected by the top surface of the paddle and the Fabry-Perot optical cavities. The model was useful for predicting expected optical behaviour, but, fortuitously, an absolute number for the optical transduction was not required since a natural cancellation of the term occurs in the treatment for Thermomechanical Calibration (refer to Chapter 2, section 2.4, subsections 2.4.5 to 2.4.7).

More detail regarding the sample is provided in Chapter 3, Sample. The optical components and arrangement are discussed in Chapter 4, Apparatus. Figure 2.3.7 shows a typical laser beam position that provides an interferometric signal in response to the resonator motions along all three Cartesian axes.

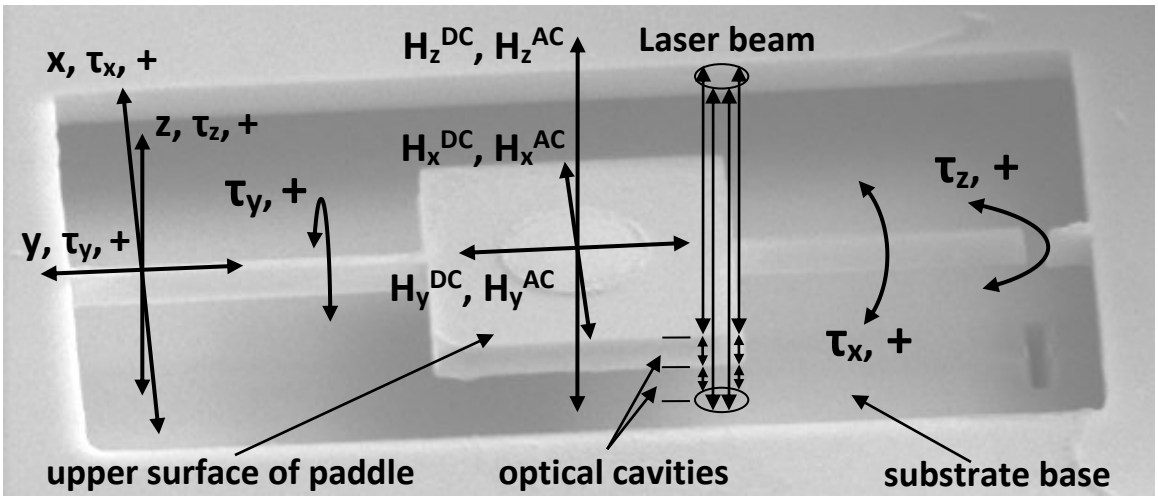

Figure 2.3.7. Typical position of laser beam.

The sample dimensions are the same as in figure 2.3.1.

2.3.7) Simultaneous, three-axis, torque generation.

Torques on the sample are generated through the cross products of magnetic moments and applied fields. The equations may appear somewhat different than one often sees since there are both DC and AC components of the moments and fields. Figures 2.3.8 to 2.3.10 show the axis and field orientations with respect to a typical resonator for each of the three torque modes. All three torque modes are generated and measured simultaneously by way of three superposed RF currents in an external excitation coil.

Generally, the torque on a magnetic moment in an applied field is,

$$\boldsymbol{\tau} = u_o(\mathbf{m} \times \mathbf{H}). \tag{2-5}$$

For AC torque magnetometry, the moments and fields are,

$$m_i = m_i^{DC} + m_i^{AC}, \tag{2-6a}$$

$$H_i = H_i^{DC} + H_i^{AC}, \tag{2-6b}$$

where the axis labels are given by i = x, y, z.

From equations (2-5) and (2-6), the torques along each of the axes are,

$$\tau_x = u_o\left[\left(m_y^{DC} + m_y^{AC}\right)\left(H_z^{DC} + H_z^{AC}\right) - \left(m_z^{DC} + m_z^{AC}\right)\left(H_y^{DC} + H_y^{AC}\right)\right], \tag{2-7a}$$

$$\tau_y = u_o\left[\left(m_z^{DC} + m_z^{AC}\right)\left(H_x^{DC} + H_x^{AC}\right) - \left(m_x^{DC} + m_x^{AC}\right)\left(H_z^{DC} + H_z^{AC}\right)\right], \tag{2-7b}$$

$$\tau_z = u_o\left[\left(m_x^{DC} + m_x^{AC}\right)\left(H_y^{DC} + H_y^{AC}\right) - \left(m_y^{DC} + m_y^{AC}\right)\left(H_x^{DC} + H_x^{AC}\right)\right]. \tag{2-7c}$$

Expanding equations (2-7) gives,

$$\tau_x = u_o(m_y^{DC}H_z^{DC} + m_y^{DC}H_z^{AC} + m_y^{AC}H_z^{DC} + m_y^{AC}H_z^{AC} - m_z^{DC}H_y^{DC} - m_z^{DC}H_y^{AC} - m_z^{AC}H_y^{DC} - m_z^{AC}H_y^{AC}) , \quad (2\text{-}8a)$$

$$\tau_y = u_o(m_z^{DC}H_x^{DC} + m_z^{DC}H_x^{AC} + m_z^{AC}H_x^{DC} + m_z^{AC}H_x^{AC} - m_x^{DC}H_z^{DC} - m_x^{DC}H_z^{AC} - m_x^{AC}H_z^{DC} - m_x^{AC}H_z^{AC}) , \quad (2\text{-}8b)$$

$$\tau_z = u_o(m_x^{DC}H_y^{DC} + m_x^{DC}H_y^{AC} + m_x^{AC}H_y^{DC} + m_x^{AC}H_y^{AC} - m_y^{DC}H_x^{DC} - m_y^{DC}H_x^{AC} - m_y^{AC}H_x^{DC} - m_y^{AC}H_x^{AC}) . \quad (2\text{-}8c)$$

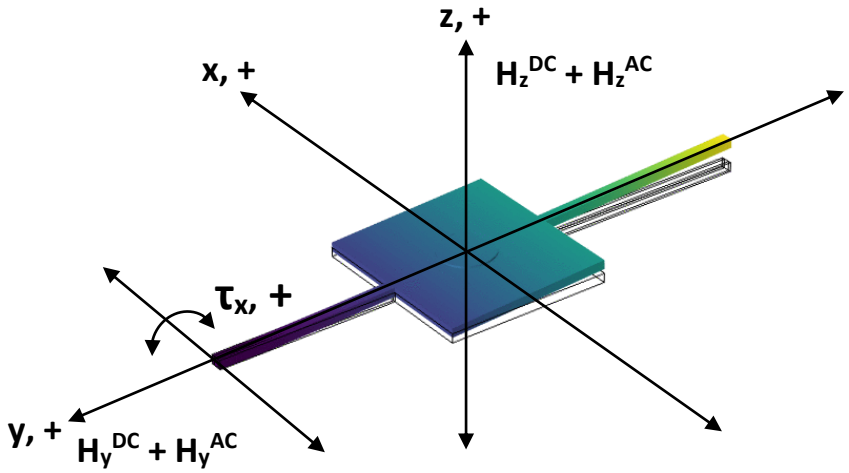

Figure 2.3.8. x torque (cantilever). The x torque mode (cantilever) is excited by the y and z components of the DC bias field and the y and z components of the AC dither field. The frequency of the AC dither field is set to the x mode resonant frequency. The torque is along the x axis.

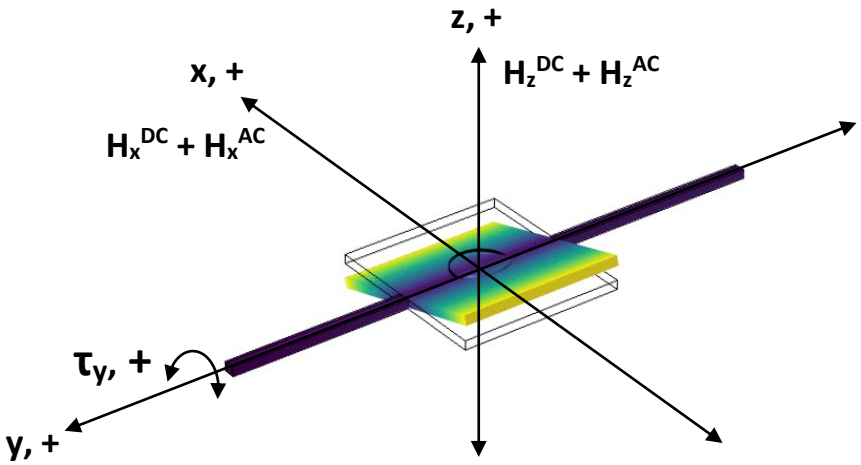

Figure 2.3.9. y torque (normal). The y torque mode (normal) is excited by the x and z components of the DC bias field and the x and z components of the AC dither field. The frequency of the AC dither field is set to the y mode resonant frequency. The torque is along the y axis.

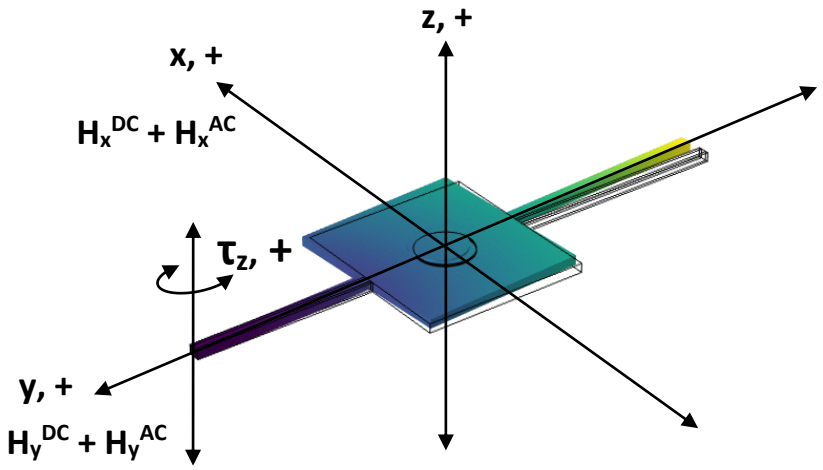

Figure 2.3.10. z torque (chop). The z torque mode (chop) is excited by the x and y components of the DC bias field and the x and y components of the AC dither field. The frequency of the AC dither field is set to the z mode resonant frequency. The torque is along the z axis.

Resonator animations generated by Michael Dunsmore in 2020.

Note the terms in equations (2-8) that have moment and field components that are either both DC or both AC. The DC-DC components cause a fixed DC offset of the resonator position, but, since synchronous (lock-in) demodulation of an AC signal is not responsive to DC signal components, the DC-DC terms do not contribute to the AC output and, therefore, can be ignored. (Synchronous demodulation always results in a complete loss of DC information.) Fortunately, the DC position of the resonator is not a required parameter since the method relies on measurement of the AC response. There is nothing lost in not knowing the DC position.

The AC-AC components result in terms that try to excite the resonator at twice the AC drive frequency, but the mechanical response of the resonator is of sufficiently high Q (>1000) that motion at harmonics of the drive frequency is substantially attenuated. To confirm this, the resonator was driven at twice the normal resonant frequency and the response was checked. There was no measurable signal. The output was at or beneath the noise floor of the system (~1/2 uV). The result meant that there was no measurable response at twice the normal drive frequency meaning that the AC-AC terms were not contributing to the signal output and that they can be ignored. Note also that AC signal components that are not at the reference frequency of the synchronous demodulator are purposefully and progressively attenuated as a function of frequency so that the demodulator response has an extremely narrow bandwidth centered at the demodulator reference frequency (hence the term “lock-in” amplifier).

The only terms in equations (2-8) that contribute to the signal output are the AC-DC and DC-AC terms so that the AC torque responses are,

$$\tau_x^{AC} = u_o(m_y^{DC}H_z^{AC} + m_y^{AC}H_z^{DC} - m_z^{DC}H_y^{AC} - m_z^{AC}H_y^{DC}) \ , \qquad (2\text{-}9a)$$

$$\tau_y^{AC} = u_o(m_z^{DC}H_x^{AC} + m_z^{AC}H_x^{DC} - m_x^{DC}H_z^{AC} - m_x^{AC}H_z^{DC}) \ , \qquad (2\text{-}9b)$$

$$\tau_z^{AC} = u_o(m_x^{DC}H_y^{AC} + m_x^{AC}H_y^{DC} - m_y^{DC}H_x^{AC} - m_y^{AC}H_x^{DC}) \ . \qquad (2\text{-}9c)$$

Equations (2-9) expose the mechanism by which the torques are generated. Our apparatus measures voltage signals that correspond to the RMS values of the resonator oscillations. The x, y, and z mode torques can be generated and measured simultaneously since the resonators are driven by three superposed RF currents corresponding to the three resonant modes of the resonator. The DC field strengths were determined by calibration. The AC field strengths were determined from a combination of analytical and modeling methods. Values for the field strengths and a thermomechanical calibration of the torque signals permitted conversion of the data to absolute torque. The reduced data were then analyzed to investigate the magnetic behaviour of the sample. Our work focused on exchange bias and interfacial coupling effects at the interface of a permalloy/cobalt oxide thin-film bilayer.

As a final comment on torque generation, it is worthwhile to examine an interesting and qualitatively informative arrangement of the torque equations wherein the moments are written in terms of DC and AC volume susceptibilities, χ_i^{DC}, χ_i^{AC}, and sample volume, V. The arrangement will show that, as in the case for DC torque, there can be no AC torque without some form of anisotropy. Begin by writing the moments as,

$$m_i^{DC} = \chi_i{}^{DC}\, V\, H_i^{DC}\,, \tag{2-10a}$$

$$m_i^{AC} = \chi_i{}^{AC}\, V\, H_i^{AC}\,. \tag{2-10b}$$

Rewrite equation (2-9a) for τ_x (the results extend equivalently to τ_y and τ_z).

$$\tau_x^{AC} = u_o V(\chi_y^{DC} H_y^{DC} H_z^{AC} + \chi_y^{AC} H_y^{AC} H_z^{DC} - \chi_z^{DC} H_z^{DC} H_y^{AC} - \chi_z^{AC} H_z^{AC} H_y^{DC}) \tag{2-11a}$$

The AC susceptibility is, in general, not equal to the DC susceptibility as a result of frequency and phase dependence[297] and, possibly, a dependency on other parameters such as temperature and applied field. Whatever the dependencies may be, just write the AC

susceptibility as $\chi_i^{AC} = \chi_i^{DC} + \Delta\chi_i$ where $\Delta\chi_i$ represents any difference between the DC and AC susceptibilities. After some algebra, equation (2-11a) becomes,

$$\tau_x^{AC} = u_o V\left[\left(\chi_y^{DC} - \chi_z^{DC}\right)\left(H_y^{DC}H_z^{AC} + H_y^{AC}H_z^{DC}\right) + \Delta\chi_y H_y^{AC}H_z^{DC} - \Delta\chi_z H_y^{DC}H_z^{AC}\right] \quad (2\text{-}11b)$$

If the substance is perfectly linear, isotropic, and homogenous, (i.e. with no anisotropies), then the DC susceptibilities will be the same in any direction so that $(\chi_i^{DC} - \chi_j^{DC})$ will be zero. The differences between the DC and AC susceptibilities, $\Delta\chi_i$ and $\Delta\chi_j$, can be considered as having negligible effect for sufficiently low frequency (the resonator frequencies were less than 5 MHz which is far below the ferromagnetic resonance frequency for the fields used). "If the frequency is not too high, the magnetization remains in quasi-static equilibrium with the field at all times."[290] The final result is that the torques for all modes will be zero, or negligibly small, in the absence of anisotropy. "If no anisotropy exists, then the equilibrium magnetization will always be parallel to the applied field, with a resultant torque of zero."[290]

A more careful and thorough treatment would consider the complete susceptibility tensor so as to admit off-diagonal DC and AC susceptibility terms that are not zero. The susceptibility tensor is,

$$\chi_{i,j}^{d} = \frac{\partial M_i}{\partial H_j}, \quad (2\text{-}12)$$

where the $\chi_{i,j}^{d}$ are the differential susceptibilities.

The usefulness of equation (2-11b) is qualitative only and is most likely confined to simply recognizing that if a torque exists then some form of anisotropy must be present

or some other mechanism, responsible for creating a directional asymmetry in response to the external fields, would have to be present.

Our apparatus generates torque by AC dithering of the magnetization direction, so, strictly speaking, the system response is sensitive to AC susceptibility, but, since the AC fields strengths are very low, thus introducing only very small perturbations to the DC field, it is the DC magnetization that is probed in very small regions of the magnetization vs. field curve. (For the exchange bias experiment, we did not use the frequency-mixing techniques described in a paper by Losby et al. from our group. The techniques permit "...simultaneous detection of both DC and time-dependent magnetic signatures...".[290])

For our work on exchange bias and interfacial coupling it was not necessary to characterize the susceptibilities as a separate task since the analysis was done by comparison of torque data to phenomenological energy models where the sought after unknowns were anisotropies. Our data were collected at fixed temperatures and, with the exception of linear hysteresis loops, the sample magnetization was saturated. At fixed temperature, fixed frequency, and at any particular fixed strength and direction of the DC bias field, the DC and AC susceptibilities could be considered adequately constant over the strengths and cycle-times of the AC excitations. The torque signals, then, could be attributed directly to anisotropies.

2.3.8) Raster scans.

Raster scans of the sample were obtained using a LabView program that automatically moves the main objective in an x-y pattern. The program was prepared by Dave Fortin sometime prior to 2019. Dave was a member of our research group and was eventually hired by the department as a technical assistant. He served until 2020.

The raster program constructs an image of the sample by monitoring the reflectance of the laser beam from the top surface of the sample. The reflectance is a DC signal that does not respond to the resonator motion. The program also constructs images of the signal amplitudes and phase as a function of position. The data are presented on the computer monitor in real time and are then stored in the control computer.

Raster images give information regarding the response of the sample to the driving fields. The specific torque mode (x, y, or z) can be identified. Studies of a sample that has not been previously examined begin with collection of rasters.

Many raster scans from several samples were collected during the period mid 2019 to mid 2021. A particular set of raster scans of sample S2A1A5 are presented here. They were collected on 19 and 20 Aug, 2020. The x, y, and z torque rasters are shown in figures 2.3.11, 2.3.12, and 2.3.13 respectively.

The raster images are all 15 um x 15 um and have 125 pixels in both x and y giving 15,625 individually measured points. Refer to the top left image in each of the figures. These are the reflectance images. They are all approximately the same since the reflectance does not depend on the torque mode. The outside dimensions of the sample are approximately 10 um x 5 um. The resonator paddle is approximately 3 um x 3 um x 0.3 um. The magnetic materials were deposited on top of the paddle. The reflectance from the deposit is slightly different than from the uncovered portions of the paddle, but the resolution of these images is too low to determine the deposit dimensions (SEM images of the samples are presented in Chapter 3). The torsion arms have cross sections of approximately 0.15 um x 0.3 um and are approximately 3.5 um long. The left torsion arm connects the resonator paddle to the leftmost edge of the structure. The right torsion arm was cut near the edge of the structure to enhance the mechanical compliance of the x and z torque modes (refer to Chapter 2, subsection 2.3.1 and to Chapter 3).

The raster image titles, X, Y, R, and Theta, in figures 2.3.11 to 2.3.13, refer to the in-phase (X), quadrature (Y), total (R), and phase relationship (theta) between the in-phase and R components. The signals are presented using the same terminology that is used to designate the outputs of lock-in amplifiers. The signals are $X = R\cos(\theta)$, $Y = R\sin(\theta)$, and $R^2 = X^2 + Y^2$. The point here is that the signal names, X and Y, do not refer to x and y torque modes or to x and y dimensions or to x and y axes.

Theta refers to the phase difference between the driving signal and the motion of the resonator. There are three factors that affect this relationship. The first is the simple fact that the resonator *is* a resonator and that it is a *driven* resonator meaning that the driving function and the resonator response do not necessarily follow the same phase. The second is propagation delays that result from the cable runs to the driving coil and, also, optical path delays (though this last effect is relatively small). The third is propagation delays in the signal processing circuits contained in the lock-in amplifier. A standard feature of lock-in amplifiers (since they were first introduced) is the ability to arbitrarily "zero the phase" before recording begins. Forcing the phase to zero causes the initial phase to be zero so that the initial outputs are $X = R\cos(0) = R$ and $Y = R\sin(0) = 0$. Once the phase is zeroed, any change in phase thereafter will cause the magnitude of X to be less than R and the magnitude of Y to be greater than zero. The signs of the X and Y components depend on the value of any phase difference that develops after it was zeroed. The R component, which always gives the RMS amplitude of the motion, is phase independent so that it is recoverable through the relationship $R^2 = X^2 + Y^2$. The phase can be extracted from the arctangent of Y/X. The phase can be in any one of four quadrants meaning that disambiguation of the arctangent function is necessary. Modern, dual phase, lock-in amplifiers do all of the math internally and report the data as R, X, Y, and theta with no need of further manipulation to obtain the raw data.

The top right images in figures 2.3.11 to 2.3.13 are generated by the in-phase signal, X, from the lock-in amplifier. The quadrature signal, Y, appears in the middle left images. The middle right images show the total signal, R. The bottom left images show the phase, Theta. The bottom right images had no inputs and can be ignored.

The X, Y, and Theta, raster images are extremely valuable since they provide verification of the torque mode. One need not worry that what was thought to be one type of motion is, somehow, some other type. The raster images expose the actual resonator motion thus confirming that the torque mode is as expected. There is some possibility that the resonator motion is a higher order harmonic of the drive signal. Fortunately, the lock-in amplifier can be configured to detect harmonic components. No harmonic components were found in any of the samples that were studied. (There is no such thing as a perfectly linear drive signal, a perfectly linear response or a perfectly linear amplifier, so some harmonic components, however small, must always exist in the recovered signal. We found none that were above the noise floor of the lock-in amplifier.)

Refer to figures 2.3.8 to 2.3.10 which show the motions associated with the x, y, and z torque modes. The orientation of the resonators in these figures is the same as in the raster scans shown in figures 2.3.11 to 2.3.13 which means that the left, right, upper, and lower edges of the resonator paddles in figures 2.3.8 to 2.3.10 are also the left, right, upper, and lower edges of the resonator paddles in the raster images shown in figures 2.3.11 to 2.3.13.

Begin by examining figure 2.3.8. The x mode torque is shown. Do a “mental” raster scan. Imagine that the beginning point of the scan is at the lower left corner of the resonator paddle. Put the laser spot at this point and then “zero the phase”. (Forcing the phase to zero causes the initial phase to be zero so that the initial outputs are $X = R\cos(0) = R$ and $Y = R\sin(0) = 0$. The value of the X signal component will be the RMS

amplitude of the motion. R will have the same value as X. Y will be 0. The amplitude, here, means how far, up and down, the resonator paddling moves in the direction of the z axis. The motion in the z direction is greater on the right side than on the left. Begin the raster scan by moving the laser spot toward the right and along the lower edge. While scanning from left to right, the amplitude of the motion will be increasing so that the R signal component will be increasing and, since the motion is in phase with the drive signal, the other signals will be X = R, Y = 0 and Theta = 0. Stop scanning once the right edge is reached. Pick up the laser spot and put it back down on the left edge at a point that is one pixel higher, toward the top, than it was for the first scan. Start scanning toward the right again. The signal behaviour will be the same as it was in the first scan. The raster is completed by scanning from left to right while each time moving the laser spot one pixel toward the upper edge. The signal behaviours will be the same for all of the left to right scans.

Refer to the raster images in figures 2.3.11 to 2.3.13. The scales for the raster images are “auto-gained” so that the most positive signal level is always represented by bright red and the most negative signal level is always represented by black. The scaling for the Theta raster images is such that bright red corresponds to +90 degrees and black corresponds to -90 degrees.

Now refer to the raster images in figure 2.3.11 for the x mode torque. The reflectance image confirms that the sample is adequately positioned near the centre of the scan area. It also confirms that the top surface is reasonably uniform and that it is most likely free of large scale defects (the laser spot size is approximately 0.3 um in diameter and the pixel size is approximately 15 um/125 x 15 um/125 = 0.12 um x 0.12 um meaning that a defect would have to be considerably larger than 0.12 um x 0.12 um to be resolvable).

Examine the regions, in all of the raster images shown in figure 2.3.11, from x pixel values 75 to 100 and y pixel values from approximately 60 to 70. The signals in these regions were generated by the torsion arm that was cut and, therefore, free to move with the resonator paddle. The nature of the signals coming from the torsion arm are rather complicated because the laser spot is larger than the width of the torsion arm. It is not a simple matter to describe the motion of the right side torsion arm because the optical interference relationship is not nearly as straight forward as it is for the resonator paddle. A small amount of work was done on this by myself and a few other members of our group, but full understanding of why the right side torsion arm appears to be moving out of phase with the right edge of the resonator paddle was not achieved. Note that the image on the bottom right did not have a signal input and can be ignored.

Recall the image that was obtained from the "mental" raster scan. The amplitude increased as the scan moved from left to right. The X and R signals were equal. Y was zero and Theta was zero. Look at the R raster image (middle right of figure 2.3.11). Ignore the right side torsion arm. As expected, the amplitude increases from left to right. Ideally, the amplitude would be the same in a y-y cut for any fixed position of x. The image shows that the amplitude changes in the y-y cuts, but this is because the surface of the paddle is not perfectly uniform either physically, optically, or both. The general behaviour of increasing amplitude remains and is consistent with motion attributable to the x torque mode.

Now examine the Theta image in the lower left of figure 2.3.11. Ignore the right side torsion arm. The phase, though not zero, is constant. It is not zero because the phase was zeroed at the lower left corner of the entire raster image and not at the lower left corner of the resonator paddle as it was for the "mental" raster scan. It is the constancy of the phase that is relevant and it is consistent with motion attributable to the x torque mode.

The non-zero phase indicates that the resonator paddle was not at precisely the same height as the lower left corner of the image where the phase was zeroed. Look at the scale. The indication is that the phase signal is approximately -3.2 volts. The scale range is +/- 10 volts for +/- 90 degrees so that -3.2 volts corresponds to roughly -30 degrees.

The X signal would have been precisely equal to the R signal if the phase would have been zero. A phase of -30 degrees gives X = Rcos(-30) ~ .87R. The scale indications for the X and R components show that the X signal is roughly 0.8 of the R signal, but, more importantly, the X signal confirms what is seen in the R signal. The amplitude is increasing toward the right. The Y signal should be Rsin(-30) ~ -1/2 of R. The peak R value is approximately 5 volts. The Y signal is approximately -1/2 of this as expected.

The y and z torque modes are shown in figures 2.3.12 and 2.3.13. Verification of the torque modes follows the same procedure as for the x torque mode. Sometimes things are easy. For example, take a quick look at the phase image for the y mode torque in figure 2.3.12. It shows, very clearly, that the upper and lower edges of the resonator paddle have a 180 degree phase difference, as they should for the y torque. The signal cannot be coming from x torque and is very unlikely to be coming from z torque. The raster images provide quick and comforting confirmation that all is well.

A sometimes frustrating situation occurs while examining rasters or any other data from this experiment. We have x, x, x, and x, along with y, y, y, and y, topped off by z, z and z which can be confusing. There is an x mode torque, an x position, an x axis and an X signal with similar repetitive uses of y and z. It is easy to get mixed up.

The raster program records all of the data so that a more precise analysis can be done, but verification of the torque modes can usually be done by visual examination of the rasters.

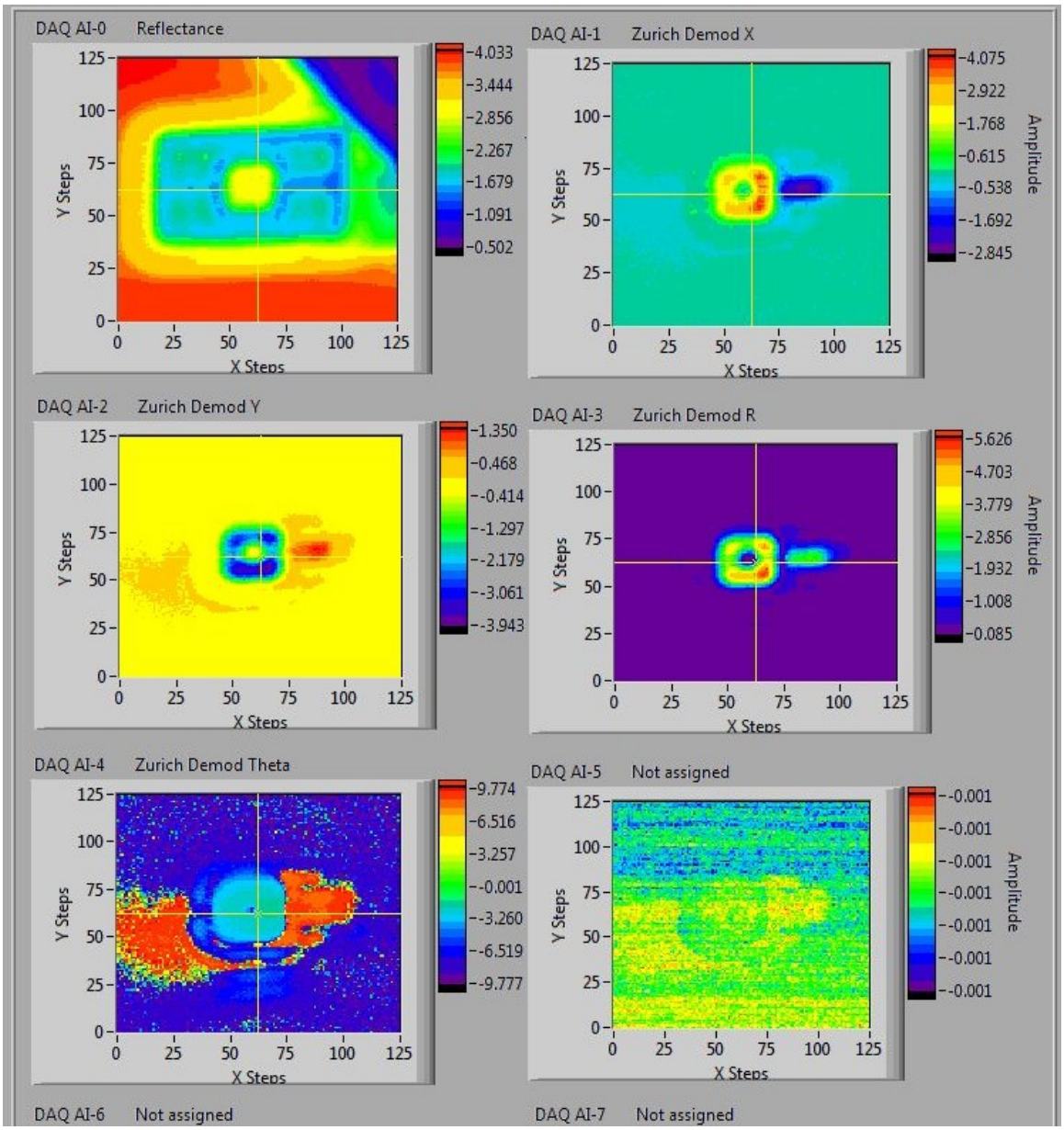

Figure 2.3.11. Raster scan of sample S2A1A5 showing the x torque response.

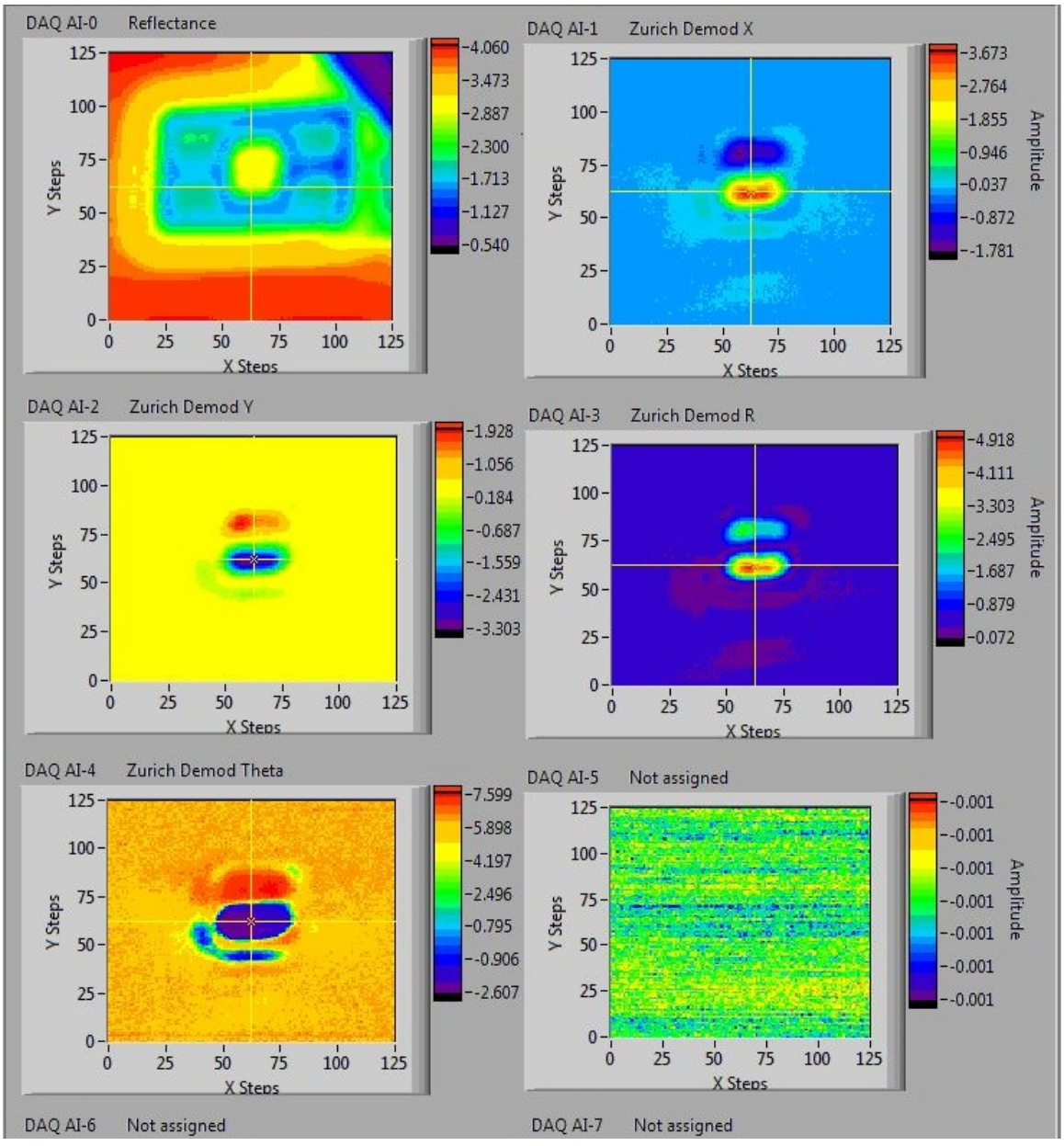

Figure 2.3.12. Raster scan of sample S2A1A5 showing the y torque response.

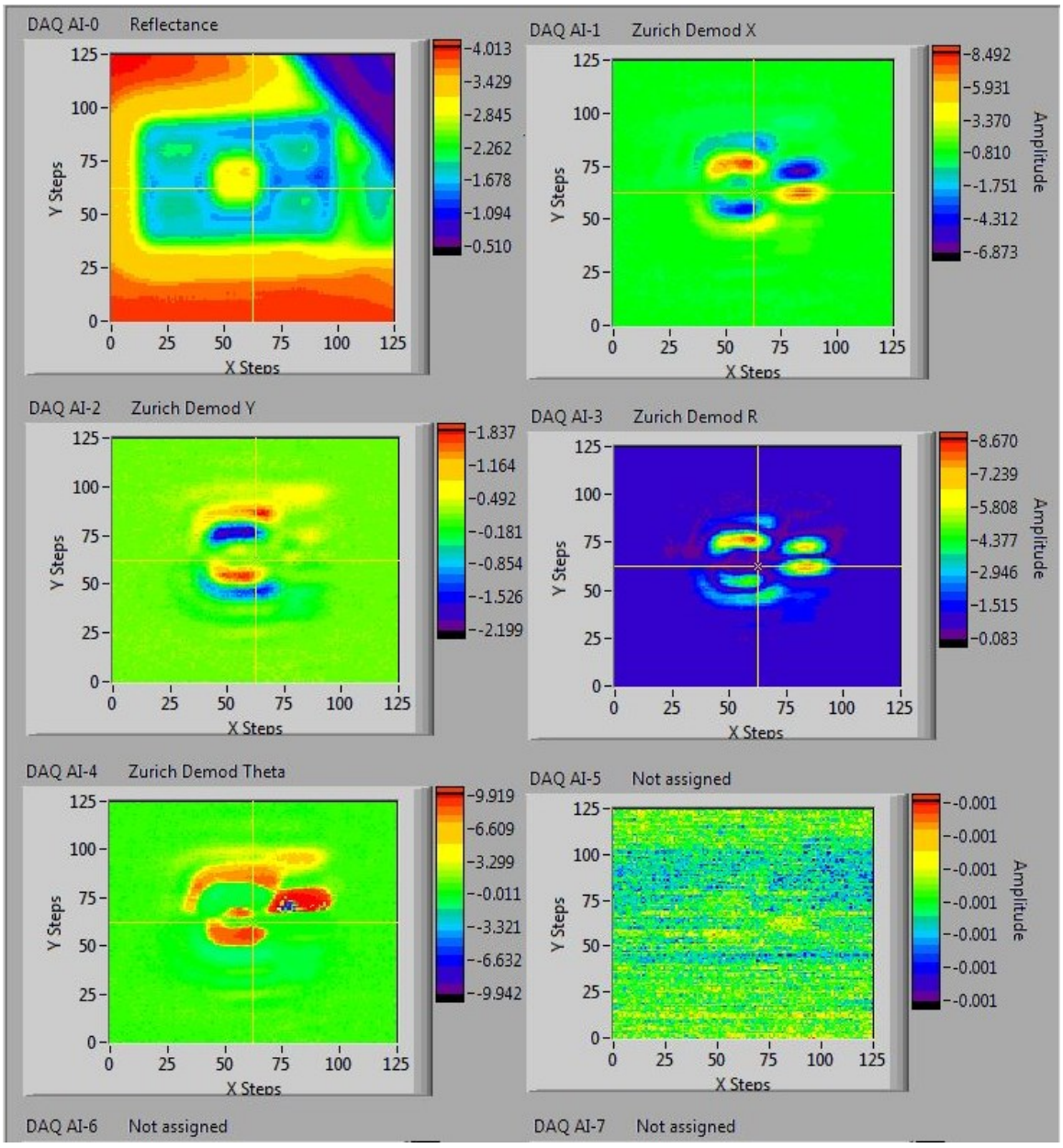

Figure 2.3.13. Raster scan of sample S2A1A5 showing the z torque response.

2.3.9) Procedures for data collection.

The procedures for collecting data begin with inspection of the vacuum, cryogenic, optical, and mechanical systems. Repairs and adjustments are made as required. The work is conducted as follows,

1) **Power up.** Main power bars, control and data storage computer, power supplies, lock-in amplifier, laser, photo receiver, RF amp, stepper motor controllers for the magnet translation and rotation stages, external DAQ, stepper and piezo controllers for the objective positioning stage, Gauss meter, and temperature controller.

2) **Field-cooling.**

i) Move magnet to front of cryostat at desired angle (normally at zero degrees so that the DC field will be at its positive maximum).

ii) Set temperature controller to desired setpoint. Set voltage limit to 10 V. If the desired temperature is the base temperature of the cryogen then it is not necessary to engage the PID loop of the temperature controller. For setpoint temperatures above the base temperature, engage the PID loop well before the setpoint temperature is reached.

iii) Start the cryo system vacuum pump. Open purge flow valves. Purge for one minute.

iv) Close purge flow valves. Open main flow valve. Monitor pressures and temperature. If the temperature does not begin to drop within five minutes then there is a problem. The most common problem is a blocked cryogen

transfer line. To stop the system, close the main flow valve and turn off the cryo system vacuum pump. Make repairs as necessary.

Normal cooling is at a rate of five to ten degrees per minute. Adjust the main flow valve to achieve and maintain this rate.

v) The system requires continuous monitoring of the pressures and temperature. Adjust the main flow valve as required to stabilize the system. It may take up to two hours to reach a reasonably stable state, but data collection should not be attempted for at least 4 hours (preferably 24 hours).

3) Alignment.

i) Select a sample. Set the drive frequencies to the approximate resonant frequencies for the sample. Set the drive levels.

ii) Place an imaging target in front of the objective for the photo receiver. A thin piece of cardboard is sufficient (there is an ample supply of IBM punch cards in the lab that we have found to be most convenient for this purpose). Adjust the position and focus of the main objective using the stepper motors for the positioning stage until a clear image of the sample wafer is produced. Locate the desired array. Centre the image of the array. Locate the desired sample in the selected array. Centre the image of the sample. Inspect. Confirm that this is the desired sample. Move the image of the sample so that it is centred on a lower or upper edge. Adjust the focus until the sample is noticeably blurred. Remove the imaging target.

iii) Adjust the focus and position of the main objective and increment the resonant frequency in 10 Hz to 100 Hz steps until a signal is registered. This procedure will take a few minutes. If a signal cannot be found then start over at step (ii). With experience, the sample and a signal can be found within a few minutes. On bad days, it has taken several hours to find the sample and to get a signal. Work slowly, carefully and methodically.

iv) Once a signal is registered, use the piezo actuators for the positioning stage to obtain precise alignment and maximum signal. Adjust the frequencies to maximize the signals from each of the resonator axes.

v) Select the plotting function for the lock-in amp. Set to 5 minute plot length. Monitor the signal drift. The drift will be such that several adjustments of the alignment will be required over a period of approximately 30 minutes to one hour. Once the signals appear to be stable, set the plot length to 30 or 60 minutes. Monitor and adjust the alignment once every five to 10 minutes.

vi) The signals will drift over a period of four to six hours as the temperatures of the mechanical components stabilize and as the temperature of the sample stabilizes. There is no point in collecting data while the system is unstable. Be patient. It is often best to wait until the next day to collect data.

4) Linear hysteresis loops.

A linear hysteresis loop is generated as follows,

i) Set the linear translation speed to 1000 steps per second. This will give a velocity of 0.125"/s (3.175 mm/s) for forward and backward translation of the DC magnet.

ii) Set the linear travel to 175,000 steps. This will give a travel length of 21.875" (555.625 mm) which will be sufficient to move the magnet to the back of the rail. The same travel length is used for moving from the back of the rail to the front of the cryostat.

iii) Set the rotating speed to 512 steps per second. This will give an angular rate of 25 seconds per revolution (12.5 seconds for 180 degrees).

iv) Set the rotation angle to 6,400 steps, counterclockwise. This will give a 180 degree, counterclockwise, rotation of the DC magnet.

v) Adjust the alignment and frequencies as necessary.

vi) Set the lock-in amplifier to record. Record for five seconds before moving the magnet. Do not stop recording.

vii) Confirm that the linear speed and travel are set correctly. Set the linear translation direction to backward and start the translation motor. The magnet will stop automatically when it reaches the back of the rail (the travel length was set in step ii). Wait five seconds.

viii) Confirm that the rotating speed and direction are set correctly. Start the rotating motor. The motor will stop automatically after it has completed one half turn (the degrees of rotation were set in step iv). Wait five seconds.

ix) Set the linear translation direction to forward and start the translation motor. The magnet will stop automatically when it reaches the front of the cryostat. Wait five seconds.

x) Set the linear translation direction to backward and start the translation motor. The magnet will stop automatically when it reaches the back of the rail. Wait five seconds.

xi) Start the rotating motor. The motor will stop automatically after it has completed one half turn. Wait five seconds.

xii) Set the linear translation direction to forward and start the translation motor. The magnet will stop automatically when it reaches the front of the cryostat. Wait five seconds.

xiii) Stop recording. Save the data to file.

5) Rotating hysteresis loops.

A rotating hysteresis loop is generated as follows,

i) Set the magnet angle to the desired position using the rotation motor.

ii) Set the rail position of the magnet to the desired location. Ensure that there will be sufficient clearance between the corners of the magnet and the main objective when the magnet is rotated.

iii) Set the rotating speed to 64 steps per second. This will give an angular rate of 200 seconds per revolution. Slower rates may be required.

iv) Set the rotation angle to 12,800 steps. This will give a 360 degree rotation of the magnet.

v) Adjust the alignment and frequencies as necessary.

vi) Set the lock-in amplifier to record. Record for five seconds before moving the magnet. Do not stop recording.

vii) Confirm that the rotating speed is set correctly. Set the direction to counterclockwise. Start the rotating motor. The motor will stop automatically after it has completed one turn (the degrees of rotation were set in step iv). Wait five seconds.

viii) Set the direction to clockwise. Start the rotating motor. The motor will stop automatically after it has completed one turn. Wait five seconds.

ix) Stop recording. Save the data to file.

6) Manual data collection.

The effects of drift and the decrease of signal in high DC bias fields can be nearly eliminated if the data are collected using a manual, instead of semi-automatic, procedure. Manual data are collected by setting the magnet angle and translation position, adjusting the alignment and frequencies, and then recording the data for approximately 20 seconds. The magnet is moved to the next position and the procedure is repeated. It can take up to several hours to collect sufficient data points for a linear or rotating hysteresis loop.

7) Preliminary data reduction.

The data are stored in the apparatus control computer. Make a new folder for each day. Name the folder with the date. Keep a record of data files names in a notebook. Write down a short description of the type of data (linear, rotating, etc) and the time that the data were collected. Beware that transferring data to a different computer sometimes results in a change of the file dates and time stamps. Failure to keep a hard copy log will inevitably lead to confusion, and potential disaster, regarding what data were collected on what day and for what purpose. The rule to remember in aviation is that "your auto-pilot is trying to kill you".[a] Unfortunately, and all too often, the auto-pilot sometimes wins. Keep this thought in mind when using personal computers for scientific work. The operating systems of these computers were not designed with data integrity and manipulation as priorities.

[a] From my private and commercial pilot training, 2008 to 2014. For example, the Garmin G1000 auto-pilot system allows you to configure an automated climb at a rate far above the capability of the aircraft to maintain even at the highest power levels. The aircraft eventually stalls during the climb. The auto-pilot is not intelligent. It doesn't care. The assumption is that the pilot actually wanted the impossibly high rate of climb. It seems that Garmin allows this so that the pilot can choose to engage automatic control of manoeuvres at the edge of the flight envelope even though they might not be sustainable.

Make daily transfers of data from the control computer to another computer that is used for backup storage, data reduction, and plot preparation. The raw data from the Zurich lock-in amplifier requires considerable post-processing manipulation before they can be plotted. Each channel of raw data must be separated from the others. The Zurich sometimes makes errors in the number of points per channel. Some points can be missing either at the beginning or at the end of one or more channel records. A reduction program that assumes equal lengths for all of the channel records will not work. Prepare a program that is sufficiently robust to overcome inconsistencies in the format of the raw data.

Once the raw data have been reduced to suitable form they can be plotted and examined.[b] Make a decision on how to proceed. If a plot shows features that are deserving of immediate attention then conduct an analysis before continuing with data collection. Balance the need to address interesting plot features with other requirements. For example, if the system is at cryogenic temperature then ice will be accumulating on the sample thus rendering it, after approximately 4 to 7 days, unsuitable for investigation until the system is warmed up and then cooled again (ice load lowers the resonant frequencies). If more data are needed for a particular study then it may be necessary to continue with data collection before spending time to analyze other data.

Review plots with other members of the research group. Interpretation is by no means obvious. A little help with recognizing important features in the data go a long way toward making the correct decisions regarding how the work should be continued.

[b] I admit to having done a terrible job of this. I managed to avert any costly cryo, vacuum, or electronic equipment catastrophes, but, many times, ended up frustrating my otherwise extremely patient and highly tolerant supervisor which I regret wholeheartedly. Preparation of the raw data for plotting was an extremely cumbersome, aggravating, and tedious task that most often required manual manipulation. The process would sometimes take more than two days to complete. I should have spent more time preparing a better reduction program. The upside to all of this is that many, many, experiments were conducted. There is enough good data to warrant preparation of at least one additional paper for publication.

2.3.10) Signal drift due to alignment instability.

The procedures given in subsection 2.3.9, paras (4) and (5), for obtaining data from linear and rotating hysteresis loops are semi-automated. Linear or rotating movements of the magnet are automated with the exception of brief interruptions while changing the directions. The recording is continuous. The alignment cannot be adjusted while the data are being collected. The semi-automated procedures are not adequate if alignment instability causes an unacceptably large signal drift while the data are being collected.

The primary cause of signal drift is alignment instability. The alignment drifts with time due to instability of the ambient temperature and also drifts with magnet position due to magnetic attraction of the main objective positioning stage toward the magnet as the magnet approaches the cryostat. Manual collection of data is necessary if either of these drift components is unacceptably large.

2.3.11) Signal response in high DC bias fields.

High DC bias fields will cause significant reduction in signal strength if one of the terms in the torque equation, $\vec{\tau} = \mu_o \vec{m} \times \vec{H}$, is saturated while the other is increasing. This will happen if the magnet moves closer to the sample after one of the magnetization components is saturated. For example, the y mode torque signal will begin to decrease if the DC bias field is sufficiently strong to saturate the x component of the ferromagnetic magnetization while the magnet is still moving closer to the sample. This occurs because the term $m_x H_z$ will remain approximately constant after saturation while the term $m_z H_x$ will continue to increase as the magnet is brought closer. The cross product term, ($m_x H_z$ - $m_z H_x$), will become (~constant - $m_z H_x$) the value of which will decrease as $m_z H_x$ increases thus reducing the y mode torque signal. The effect can be seen in figure 5.4.4 where the DC bias field magnitude exceeds approximately 20 kA/m. The slopes in these regions were used to extract the saturation magnetization (see Chapter 6, 6.3.3, ii).

Significant reduction in signal strength also occurs due to a dependence of resonant frequency on DC bias field magnitude. As the DC bias field magnitude increases, the resonator system "stiffens" thus causing the resonant frequency to increase. The resonator system includes a torsion spring constant attributable to the torsion arm as well as an additional spring constant that results from the torques that are generated inside of the sample. The torques in the sample arise from anisotropy, Zeeman, and demagnetizing energy terms with their combined effect acting to oppose the resonator motion just as the torsion arm does. The combined effect increases with increasing field magnitude so that the total torsion spring constant also increases. A higher spring constant results in a higher resonant frequency through $f_o = (\frac{1}{2\pi})\sqrt{k/I}$ where k is the total spring constant and I is the moment of inertia of the resonator.

Figure 2.3.14 shows the y mode torque signal recorded during a linear hysteresis loop obtained at ambient temperature. The drive frequency was adjusted for each data point so that the changes in resonant frequency would not affect the data. The change in resonant frequency is plotted on the right vertical axis in units of parts per million of the initial frequency (ppm is the standard unit for changes in oscillator frequency). The maximum increase was approximately 1270 Hz. Note that the decrease in signal strength as the field magnitude increases (high positive and high negative fields) is not due to changes in resonator frequency since the frequency was adjusted for each point, but is due to saturation as discussed in the first paragraph of this subsection.

If the drive frequency is not adjusted to match the change in resonant frequency then the signal will decrease since the peak response of the resonator will be higher or lower than the drive frequency. The decrease in signal is observable. For example, the data collected on 08 Sep, 2021, show an increase in the y mode resonant frequency from approximately 4233.7 to 4234.8 kHz as the DC bias field was increased from approximately 25 to 200 kA/m. The change was approximately 1.1 kHz. The resonator Q

was above 2000. The 3 db bandwidth was approximately 4234 kHz/2000 ~ 2.1 kHz which means that the change in resonant frequency of 1.1 kHz put the response down by approximately 3 db. A 3 db drop in response equates to a substantial drop in signal strength down to half power or $1/\sqrt{2}$ of the signal voltage.

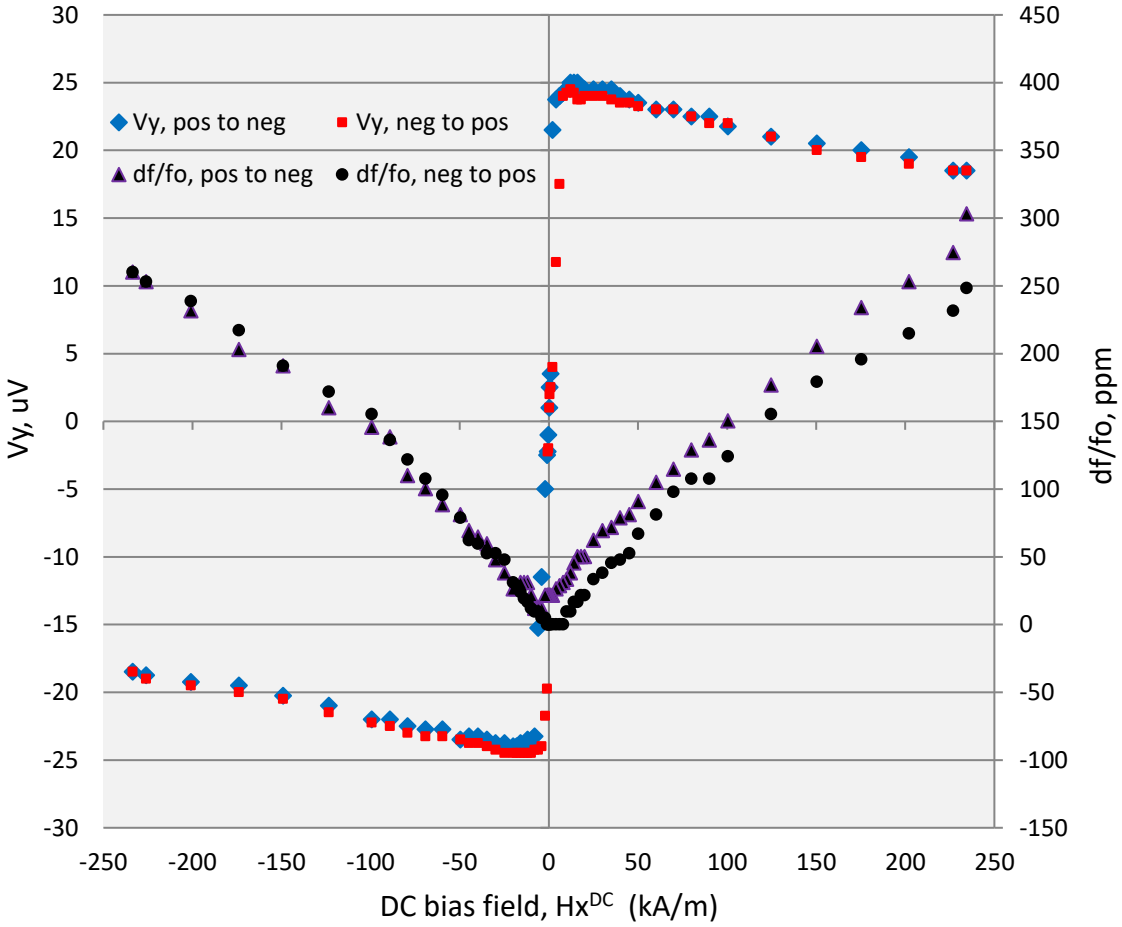

Figure 2.3.14. Sample S2A1A5. Ambient temperature. Voltage signal from y mode torque during a linear hysteresis loop. The change in y mode resonator frequency is plotted on the right vertical axis. The units for the frequency change are in parts per million of the initial frequency. The plot starts in the upper right, blue diamonds and purple triangles, and ends in the upper right, red squares and black dots.

Figure 2.3.15 shows the voltage signal and frequency change for the first linear hysteresis loop obtained after field-cooling. Figure 2.3.16 shows the data for the subsequent loop.

Compare the frequency changes in figures 2.3.15 and 2.3.16 to figure 2.3.14. The frequency change in the ambient loop, figure 2.3.14, shows that the frequency difference between the start and end of the loop was approximately 50 ppm. The frequency nearly returned to its starting value. The plots in figures 2.3.15 and 2.3.16, field-cooled loops, show that the difference between start and end frequencies was approximately 160 ppm and that the frequency change evolved throughout the loops. The cause for the evolution is unclear. The torque signals returned to their starting points, so the explanation for the frequency difference from start to end cannot be limited to simple considerations of changes in anisotropy strengths or directions.

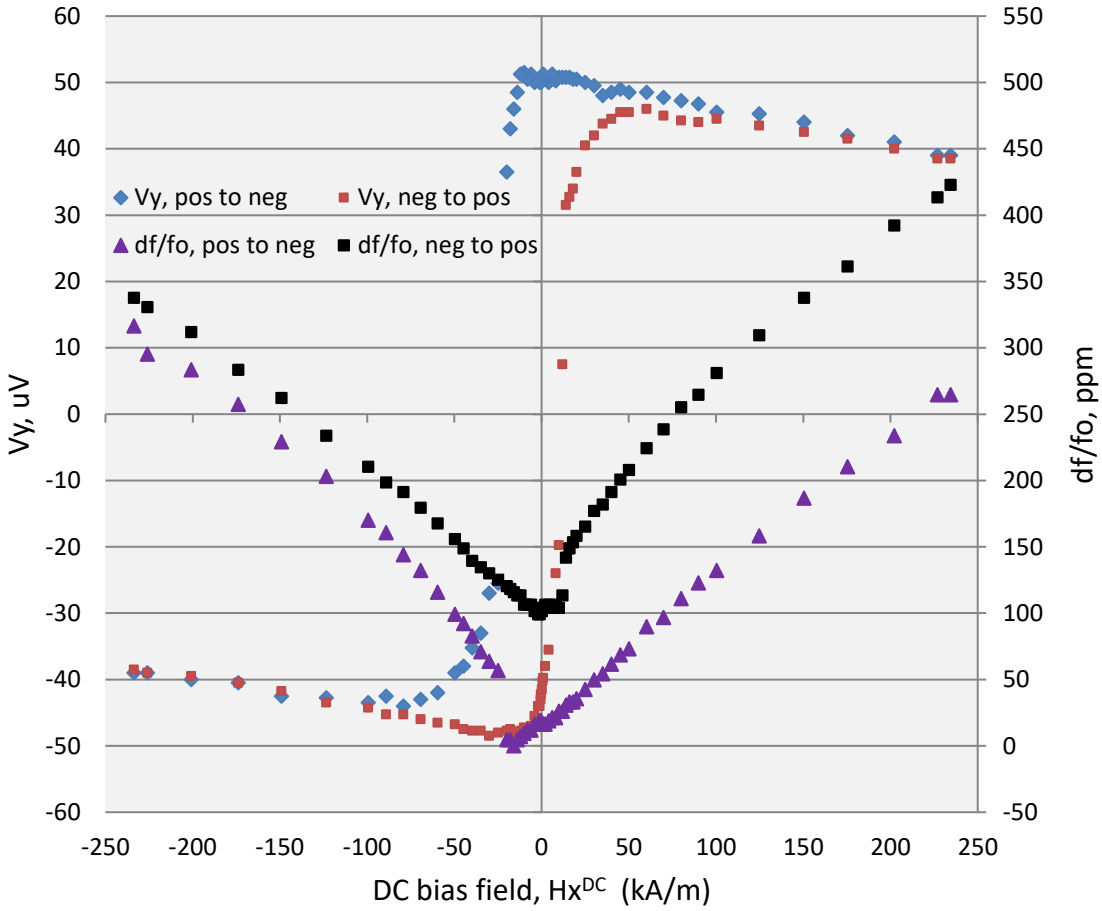

Figure 2.3.15. Sample S2A1A5. Field-cooled to 68.3° K in a positive, saturating, field. Voltage signal from y mode torque during the first linear hysteresis loop after field-cooling. The change in y mode resonator frequency is plotted on the right vertical axis. The units for the frequency change are in parts per million of the initial frequency.

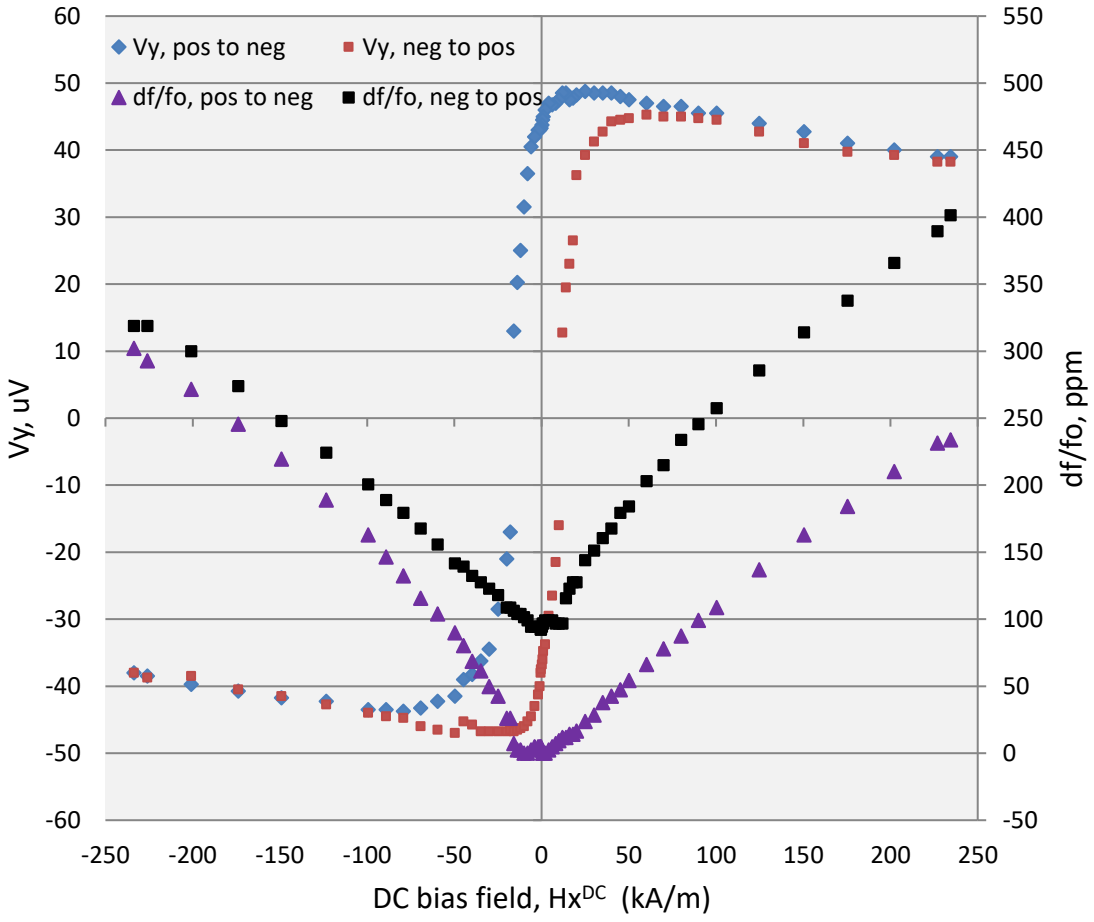

Figure 2.3.16. Sample S2A1A5. Field-cooled to 68.3° K in a positive, saturating, field. Voltage signal from y mode torque during the second linear hysteresis loop after field-cooling. The change in y mode resonator frequency is plotted on the right vertical axis. The units for the frequency change are in parts per million of the initial frequency.

Cullity and Graham discuss the contribution of anisotropy to the total spring constant of a torsion-pendulum DC magnetometer.[298] The additional spring constant, k_s, (using Cullity and Graham's notation), is due to a restoring torque, generated by anisotropy, and is determined from $k_s = d\tau/d\theta = d^2E/d\theta^2$ (second derivative with respect to energy since $\tau = dE/d\theta$).

To investigate the change in resonant frequency of our samples, a simple form of an energy equation was used to obtain an estimate of k_s for our resonator (refer to equations 2-2 and 2-3 in Chapter 2, subsection 2.1.6, ii and iii). The energy was minimized in software to obtain the angle between the magnetization and an externally applied DC bias field. The geometry was the same as that of our apparatus and sample arrangement.

The elements in the energy equation were the demagnetization and Zeeman terms. The calculation was done for the y mode torque signal. For a thin film, the demagnetization factors, N_x and N_y, for the in-plane directions are small compared to the factor, N_z, for the out-of-plane direction. The demagnetization factors were taken to be $N_x = 0$, $N_y = 0$ and $N_z = 1$. The anisotropy for permalloy was taken as zero and contributions from the antiferromagnetic cobalt oxide were considered to be negligible. A DC bias field along the apparatus x axis causes the magnetization to be in-plane and in the x direction. The z component of AC dither causes the magnetization to rotate, very slightly, in the out-of-plane direction thus generating an AC torque about the y axis (hence a y mode torque signal). With these parameters and assumptions, the energy equation is,

$$\varepsilon = -\mu_o M_S H_T V \cos(\Phi_{HT} - \Phi_M) + \frac{1}{2}\mu_o M_S^2 N_Z V \sin^2(\Phi_M) . \qquad (2\text{-}13)$$

The saturation magnetization of the ferromagnetic permalloy layer was taken as M_S = 763 kA/m. H_T is the time varying magnitude of the total field, $(H_X^{DC} + H_X^{AC} + H_Z^{AC})$. H_X^{DC} is the DC bias field. It was varied from -240 to 240 kA/m. The AC field magnitudes were

taken from the AC field calibration, $H_X^{AC} = 10.7\ A/m$, and, $H_Z^{AC} = 13.9\ A/m$. V is the sample volume, (1.36 um diameter, 16.1 um permalloy thickness). The angles, Φ_{HT} and Φ_M, are the external field and ferromagnetic magnetization directions respectively. The angles are measured counterclockwise from the x axis (standard convention).

Energy minimization produced values of Φ_M corresponding to the time-dependent field strength and orientation. A value of k_s was calculated for each point in a 100 point cycle of the AC torque using Cullity and Graham's equation $k_s = d^2E/d\theta^2$ where θ is Φ_M in equation (2-13). k_s varied sinusoidally with the torque signal. The maximum value of k_s was used to calculate the change in resonator frequency (use of an RMS or average rectified value of k_s was found to make little difference since the change in resonator frequency during the time of one resonator cycle was very small). The process was repeated for each value of the DC bias field (stepped by 8 kA/m from -240 to 240 kA/m).

The change in resonator frequency was obtained by first using the measured resonant frequency in low field to obtain an estimate of k_o (the torsion spring constant due only to the torsion arm). A value for the resonator moment of inertia was required for this calculation. Michael Dunsmore obtained the moment of inertia constants for each of the resonator axes. The constant for the y mode torque is 4.6×10^{-27} kgm^2 (refer to Chapter 2, subsection 2.4.6, para A). The low field resonator frequency was 4188.930 kHz. The value of k_s was added to k_o and the resonant frequency was recalculated.

The simulated changes in resonator frequency as a function of the externally applied DC bias field are plotted in figure 2.3.17. Note that the best fit to the observed change in frequency was obtained only by applying a correction factor of 0.47 to the simulated results. This means that, although the energy equation did not describe the effect precisely, it did give results consistent with shape anisotropy as the cause for the change in frequency. A more refined form of the energy equation may have given better results.

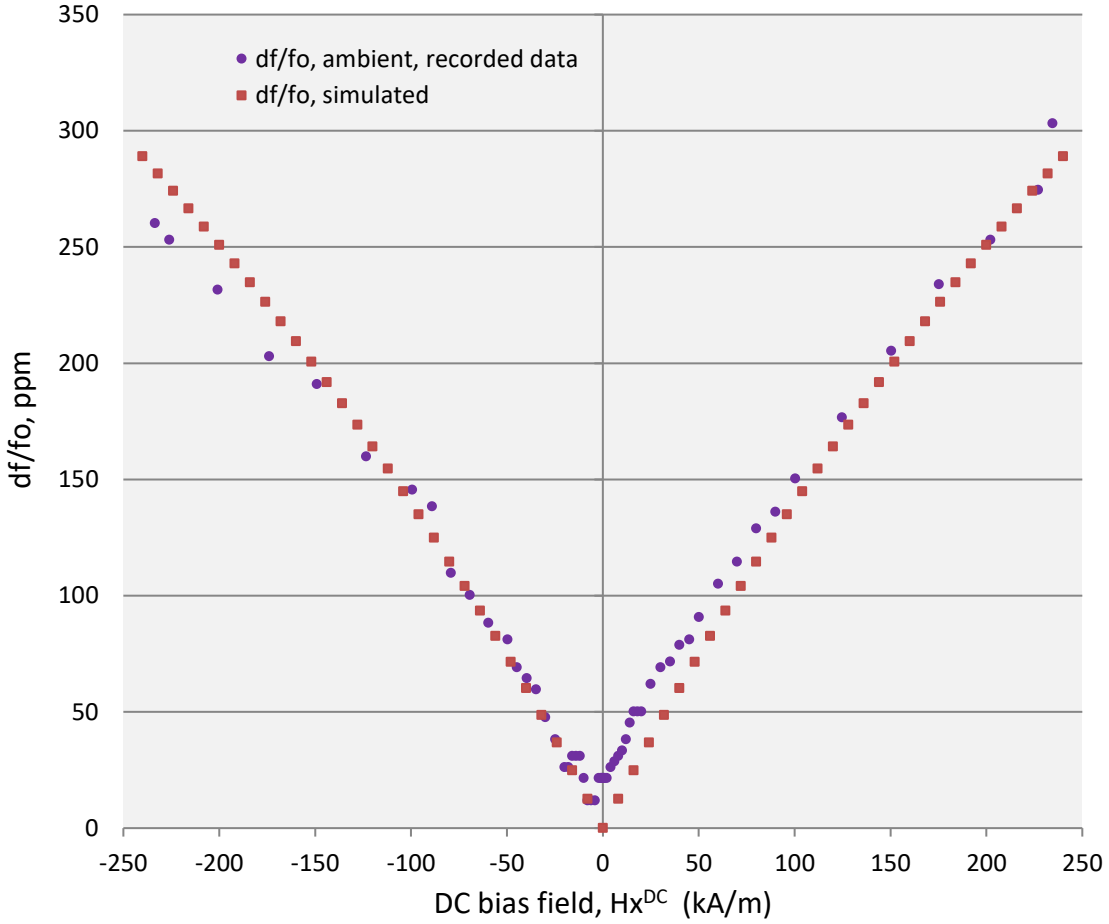

Figure 2.3.17. Sample S2A1A5. Ambient temperature. Change in y mode resonator frequency in parts per million of the initial frequency. The recorded data are the same as in figure 2.3.14 for the positive to negative sweep of the DC bias field. The simulated data were obtained by considering contributions from the demagnetizing and Zeeman energies to the y mode spring constant of the resonator. The total y mode spring constant increases as the bias field increases thus increasing the resonant frequency. (A factor of 0.47 was applied to the simulated data to obtain a fit to the recorded data.)

2.4) Thermomechanical calibration.

2.4.0) Section introduction.

This section will describe the method by which voltage measurements, obtained from a synchronous detector (lock-in amplifier) were converted to absolute torque. The apparatus and its functions are described in Chapter 4.

The topics in this section are,

2.4.1) Importance of calibration.
2.4.2) Motivation.
2.4.3) Introduction to calibration.
2.4.4) Equipment calibration.
2.4.5) Thermomechanically driven motion.
2.4.6) Procedure for obtaining thermomechanical signatures.
2.4.7) Analysis
2.4.8) Summary.

2.4.1) Importance of calibration.

I became aware of the concept of calibration in the early 1980's during my first two years of service as a communicator in the Canadian Armed Forces. Repair and calibration of electronic test equipment was conducted at the 202 Workshop Depot located at Canadian Forces Base, Montreal. I never had an opportunity to visit the 202 Workshop, but sometimes had the duty of administering the tracking of equipment that was sent out for calibration. Having no experience with calibration, I regarded the seemingly constant requirement to send equipment out for cal as somewhat of a nuisance since our electronic repair sub-unit was often without required test equipment for several weeks. I learned a valuable lesson, however, regarding a very necessary and important requirement to have the RF power output of certain transmitters limited to a very specific level. The task of

ensuring that the power output levels were accurate required the use of calibrated test equipment.

More relevant to scientific investigations, my next introduction to calibration came while working as a summer student in the Department of Physics, at the University of Alberta, while on leave from the Canadian Forces. These were the summers from 1985 to 1989. I carefully watched, over a period of several days in the summer of 1986 or 1987, as Dr. Jim Rogers went about the task of calibrating the instruments (tiltmeters) we used for geophysical studies. The group[c] published several papers.[299-304]

It was good experience for me to see that the procedure required a high level of in-depth technical knowledge regarding function of the tiltmeters and the calibration equipment used. It became obvious to me that his skill was uncommon and that the quality and integrity of our findings were much enhanced by his efforts.

The study of surface inflation and Earth tides was the primary work conducted by our research group[d] (I served as the group electronics technician and also collected data from the field installations). The importance of calibration was made all the more apparent when, in the early 1990's, our group was enlisted by Dr. James Pinfold[e] to assist CERN with determining the effects of weather and tidal forces, generated by the solid Earth tides, on the accelerator beam alignment.[f] (The solid Earth tides result from deformation of the solid Earth by the Moon.)

[c] The research group at the time, in the mid 1980's, was Dr. Walter Jones, Department of Physics, University of Alberta, Ret., Dr. Jim Rogers, Department of Physics, University of Alberta, Ret., Pierre Rouleau (analyst), now Dr. Pierre Rouleau, Department of Physics, Grenfell Campus, Memorial University of Newfoundland, Miles Ertman (research assistant), and John Thibault (technician).

[d] The tiltmeters were installed at the University of Alberta, Leduc Observatory, Rollyview, AB, for extended periods of time (more than one year) for study of Earth tides. They were also installed near Anzac, AB, for studies of surface inflation for several months preceding, during, and for several months

after, hydro-fracture of an underlying formation. The projects were cooperative efforts supported by the University of Alberta, the Alberta Oil Sands Technology and Research Authority (AOSTRA, Provincial Government of Alberta), and Amoco Canada.

[e] Dr. James Pinfold, Department of Physics, University of Alberta, currently serving as of 2022.

[f] CERN, Conseil Européen pour la Recherche Nucleaire, now the European Organization for nuclear Research, Fr. Organisation Européenne pour la Recherche Nucleaire. Tiltmeters were installed in the Canadian detector hall for a proof of concept period. The location was near the accelerator ring (26.7 km circumference and 100 m below ground level). In the days following the installation there was a rainfall that caused loading of the main structure. The tiltmeters responded to the loading thus indicating deformation of the structure. In the months following the proof of concept period, the tiltmeters were moved to locations nearer and adjacent to the beam path. Approximately one year later, it was determined that there was no correlation between the solid Earth tides and the accelerator beam alignment. The lack of correlation may have been due to the much different time scales that were involved. The solid Earth tides vary over a period of hours whereas stability of the beam alignment may be due to parameters that vary on a timescale much less than one second.

2.4.2) Motivation.[g]

It is sometimes sufficient to conclude an investigation be reporting results that are referenced to themselves. An example of this method would be reporting numbers that are compared to some maximum measured value (normalized results). Another example would be comparison of measurements to an established reference such as the "zero" reading obtained from an electronic bridge circuit or a temperature measurement referenced to ambient temperature. These are examples of relative, not absolute,[h] numbers since their values are not directly connected to some universally accepted standard.

[g] The sources for the comments in this subsection regarding reporting of results, measurement equipment, and calibration are my own direct experience with these subjects. My company, Terracene International

Ltd, conducts calibrations of industrial instrumentation (e.g. infrared pyrometers and length transducers) and provides strain gaging and stress analysis services to the industrial sector. Specifically, the instrument calibrations require annual, NIST traceable, calibration of our measurement equipment and the stress analysis work requires compliance with industry standards API-8C, ASTM-E4, and ASTM-E74 as well as annual, NIST traceable, calibration of our strain analyzer.

[h] "Absolute" numbers are not "exact". Determination and reporting of uncertainties is still required.

The desire or necessity to be in a position whereby absolute numbers can be reported represents the motivation toward calibration of measurement equipment. Measurements obtained from an apparatus provide information pertaining to the response of the apparatus to some stimulus. By themselves, the measurements do not correspond directly to the stimulus and are often not in the same units as the stimulus parameters being investigated. For example, in the experiment that was conducted, voltage and magnetic field strengths had to be converted and combined, somehow, to give torque.

To make the connection between measurement and stimulus, a deterministic relationship, usually in mathematical form, that describes the apparatus response to a stimulus is required. The sought after relationship can be referred to as the *total apparatus transfer function*. The total function may have many terms each of which corresponds to a transfer function describing the behaviour of a specific apparatus component. Once determined, the total apparatus transfer function provides a means by which information regarding the stimulus can be extracted from measured data. Note that only relative, not absolute, results are available from a total apparatus transfer function unless each and every term in the function has been connected to an appropriate standard through a calibration process.

Determination of the total apparatus transfer function can be an extremely tedious and time consuming procedure. The task is often aborted prematurely upon recognizing that required equipment for determining and calibrating the transfer function of one or more

apparatus components is either unavailable or cost prohibitive. Even if adequate equipment is immediately available, there may be some procedure that is not practical to perform or that requires more time than allotted to complete. It remains, however, that failure to complete the task means that only relative results can be reported.

2.4.3) Introduction to calibration.

A calibration procedure normally begins by first confirming that the calibration of all required measurement equipment is current. Calibration cycles are normally annual, but some standards allow for two-year cycles (this is rare and usually requires some sort of justification). Calibration labels giving the date of calibration, name of technician, and the next calibration due date should be attached to the instrument. A missing label must be assumed to indicate that the instrument is past due for calibration. Calibration reports are provided by the company that did the calibration and should be kept with the instrument records. A review of calibration records over several years sometimes exposes undesirable behaviours that worsen over time such as drift, gain error, and nonlinearity.

Calibration standards are available from the National Institute of Standards and Technology (NIST) website. Other standards that may be applicable are available from the governing bodies for the particular area of interest (e.g. Canadian Standards Association (CSA), Factory Mutual Laboratories (FM), Underwriters Laboratories (UL), American Petroleum Institute (API), American Society for Testing and Materials (ASTM), American Society of Mechanical Engineers (ASME), Society of Automotive Engineers (SAE), Conformité Europoéenne (CE), European Committee for Electrotechnical Standardization (CENELEC) , etc.) though a fee is usually charged for obtaining access to the documents.

The calibration requirement given by NIST is that "Metrological traceability requires the establishment of an unbroken chain of calibrations to specified reference standards...".[305] The unbroken chain can only be maintained if all of the individual pieces of equipment used for a calibration are themselves calibrated to specified standards with their own unbroken chain. Calibration requires traceability to fundamental references called *primary reference standards*.[306] Examples of primary standards are internationally agreed upon values for the kilogram, meter, second, etc. A piece of equipment that is calibrated, following the appropriate procedure for calibration, to a primary reference standard becomes a *secondary reference* standard. This piece of equipment can then be used to perform calibrations of other like equipment. The point here is that although primary reference standards are never available, traceable calibrations can still be performed as long as the unbroken chain is traceable back to the primary reference standard. Verification of traceability is not difficult, but it is tedious, time consuming, and sometimes costly. The task is by no means impossible. For example, annual calibration of data loggers, voltmeters, pressure transducers, load cells, frequency counters, and other such common laboratory equipment can be done by calibration companies that, quite commonly, have facilities in most major cities (there are several in Edmonton and Calgary).

Familiarization with the calibration standards applicable to each type of instrument is essential. For instance, some standards ask only for "3-point" calibration of instruments that have linear outputs. The 3 points are zero (sometimes 10% of full scale), mid-range, and full scale (sometimes 90% of full scale.) The trouble with a 3-point cal is that it will not expose nonlinearities that often exist between the points. A so called "+ /- 1% of reading" calibration that has only 3 points is virtually meaningless. If the calibration standard is found to be inadequate for what is required then it is up to the user to tell the calibration company that a calibration procedure beyond the requirements of the standard must be performed.

2.4.4) Equipment calibration.

The apparatus used for the experiment does not function in a way that allows for straight forward calibration of the output. The input to output transfer functions of the lock-in amplifier, Gauss meter, external DAQ (data acquisition system), temperature controller, pressure gauges, and vacuum gauges can be calibrated using standard procedures, but the transfer functions for the RF amplifier and, particularly, the optical path are much more difficult to determine and calibrate.

Cost and time delay were considered to be prohibitive factors for calibration of the lock-in amplifier, Gauss meter, external DAQ, temperature controller, pressure gauges, vacuum gauges, and RF amplifier. The transfer functions of these instruments were assumed to be linear and the outputs from them were taken as “true”.

The DC bias field strengths were determined during the spring and summer of 2020. The field components were measured at many positions along the magnet translation axis and at many angles of rotation. The x, y, and z components of the field had to be measured separately since the Gauss meter is a single channel instrument. The field sensor was mounted so as to sense the field along one axis, the data were collected, and then the sensor was repositioned to sense the field along another axis, data were collected, etc. Sufficient data were collected to permit interpolation between the measurement points for both translation and rotation. Some specialized electronics and a control system were required. I brought these from my company and modified them as necessary for the task. The procedure took approximately two months to complete. The Gauss meter did not have a traceable calibration so the field strengths are not calibrated, but are, instead, only referenced to the Gauss meter.

Determination of the AC field strengths was not done in accordance with a recognized calibration standard since, to our knowledge, no such standard exists that would be

adequate for the purpose. Instead, we had to assume that the drive signal levels from the lock-in amplifier were true and that the gain of the RF amplifier was also true. This allowed for estimation of the output currents from the RF amplifier. The drive coil was a hand wound solenoid with approximately seven turns (refer back to figure 2.3.6). The inductance, winding resistance, and impedances for each of the three drive frequencies were calculated, not measured. The change in winding resistance as a function of temperature was negligible since the winding resistance was always much smaller than the drive coil reactances. The calculated impedance values were used to determine the currents by assuming that the transfer function from the lock-in amplifier output through the RF amplifier was as given and was true. The output currents generated solenoidal fields in the drive coil. The drive coil was positioned on top of the sample wafer so that the field components external to the coil were what excited the sample and not the much more uniform solenoidal fields in the centre of the drive coil.

On 17 and 18 July, 2021, the linearity of the drive coil fields as functions of drive level, frequency, and temperature were checked. The data were obtained from a pick-up coil that was positioned a small distance directly above the drive coil. The signal in the pick-up coil was measured as a function of drive level, frequency, and temperature which, by way of the mutual coupling between the two coils, gave a fair representation of the drive level, frequency, and temperature dependencies of the fields produced by the drive coil. The responses were checked at five different drive levels and at two temperatures over a frequency range wider than used in the experiment. The drive levels were also over a range wider than used in the experiment. The responses were checked for each of the three drive signal oscillator outputs from the lock-in amplifier. 15 data sets were collected at ambient temperature and 15 were collected at a helium cryogen temperature of 6.5° K.

The results from oscillator 1 at a 75 mv drive level are shown in figure 2.4.1 at ambient temperature and in figure 2.4.2 at 6.5° K. The maximum non-linearity in figure 2.4.1 is

-0.4% of full scale from 1000 kHz to 5000 kHz. The plots for the other oscillators gave similar results. The measured torques were functions of the AC fields generated by the drive coil. Verification of field linearity with drive level, frequency, and temperature made the task of torque calibration much easier and more straight forward.

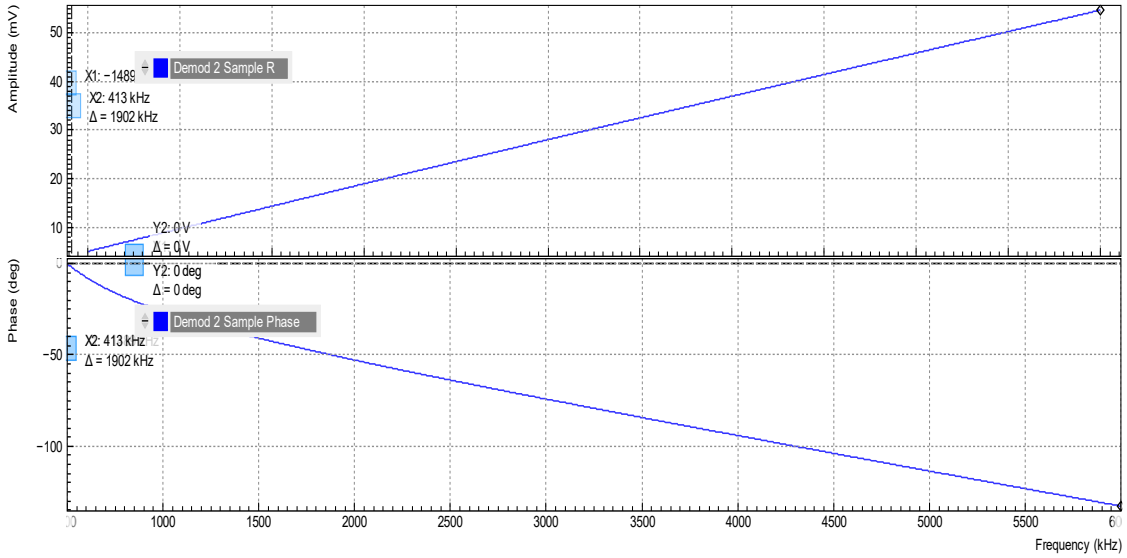

Figure 2.4.1. Drive coil field as a function of drive frequency at ambient temperature.

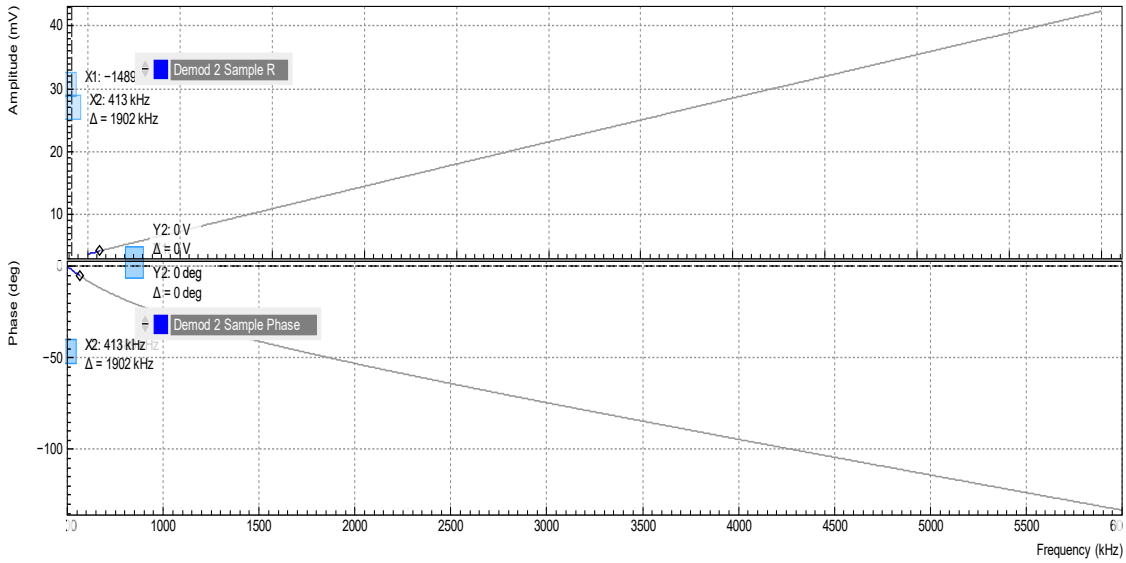

Figure 2.4.2. Drive coil field as a function of drive frequency at 6.5° K.

In the fall of 2021, Michael Dunsmore prepared a COMSOL[293] simulation that considered the proximity of the drive coil to the sample wafer and the proximity of the sample wafer to the copper cold-finger of the cryostat (the sample wafer was fixed to the top of the cold-finger). The geometrical arrangement of the components and the drive coil currents were the inputs to the simulation program. The output of the program was a field map giving the strengths and directions of the fields at the location of the specific resonator that was examined during the experiment.

The results from the field simulation are shown in figure 2.4.3. Michael Dunsmore ran the simulation, obtained the results, and produced the field map shown in the figure. The x, y, and z field components produced by the simulation had the expected relationship. The field direction at the resonator was primarily in the direction of z (the drive coil axis). The simulation gave a value of H_Z^{RF} = 350 +/- 20 A/m per amp of drive current. The x component of the field at the resonator was smaller since the resonator position was at the bottom of the coil and was displaced from the coil axis. The simulation gave H_X^{RF} = 270 +/- 20 A/m per amp of drive current. The y component was expected to be quite small since the resonator was very near the x axis where a y null in the field should exist. The simulation gave H_Y^{RF} = 0 +/- 20 A/m per amp of drive current.

Note that only one set of field strength numbers is given in the above paragraph. One for H_X^{RF}, one for H_Y^{RF}, and one for H_Z^{RF}. The drive coil is an inductor and has a frequency-dependent impedance. Why, then, are there not a different set of field strength numbers corresponding to each of the three different drive frequencies? The answer lies in the fact that the drive coil impedance is much smaller than the 50 ohm output impedance of the RF amplifier. The SWR is high as a result of the impedance mismatch and, thus, the reflection coefficient is also high. The drive coil impedances are approximately 1.2 ohms at the z torque resonant drive frequency of 960 kHz (the lowest frequency used) to approximately 5.4 ohms at the y torque resonant drive frequency of 4230 kHz (the

highest frequency used). Solving for the drive coil current as a function of drive level, while including the effects of the high SWR, one obtains a drive coil current of I^{RF} = (drive voltage x 0.02) +/- 0.27% where the 0.27% is not an uncertainty, but is the percent change in I^{RF} over the frequency range used. The drive coil current does have a frequency dependence, as it should, but it is sufficiently small to be neglected. This means that the drive levels alone are adequate for giving the AC field strengths and that only one, frequency independent, sensitivity number is required for each field component, H_X^{RF}, H_Y^{RF}, and H_Z^{RF}.

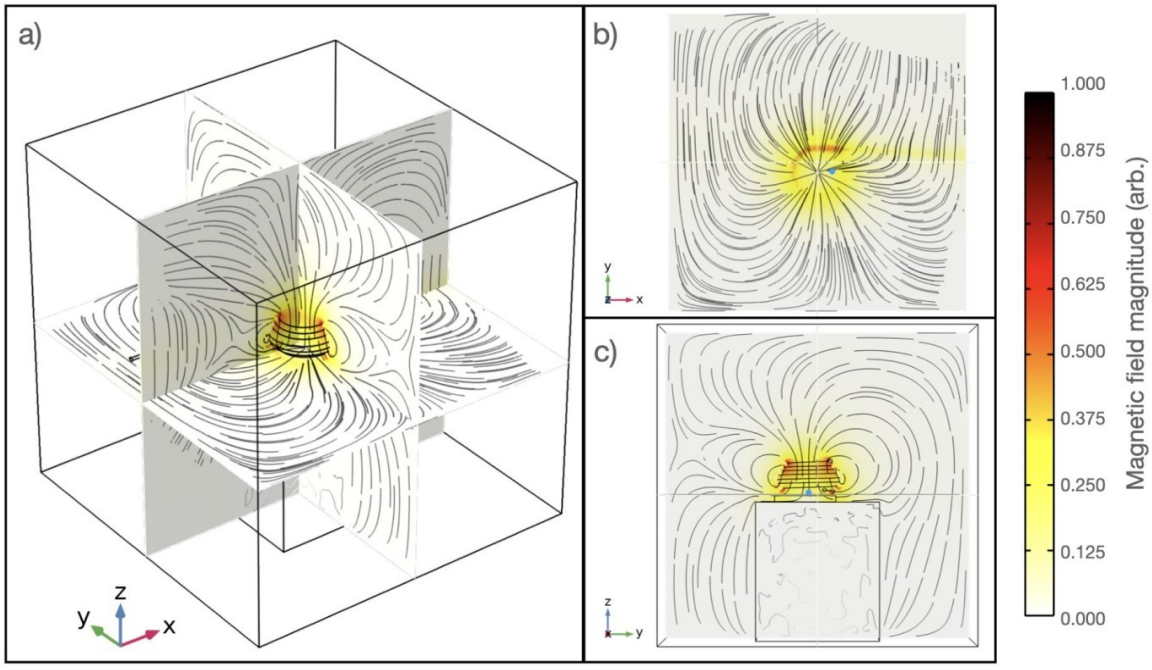

Figure 2.4.3. AC field strength and direction results from the COMSOL[293] simulation prepared by Michael Dunsmore. Blue dot in panels (b) and (c) show the position of the resonator that was studied. Michael Dunsmore prepared the simulation program, generated the results, and produced the field map shown in the figure.

2.4.5) Thermomechanically driven motion.

The transfer functions for the optical path, photo receiver, and lock-in amplifier are difficult to ascertain. In principle, the photo receiver and lock-in amplifier transfer functions could be determined and a traceable calibration of these two pieces of equipment could be obtained, but, since the transfer function of the optical path cannot be precisely known[i], it is not possible to obtain a calibration of the interferometrically derived signal unless some means exists for providing a controlled movement of the resonator paddle through some fixed, calibrated, deflection. If a source for a controlled movement could be found, then the optical path could be calibrated by observing the response of the received optical signal to the deflection. What one is asking for is a machine, a machine that is itself amenable to traceable calibration, that can somehow push on a nanoscale resonator, without damaging it, and deflect it through some precisely known distance. We are aware of no such machine.

The situation concerning calibration of the optical path would be hopeless if it were not possible to extend the results obtained by Nyquist[307] regarding thermally generated noise in resistors to the problem of obtaining a calibration of the resonator motion. Nyquist's work was expanded upon by Callen and Welton[308] to include Brownian motion systems, vacuum fluctuations of the electric field, and fluctuations in the pressure of a gas.

[i] Refer back to figure 2.3.7 and take note of the optical paths in and beneath the resonator. A portion of the beam is reflected from the top surface of the resonator while another portion is transmitted into the resonator where it undergoes multiple internal reflections. Some of the beam is transmitted through the resonator and multiple reflections of this portion occur between the bottom surface of the resonator and the substrate base. Yet another portion of the beam bypasses the resonator completely and is then reflected directly by the substrate base. The final recombination of all the beam portions can be described mathematically meaning that a simulation program would be able to provide a transfer function for this part of the beam path, but a calibrated result would not be obtainable unless one had precise measurements of the relevant physical dimensions and someway of knowing, for certain and quite beyond mathematical description, the precise behaviour of the optical cavities.

Cleland and Roukes apply the "fluctuation-dissipation" theorem (also known as the Nyquist-Johnson theorem) to the problem of quantifying the thermally driven motion of a mechanical resonator. The fluctuation-dissipation follows from the behaviour of dissipative systems. "Systems that dissipate energy are necessarily sources of noise; the converse is also often true. This is the basic statement of the fluctuation-dissipation theorem...".[309]

The key point made by Cleland and Roukes is that mechanical resonators are described as dissipative since they have finite Q and they are immersed in a thermal bath. From the fluctuation-dissipation theorem, "...the non-zero value of Q^{-1} and temperature T necessitates the presence of noise...so that in the presence of dissipation only (no driving force), the mean energy <En> for each mode n of the resonator will be given by <En> = k_BT...".[310]

What is it that Cleland and Roukes are telling us and how do we use it? What they are saying is that a special machine for generating a paddle deflection need not be designed. Nature provides the required machine in the form of a *thermal agitator*. Thermally driven motion of the resonator will always be present even when all external driving forces are absent. If one can determine "how much temperature" causes "how much resonator motion" then the optical path can be calibrated by monitoring the output of the lock-in amplifier while noting the temperature of the sample. Note that the laser power, transmission and reflection properties of the optical components, the precise behaviour of the laser beam in the optical cavities, the efficiency of the photo receiver, and the measurement accuracy of the lock-in amplifier all become irrelevant since all that is required is to record the output voltage from the lock-in amplifier that results from thermomechanically driven motion.

The mathematical formalisms that are required to determine the resonator motion due to thermomechanical noise are somewhat involved, but follow from the methods of statistics and, particularly, signal analysis. They are described in the paper by Cleland and Roukes,[309] in Cleland's textbook,[311] and in papers by Hauer et al.[312] and Losby et al.[313] (Joseph Losby is a former member of our research group). They are also presented in the supplement to our paper that was published in AIP Advances in Mar, 2022.[314] The formalisms use the equipartition theorem to connect the thermal k_BT energy, which drives the resonator thermomechanically, to the potential energy of the resonator which can be determined if the moments of inertia are known.

2.4.6) Procedure for obtaining thermomechanical signatures.

A) Moments of inertia.

The procedure for thermomechanical calibration requires that the moments of inertia for each of the resonator modes be known. These were obtained by simulation where the inputs to the simulation program were the physical dimensions of the resonator. Note that these physical dimensions could not be measured such as might be done with metrology tools. The resonator is much too small for that. One has to rely on the SEM images of the resonator to estimate the dimensions. At this point, the calibration process fails to be traceable and, thus, does not fit into the definition of calibration given by NIST. Also, it is possible that the theoretical treatment of thermomechanical noise may not be adequate for establishing it as a primary reference standard. In spite of the inability to obtain a traceable calibration, one must continue with the method since there does not appear to be any alternative. A simulation program was prepared by Michael Dunsmore. Michael estimated the required resonator dimensions, ran the program, and obtained values for the moments of inertia for each of the resonator modes of sample S2A1A5. On 31 Aug, 2021, he obtained moment of inertia constants of 1.9329×10^{-25}, 4.6114×10^{-27}, and 1.9781×10^{-25} kgm^2 for the x, y, and z torque modes respectively.

B) Thermomechanical data.

Additional requirements for thermomechanical calibration are the responses of the resonator during frequency sweeps, spanning from well below to well above the resonance frequency (wide enough so that the signal reaches the noise floor of the lock-in amplifier on both sides of the resonance peak), while driving the resonator with the external AC fields and, also, while the AC fields are off so that, in this latter case, the response is due only to excitation of the resonator by way of thermomechanical noise. The calibration procedure is repeated for each of the three torque modes. The data are used to calculate the resonance frequencies, resonator Q's, and power spectral densities of the thermomechanically driven resonator responses for each resonator mode.

A typical set of plots required for thermomechanical calibration are shown in the two panels of figure 2.4.4. The data were obtained on 10 Feb, 2021, from the y mode torque signal of sample S2A1A5 while at a temperature of 4.5 °K. The upper panels show the frequency and phase responses of the resonator while it was being driven by the external AC excitation fields. These data were used to calculate the driven resonance frequency and resonator Q for the y mode torque. The thermomechanical calibration procedure does not require these data, but they are collected anyway since they provide a quick determination of driven resonance frequency and Q.

The lower panels of figure 2.4.4 show the frequency and phase responses of the resonator while it was being excited only by thermomechanical noise. Note that the signal level is much lower than the driven signal level. Note also that the phase is incoherent which is consistent with a drive signal that has a random frequency and phase. The resonator is being driven by noise, so there should be no specific drive frequency and the phase should be random.

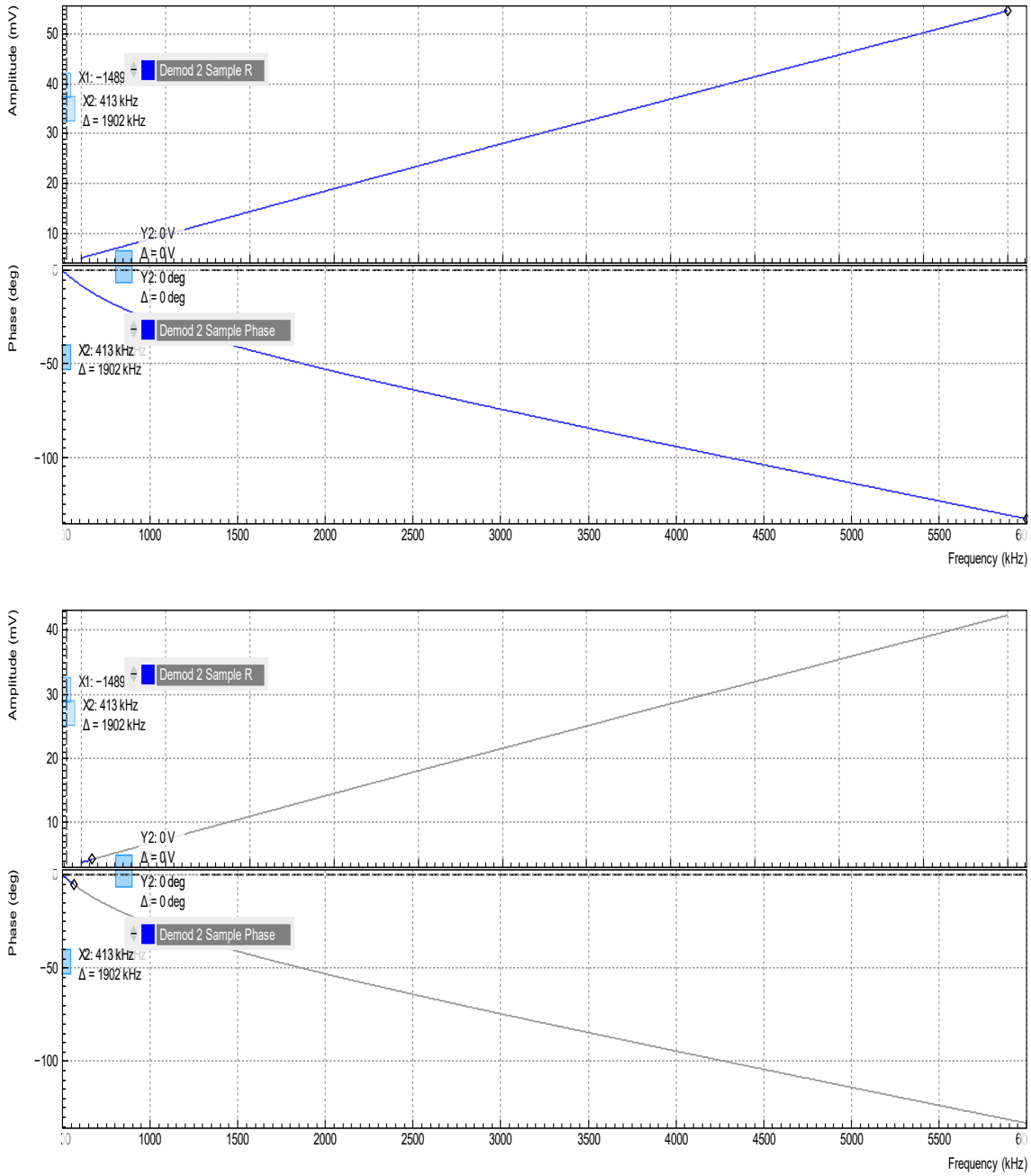

Figure 2.4.4. Frequency and phase responses of the y mode torque signal from sample S2A1A5, 4.5 °K, 10 Feb, 2021. Upper two panels are the responses obtained while the resonator was being driven by the AC excitation. Lower two panels show the thermomechanical responses obtained after turning off the AC excitation.

2.4.7) Analysis.

Reduction of the frequency sweep data can be done by a suitable program. The inputs to the program are the voltage output from the lock-in amplifier as a function of frequency (the frequency sweep data), the moment of inertia constants for the three resonator modes and the sample temperature. The output of the program is three sensitivity constants, in units of resonator torque per millivolt of signal, corresponding to the sensitivities for each mode. Michael Dunsmore prepared a program and was able to obtain the required sensitivity constants.

The first step of the analysis is application of a Lorentzian fit to the frequency response data. The resonance frequency and resonator Q are obtained from the Lorentzian fit to the thermomechanical data (lower panels of figure 2.2.4, not the AC driven data in the upper panels). Next, the power spectral density is calculated, and then, using the moment of inertia constant, resonance frequency, Q, and temperature, a torque sensitivity factor is extracted by equating the measured resonator energy to the thermomechanical energy through the equipartition theorem. The final result provides a calibrated sensitivity factor in units of torque per millivolt of signal. The process is repeated to obtain calibrated sensitivity factors for all three torque axes.

Once the torque sensitivity factors have been determined, the voltage signals from the three torque modes can be converted to absolute, calibrated, torque by applying the appropriate sensitivity factor to the voltage data.

Michael Dunsmore conducted the calibration procedure for sample S2A1A5. The torque sensitivity factors at 295° K were 8.6 +/- 0.4, 5.0 +/- 0.5, and 11.1 +/- 0.6 aNm per mV of signal for the x, y, and z torque modes respectively. At 69° K the factors were 2.67 +/- 0.05, 2.90 +/- 0.09, and 6.4 +/- 0.4 aNm per mV of signal for the x, y, and z torque modes respectively.

2.4.8) Summary.

A final comment on the thermomechanical calibration procedure is that it is highly sensitive to parameters that cannot be measured, but, instead, must be estimated. The estimated parameters are the moments of inertia that can only be determined by estimating the physical dimensions of the resonator and the sample temperature that must be inferred from a sensor that is not coupled directly to the sample. The k_BT energy is required and is connected to the potential energy of the resonator. The temperature of the sample is inferred from the temperature that is recorded by a sensor that is coupled to the cold-finger of the cryostat, but this does not give the sample temperature directly since the sensor is not coupled directly to the resonator. The trouble, here, is that the laser pumps heat into the resonator so that the resonator temperature simply cannot be the same as the temperature where the sensor is mounted. It gets worse. The laser power is not distributed uniformly over the sample area, but is spot focused on a region that may be as small as 1% of the total surface area of the resonator so that local heating occurs. How is one to know what the sample temperature actually is and how can one be certain that local heating has not somehow affected the thermomechanical behaviour of the sample? Unfortunately, there is nothing in the procedure that addresses these problems, so answers cannot be provided. It is possible that collecting data at many temperatures and at different laser powers would provide the missing information. In fact, some of this work was conducted, but not enough data were collected and there was not enough time to complete the investigation.

Thermomechanical calibration is most certainly not “fool proof” and it does not adhere to traceability requirements, but it does provide a result where otherwise one would have no way of continuing. The final results of the thermomechanical calibration gave the torque sensitivities that were required to continue the work. The sensitivities were determined using the best and only possible method available.

Chapter 3

Sample

3.1) Sample.

3.1.1) General Description.

The samples were bilayers of permalloy and cobalt oxide deposited on nanomechanical resonators. The samples were fabricated in a silicon-on-insulator (SOI) wafer using standard lithography, etching, and micromachining techniques. Two sample sets, with each set having six arrays containing twenty samples, were prepared on a single 5 x 5 x 0.5 mm thick SOI wafer (240 samples total). The resonators were designed by Joseph Losby sometime prior to 2014. Fabrication was conducted at the University of Alberta nanoFAB and National Research Council of Canada Nanotechnology Research Centre (located on the University of Alberta main campus).

Sample sets 1 and 2 are shown in figures 3.1.1 and 3.1.2. Each set has six arrays of samples. Sample designations within an array are shown in figure 3.1.3. The outside dimensions of the samples vary from approximately 4 um x 5 um to 10 um x 5 um. The data for the thesis were collected from samples S2A1A5 and S2A6A1 in figure 3.1.2.

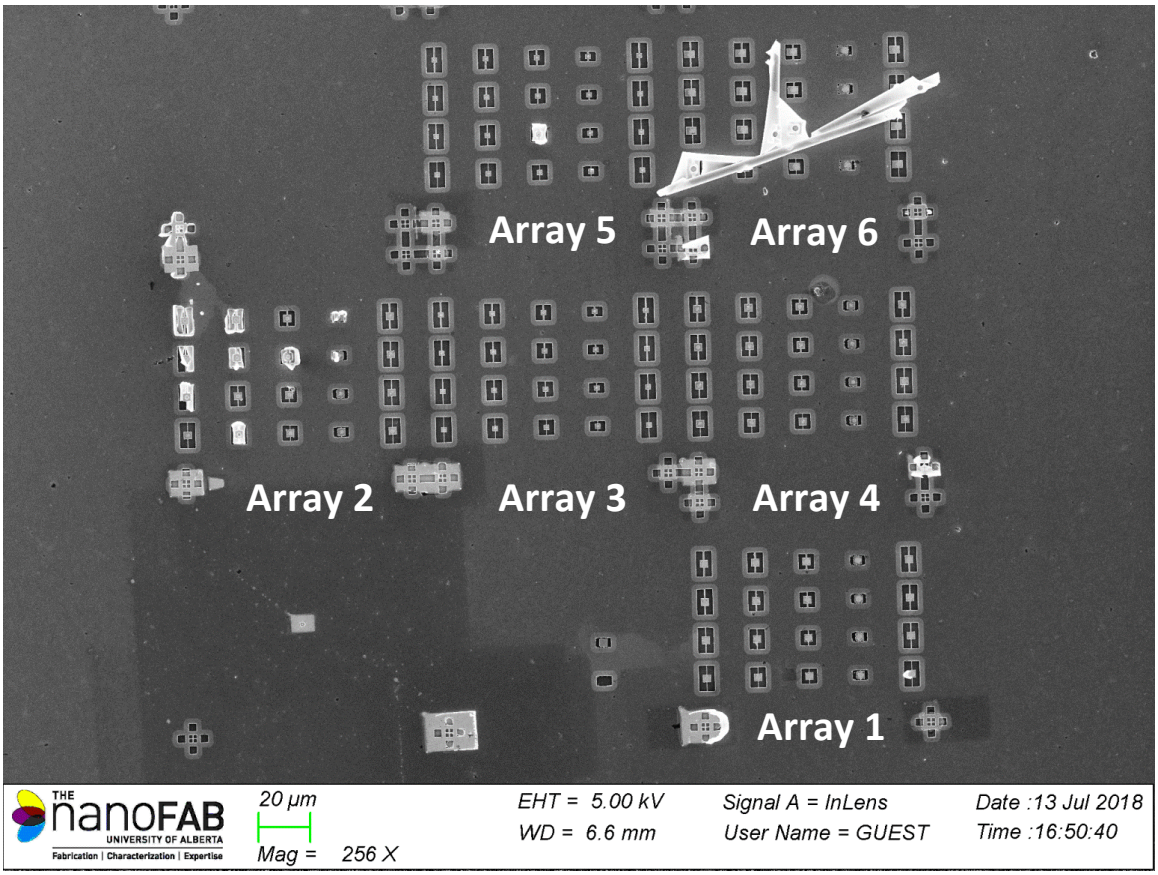

Figure 3.1.1. Sample set 1. Six sample arrays with twenty samples in each array.

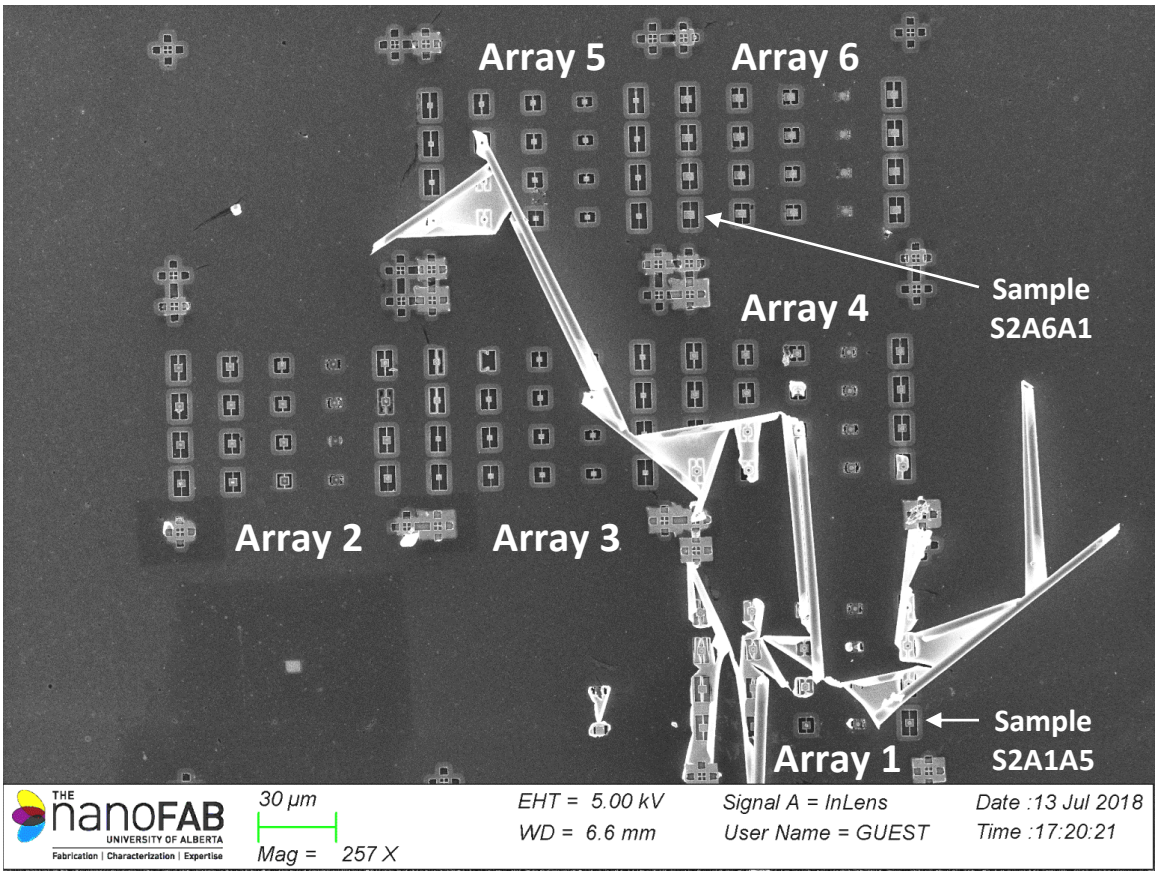

Figure 3.1.2. Sample set 2. Six sample arrays with twenty samples in each array. The data for the thesis were collected from samples S2A1A5 and S2A6A1.

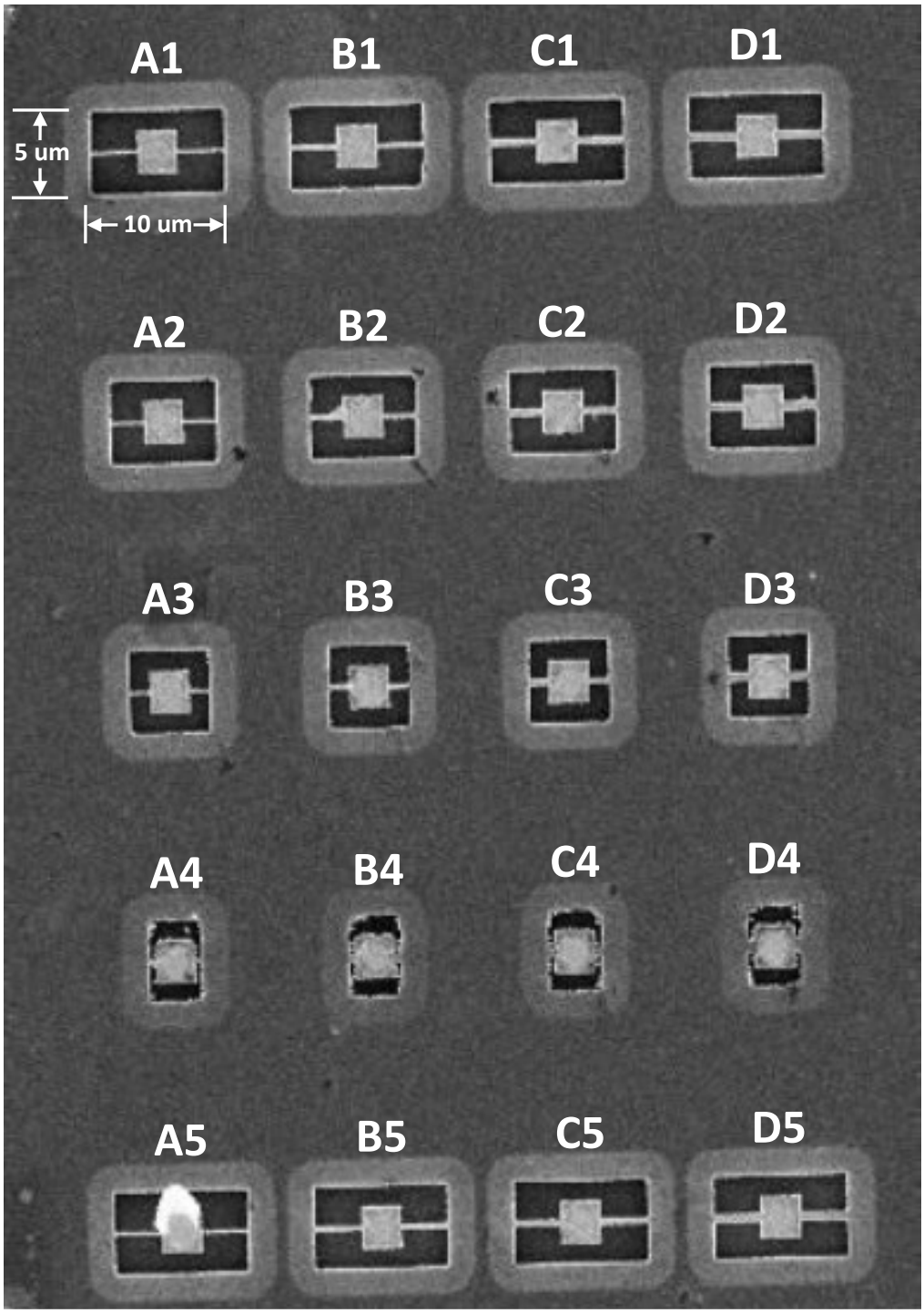

Figure 3.1.3. Sample designations within an array. Sample set 1, Array 1, is shown. The designation for the top left sample is S1A1A1.

3.1.2) Fabrication.

A) Nanomechanical Resonator.

Dimensional detail for design of the resonators was obtained from finite element analysis using COMSOL.[293] Primary considerations for the resonator design were paddle size, mechanical constants of the torsion arms, resonant frequency, torque sensitivity, and depth of undercut which forms a Fabry-Perot optical cavity between the resonator and substrate base. The depth of undercut was approximately 0.3 um for all of the resonator samples (the depth is purposefully selected to be approximately 1/2 wavelength of a helium-neon laser). The design work was done by Joe Losby, a former member of our research group.

During the design process, it was not known which resonant behaviour would be optimum for investigation of exchange bias, so dimensions of the resonator paddle, torsion arm length, and torsion arm cross section were varied so as to produce resonators with different resonant frequencies. A symmetric paddle with long, thin, torsion arms is shown in figure 3.1.4. Compare to figures 3.1.5 and 3.1.6 for examples of dimensional variation.

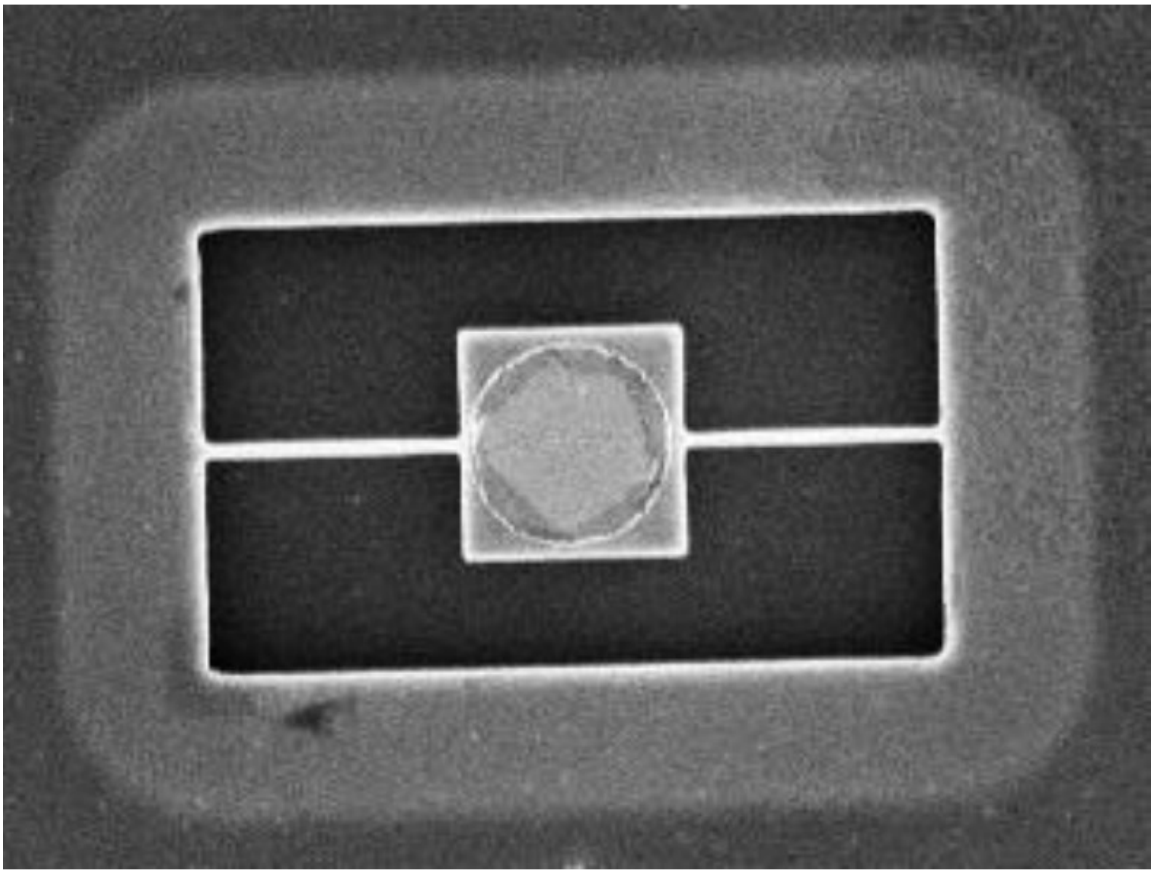

Figure 3.1.4. Sample S2A1A1. Symmetric paddle with long, thin, torsion arms. The sample dimensions are the same as in figure 2.3.1 except that the deposits of Py and CoO are approximately 2.6 um in diameter instead of 1.36 um.

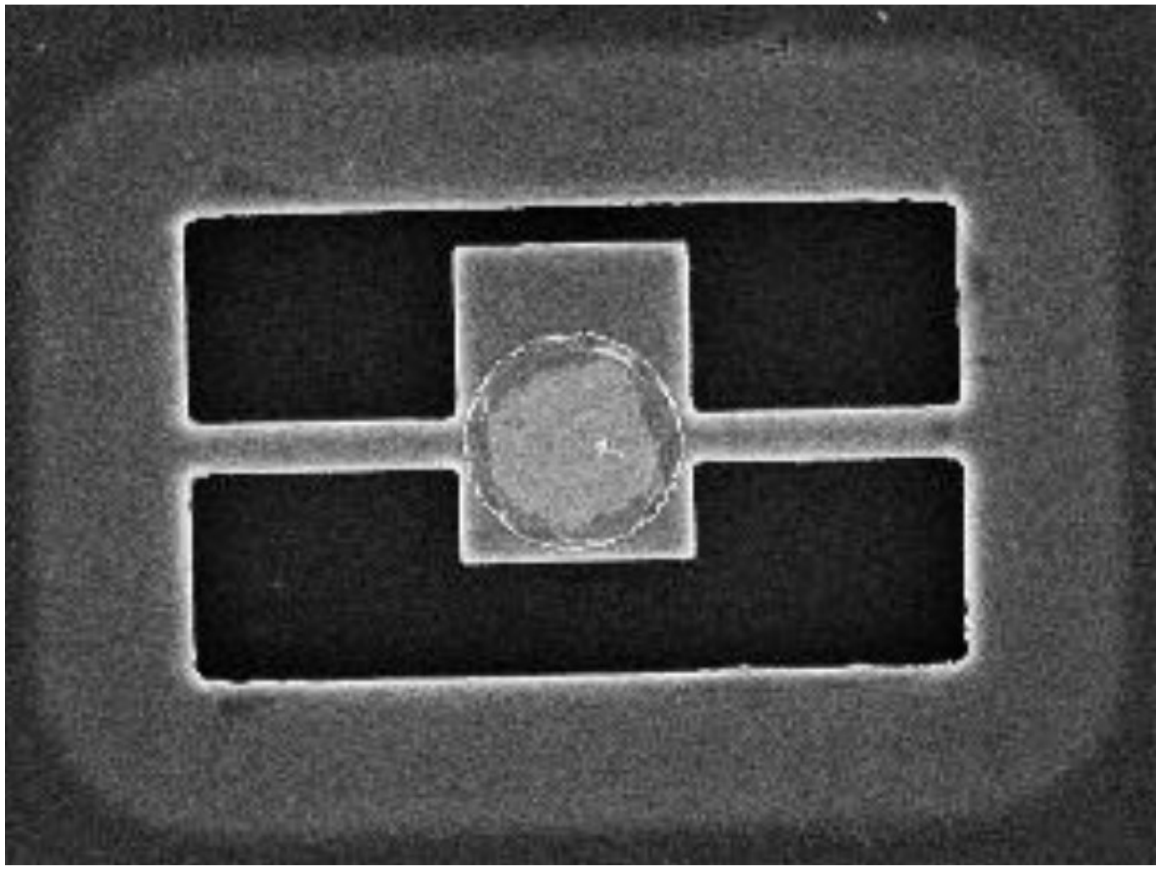

Figure 3.1.5. Sample S2A6D1. Asymmetric paddle with long, thick, torsion arms. The sample perimeter is 10 x 5 um as in figure 2.3.1. The torsion arms are 0.6 x 0.3 um instead of 0.15 x 0.3 um. The resonator paddle is 3 x 3.5 um instead of 3 x 3 um. The deposits of Py and CoO are approximately 2.6 um in diameter instead of 1.36 um.

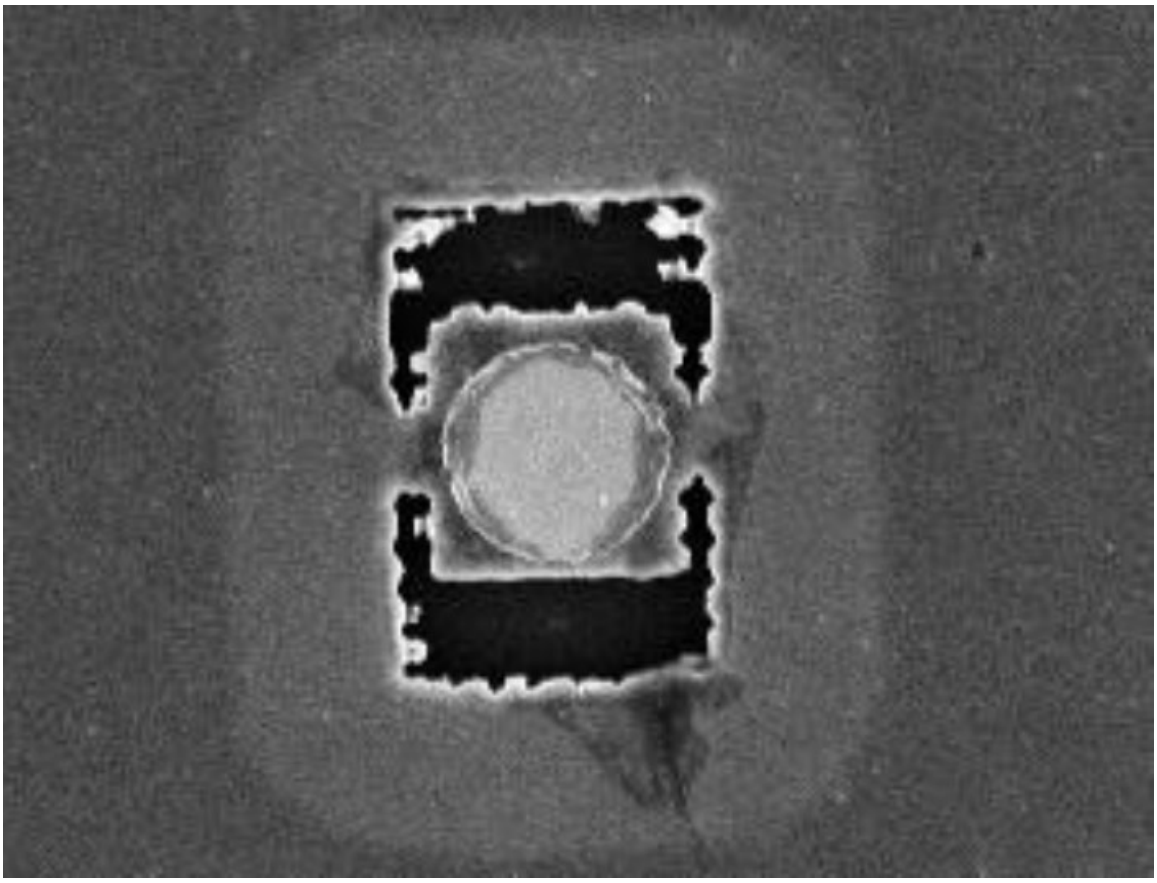

Figure 3.1.6. Sample S1A1D4. Symmetric paddle with short, thick, torsion arms. The outer perimeter is 3.7 x 5 um. The paddle is 3 x 3 um, the torsion arms are 0.8 um wide x 0.3 um thick x 0.36 um long. The deposits of Py and CoO are approximately 2.6 um in diameter.

B) Deposition.

Magnetic materials were deposited on the top surfaces of the resonator paddles by confocal magnetron sputtering sometime prior to 2014. The sputtering system was an ATC Orion 8, manufactured by AJA International, located at the University of Alberta nanoFAB. The sputtering targets, 2" diameter, were manufactured by Plasmaterials Inc. The deposition was performed by Dr. Erik Luber.

The first layer, in contact with the resonator paddle, was cobalt oxide (antiferromagnetic) that was reactively sputtered from a cobalt target. The deposition rate was 0.228 nm/min at an RF power of 118 Watts. The sputtering gas flow rates and pressures were 14 SCCM at 4 mTorr for argon and 6 SCCM at 4 mTorr for oxygen.

The second layer, permalloy (ferromagnetic) was deposited on top of the cobalt oxide layer after residual oxygen was purged from the sputtering chamber. The chamber was pressure cycled five times by filling to 40 mTorr with argon, holding for 60 seconds, and then pumping down for 60 seconds. The argon purge inhibited formation of an antiferromagnetic oxide layer on the surface of the ferromagnetic permalloy. Torque effects due to formation of nickel oxide on permalloy were studied by Prosen et al.[315] and, for our work, minimization of any such effects was desirable. The permalloy layer was deposited by reactive sputtering from nickel and iron targets. The deposition rates and RF powers were 1.13 nm/min at 40 Watts for nickel and 0.31 nm/min at 13 Watts for iron. The sputtering gas was argon at a flow rate of 20 SCCM and pressure of 4 mTorr.

A quartz crystal monitor was used to determine the deposition rates. The densities were assumed to be 6.44 g/cm^3 for the cobalt oxide, 8.91 g/cm^3 for the nickel, and 7.86 g/cm^3 for the permalloy. Cobalt oxide was the preferred molecule, but other oxides of cobalt may have been formed in small quantity. The preferred stoicheometry for the nickel and

iron was $Ni_{80}Fe_{20}$ so as to produce permalloy. The densities for the nickel and iron indicated that $Ni_{80}Fe_{20}$ was formed.

The cobalt oxide and permalloy layers were both 20 nm thick (40 nm total) and were in the shape of thin disks with a diameter of 1.36 um as determined from scanning electron microscopy. The top layer, permalloy, was not capped. Oxide formation on the top of the permalloy layer was a possibility since the layers were deposited prior to 2014 and the experimental work was not conducted until much later during the period 2018 to 2021. In the early winter of 2022, an analysis of collected data indicated that the effective thickness of the permalloy layer was only 16 +/- 1 nm suggesting that the thickness determined from the sputtering parameters was higher than actual and/or that oxide(s) had formed on the upper, uncapped, permalloy surface. Refer to Chapter 6, subsection 6.3.3, para (i), for details of how the effective thickness of the permalloy layer was determined.

C) <u>Modification.</u>

Experimental investigations began by studying exchange bias effects observed in the data obtained from room temperature and field-cooled linear hysteresis loops. The torque sensitivity about the torsion arm axis (y torque in our geometry) was adequate, but the sensitivities about the x and z axes were marginal. A novel scheme to remedy this problem was proposed by one of our researchers, Vince Sauer, whereby a substantial increase in the mechanical compliance of the x and z torque modes could be obtained by severing one of the torsion arms. One torsion arm of several selected resonators was cut using a focused ion beam (FIB) machine at the National Research Council of Canada Nanotechnology Research Centre, located on the University of Alberta main campus. The resonator modifications were successful. Subsequent experimental data showed torque responses from all three torque axes that were sufficiently above the system noise floor.

3.1.3) Mechanical constants of the resonator.

Data for the experiment were collected mostly from sample S2A1A5 (refer back to figure 3.1.2, lower right of the figure). The outside dimensions of the sample are approximately 10 um x 5 um. The resonator paddle dimensions are approximately 3 um x 3 um x 0.3 um. The torsion arms have dimensions of approximately 0.15 um x 0.3 um x 3.5 um long. Note that the right side torsion arm was cut (refer back to figures 2.3.2 and 2.3.7).

The spring constants of the resonator torsion arms are temperature dependent. The torsion arms "stiffen" with decreasing temperature. As a result of the stiffening, the resonance frequencies of the x, y, and z torque modes increase with decreasing temperature (an increase in the resonator Q's accompanies the increase in resonance frequencies). The spring constants also increase with increasing DC bias field (refer to Chapter 2, section 2.3, subsection 2.3.11). An additional effect, observed only at cryogenic temperatures, is a continuous decrease in the resonance frequencies and a corresponding decrease in the resonator Q's, over a period of several days, due to accumulation of ice on the resonator surfaces (ultimately, the system has to be warmed to ambient temperature when the resonator responses become too low). Michael Dunsmore obtained the moment of inertia constants for the three resonator modes from a program that he prepared and, on 31 Aug, 2021, he reported moment of inertia constants of 1.9329 x 10^{-25}, 4.6114 x 10^{-27}, and 1.9781 x 10^{-25} kgm^2 for the x, y, and z torque modes respectively (refer to Chapter 2, subsection 2.4.6, para A).

On 10 Nov, 2020, the system was at an ambient temperature of 295.3° K. Data from sample S2A1A5 showed that the resonance frequencies for the x, y, and z torque modes were 1881.3, 4188.7, and 952 kHz respectively. Data from sample S2A6A1 were also

collected. On 26 Mar, 2020, the resonance frequencies were 1561.7, 2756.9, and 792.2 kHz for the x, y, and z torque modes respectively at an ambient temperature of 298.0° K.

On 18 Nov, 2020, the cryogen system was running on liquid nitrogen at a temperature of 69.9° K. The cryostat temperature is always stable (+/- 0.05°), but it can range from 66° to 70° K depending on coolant pressure and flow rate. The resonance frequencies for the x, y, and z torque modes of sample S2A1A5 were 1895.35, 4232.70, and 964.34 kHz respectively.

In February and March of 2021 the cryogen system was running on liquid helium. On 10 Feb, 2021, one day after initial cooling, the temperature was 4.5° K. The cryostat temperature ranges from approximately 4° to 7° K depending on coolant pressure and flow rate. The resonance frequencies for the x, y, and z torque modes of sample S2A1A5 were 1897.8, 4239.3, and 965.6 kHz respectively. Note that the resonance frequencies were higher than they were at ambient and liquid nitrogen temperatures as expected. Data from hysteresis loops were collected with the system at liquid helium temperature, but these data are not reported on herein.

Chapter 4

Apparatus

4.1) Overview.

The apparatus was designed to investigate the magnetic properties of nanoscale samples. The samples were prepared by thin-film deposition of magnetic materials on the moveable paddle of a nanomechanical resonator. The resonators were subjected to a DC magnetic field, that could be varied in magnitude and direction, and to time varying RF fields. The combination of fields resulted in generation of AC torques about the resonator axes (refer to Chapter 2, subsection 2.3.7, for the description of torque generation).

Refer to the Apparatus block diagram in figure 4.1.1. The primary components of the apparatus are a cryostat, cryogen and vacuum systems, DC magnet and positioning system, Gauss meter, He-Ne laser, steering optics, three-axis objective positioning stage, photo receiver, UHF lock-in amplifier, RF amplifier, control computer, and power supplies.

Coarse adjustment of the cryostat temperature is done by manual control of the cryogen flow valves. Fine (+/- 0.05° K) temperature stabilization is provided by PID control of a heater that is mounted in the cryostat. The system will stabilize at any desired operating point from liquid helium temperature to 300° K. The system can be run on liquid helium or liquid nitrogen. The apparatus is assembled on a standard optics table and is housed in an enclosure that provides stability of the ambient temperature.

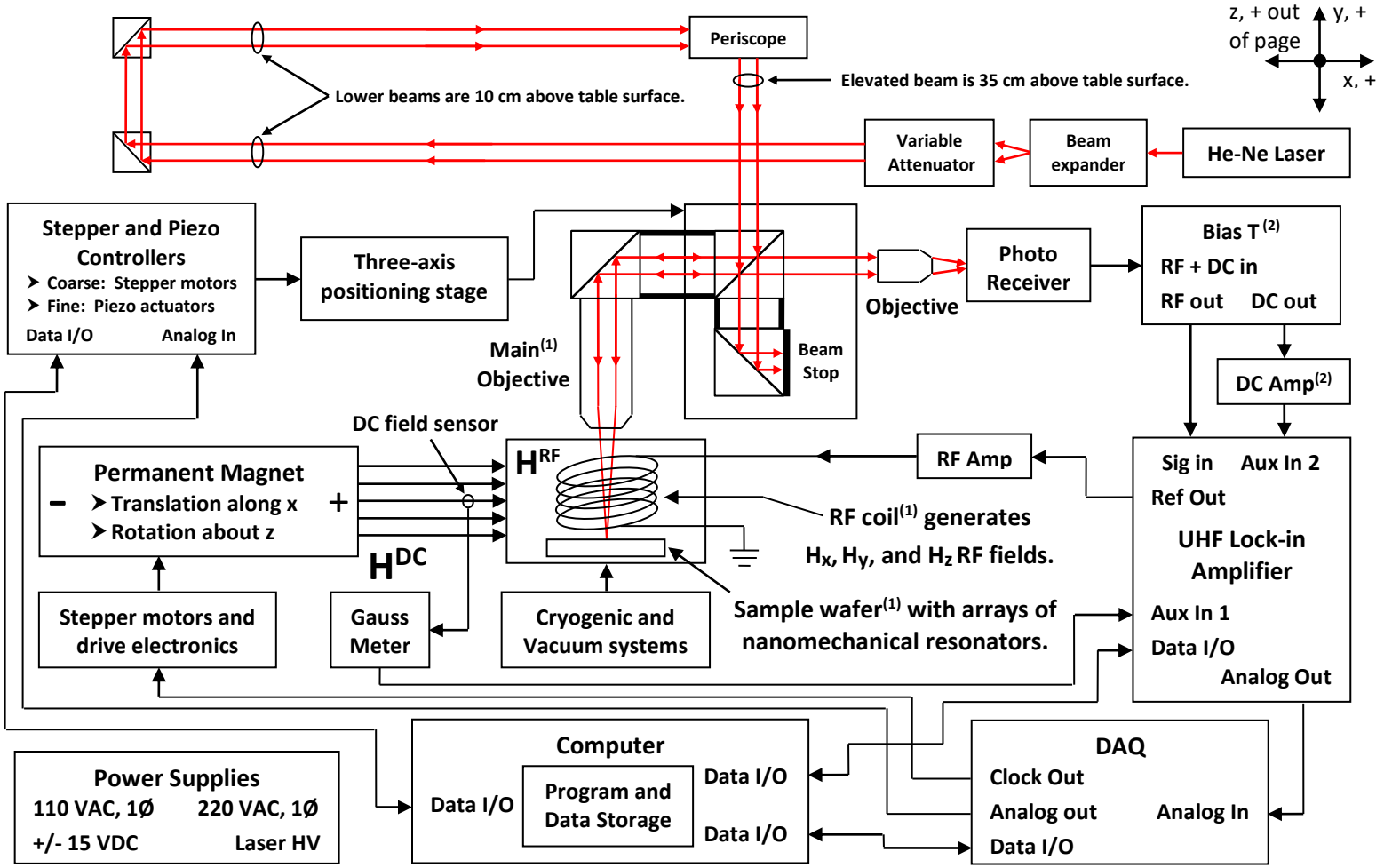

(1) Orientations of Main objective, RF coil, and Sample wafer are not as drawn. Refer to photos in figures 2.3.5, 2.3.6, and 4.4.2 for actual orientations.

(2) The Bias T and DC Amp are in circuit only for raster scans of the sample. They are removed for torque measurements.

Figure 4.1.1. Apparatus block diagram.

The sample wafer was mounted on a pillar that was thermally coupled to the cryostat cold-finger. An air-core RF excitation coil was positioned over the top surface of the wafer. The coil axis was normal to the sample wafer top surface. The coil was driven, through an RF amplifier, by the reference output of the lock-in amplifier. The reference output was configured to provide three, simultaneous, drive frequencies corresponding to the fundamental resonance frequencies of the nanomechanical resonator. These frequencies are specific to each of the three torque modes, (one frequency for torque along the x axis, one for torque along y, and one for torque along z).

The RF fields generated by the excitation coil were primarily in the direction of the coil axis (apparatus z), but also had x and y components at the coil ends that were much smaller in magnitude while being of sufficient strength for generation of AC magnetization components (the y component of the RF field was very small since the excitation coil was purposefully positioned over the sample wafer so that the sample arrays were near a null in the y field component). The arrangement provided three-axis AC dither of the magnetization so that there was AC excitation of all three torque modes.

The DC magnet and positioning system provided a DC bias field. The field magnitude could be changed by motor controlled translation along a rail parallel to the apparatus x axis. The field direction could be changed in the x-y plane by motor controlled rotation. The system configuration resulted in generation of the required DC and AC magnetic fields for simultaneous AC excitation of torque components along the x, y, and z axes.

Finally, the AC torque signals were sensed interferometrically. A Fabry-Perot cavity is formed between the sample and the base of the substrate. A time varying optical interference of the laser beam was generated by the time varying motion of the resonator with respect to the substrate base. The AC optical field was converted to an AC voltage by the photo receiver. Lock-in detection of the photo receiver output was possible since

the resonator motion was driven by the reference output of the lock-in amplifier (the reference output of the lock-in amplifier was fed to an RF amplifier, the output of which drives the excitation coil).

4.2) Original configuration.

The original form of the apparatus was constructed and assembled sometime prior to 2014 by former members of our research group. Single axis resonators were used in studies conducted by several previous graduate students and several theses were generated.

4.3) Exchange bias configuration.

In 2014, a permalloy/cobalt oxide sample was prepared for studies of exchange bias systems. From 2018 to mid 2019, Vincent Sauer, a post doctoral fellow in our group, conducted investigations of exchange bias behaviour using three-axis torque magnetometry. In early 2019, the sample was removed and then modified to improve the responses to torque components normal to the resonator torsion arms (x and z torque modes). The investigations were continued and much improved results were obtained.

In May and June of 2019, Vincent Sauer provided apparatus familiarization and training to myself, John Thibault. I continued the experimental work from the summer of 2019 until mid 2021. The work was sometimes a cooperative effort with graduate students Michael Dunsmore and Katryna Fast being particularly helpful.

4.4) Component identification.

Refer to the photo in figure 4.4.1. The optical and mechanical components were assembled on a standard optics table. Ancillary components for the vacuum and cryogenic systems were mounted on the floor beneath and toward the left side of the optics table. The control electronics and a computer were mounted in an instrument rack on the right side of the optics table. The stepper and piezo motor controllers (not visible in the photo) for a three-axis positioning stage and an external DAQ were mounted in the instrument rack below the computer keyboard.

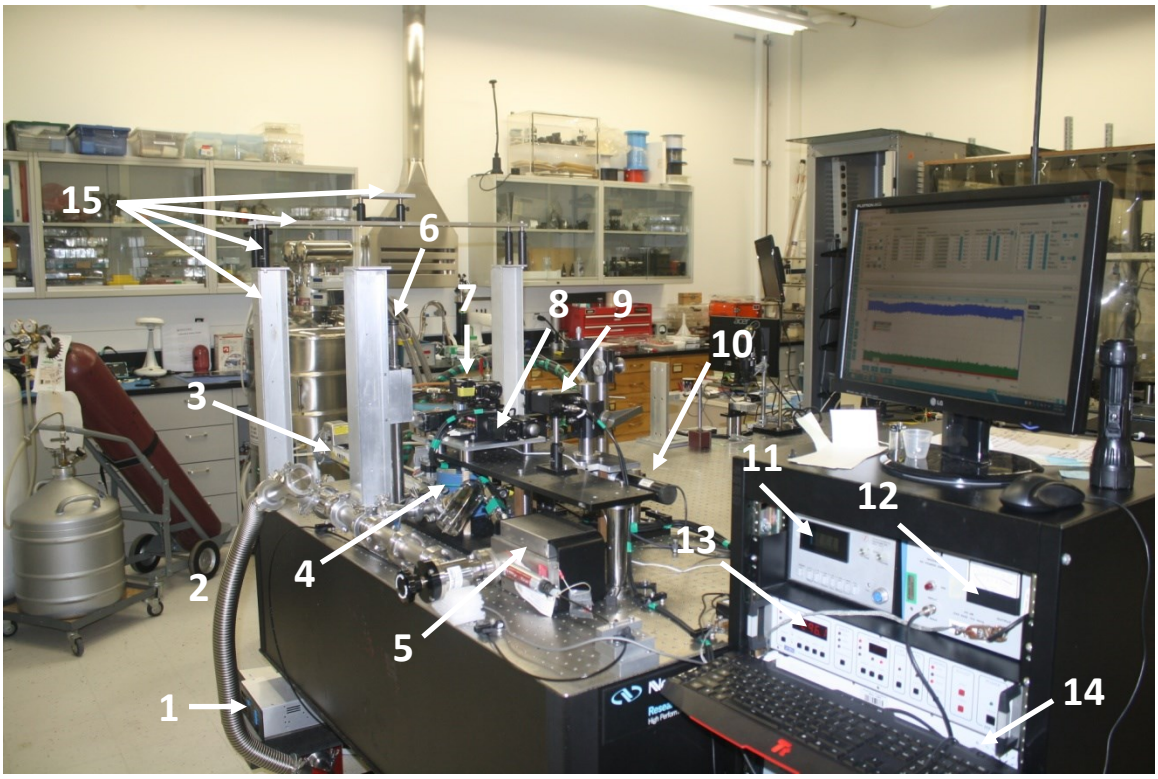

Figure 4.4.1. View of apparatus from front right.

1) Ion pump controller, 2) Vacuum conduit, 3) Linear stage for magnet translation, 4) Cryostat, 5) Ion pump, 6) Cryogen entry tube (the cryogen transfer line is not connected in this photo), 7) Beam splitter, 8) Main objective positioning stage, 9) Photo receiver, 10) Laser, 11) Gauss meter, 12) RF amplifier, 13) Temperature controller, 14) Lock-in amplifier, 15) Support system for cryogen transfer line.

Additional details of some of the apparatus components are shown in the photos in figures 4.4.2 and 4.4.3.

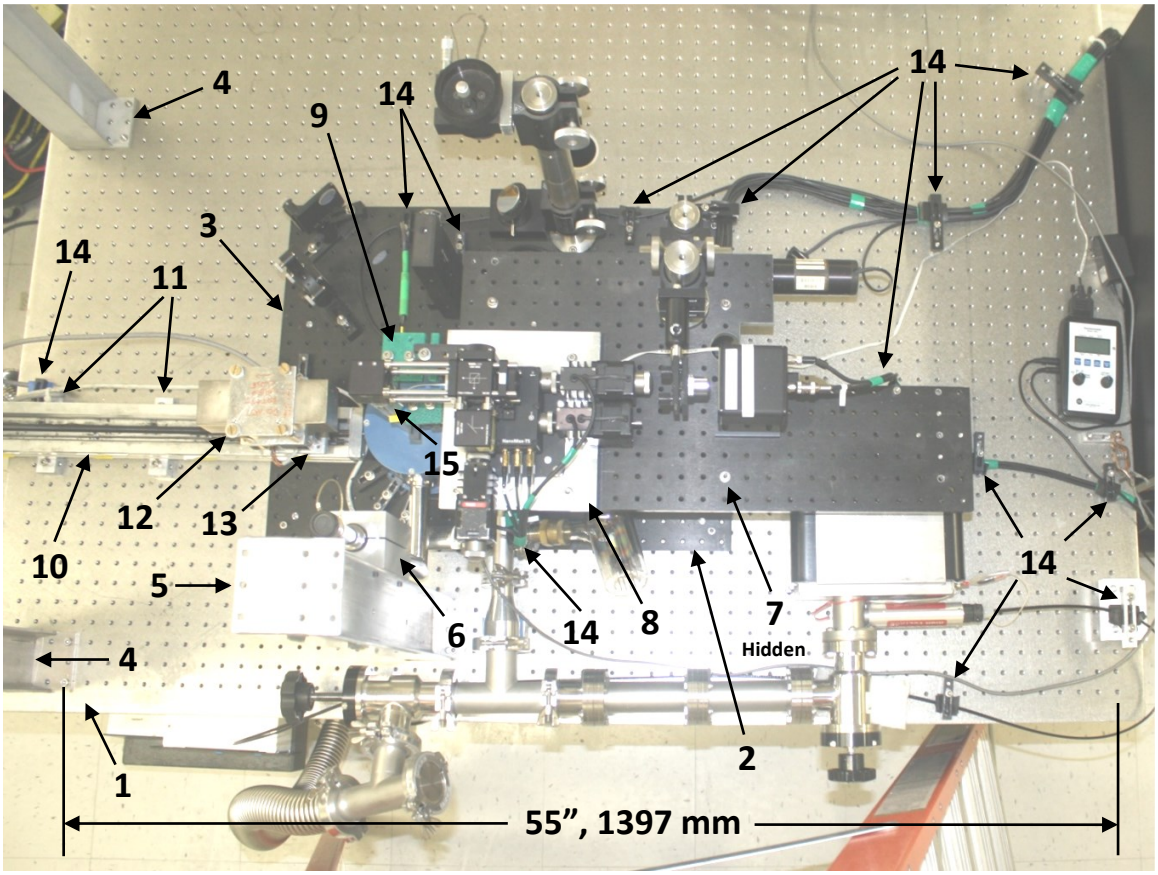

Figure 4.4.2. Top view of apparatus. Mechanical component identification.

Legend

1) Optics table.
2) Lower breadboard.
3) Upper breadboard.
4) Support post for cryogen transfer line.
5) Support post for cryogen entry tube.
6) Support clamp for cryogen entry tube.
7) Posts between upper and lower breadboards. (Five places. Hidden in this photo.)
8) Positioning stage mounting plate.
9) Bracket for DC field sensor.
10) Magnet translation rail.
11) Translation rail mounting bracket.
12) Magnet holder.
13) Magnet carriage.
14) Cable restraint.
15) Main objective.

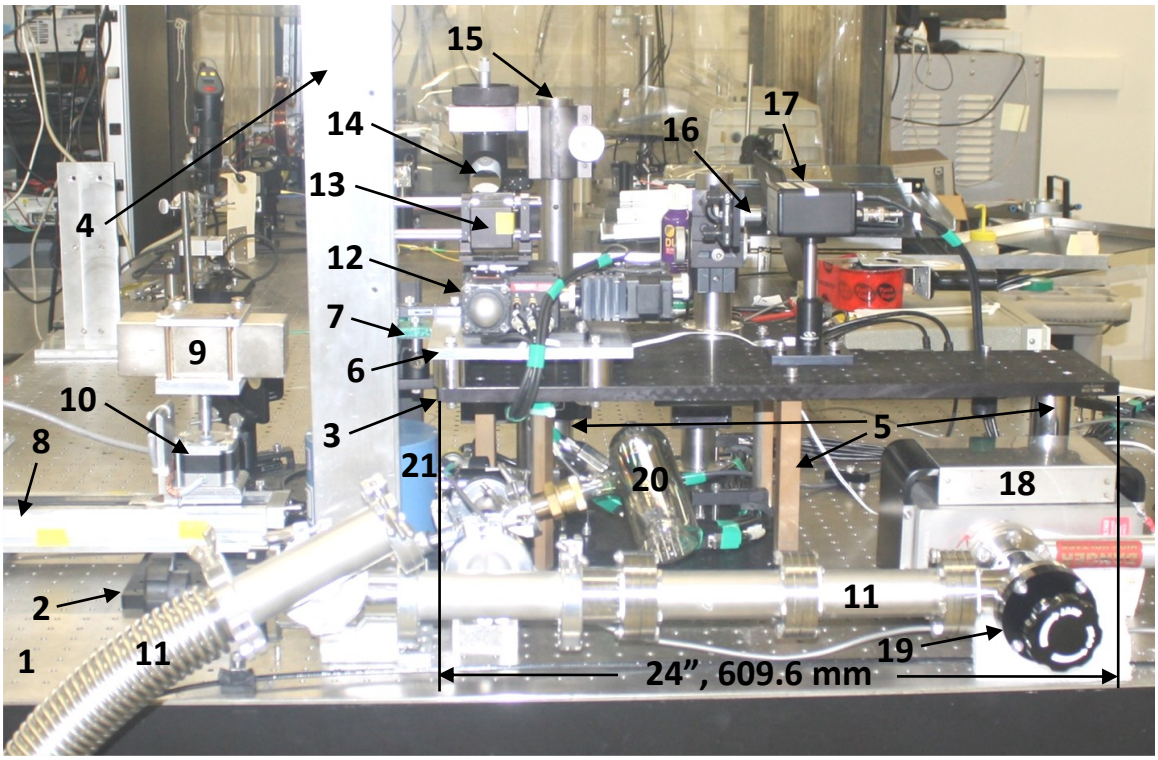

Figure 4.4.3. Front view of apparatus.

Legend

1) Optics table.
2) Lower breadboard.
3) Upper breadboard.
4) Support post for cryogen entry tube.
5) Support posts for upper breadboard.
6) Positioning stage mounting plate.
7) Support bracket for DC field sensor.
8) Magnet translation rail.
9) DC magnet.
10) Magnet rotation motor.
11) Vacuum conduit.
12) Positioning stage.
13) Beam splitter.
14) Periscope mirror.
15) Periscope post.
16) Photo receiver objective.
17) Photo receiver.
18) Ion pump.
19) Vacuum crossover valve.
20) Vacuum gage.
21) Cryostat (blue canister).

4.5) Functional description.

Refer back to the Apparatus block diagram in figure 4.1.1. The permanent magnet generates the DC bias field. The field strength can be varied by moving the magnet along the translation rail (travel length 22.5", 571.5 mm). The direction of the rail is along the apparatus x axis. The DC field direction can be changed by rotating the magnet about the apparatus z axis. Linear translation along x and rotation about z are controlled from the computer through the digital clock outputs of an external Data Acquisition System (DAQ). The clock signals from the DAQ are routed to the stepper motor drive controllers. The control program was written in LabView sometime prior to 2017 by Dave Fortin, a former department research assistant who served until 2020.

The strength of the DC field is provided by a sensor that is mounted near the top of the cryostat window. The sensor is connected to a Gauss meter. The output from the Gauss meter is a DC voltage that is recorded by an auxiliary input channel to the lock-in amplifier. Note that the field sensor is above the sample wafer and is displaced so that it does not interfere with the laser beam. The sensor is not in the same field as the sample, but correction was made for this during the DC field calibration that was conducted in the spring and summer of 2020 (refer to Chapter 2, subsection 2.4.4, for details regarding the DC field calibration).

The electronic signal path begins with the reference output of the lock-in amplifier. The lock-in amplifier generates three simultaneous, but independent, frequencies that are routed to an RF amplifier. The reference frequencies are manually set to match the resonance frequencies of the three resonator torque modes. The RF amplifier drives an excitation coil that is mounted on top of the sample wafer. The excitation coil is a hand wound, air-core, inductor that converts the RF currents into RF magnetic fields. The RF fields were calibrated by way of calculation and computer simulation (refer to Chapter 2, subsection 2.4.4, for details).

The optical path begins with a helium-neon laser. The laser beam is first expanded, attenuated, and then steered with mirrors and a periscope to bring it to the location and height of a beam splitter that is mounted to a three-axis positioning stage. Posts mounted to the beam splitter attach to a mirror that steers the beam into the main focusing objective (Mitutoyo, M Plan APO, Model 378-804-3, 20x, 10 mm focal length, 0.42 N.A.). The main objective focuses the beam on a selected resonator. The laser power at the entrance port to the beam splitter was measured on 25 Feb, 2020. The power was 186 uW. The power at the entrance pupil of the main objective would have been approximately 90 uW. Alignment of the beam onto a resonator is accomplished by manual control of the three-axis positioning stage to which the beam splitter and main objective are attached. The three-axis positioning stage has a low resolution mode driven by stepper motors and a high resolution mode driven by piezo actuators. The high resolution mode has a 5 nm resolution in x, y, and z (x and y for alignment of the beam and z for focus). The stepper motors and piezo actuators are driven through a control program that was written in LabView by Dave Fortin.

The return optical path is from the selected resonator sample, back through the main objective, off of the main objective mirror, and then through the beam splitter. The output from the beam splitter is brought to an objective (7x, 0.20 N.A.) that focuses the beam onto the sensitive element of the photo receiver (New Focus, Model 1801, DC - 125 MHz, low noise). The beam is intensity modulated by way of interferometric interaction with the oscillating resonator. The return beam contains three components of intensity modulation each of which corresponds to one of the resonance frequencies.

The electronic signal path is closed by routing the output of the photo receiver to the input of the lock-in amplifier. The lock-in amplifier demodulates the three signal components contained in the output of the photo receiver, converts them to RMS values of the signal amplitudes, and then converts the results to digital format for transmission to the control and data storage computer.

The Bias T and DC amplifier in the block diagram are used for obtaining reflectance data that are generated during a raster scan of a sample (refer to Chapter 2, subsection 2.3.8). The Bias T separates the DC and AC components of the signal. The DC component corresponds to the reflectance from the top of the resonator. This signal is filtered and amplified by the DC amplifier and is then recorded by an auxiliary input channel to the lock-in amplifier. The AC component of the signal contains the X, Y, R, and Theta components of the signal that was generated by motion of the resonator. The Bias T and DC amplifier are required only for obtaining raster scans. They are removed from the signal path when collecting hysteresis data so that noise from them will not be in the data. (All components, including cabling, either generate or conduct noise, so unnecessary items should not be in the signal path.)

4.6) Performance deficiencies.

Deficiencies in function of the apparatus were observed and noted during the period July to December, 2019. These deficiencies were,

1) Cryomech helium Dewar, plumbing, and vacuum pump require repair,
2) Software error in LabView program for magnet rotation stepper motor,
3) No calibrations for the DC and AC magnetic fields,
4) Signal drift due to,
    a) mechanical instability of upper breadboard,
    b) mechanical instability of mounting plate for positioning stage,
    c) mechanical instability and vibration from cryogen transfer line,
    d) temperature instability of mechanical components.

Details of the deficiencies, including when they were noticed and how they were rectified, are described below.

1) <u>Cryomech helium Dewar, plumbing, and vacuum pump require repair.</u>

In July of 2019, the liquid helium cryogen system failed. A line filter in the pressure side of the vacuum pump blocked over time. The worsening situation continued and went unnoticed. The cooling capacity of the system continued to drop until it was no longer able to cool the cryostat. The system was inspected and poor flow through the filter was identified as the cause of the problem. The filter blocked as a result of long term accumulation of very fine particles from the wear rings in the vacuum pump (particles coming off of the wear rings is normal, hence the filter). Unfortunately, a considerable amount of the wear ring particles ended up getting into all of the vacuum lines, the helium gas ballast tank, and, worse, the liquid helium Dewar thus contaminating them and rendering them unserviceable.

In the late summer of 2019, a liquid nitrogen cryogen system was assembled from components available in our lab, from department stores, and from suppliers. Some components were fabricated by me in the student machine shop. The liquid nitrogen system allowed for continuation of the experimental work while the helium cryogen system was out of service.

In the summer of 2019, the helium Dewar was serviced by department technician James Chaulk. Progress of the experimental work was adequate using the liquid nitrogen system, so it was deemed unnecessary to expedite repair of the helium system, however, by late 2020, interest in sample behaviour at liquid helium temperature prompted completion of the repair work. During the period Dec, 2020, to mid Feb, 2021, I reassembled the helium system ancillary components. Some components had to be

purchased and some were fabricated by me in the student machine shop. Repairs and reassembly of the system were completed in the morning of 09 Feb, 2021. The system was started and by mid afternoon on 09 Feb the base temperature was 3.51° K. The repairs were successful and complete. The helium system is still operating as of late spring 2022 and continues to function normally.

2) Software error in LabView program for magnet rotation stepper motor.

A software error in the LabView program that controls rotation of the DC magnet causes undesired rotation of the magnet when it is moved along the translation rail. The undesired rotation occurs when the translation motor stops and then starts again in the reverse direction, so that, during an automated linear hysteresis loop, the DC field direction changes by some small, though significant and not negligible, amount thus corrupting the data.

Corrections to the LabView control program were deemed to involve an intolerable risk. The LabView development tools required upgrading which would then render older programs unusable. An inadvertent, automated, upgrade happened at least twice whereafter the upgrade had to be reversed and all of the programs had to be restored. All of the LabView control software would have to be reworked if the system was upgraded. The problem was lack of backward compatibility within LabView's operating system. Without functioning LabView control programs, the apparatus would be essentially unusable, so, due to the risk of losing the whole system, it was decided that the system should not be upgraded and that changes to the programs should not be made. This left the problem unresolved.

Fortunately, failure to correct the fault that was causing undesired magnet rotation did not prevent the work from continuing. Other problems with automated data collection,

problems that could not be corrected, forced the use of a manual procedure for data collection (refer to Chapter 2, subsection 2.3.9, para 6).

3) No calibrations for the DC and AC magnetic fields.

The initial experimental work that was conducted by Vince Sauer in 2018 and 2019 was aimed at investigating vortex behaviour in the presence of exchange bias. Exchange bias effects were observed and efforts were made to determine their influence on vortex behaviour. A precise calibration of the DC and AC magnetic field strengths and directions was not required for this initial work and did not become a priority until mid 2020 when we decided that the ability to report absolute, as opposed to normalized, torques was preferable. Calibration of the DC field strengths and directions was performed in the summer of 2020. The AC field strengths and directions were determined in the fall of 2021 (refer to Chapter 2, subsection 2.4.4).

4) Signal drift due to,

a) mechanical instability of upper breadboard,

b) mechanical instability of mounting plate for positioning stage,

c) mechanical instability and vibration from cryogen transfer line,

d) temperature instability of mechanical components.

Signal drift resulting from deficiencies in mechanical and temperature stability were particularly problematic. Approximately 12 minutes is required to obtain data from a linear hysteresis loop. Over the 12 minute period, the drift component of the signal was often as large as the signal itself meaning that extraction of the true signal from the data was impossible. Constant drift is removable, but, here, the drift was a combination of several contributing factors that caused a continuous decrease in signal strength at a

variable and somewhat random rate with many positive and negative excursions from an ideal linear fit to the drift.

In the fall of 2020, ideas regarding sources for the drift components were tested. The final determination was that mechanical instability, vibration, and temperature instability were the primary causes of the drift. Instabilities in the laser power or in the electronic systems were ruled out, though, of course, there is always some degree of instability in any system, but the laser and the electronics were not the primary culprits in this case.

During the period Dec 2019 to Feb 2020, signal drift due to instability and vibration was substantially reduced. Deficiency item (4a), mechanical instability of the upper breadboard, was addressed by installing more support posts between the lower and upper breadboards and by adding some support posts between the optics table and the upper breadboard (refer to figure 4.4.3).

Deficiency item (4b), mechanical instability of the mounting plate for the positioning stage, was addressed by removing the original mounting plate (that was fixed to a scissor jack) and replacing it with a machined aluminum plate supported by machined stainless steel posts that were bolted to the plate and the upper breadboard (refer to figures 4.4.2 and 4.4.3). The scissor jack had been in place since the apparatus was first assembled (sometime much prior to 2018). It was used so that precise determination of the required height of the positioning stage was not necessary. An interesting, but unfortunate, problem is that cooling to cryogenic temperatures causes the cryostat cold-finger to contract substantially so that adjustment of the height becomes necessary in order to establish focus after changing the cryostat temperature. There is a 5 mm height adjustment available through the z axis stepper motor on the positioning stage, but having no knowledge of what the height should be for both helium and ambient temperatures meant that the scissor jack was the most expeditious way of proceeding. Contraction of

the cryostat cold-finger while cooling was measured and was found to be considerably less than the 5 mm height adjustment range of the positioning stage stepper motor. An average height for the positioning stage was calculated and support posts of the required dimensions were fabricated in the student machine shop.

Deficiency item (4c), mechanical instability and vibration of the cryogen transfer line, was addressed by installing two 3" x 3" x 24" aluminum I-Beam support posts, an aluminum support plate, and a clamp for the line at the left edge of the optics table approximately mid distance between the Dewar and the cryostat (refer to the items labeled as (15) in figure 4.4.1). The cryogen entry tube that is attached to the cryostat was originally supported by hose clamps and thin vibration pads that proved to be inadequate for isolating movements of the transfer line. The transfer line moves and vibrates considerably as a result of the reciprocating cryogen compressor at the top of the Dewar. A support bracket for the entry tube was fabricated in the student machine shop (refer to item (6) in figures 4.4.1 and 4.4.2).

Deficiency item (4d), temperature instability of the mechanical components, was addressed by constructing an enclosure to stabilize the temperature of the apparatus and isolate it from changes in the external ambient temperature. The enclosure was constructed during the period Dec, 2019 to Feb, 2020. This deficiency required considerable time and effort to correct and, so, is described in more detail than the others.

4.7) Temperature instability.

The primary deficiency was ambient temperature instability of the optical alignment.

The signals are derived interferometrically. A Fabry-Perot cavity is formed between the resonator and the base of the substrate. A time-varying optical interference is generated

by the time-varying position of the resonator edges with respect to the substrate base. Correct optical alignment requires that the laser beam illuminate a resonator edge and the substrate base simultaneously. The signal magnitude depends on the amplitude of the resonator motion, but also depends on the beam distribution over the resonator edge and the substrate base. Stability of the beam distribution depends on stability of the beam alignment which, in turn, depends on the dimensional stability of the mechanical components that affect alignment. These components are the optics table, upper and lower breadboards, optical component holders, and all of the posts, brackets, etc, that secure the components to the optics table.

A typical measurement involves collection of data during a full linear hysteresis loop. The collection time varies from eight to twelve minutes. The alignment stability during the collection period must be such that uncertainty in the signal magnitude, due to changes in alignment, is not so large that it causes misinterpretation of the data.

The undesired change in signal magnitude that results from a change in optical alignment can be estimated by using the positioning capability of the piezo actuators. For all three measurement axes, the largest signal is developed by aligning and focusing the laser on a resonator edge that is parallel to the torsion arms.

Once aligned, an order of ten decrease in signal magnitude results from a change in alignment, either toward or away from the resonator edge, of approximately one half to one micron. The sensitivity to a change in focus is comparable, but somewhat less. The results indicate that the dimensional stability of the alignment components, taken as an assembly, must be considerably less than one half micron during a measurement.

Most of the components that affect optical alignment are made of aluminum and 304 or 316 stainless steel and are of various shape and dimension. There is no single thermal

expansion coefficient that can be used to precisely calculate the multi-dimensional stability of the assembly of components, but one can obtain an estimate of the alignment variation with ambient temperature by considering thermal expansion in the direction that has the greatest affect on alignment. This dimension is parallel to the x axis of the apparatus. The dimensional stability of a single component is approximated by,

$$\Delta L = \alpha L \Delta T\,, \tag{4-1}$$

where ΔL is the change in length, α is the coefficient of thermal expansion, L is the initial length at temperature, T, and ΔT is the change in temperature. α is $\sim$ 0.12 um/cm/°C for carbon and alloy steels and $\sim$ 0.25 um/cm/°C for the various grades of aluminum.

Refer to the Apparatus block diagram in figure 4.1.1 and to the apparatus photos in figures 4.4.1 to 4.4.3. The mechanical, optical, and thermal paths from the laser to the sample include many components, with various thermal expansion coefficients, and with lengths and spacings from a few cm to several tens of cm along the x axis.

An absolute worst case, and rather unrealistic, approximation of the required ambient temperature stability is obtained by allowing for thermal expansion over the entire 60 cm length, along x, of the lower aluminum breadboard. The result is that an ambient temperature stability of approximately +/- 0.02 °C is required in order to maintain a dimensional stability of approximately +/- 0.25 um. For a twelve minute measurement, this corresponds to a change in laboratory ambient temperature of only +/- 1.2 °C over a twelve hour period.

An absolute best case, also rather unrealistic, approximation is obtained by considering only the ten cm long stainless steel posts between the beam splitter and objective holder.

The ambient temperature stability for +/- 0.25 um dimensional stability is approximately +/- 0.2 °C over twelve minutes. This corresponds to a lab temperature variation of +/- 12 °C over twelve hours.

The ambient temperature of the lab was recorded using a bead thermistor that was loosely attached to an aluminum plate. The plate was placed on the top surface of the optics table. The thermistor was connected in a four wire configuration to an HP Model 3458A benchtop multimeter that had recording capability and a GPIB bus. A laptop with a GPIB interface was used to collect the data. Inspection of several days of data indicated that the lab temperature varied by several degrees during a twelve hour period.

An exhaustive effort to determine the dimensional stability of all of the components and their mountings was not undertaken. Such an effort would have required approximately 20 to 50 thermistors and several weeks of data collection. Instead, the posts between the beam splitter and objective were deemed to be the most significant contributors to alignment instability and were thus chosen for measurements of dimensional stability with ambient temperature.

The temperature of one of the posts was recorded. A bead thermistor was placed in thermal contact with the post and then wrapped with foam insulation. The insulation was used so that the recorded temperature would more directly reflect that of the post by filtering the relatively rapid temperature variations caused by convection. A more thorough procedure would have included recording without insulation.

The thermistor was connected in the same configuration as was used for recording the lab temperature. Data were collected for several days. The results indicated that the variation in post temperature, and the resulting variation in post length, was beyond what would be allowed in order to maintain the required stability.

The temperature measurements indicated that the primary cause of alignment instability was variation of the ambient temperature. Instability of the air column surrounding the apparatus was also observed to cause alignment instability. These observations were made by real-time monitoring of the signal from the lock-in amplifier while lab personnel were moving about and while lab doors in near proximity to the apparatus were opened and closed.

The final conclusion regarding temperature instability was that the apparatus would have to be housed in an enclosure. The enclosure was fabricated using aluminum framework and 1/8” acrylic panels. The work was straight forward, but time consuming. It took from late Dec, 2019 to mid Feb, 2020 to complete the enclosure. Refer to figures 4.7.1 and 4.7.2.

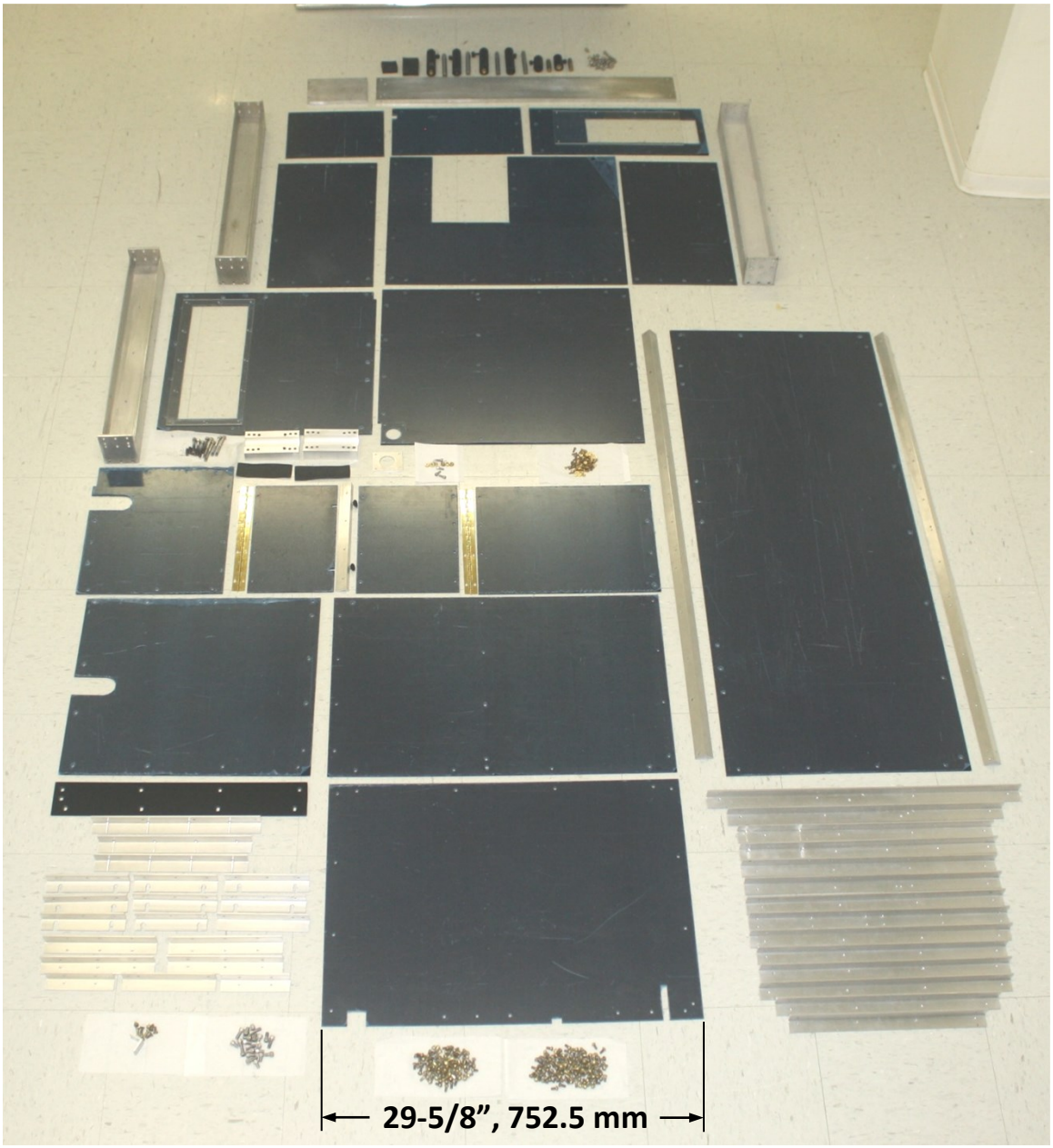

Figure 4.7.1. Enclosure components. The acrylic panels were cut from 4’ x 8’ sheets on a table saw in the Chemistry woodworking shop. The aluminum rails were fabricated in the Physics student machine shop. The hardware was obtained from the Physics storeroom.

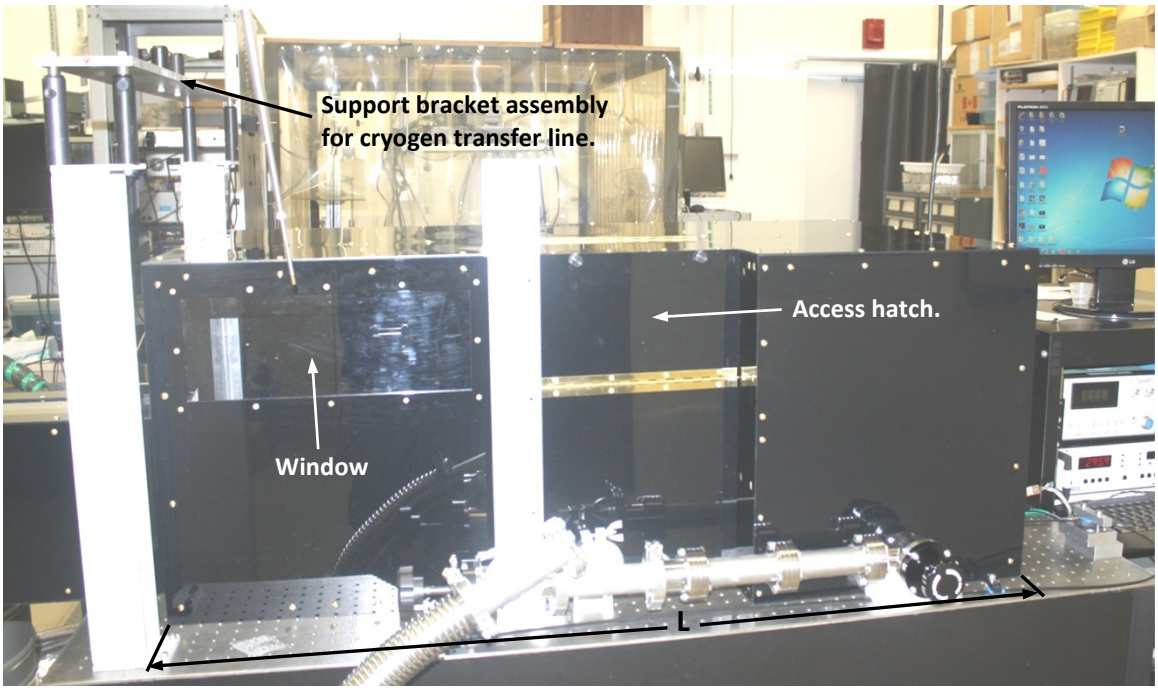

Figure 4.7.2. Assembled enclosure. Dimension L is 48-5/8”, 1235 mm. The access hatch is opened to expose the main objective positioning stage and photo receiver. Changing the alignment to a different sample requires coarse optical adjustments that are done with an imaging card placed in front of the photo receiver. The DC bias field magnet can be seen through the window. Care is taken to ensure that the magnet does not contact the main objective when it is near the cryostat. The support bracket assembly for the cryogen transfer line isolates the cryostat from vibrations generated by the helium compressor.

Chapter 5

Experimental Work

5.0) Chapter introduction.

The apparatus was constructed by former members of our research group sometime prior to 2014. Refer to Chapter 4 for details regarding the apparatus. The samples that were studied are described in Chapter 3. Refer also to Chapter 2, subsection 2.3.1, for additional details regarding the sample.

Preliminary work toward investigations of exchange bias was conducted by Vince Sauer, a former member of our research group, during the period 2018 to mid 2019. Data for the experiment reported on herein were collected during the period mid summer 2019 to early fall 2021. Conduct of the experiment required collection of several different types of data. Each data type will be described.

Results obtained from the experiment were reported in a paper that was prepared in the fall of 2021. Michael Dunsmore and I were the primary contributing authors, but the effort benefited from contributions provided by all of the current and some of the former members of our group. The paper and a supplement were published in AIP Advances in March of 2022.[1]

5.1) Previous work.

Apparatus construction and sample fabrication were undertaken by former members of our research group. The apparatus was assembled prior to 2014. The samples were designed by Joseph Losby and were fabricated at the University of Alberta NanoFAB sometime between 2012 and 2014.

Vortex behaviour in single layer thin-film samples of permalloy was studied by former members of our group.[7] The original intent of the exchange bias experiment was to investigate the effects of exchange bias phenomenon on vortex behaviour in thin-film bilayer samples of permalloy and cobalt oxide. The sample was mounted in the apparatus cryostat in mid 2018 and investigations, conducted by postdoctoral fellow Vincent Sauer, began shortly thereafter.

Cooling the sample, while in a saturating DC bias field, from a temperature above to a temperature below the Néel temperature of the antiferromagnetic cobalt oxide, resulted in a shift of the coercive field points in a linear hysteresis loop as compared to the location of these points in an ambient temperature linear hysteresis loop. The shift in coercive field points is a signature that is taken as evidence for exchange bias effects. Observation of exchange bias demonstrated that the apparatus, samples, and measurement techniques were adequate and that useful information could be extracted from further work.

The apparatus was designed to monitor three axes of torque. The preliminary work showed that the signal strengths from two of the torque axes were marginal to inadequate. In April of 2019, the sample wafer was modified by severing one of the two resonator torsion arms using a focused ion beam (FIB) process. The modification resulted in a substantial increase of the torque signals that had previously been too low (refer to Chapter 2, subsection 2.3.1, and to Chapter 3, subsection 3.1.2, last para, Modification).

5.2) Training

I was assigned to the exchange bias project in January of 2019. Though having developed a well-rounded background in instrumentation during my first four years of service in the Canadian forces, as a summer student in the physics department at the University of Alberta, and professionally from 1997 to present, my knowledge and experience with vacuum and cryogenic systems was very limited.

Operation and maintenance of the exchange bias apparatus required capabilities that I did not have, but, fortunately, Vince Sauer was available to provide training for operation of the vacuum and cryogenic systems, apparatus instrumentation, and apparatus control systems. Vince also showed me the procedures for aligning the optics, acquiring the torque signals, and collecting data. He also provided supervision for a few weeks until I had become proficient at using and maintaining the apparatus and all of its systems.

5.3) Data requirements.

Sometime in the summer of 2019, the goal of describing how exchange bias effects influenced vortex behaviour was set aside and the focus of the work was reoriented toward a more general study of exchange bias and interfacial coupling effects. Data requirements for the more general study were similar to the original requirements in that data from linear hysteresis loops, obtained at ambient and cryogenic temperatures, had to be collected, reduced, analyzed, and examined. Additional data requirements were the torque responses from rotating hysteresis loops at ambient and cryogenic temperature. The torque responses as a function of temperature were also of interest since a temperature-dependence of the torques would suggest a temperature-dependence of the anisotropy terms in the phenomenological energy equation that was used to analyze the data (the phenomenological energy equation is presented in Chapter 2, subsection 2.1.6).

5.4) Collected data.

Several different types of data were required to characterize the sample behaviour. The various types of data and their relevance to the work are described in this section.

5.4.1) Raster images.

Raster images of a sample are obtained by collecting reflectance and torque signal data while the position of the laser focusing optics is stepped in an x-y grid pattern. The step increments, signal measurements, and data collection are controlled by software so that the procedure is automated. The procedure for obtaining a raster image and how the image data are interpreted are described in Chapter 2, subsection 2.3.8.

Raster images provide confirmation that the resonator torque modes are as expected (i.e. excitation of the x, y, and z torque modes results in generation of x, y, and z torques respectively). The raster image obtained from the reflectance data provides information regarding uniformity of the sample surface. Several raster images are presented in Chapter 2, subsection 2.3.8, figures 2.3.11 to 2.3.13.

The raster images of the reflectance data and X component of the y mode torque signal in figure 2.3.12 are presented here in figures 5.4.1 and 5.4.2 for quick reference. Note that the X component of the signal does not mean x mode torque. Here, X refers to the component of the signal that is in phase with the reference signal of the lock-in amplifier. The X, Y, R, and theta components of the signal output from the lock-in amplifier are described in Chapter 2, subsection 2.3.8.

The reflectance image in figure 5.4.1 shows the outer perimeter of the sample, the resonator paddle, and the bilayer deposit. The location of the torsion arms is indicated, but the torsion arms are two thin to be resolved. Figure 5.4.2 shows the in-phase component of the signal. The signal is positive on the lower edge of the paddle and negative on the upper edge. This confirms that the motion of the paddle is about the y axis and, thus, the signal is due to the y mode torque.

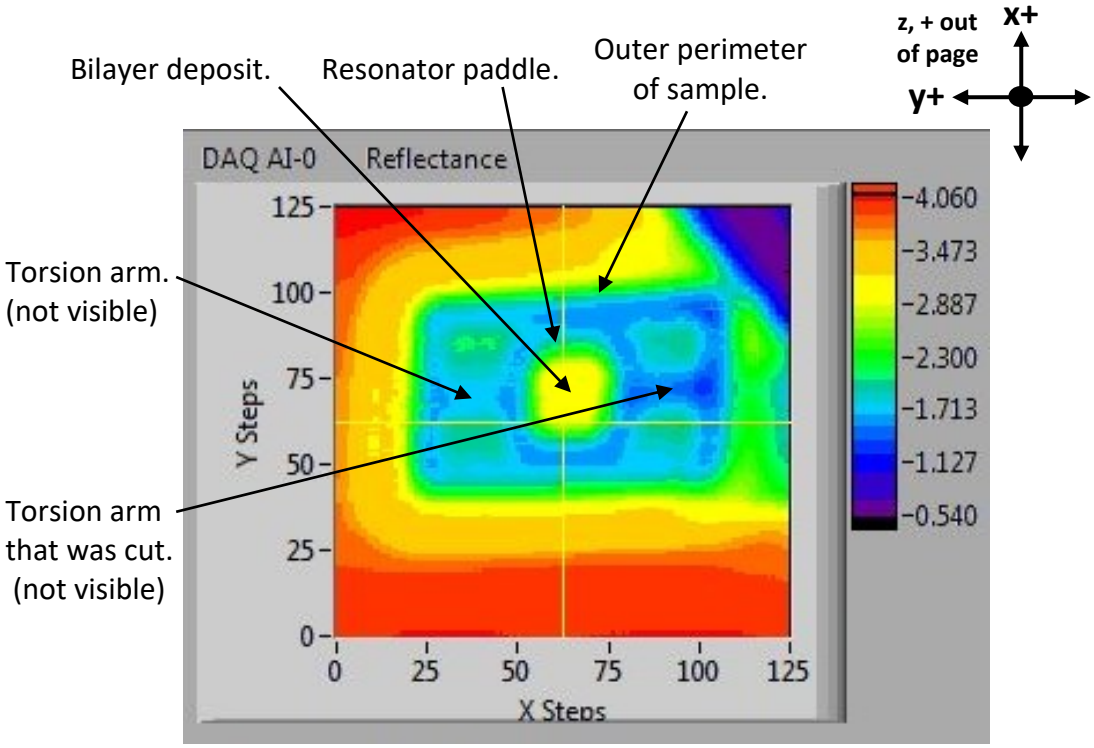

Figure 5.4.1. Raster image showing the reflectance data from sample S2A1A5.

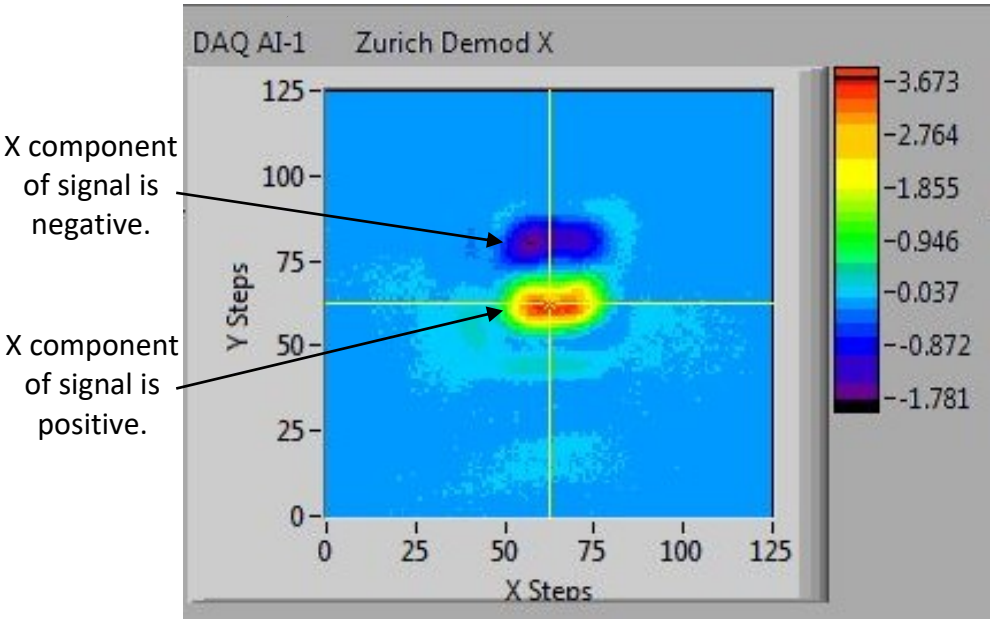

Figure 5.4.2. Raster image showing the X component of the y mode torque signal from sample S2A1A5. The image confirms that the torque is y mode.

5.4.2) Linear hysteresis loops.

Linear hysteresis loops were obtained at ambient and cryogenic temperatures. Cooling was done in a positive or negative saturating field or in zero field. The cooling-field angle was most often in the direction of the apparatus x axis, but some field-coolings were done at an angle to the x axis and some were done in the direction of the apparatus y axis.

Figure 5.4.3 shows plots of the x, y, and z components of the DC bias field. The x axis of the plots corresponds to the apparatus x axis. The cryostat is on the right of the plots with the sample position at 0 mm. The DC magnet moves along a translation rail extending from the cryostat toward the left side of the apparatus (the left side is toward the direction of negative x). The maximum travel length is 22.5" (571.5 mm). Refer to Chapter 4, figures 4.4.2 and 4.4.3, for photos. The blue traces in figure 5.4.3 are for the magnet at 0° and moving to the left (backing away from the cryostat). The red traces are for the magnet at 180° and moving to the right (forward and toward the cryostat).

Hysteresis loops obtained at ambient temperature should show features associated with permalloy alone since the magnetization in the antiferromagnetic cobalt oxide is considerably less then in the ferromagnetic permalloy (cobalt oxide is paramagnetic above the Néel temperature and has a susceptibility much less than that of permalloy).

Figure 5.4.4 shows the y torque voltage signal obtained during an ambient temperature linear hysteresis loop. The dominant mechanism producing the features in the loop is shape anisotropy since the uniaxial anisotropy in Permalloy is very low (~ -1 kJ/m^3).[316] The y torque signal derives primarily from the out-of-plane component (z direction) of the AC excitation. The demagnetizing field in the out-of-plane direction is large for thin films so that shape anisotropy is responsible for the observed signal. Note that the coercive fields are at or near zero showing that the sample demagnetizes easily and quickly in low field as would be expected for permalloy alone.

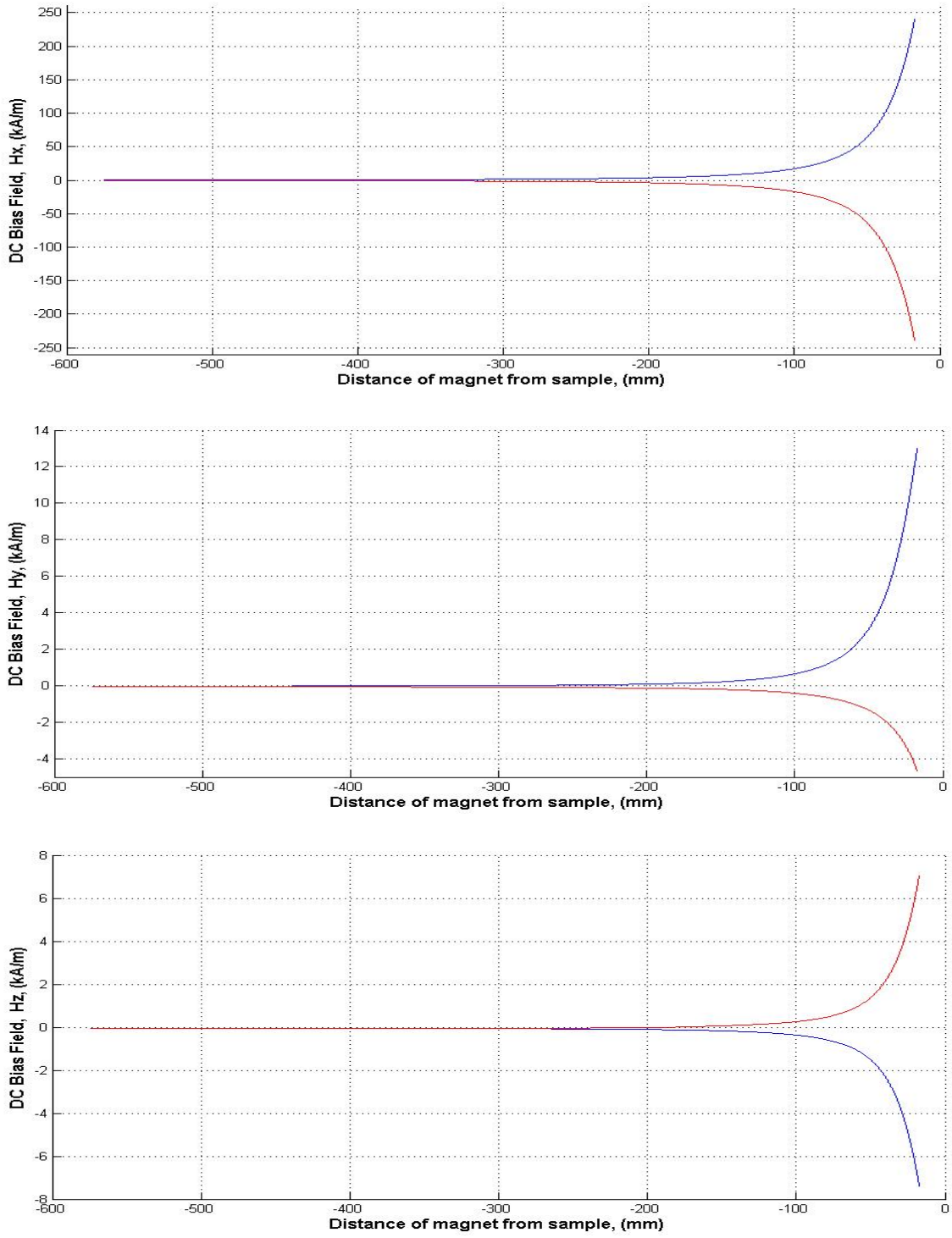

Figure 5.4.3. DC bias fields, H_X^{DC}, H_Y^{DC}, and H_Z^{DC}, with magnet at 0° and 180°.

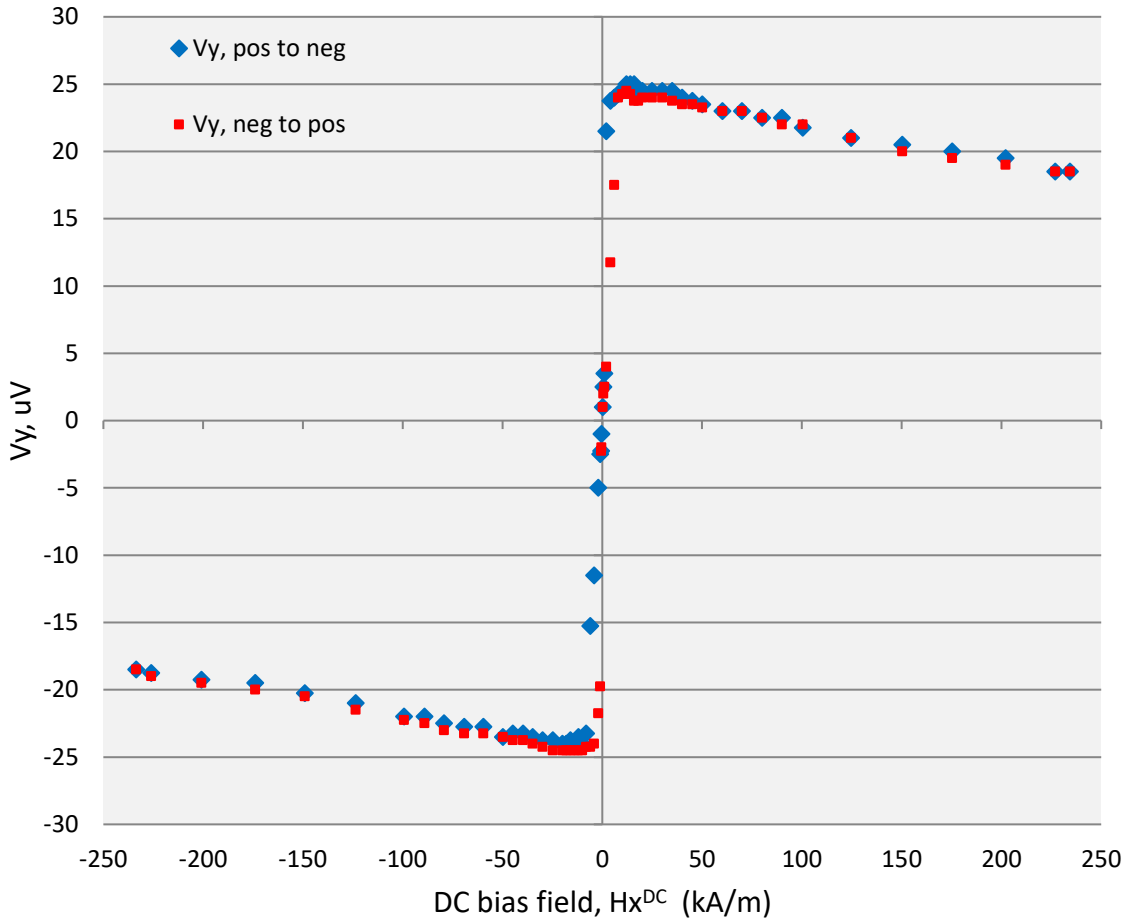

Figure 5.4.4. Sample S2A1A5. y mode torque signal. Linear hysteresis loop obtained at an ambient temperature of 295.4° K on 01 Sep, 2021. The plot starts at the upper right in the highest positive field, blue diamonds, continues to zero field where the DC bias field magnet rotates through 180° at the back of the translation rail, and then continues to the highest negative field in the lower left of the plot. The return path starts in the lower left of the plot, red squares, continues to zero field where the magnet again rotates through 180°, and then continues to the highest positive field in the upper right.

Both of the coercive field points are at, or are very near to, zero as would be expected for permalloy alone. The hysteresis loop shows no evidence of interaction between the permalloy and cobalt oxide layers.

Field-cooling in a positive or negative saturating field causes the antiferromagnetic ordering of the cobalt oxide layer to align with the spins in the ferromagnetic permalloy layer. Coupling of the ferromagnetic and antiferromagnetic spins occurs at the interfacial layer between the two materials. Coupling results in creation of a unidirectional anisotropy that causes a shift of the coercive field points so that the loop is not centered at zero applied field.

Figure 5.4.5 shows a field-cooled hysteresis loop that was obtained immediately after field-cooling to 68.3° K. The cooling-field angle was 0°. Note that the loop is shifted toward negative field which means that the unidirectional exchange bias anisotropy is positive. The loop shift gives the value for the exchange bias energy, σ_{ex}, per unit area of the film, $\sigma_{ex} = \mu o M_s H_{ex} t$. H_{ex} is the field corresponding to the centre of the shifted loop. The shift in figure 5.4.5 is approximately 5 kA/m, M_s is 801 kA/m, and the film thickness, t, is approximately 16 nm (refer to Chapter 6, section 6.3, subsection 6.3.3, paras (i) and (ii), for determination of the film thickness and M_s). From these numbers, the exchange bias energy is σ_{ex} ~ 0.08 mJ/m^2 which is in the range of typical values given by Coey for various exchange bias systems. The range given by Coey is 0.05 to 0.33 mJ/m^2.[317] The maximum value of exchange bias energy from the sample we tested was 0.11 mJ/m^2. This value was obtained from data that were collected on 26 Sep, 2019.

Figure 5.4.6 shows the hysteresis loop obtained subsequent to the first loop. Note that the shift is reduced as compared to the first loop. The reduction in loop shift with successive loops is called the *training effect* whereby the exchange bias is reduced by an approximate factor of $1/\sqrt{N}$ where N is the number of loops. The training effect was observed in the loops obtained from several iterations of the field-cooling procedure, but there was little focus on the origins of the effect. Training effects are mentioned in much of the exchange bias literature.[284, 318 - 320] A paper by Jenkins discusses a specific training mechanism (athermal training).[321]

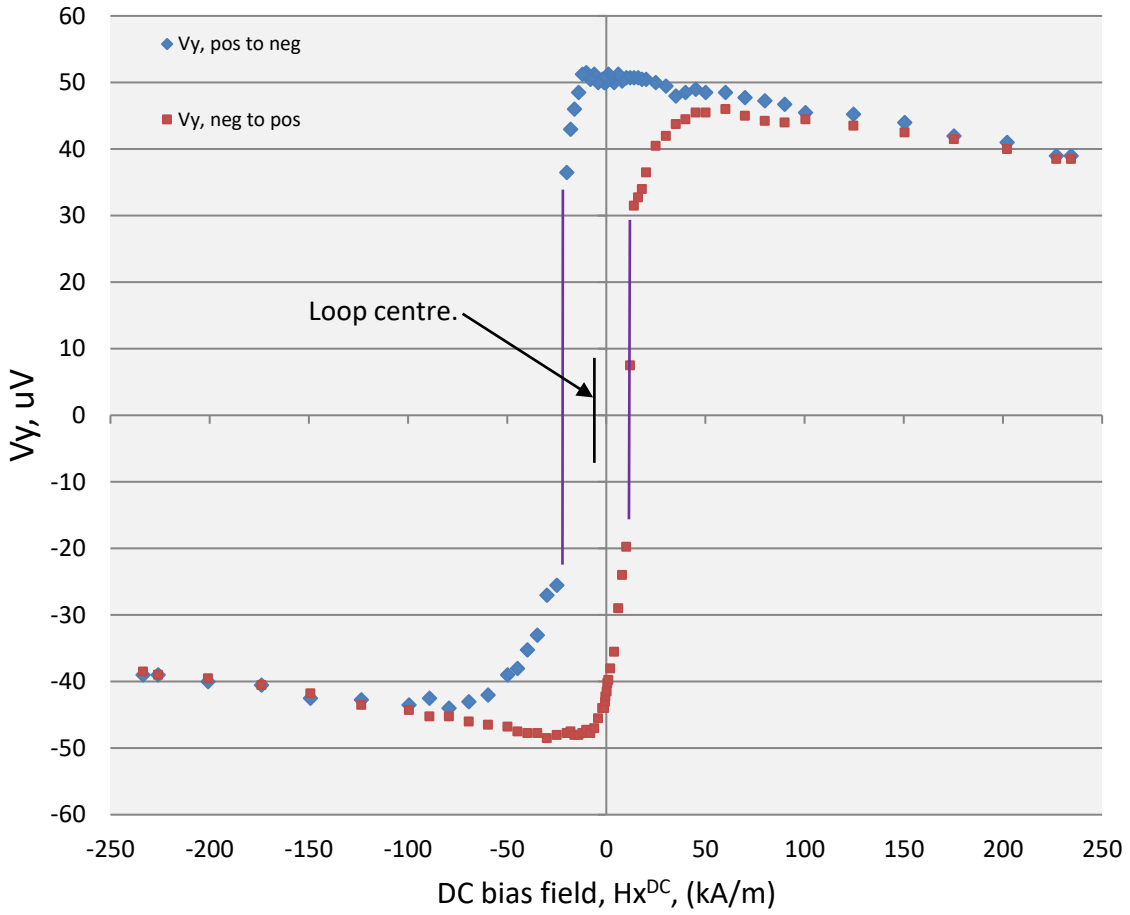

Figure 5.4.5. Sample S2A1A5. y mode torque signal. First linear hysteresis loop, obtained on 08 Sep, 2021, after field-cooling to 68.3° K in a positive saturating field. The cooling-field angle was 0°. The plot starts in the upper right, blue diamonds (refer to the caption for figure 5.4.4).

The centre of the loop is shifted toward negative field because the coercive field points are no longer equal and near zero as they were in the ambient loop. A shift toward negative field is consistent with a positive value for a unidirectional anisotropy. The shift results from exchange bias at the interface between the permalloy and cobalt oxide layers.

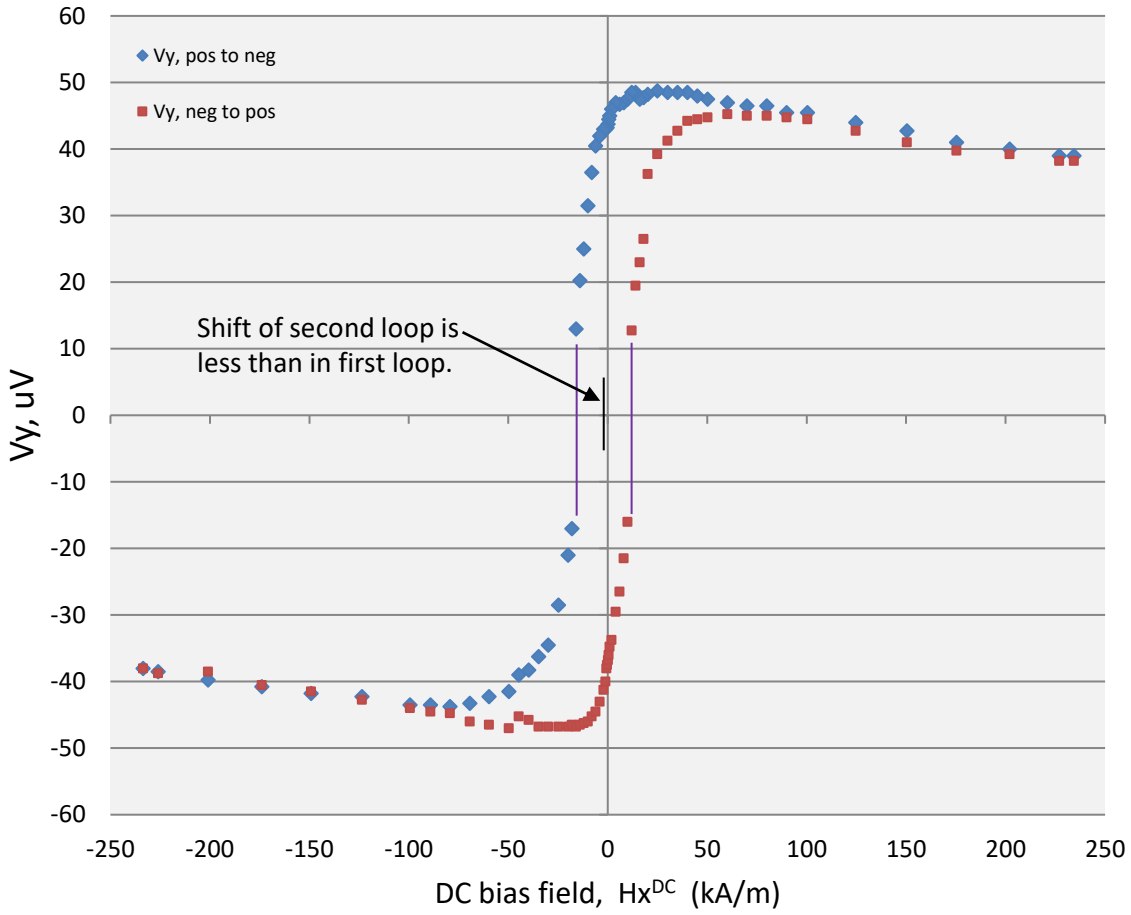

Figure 5.4.6. Sample S2A1A5. y mode torque signal. Second linear hysteresis loop, obtained on 09 Sep, 2021, after field-cooling to 68.3° K in a positive saturating field on 08 Sep, 2021. The cooling-field angle was 0°. The plot starts in the upper right, blue diamonds (refer to the caption for figure 5.4.4).

The centre of the loop is still shifted toward negative field, but not as much as in the first loop in figure 5.4.5. The reduction in loop shift is referred to as the *training effect*.

Figures 5.4.7 and 5.4.8 are provided for reference and comparison. The plots begin on the right, blue trace, and end on the right, red trace. The time evolution of the traces is the same as described in the caption for figure 5.4.4.

Figure 5.4.7 shows the data from a linear hysteresis loop that was obtained at ambient temperature. The data were collected on 27 Mar, 2020. The top, middle, and bottom panels show the voltage signals from the x, y, and z torque modes respectively. The data are not all from the same loop. The x data are from loop 96, y from loop 94, and z from loop 98. The alignment was optimized for each signal individually and then two loops were recorded. The reason why the alignments are different for each torque mode is that the optimum position of the laser spot, near an upper or lower edge of the resonator paddle, is slightly different for each mode. Refer to Chapter 2, the SEM image of a resonator in figure 2.3.7 and to the raster images in figures 2.3.11 to 2.3.13. Decrease of signal strength in high DC bias fields is explained in Chapter 2, section 2.3, subsections 2.3.10 and 2.3.11.

The plots in figure 5.4.7 are typical for linear hysteresis loops obtained at ambient temperature. The linear hysteresis loops are narrow and are centered at zero field. The z mode torque signal is near zero, except in low field, because all of the terms contributing to the torque are near zero (refer to Chapter 2, subsection 2.3.7, equation 2-9c). In low field, the z mode torque grows as the magnetization comes out of saturation. Note what appear to be spikes in the z signal near zero field. The spikes are not noise. The notes taken while the loop was running say that there were jumps in the data near, but before zero field was reached, and again as the field direction was reversed while the magnet was rotating. The cause of the jumps is consistent with the mechanisms responsible for Barkhausen steps (pinning of the magnetization at defects and irreversible discontinuities in the magnetization during field reversal).[322]

Figure 5.4.8 shows data obtained on 04 Mar, 2020, after field-cooling to 66.9° K in a positive DC bias field of 40 kA/m. The cooling-field angle was 0°. The cooling-field strength was less than for most field-coolings, but inspection of the x and y mode torque signals in figure 5.4.7 shows that the magnetization was saturated at a bias field strength of no more than 25 kA/m. This means that the cooling-field strength of 40 kA/m was sufficient to saturate the magnetization.

The data in figure 5.4.8 were obtained on 04 Mar, 2020, but field-cooling was done on 19 Feb, 2020. During the period 20 Feb to 04 Mar, 65 linear hysteresis loops and 77 raster images were obtained before collecting the data for figure 5.4.8 (loop 66.) A shift of the coercive field points in the y mode torque signal is still present even after training effects had successively reduced the exchange bias during the previous 65 loops.

The plots in figure 5.4.8 are typical for linear hysteresis loops obtained after field-cooling in a positive, saturating, DC bias field. The loops are wider and are shifted toward negative field.

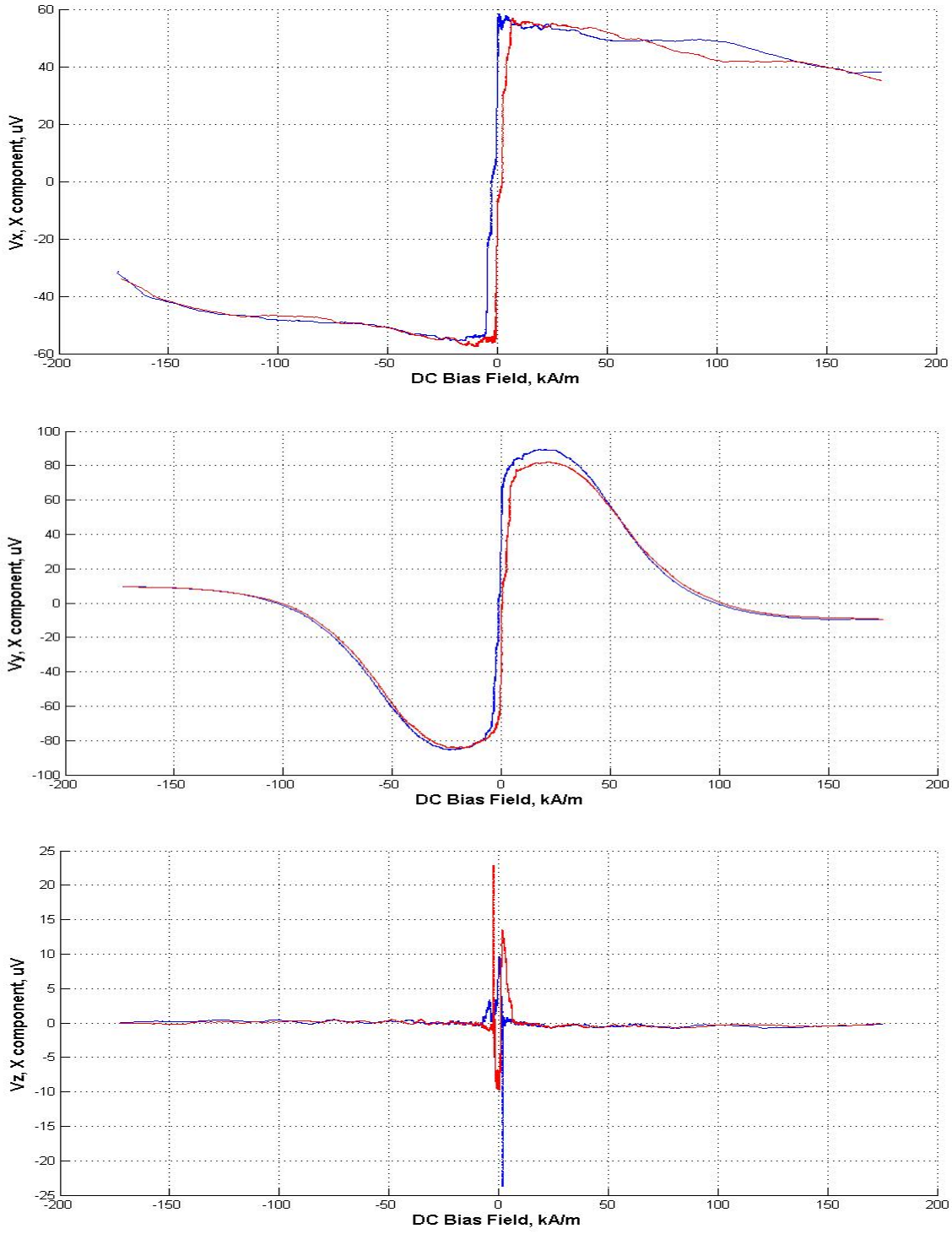

Figure 5.4.7. Vx, Vy, Vz, S2A6A1, linear loop, ambient, 296.0° K, 27 Mar, 2020.

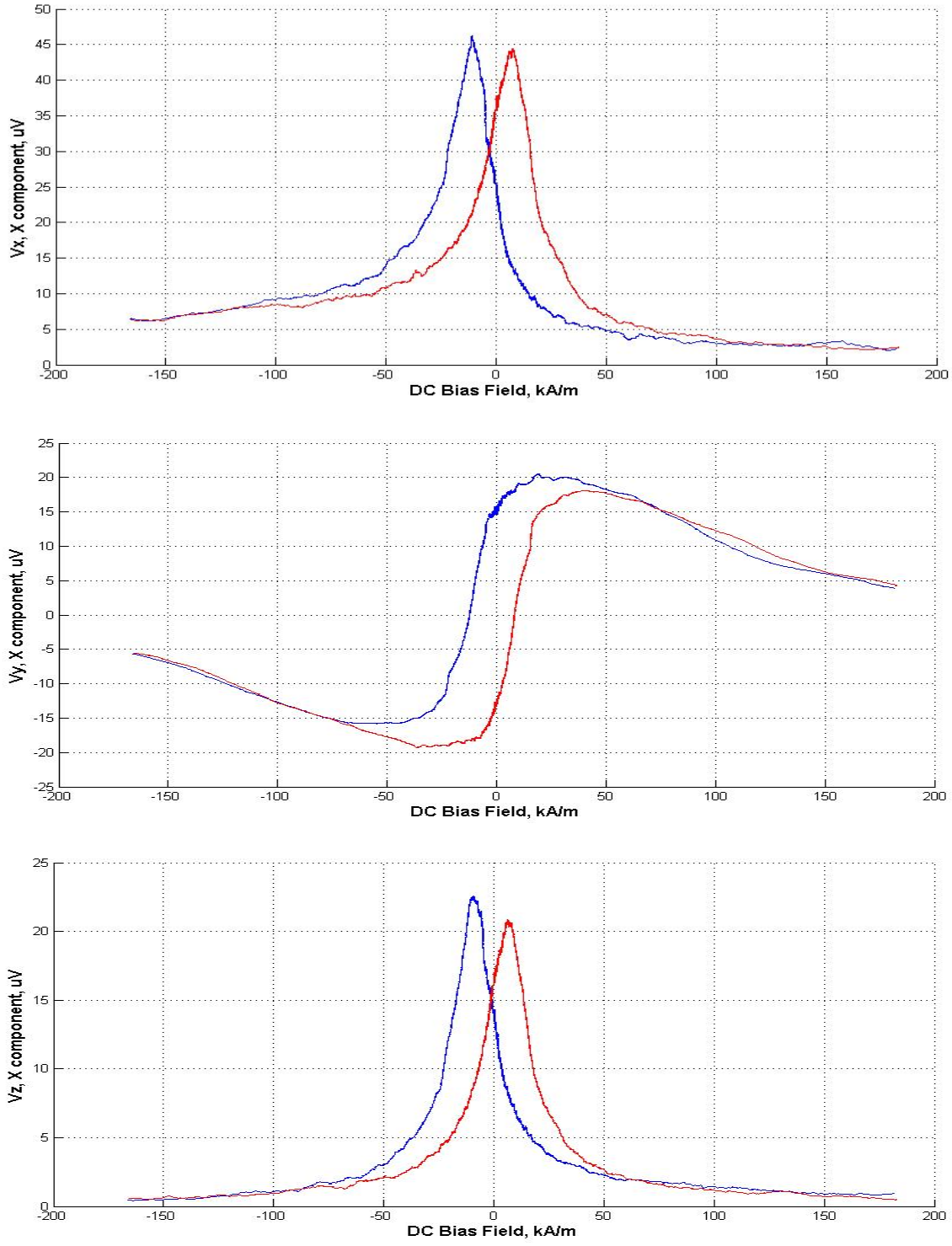

Figure 5.4.8. Vx, Vy, Vz, S2A1A5, linear loop, field-cooled to 66.9° K, 04 Mar, 2020.

The exchange bias energy calculated from the data in figure 5.4.5 is σ_{ex} ~ 0.08 mJ/m^2. A maximum of 0.11 mJ/m^2 was calculated from data collected on 26 Sep, 2019.

Gruyters obtained exchange bias energies of 0.9 mJ/m^2 for Fe/CoO and 0.8 mJ/m^2 for Ni/CoO at 10° K.[323] The substrates were 4 mm x 4 mm. The iron and nickel layer thicknesses ranged from 10 to 35 nm in nine samples. The cobalt oxide thickness was 2 nm. Mitrofanov obtained 0.3 mJ/m^2 for permalloy/CoO at 80° K.[11] The substrate was 6 mm x 2 mm. The layer thicknesses for the samples were 20 nm for the permalloy layer and 8 nm for the cobalt oxide layer.

The exchange bias energy in our sample is considerably less than the energies reported by Gruyters and Mitrofanov. Note that Gruyters used a SQUID (superconducting quantum interference device) magnetometer and that Mitrofanov used the magneto-optical Kerr effect (MOKE) to investigate their samples. Also note that the surface area of our sample is approximately *six orders of ten less* than that of the samples tested by Gruyters and Mitrofanov. It is possible that the discrepancy in reported exchange bias energies is due to sample size. We had only one sample wafer, with resonators and deposits having little dimensional variation from one to the next, and, so, could not investigate the dependence of exchange bias energy on area or layer thickness.

5.4.3) Rotating hysteresis loops.

Rotating hysteresis loops were obtained at ambient and cryogenic temperatures. The voltage signals from the sample were recorded during rotations of the DC bias field. Semi-automated and manual data collection methods were used. Data integrity from the semi-automated loops was degraded as a result of alignment drift and resonant frequency change (drift and frequency change are discussed in Chapter 2, section 2.3, subsections 2.3.10 and 2.3.11). The data obtained using the manual collection procedure is reported.

The bias field magnet is rectangular. Rotation of the magnet results in angle-dependent field strengths. Figure 2.3.5 in Chapter 2, and figure 4.4.2 in Chapter 4 show why this occurs. The panels in figure 5.4.9 show the field components as a function of magnet angle. The field strengths were determined during the field calibration that was conducted in the spring and summer of 2020 (refer to Chapter 2, section 2.4, subsection 2.4.4). The field calibration gave the field strengths at the sample as a function of magnet position along the translation rail and also as a function of magnet angle.

The procedure for obtaining a manual rotating hysteresis loop involves alignment of the laser spot, adjustment of the AC drive frequency, and positioning of the magnet for each data point. Magnet rotations of 9° per data point gave a reasonable compromise between angle resolution and required time. Clockwise and counterclockwise rotations are required to obtain a full hysteresis loop. The time to collect the data for one complete rotating loop, for only one of the three torque signals, is between four and six hours. Two and sometimes three days are required to collect data for all of the signals. Stabilization of the apparatus temperature is required so that temperature drift does not affect the data. Approximately four hours of stabilization time is required after turning on the apparatus systems at the beginning of the day. Once the data have been collected, the field components at the sample for each data point are determined from the field calibration files.

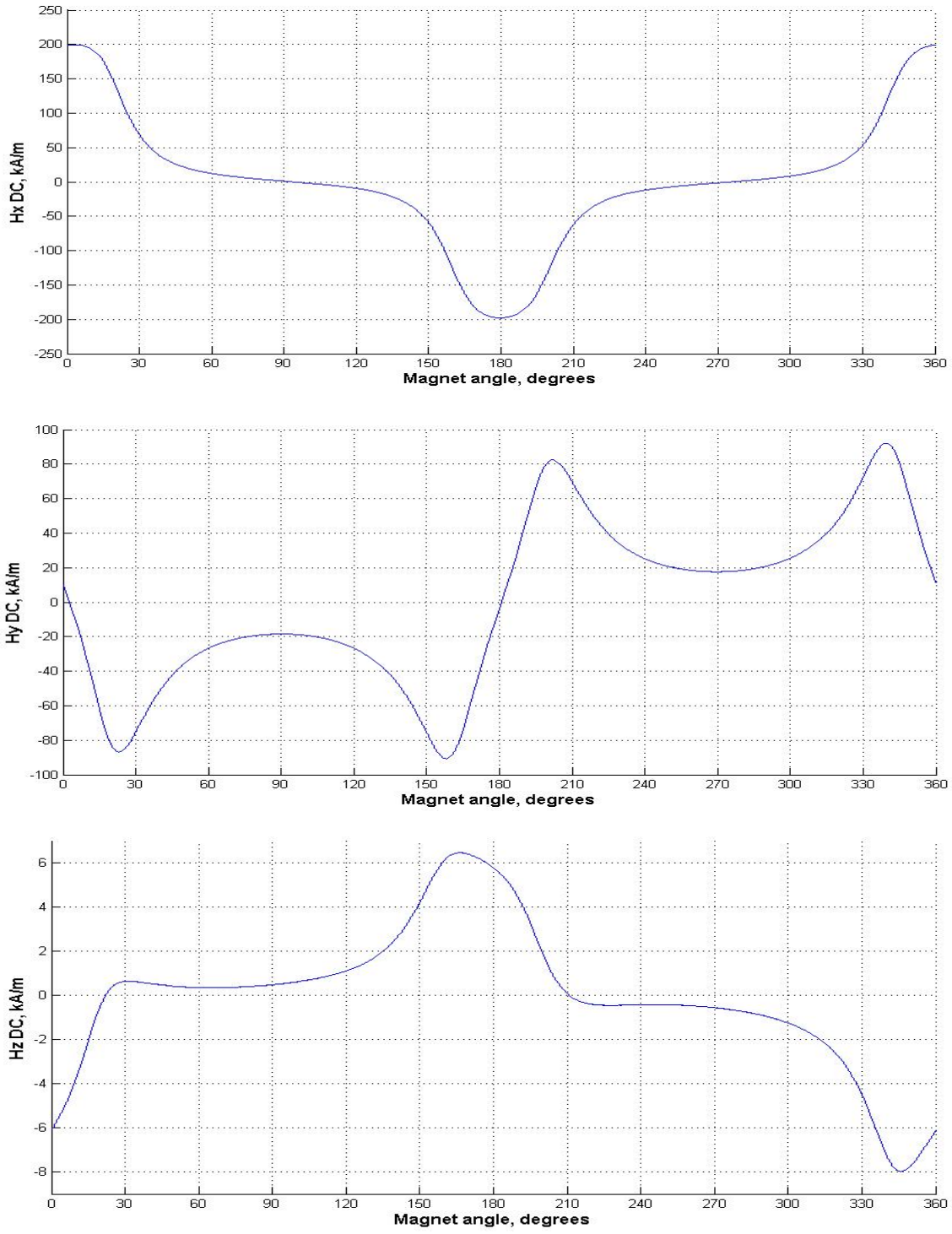

Figure 5.4.9. DC bias field components for rotating hysteresis loops.

Figures 5.4.10 and 5.4.11 show data that are typical for rotating hysteresis loops obtained at ambient and cryogenic temperatures. The figures show the voltage signals for the x, y, and z torque modes from sample S2A1A5.

Figure 5.4.10, ambient temperature data, shows little to no hysteresis in the x and y mode signals. This is the expected result for permalloy alone due to its very low, near zero, anisotropy. Note that there is some regularity in the z mode signal, but that the signal strength is barely above the system noise floor of approximately 1 uV. The z mode signal should be small at ambient temperature since the signal is due to in-plane magnetization only. The in-plane anisotropies are very low and the susceptibilities in the x and y directions are equal, or nearly equal, so that contributions to the z mode torque are small.

The data in figure 5.4.11 were obtained after field-cooling to 68.4° K. The field-cooling angle was 0°. Closure of the labs, due to Covid 19, at midnight on 13 Dec, 2020, meant that not enough time was available to align all three signals. The alignment and frequency for the z mode torque signal were adjusted as were the frequencies for the x and y mode torque signals. The procedure ensured high integrity of the z mode torque data while offering at least some possibility of reasonable data integrity for the x and y mode torque signals. The data integrity for the x and y mode torque signals was more than adequate as can be seen in the plots.

Figure 5.4.11, field-cooled data, shows the first hysteresis loop obtained after field-cooling. All of the signals show hysteresis. Note the substantial increase in the z mode torque signal as compared to the ambient data. This was expected since anisotropies induced during field-cooling hindered free rotation of the in-plane magnetization.

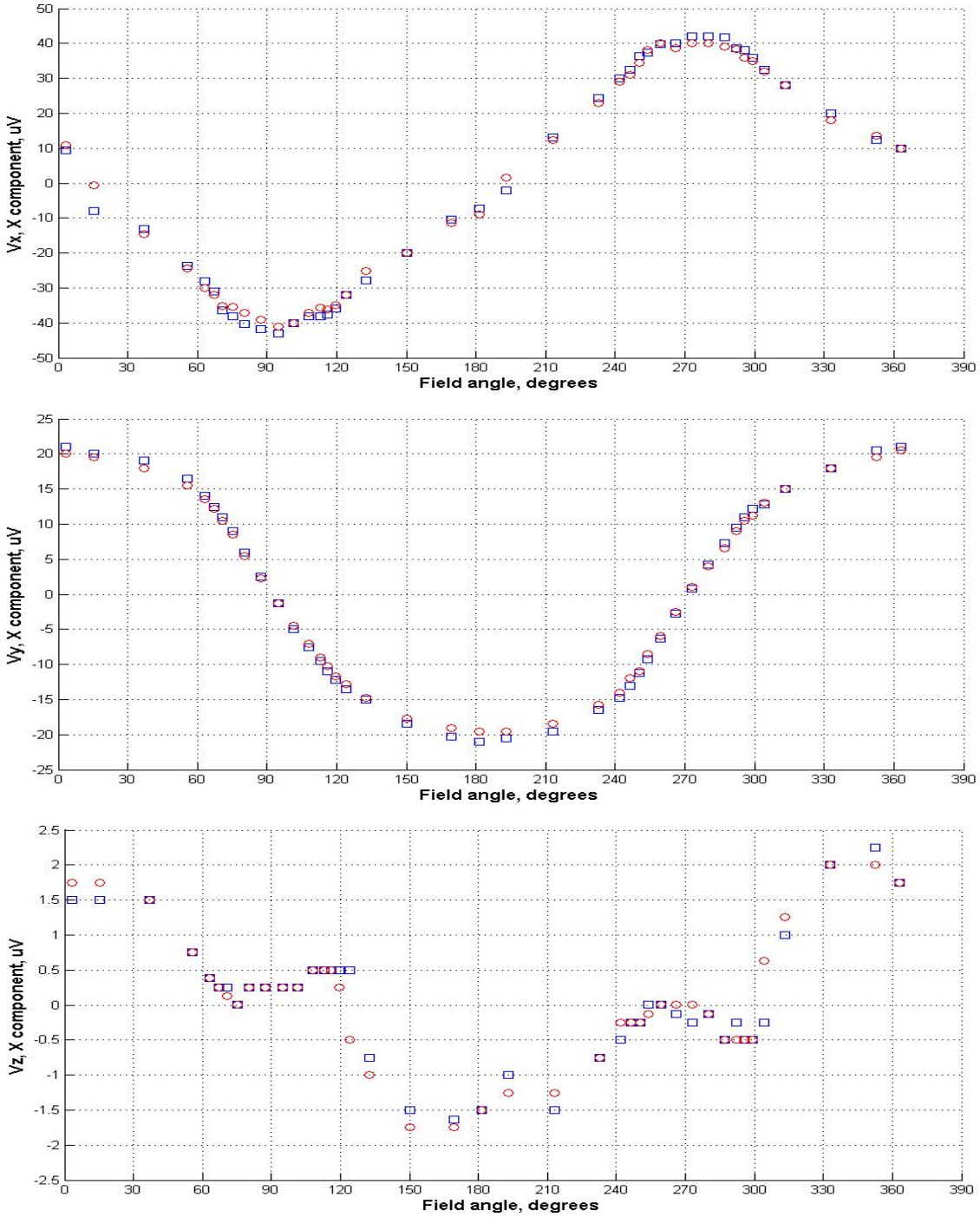

Figure 5.4.10. Rotating hysteresis loop. Voltage signals for the x, y, and z torque modes from sample S2A1A5 at an ambient temperature of 296.8° K. Data collected on 11 and 12 Dec, 2020. The plots begin on the left of the figures at a field angle of 0°. The counterclockwise rotation, blue squares, was done first followed by the clockwise rotation, red circles.

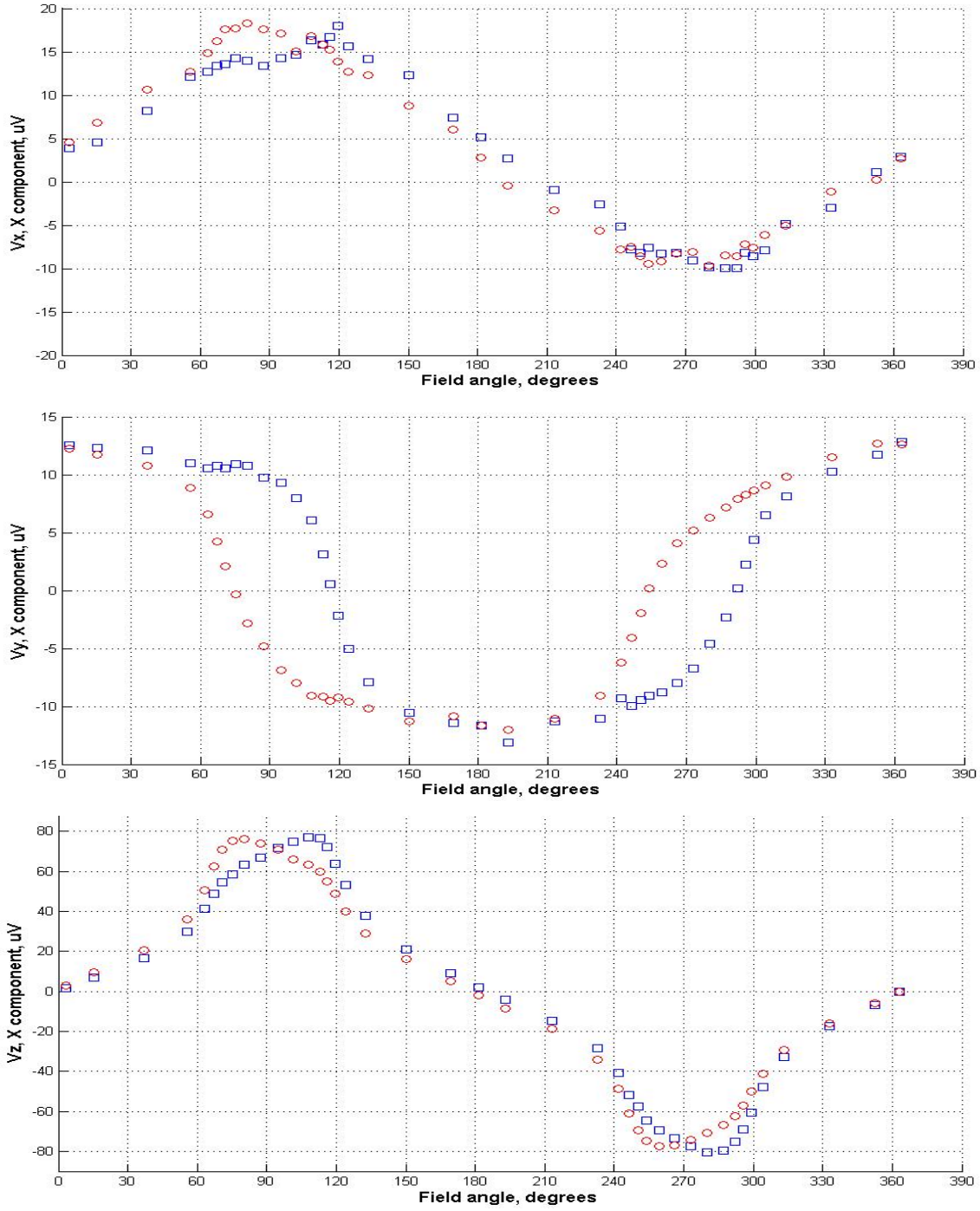

Figure 5.4.11. Rotating hysteresis loop. Voltage signals for the x, y, and z torque modes from sample S2A1A5 after field-cooling to 68.4° K at a cooling-field angle of 0°. Data collected on 13 Dec, 2020. The plots begin on the left of the figures at a field angle of 0°. The counterclockwise rotation, blue squares, was done first followed by the clockwise rotation, red circles.

5.4.4) Stepped temperature data.

On 29 June, 2020, an experiment was conducted to investigate the torque response as a function of temperature. The idea for the experiment came from my supervisor, Dr. Freeman. The thoughts were that the z mode torque signal should increase as the temperature is lowered.

As the temperature decreases, from above to below the Néel temperature of the antiferromagnetic cobalt oxide, a unidirectional anisotropy axis forms in the same direction as the cooling-field thus establishing an easy axis in that direction.[324] According to Radu and Zabel,[325] the anisotropy energy, K_{EB}, increases as the temperature decreases below the "blocking temperature" (the temperature, somewhat below the Néel temperature, at which exchange bias effects become evident). Temperature dependence of the exchange bias effect is mentioned by Kiwi[326] as an important parameter.

The z mode torque signal is generated by in-plane dithering of the applied field with respect to an in-plane anisotropy. The in-plane demagnetizing factors are very low, so changes in the response of the z mode torque signal, due to an increasing in-plane anisotropy, should be greater than for the x and y mode torques.

The geometry of the apparatus, sample position, and directions of the AC fields are such that the optimum field-cooling direction, for obtaining a z mode torque signal, is at an angle relative to the apparatus x axis instead of directly along it. An angle of 329.1° was selected after collecting many ambient temperature frequency sweeps to check the shape of the z mode frequency response. The selected angle of 329.1° gave DC bias fields of 48.3 kA/m in the direction of the apparatus x axis, 82.7 kA/m in the y direction and -4.9 kA/m in the z direction. Combination of the x and y fields gave an in-plane field magnitude of 95.8 kA/m at an angle of 59.7° at the sample. The DC magnet was kept in this position for all data points.

Interestingly, there was a range of angles between approximately 320 and 360 degrees where the frequency response was broader than normal. At ambient temperature, the shape of the broader response was dependent on the DC bias field direction. Examination of data collected on 29 June, 02 July, and 26 Oct, 2020, showed that the response was broader than normal from ambient temperature down to approximately 180° K, but that it had become normal for temperatures at and below 170° K.

The features in the broader than normal response were 1) small secondary peaks on one or both sides of the centre frequency, and 2) flattening of the response on one side of the centre frequency. The noise floor was at approximately 2/3 uV. The secondary peaks had a signal level of no more than 2-1/2 uV and were displaced by approximately 2 kHz from the centre frequency of 796 kHz. Flattening of the response occurred at approximately 0.7 kHz from the centre frequency over a range of approximately 0.3 kHz. The signal levels of the flattened responses were approximately 1/2 to 2/3 of the peak signal level.

The signal level of the primary peak increased as the temperature was lowered, but the signal levels of the secondary peaks and the regions of flattening did not. The response was normal for temperatures at and below 170° K. The signal level of the primary peak was 21.5 uV at 170° K and increased steadily as the temperature was lowered. At 68° K the signal level was 312 uV. Since the signal levels of the secondary peaks and the regions of flattening did not increase as the temperature was lowered, and since these features were either non-existent or substantially suppressed below 180° K, it was concluded that the broader frequency response at temperatures from ambient down to 180° K was due to a parameter, or parameters, that would be unlikely to interfere or compete with the cause of the primary observation, i.e. an increase in the anisotropy energy with a decrease in temperature, the effect of which is an increase in the z mode torque signal.

A broad response with small secondary peaks and flattening is not a characteristic of high Q resonator systems (our samples have Q > 1000) and is somewhat difficult to explain. The broader response from ambient temperature down to 180° K may have been due to magnetic or mechanical behaviour or a combination of both. Examination of the thermomechanical data showed that the thermomechanical frequency response was always normal for all temperatures suggesting that the broader response was not due to mechanical behaviour, but the thermomechanical drive level is only a small fraction of the drive level from the AC excitation coil. This means that anomalies in the frequency response, due to mechanical behaviour, may have been present, but discernible only at external AC drive levels sufficiently above the thermomechanical drive level.

The broader than normal frequency response is deserving of investigation, characterization, and explanation for its cause. The time required to undertake such an endeavour would be several months to more than one year since a variety of resonators with different deposits would have to be fabricated and then tested.

At the time when the stepped temperature experiment was conducted, it was reasoned that the best way to proceed was to choose a magnet angle for which the frequency response was as pure as could be obtained, proceed with data collection, and then examine the data to see if it had been corrupted by the abnormal frequency response. For temperatures at and below 170° K there was no indication of corruption and for temperatures at and above 180° K it was not possible to conclude whether or not the data were corrupted.

The best way to think about the plots in figures 5.4.12 and 5.4.13 is that they show a response consistent with the premise that the exchange bias energy increases as the temperature is lowered and that the response and premise are in accord with current knowledge regarding the temperature behaviour of exchange bias systems.

The experiment was conducted by collecting frequency sweep data at stepped temperatures. The first temperature was ambient (no anisotropy) followed by successive ten degree reductions in temperature. Approximately 40 minutes was given for the temperature to stabilize at each step before collecting the data. Data were collected on 29 June, 2020. Unfortunately, accumulation of ice on the resonator prevented completion of the task. The system was warmed to ambient temperature and the procedure was continued on 02 Jul, 2020.

Frequency sweep data were required as opposed to single measurements of the signal strength because the resonator Q increases as the temperature is decreased. Increased Q results in larger signal, so the data have to be corrected to account for the effect. The correction was determined for each data point ("point", here, means one frequency sweep file obtained at one stabilized temperature). The areas under the signal traces were calculated. The bandwidths used for the calculations were such that the same effective width was used for all files (same number of line widths from the centre frequency of each file). The area for each file represented the signal level with correction for variation in Q. Normalizing each of the areas to the area obtained at ambient temperature gave the corrected, relative, change in signal level. The normalized areas are what were plotted and examined.

Figure 5.4.12 shows the raw, uncorrected, voltage signals as a function of temperature. Figure 5.4.13 shows the same data after correction for the increase in Q. The plots confirm that the z mode torque increased as the temperature decreased. They provide information regarding the temperature dependence of the exchange anisotropy.

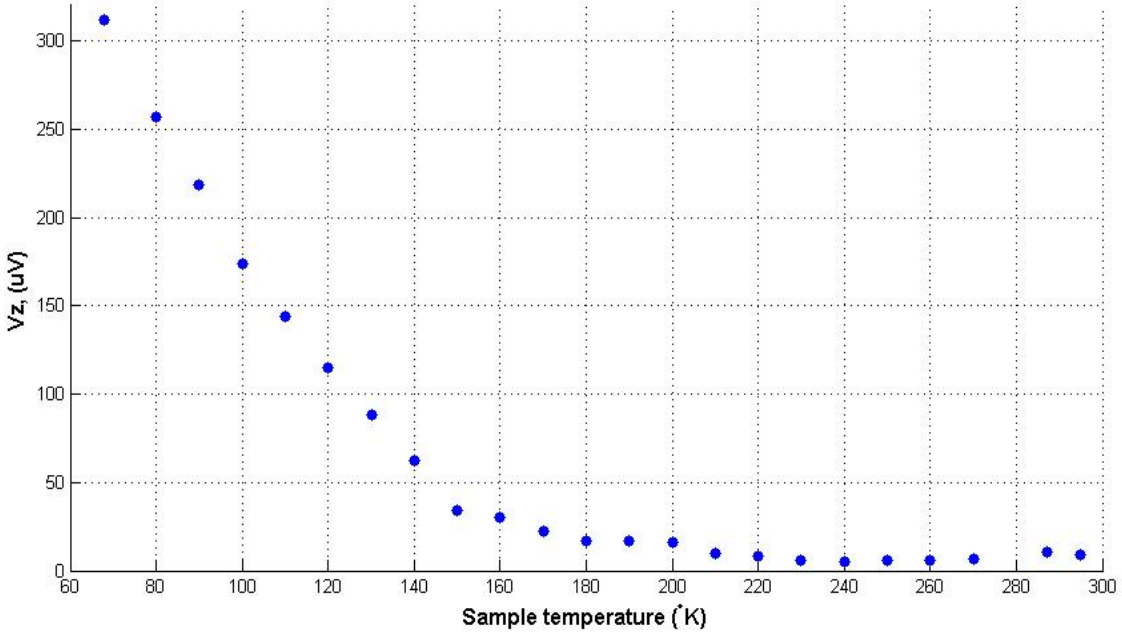

Figure 5.4.12. Sample S2A6A1. Raw data. z torque signal as a function of temperature.

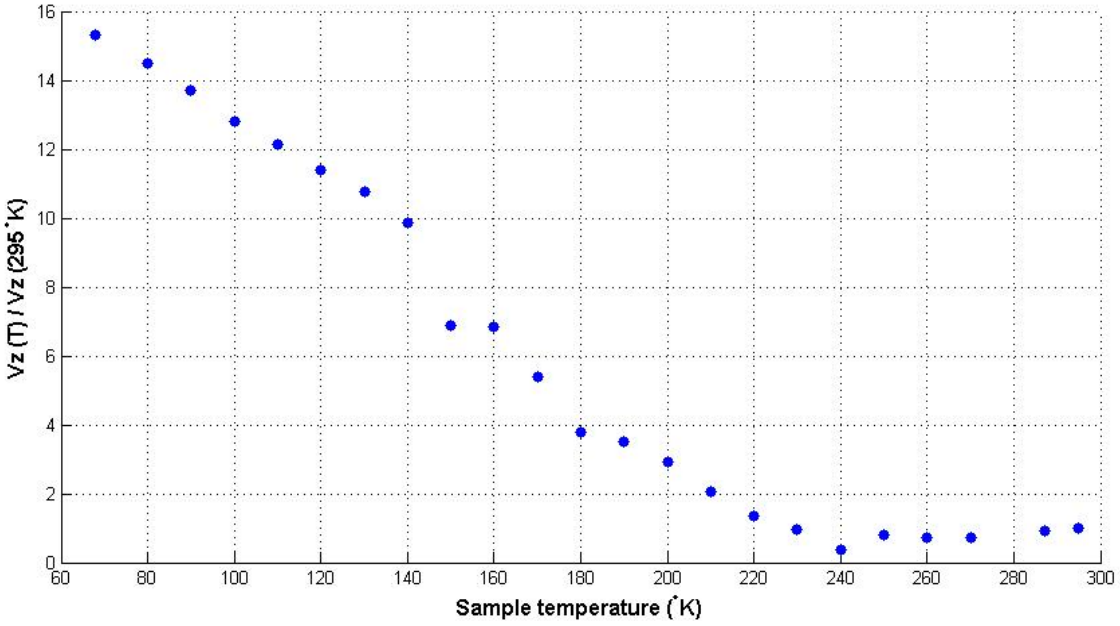

Figure 5.4.13. Same data as figure 5.4.12, but corrected for the increase of resonator Q with decrease in temperature and then normalized to the signal level at 295° K.

5.4.5) Summary.

Investigation of exchange bias and interfacial coupling effects in the bilayer sample required collection of several different data types. Raster images of several samples were examined to confirm that the torque responses were correct. Linear hysteresis loops collected at ambient and cryogenic temperatures showed shifts, in the field-cooled data, of the coercive field points. The shifts were due to influence from a unidirectional anisotropy.

Ambient temperature rotating hysteresis loops showed little to no hysteresis as was expected. The field-cooled rotating loops showed hysteretic effects thus confirming the presence of a temperature and field-induced anisotropy.

Stepped temperature data confirmed that the strength of the exchange bias (or combined effects of exchange bias and interfacial coupling) was temperature dependent with the strength increasing with decreasing temperature.

Thermomechanical calibration data were collected either before a hysteresis loop was started or after it had finished. Frequency sweeps with the AC drive fields turned on were also collected to provide quick determination of centre frequency and resonator Q.

Other types of data were collected during the period mid 2019 to late 2021. These were linear hysteresis loops collected with the DC bias field at different angles and rotating loops with the DC bias field magnet at various positions along the translation rail. Ambient, field-cooled, and zero-field-cooled data were collected for each of the loop types. The data presented here are from ambient and field-cooled linear loops taken with the DC bias field in the direction of the apparatus x axis and from ambient and field-cooled rotating hysteresis loops where the DC bias field was sufficient to saturate the magnetization throughout the full 360° rotations of the bias field.

Chapter 6

Results, Analysis, and Discussion.

6.0) Chapter introduction.

A review of the experiment will be presented followed by presentation of the results obtained from linear and rotating hysteresis loops and from the stepped temperature data. The method of analysis will be explained. The chapter closes with a discussion of the results and what was learned.

6.1) Review of experiment.

The sample wafer had 240 resonators with thin-film, bilayer, deposits on their paddles. Many of them had one of their torsion arms cut to enhance the x and z mode torque signals. Several resonators were examined by first finding their resonant frequencies and then collecting data to determine the Q of each of the three resonator torque modes. A "good" resonator was one that had a Q for each torque mode that was greater than 1000 at ambient temperature (2000 or more was preferable) and that gave signal levels for all three torque modes that were adequately above the noise floor of the lock-in amplifier. Raster images of selected resonators were then collected to confirm that there were no obvious defects and to verify that the resonator responses for each torque mode were correct.

After much work to examine many samples, resonators S2A1A5 and S2A6A1 were selected for investigation of exchange bias and interfacial coupling effects. Both of these resonators were of the type that had one torsion arm cut.

The apparatus control systems were designed so that a software controlled semi-automatic procedure could be used for convenient collection of the data from complete hysteresis loops. However, precise alignment of the laser beam position on the resonator edge and sufficient time for the magnetization of the sample to stabilize after a change in DC bias field required manual collection of the data after successive increments of the DC bias field, realignment of the laser beam position, and adjustment of the resonator drive frequencies. The integrity, repeatability, and feature detail of the data obtained manually was much better than for the semi-automated data. Of particular importance was recognizing that the semi-automated collection procedure was too quick and, thus, failed to capture the sometimes several minute long durations of magnetization rotation after a change of the DC bias field strength or direction. These features were successfully recorded using the manual data collection procedure.

Conduct of the experiment required collection of data from linear and rotating hysteresis loops at both room and cryogenic temperatures. A record of the training effect that is seen in exchange biased systems was also required for comparisons of hysteresis loops obtained immediately after field-cooling to those obtained subsequently. Data for determining the component of out-of-plane torque (z mode torque) as a function of temperature was also obtained.

6.2) Results.

6.2.1) Results from linear hysteresis loops.

A) Ambient temperature.

Linear hysteresis loops obtained at ambient temperature showed that the sample behaviour was consistent with previously obtained data for permalloy alone.[7] Refer to the plots in figures 5.4.4 and 5.4.7. At ambient temperature, the linear hysteresis loops are narrow and centred at zero applied field (no shift of coercive field points). The slopes in the high field regions are not due to exchange bias or interfacial coupling effects. They occur because one of the terms in the torque equation, $\vec{\tau} = \mu_o \vec{m} \times \vec{H}$, is still increasing while the other is in saturation and, for the semi-automated loop in figure 5.4.7, because the alignment and resonant frequencies are changing (drift and decrease of signal strength in high DC bias fields is discussed in Chapter 2, section 2.3, subsections 2.3.10 and 2.3.11).

Though not shown, the signatures of vortex nucleation and annihilation were confirmed to be present in the ambient linear hysteresis loops.[291] The signatures can be seen on plots where the field range is approximately +/- 5 to +/-20 kA/m (much less than in figure 5.4.4). The vortex signatures were as expected for permalloy alone. There was no evidence of influence from the antiferromagnetic cobalt oxide. The sample behaved as though it was a single layer of permalloy.

The vortex signatures in the ambient loops were used to estimate the thickness of the permalloy layer. During deposition, the thickness was determined to be 20 nm. The permalloy was the top layer. A cap layer was not deposited. A micromagnetics software package, mumax3,[292] was used to generate simulations with thickness as an input parameter.[327] The simulations were run with thicknesses of 12, 16, and 20 nm and were then compared to recorded data. The simulation results were fit to the data and an

effective thickness of 16.1 nm was obtained. The simulation work was conducted by Michael Dunsmore. A reasonable explanation for why the thickness should be 16 instead of 20 nm is oxidation of the uncapped surface thus resulting in an effective thickness less than the deposited thickness.

Confirming that the behaviours of the bilayer, permalloy/cobalt oxide, samples were the same as for samples of permalloy alone was a necessary and crucial step. The confirmation provided a reference to which the sample behaviours after field-cooling could be compared. The reference corresponded to a magnetic system that had very little or no anisotropy and that had no exchange bias or coupling effects attributable to the permalloy/cobalt oxide interface. At ambient temperature, the bilayer samples behaved as though they were just single layers of permalloy. The ambient temperature linear hysteresis loops and the knowledge gained from them provided a reliable starting point for investigation of effects induced by lowering the sample temperature.

B) <u>Cryogenic temperature.</u>

Linear hysteresis loops obtained at cryogenic temperatures showed a shift of the coercive field points. Compare figure 5.4.5, field-cooled loop, to figure 5.4.4, ambient loop. The field-cooled loop in figure 5.4.5 is wider and shows that the centre of the loop has been shifted toward negative field as compared to the ambient loop in figure 5.4.4. The shift of the coercive field points is due to a uniaxial anisotropy, in the direction of the cooling-field, that was formed as the sample temperature fell below the Néel temperature of the antiferromagnetic cobalt oxide. The direction of the shift, toward negative field, indicates that the value of the exchange bias anisotropy constant, K_{EB}, is positive. The exchange bias term appears in phenomenological energy equations as $-K_{EB}\cos(\Phi)$ where Φ is the angle between the magnetization and the anisotropy axis.

The linear hysteresis loop shown in figure 5.4.5 was the first loop obtained after completing the field-cooling procedure. The shift was approximately 5 kA/m from which a value of 0.08 mJ/m^2 for the exchange bias energy per unit area of film was obtained (refer to Chapter 5, section 5.4, last page of subsection 5.4.2).

The hysteresis loop shown in figure 5.4.6 was the second loop obtained after field-cooling. The loop shift is much less than in the first loop. The decrease in loop shift is consistent with the training effect which results in a decrease of the exchange bias anisotropy constant in each successive hysteresis loop. The training effect and empirical relations for describing the decrease in exchange bias with number of loops is discussed by Radu and Zabel.[328] Though recorded and noted, the training effect was not an area of focus and so was not investigated further. This is not to say that there is nothing to be learned from studies of the training effect. There is, but it did not fit into the scope of work for the experiment. What was useful regarding the training effect was that observations of it would be expected in an exchange biased system. Training effects were observed thus providing additional confirmation that the sample behaviours after field-cooling were due to exchange bias.

6.2.2) Results from rotating hysteresis loops.

An analysis requirement demanded that the magnetization be in a condition of saturation throughout the full 360° rotations of the DC bias field. Confirmation of saturation will be discussed in the analysis section.

A) Ambient temperature.

Several sets of rotating hysteresis loops were obtained at ambient temperature. Refer to figure 5.4.10. The behaviour of the x, y, and z mode torque signals during the clockwise

field rotation repeated, or approximately repeated, during the counterclockwise field rotation thus showing that there was little to no hysteresis. At ambient temperature, the signals result from behaviour of the permalloy alone just as in linear loops at ambient temperature. The absence of hysteresis in the rotating loops confirmed an absence of in-plane anisotropy which is consistent with the low to extremely low value of anisotropy in permalloy. With little to no in-plane anisotropy, the z mode torque signal should have been small to very small. The data show that the z mode torque signal was only slightly above the noise floor of the lock-in amplifier consistent with expectation.

B) <u>Cryogenic temperature.</u>

Rotating hysteresis loops were obtained after field-cooling to cryogenic temperature. Field-coolings were done in a positive, saturating, DC bias field at an angle of either 0° or 59.7° at the sample. The field-cooling procedure should have established a unidirectional anisotropy axis in the same direction as the cooling-field (at 0°, along the direction of the apparatus positive x axis for the field-coolings done with the bias field at 0°, or at 59.7° with respect to the apparatus positive x axis for the field-coolings that were done with the bias field at 59.7°).

Refer to figure 5.4.11. The data are from the same sample that was monitored during the ambient temperature rotating hysteresis loop. The hysteresis loop was the first one recorded after field-cooling. Compare figure 5.4.11, field-cooled, to figure 5.4.10, ambient. All of the torque signals in the field-cooled data show hysteresis. The hysteresis confirms that the field-cooling procedure resulted in formation of an in-plane anisotropy axis. The substantial increase in the z mode torque signal compared to the signal level at ambient temperature also provides evidence for the presence of an anisotropy axis.

6.2.3) Results from stepped temperature data.

Refer to figures 5.4.12 and 5.4.13. The record of the z mode torque signal obtained during field-cooling, in increments of 10° K, showed that the signal increased as the temperature was decreased. The data confirmed that an anisotropy axis was formed as the temperature was lowered below the Néel temperature of the antiferromagnetic cobalt oxide and that the strength of the anisotropy increased with decreasing temperature.

The data in figures 5.4.12 and 5.4.13 show an additional feature. The temperature at which exchange bias effects are first noticed is defined as the *blocking temperature*, T_B.[329] The blocking temperature is lower than the Néel temperature for several possible reasons which include the influences of variations in sample size, thickness, and stoicheometry.[330] The data show that the blocking temperature for the sample that was measured was somewhere between 220° and 230° K which is well below the Néel temperature of the cobalt oxide (293° K as reported by Cullity and Graham[331]). This result, that there is a blocking temperature lower than the Néel temperature, is also consistent with an exchange bias that results from formation of an anisotropy axis.

6.3) Analysis.

6.3.1) Data.

The analysis was performed on linear and rotating hysteresis loops obtained from sample S2A1A5 at ambient and cryogenic temperatures. The data were,

1) Ambient temperature linear hysteresis loop obtained on 01 Sep, 2021, y mode torque signal.

2) Field-cooled linear hysteresis loop obtained on 08 Sep, 2021, y mode torque signal. First loop after field-cooling. The cooling-field strength was 240 kA/m and the cooling-field angle at the sample was 0°.

3) Field-cooled linear hysteresis loop obtained on 09 Sep, 2021, y mode torque signal. Second loop after field-cooling.

4) Ambient temperature rotating hysteresis loops obtained on 11 and 12 Dec, 2020, x , y, and z mode torque signals.

5) Field-cooled rotating hysteresis loops obtained on 18, 19, and 20 Nov, 2020, x, y, and z mode torque signals. The cooling-field strength was 95.8 kA/m and the cooling-field angle at the sample was 59.7°. Five preliminary rotating loops were performed prior to collecting the data. The preliminary loops were done to stabilize the sample by reducing the effects that are caused by training. The recorded data are the sixth, seventh, and eighth loops after the field-cooling procedure.

6) Field-cooled linear hysteresis loop obtained on 13 Dec, 2020, z mode torque signal. First loop after field-cooling. The cooling-field strength was 240 kA/m and the cooling-field angle at the sample was 0°.

6.3.2) Analysis model.

The model used for the analysis is based on a phenomenological energy equation. The form of the energy equation follows from what has been used by others (e.g. Stiles and McMichael,[8] da Silva et al.[9] and Müglich et al.[282]). Figure 6.3.1 shows a diagram of the field components and their orientations with respect to the apparatus x axis. The diagram includes field components that are present only after field-cooling of a sample. These are the unidirectional anisotropy field, H_{EB}, the rotatable anisotropy field, H_{ROT}, and the spin-flop field, H_{SF}. These fields are due to exchange bias and interfacial coupling effects that result from interaction between the ferromagnetic and antiferromagnetic layers of the sample. The interaction is active only after the sample has been cooled, while in a saturating DC bias field, to a temperature below the Néel temperature of the antiferromagnetic layer (293° K for cobalt oxide). The ferromagnetic magnetization is shown as m_{FM} and the externally applied DC bias field is shown as H_{ext}^{DC}.

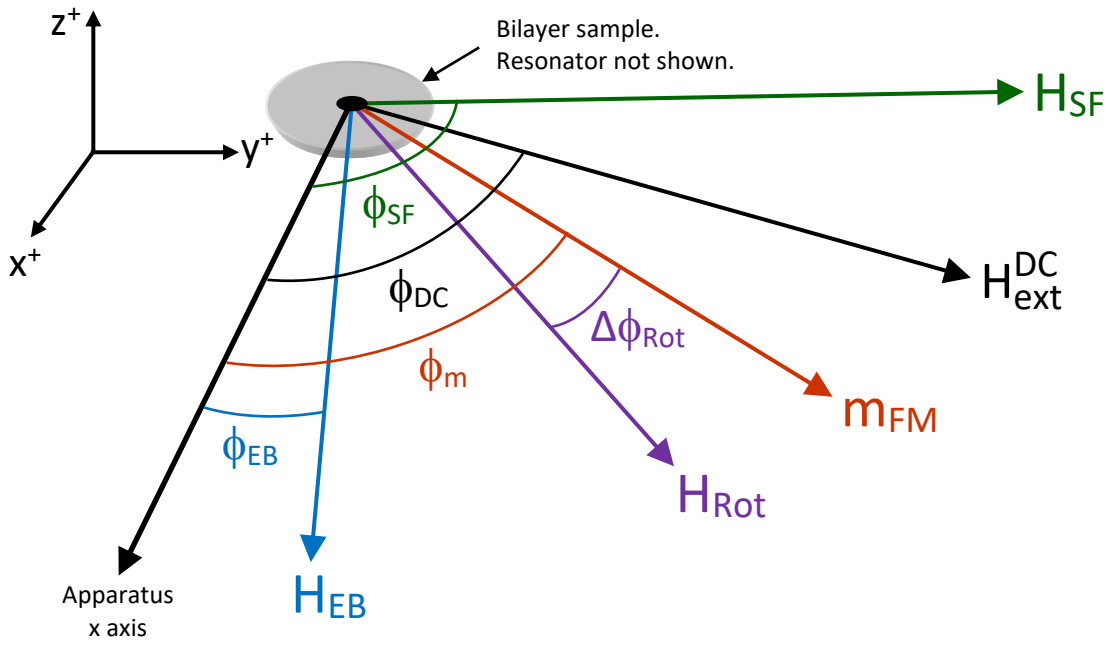

Figure 6.3.1. Field components and orientations with respect to the apparatus x axis. Figure prepared by Michael Dunsmore, fall 2021.

The phenomenological energy equations that were used for the analysis were presented in Chapter 2. The equations are presented again here for quick reference and with short descriptions of the terms. Refer to Chapter 2, section 2.1, subsection 2.1.6, for complete descriptions.

The equation that was used was assembled by Michael Dunsmore of our research group and is expressed by writing the total energy density, ε_T, as the sum of the densities for the anisotropy energy, ε_A, the demagnetization energy, ε_D, and the Zeeman energy, ε_Z.

i) <u>Anisotropy energy density.</u>

The expression for the anisotropy energy density, ε_A, is,

$$\varepsilon_A = -K_{SF}\sin^2(\theta)\cos^2(\Phi - \Phi_{SF}) - K_{EB}\sin(\theta)\cos(\Phi - \Phi_{EB}) - K_{Rot}\cos(\Delta\Phi_{Rot} - \Delta\Phi_m). \quad (2\text{-}1)$$

The anisotropy constants and angles in the equation above are,

1) θ and Φ are the polar and azimuthal angles in a standard spherical coordinate system that was used to approximate the geometry of the sample. These angles give the orientation of a macrospin moment that describes the magnetization of the sample as a whole.

2) Spin-flop coupling, K_{SF}. θ and Φ are as given in (1). The spin-flop coupling is uniaxial and results from canting of the antiferromagnetic sublattices with respect to their natural, equilibrium, orientations. Φ_{SF} is the angle between the direction of the spin-flop field and the zero reference.

3) Unidirectional anisotropy due to exchange bias, K_{EB}. θ and Φ are as given in (1). Φ_{EB} is the angle between the exchange bias field and the zero reference.

4) Rotatable anisotropy, K_{Rot}. The anisotropy is represented by the anisotropy constant, K_{Rot}, while the angle between the spins that participate in this interaction is given by a small angle, $\Delta\Phi_{Rot}$.[283, 285] Once set, $\Delta\Phi_{Rot}$ remains constant. $\Delta\Phi_M$ is the dither in the direction of the ferromagnetic magnetization. The dither is induced by the externally applied AC fields.

ii) <u>Demagnetization energy density.</u>

The expression for the demagnetization energy density, ε_D, is,

$$\varepsilon_D = \frac{1}{2}\mu_0 M_S^2\left[N_x\cos^2(\Phi)\sin^2(\theta) + N_y\sin^2(\Phi)\sin^2(\theta) + N_z\cos^2(\theta)\right]. \quad (2\text{-}2)$$

The constants and angles in the equation above are,

1) μ_o is the free space permeability.

2) M_S is the saturation magnetization of the ferromagnetic layer.

3) N_x, N_y, and N_z are the demagnetization factors in the x, y, and z directions. These directions coincide with the x, y, and z reference directions of the apparatus.

4) θ and Φ are as given for equation (2-1).

iii) Zeeman energy density.

The expression for the Zeeman energy density, ε_Z, is,

$$\varepsilon_Z = -\mu_o \vec{m}_{FM} \cdot \vec{H}_{ext}^{DC} = -\mu_o m_{FM} H_{ext}^{DC} \cos(\Phi_{DC} - \Phi_m), \quad (2\text{-}3)$$

where m_{FM} is the magnetization of the ferromagnetic layer, H_{ext}^{DC} is the externally applied DC field, Φ_m is the angle between the ferromagnetic magnetization and the zero reference, and Φ_{DC} is the angle between the externally applied DC bias field and the zero reference.

iv) Total energy density.

The total energy density, ε_T, is given by the sum of the individual energy terms,

$$\varepsilon_T = \varepsilon_A + \varepsilon_D + \varepsilon_Z. \quad (2\text{-}4)$$

The phenomenological energy equation was solved by using the Landau-Lifshitz-Gilbert equation (LLG equation). Details of the analysis are provided later in subsection 6.3.3, para (vii), subparas (A) and (B).

6.3.3) Analysis methods.

Data that could be presented as normalized did not require calibration. Data from which values of anisotropy constants could be extracted did require calibration. Data that were used to investigate the training effect also required calibration. The calibration method is described in Chapter 2, section 2.4, Thermomechanical calibration, subsections 2.4.5 to 2.4.7, with further description provided in section S3 of the supplement to our paper that was published in AIP Advances in March of 2022.[1]

i) Thickness of ferromagnetic layer. The y mode torque signal obtained from an ambient temperature linear hysteresis loop was used to obtain an estimate of the effective thickness of the ferromagnetic layer. In low field (less than a few kA/m), the sample demagnetizes and a vortex structure is then formed. The recorded data show the fields at which vortex nucleation occurred. The field region where nucleation occurs in the down sweep of the field and this same field region where the nucleation occurs in the up sweep of the field is approximately linear. Since the magnetic anisotropies in the sample are very low at ambient temperature, it is only shape anisotropy that can be responsible for the features in the data. The slope of the data in the low field region, between the fields where vortex nucleation occurred, is a function of the aspect ratio of the sample.[327 and [j]] A micromagnetic simulation program (mumax3[292]) was prepared with sample geometry and thickness of the ferromagnetic layer as inputs. The output of the program was compared to the recorded data. The thickness for which a fit to the data was obtained was taken as an estimate of the true thickness. The simulations gave a value of 16.1 nm for the effective thickness of the ferromagnetic layer (less than the deposited thickness of 20 nm due, most likely, to oxidation of the uncapped surface). The recorded and simulated data are shown in figure 6.3.2. The program and results were generated by Michael Dunsmore.

[j] I did not know this. My supervisor was of much help here, and elsewhere, regarding analysis of the data.

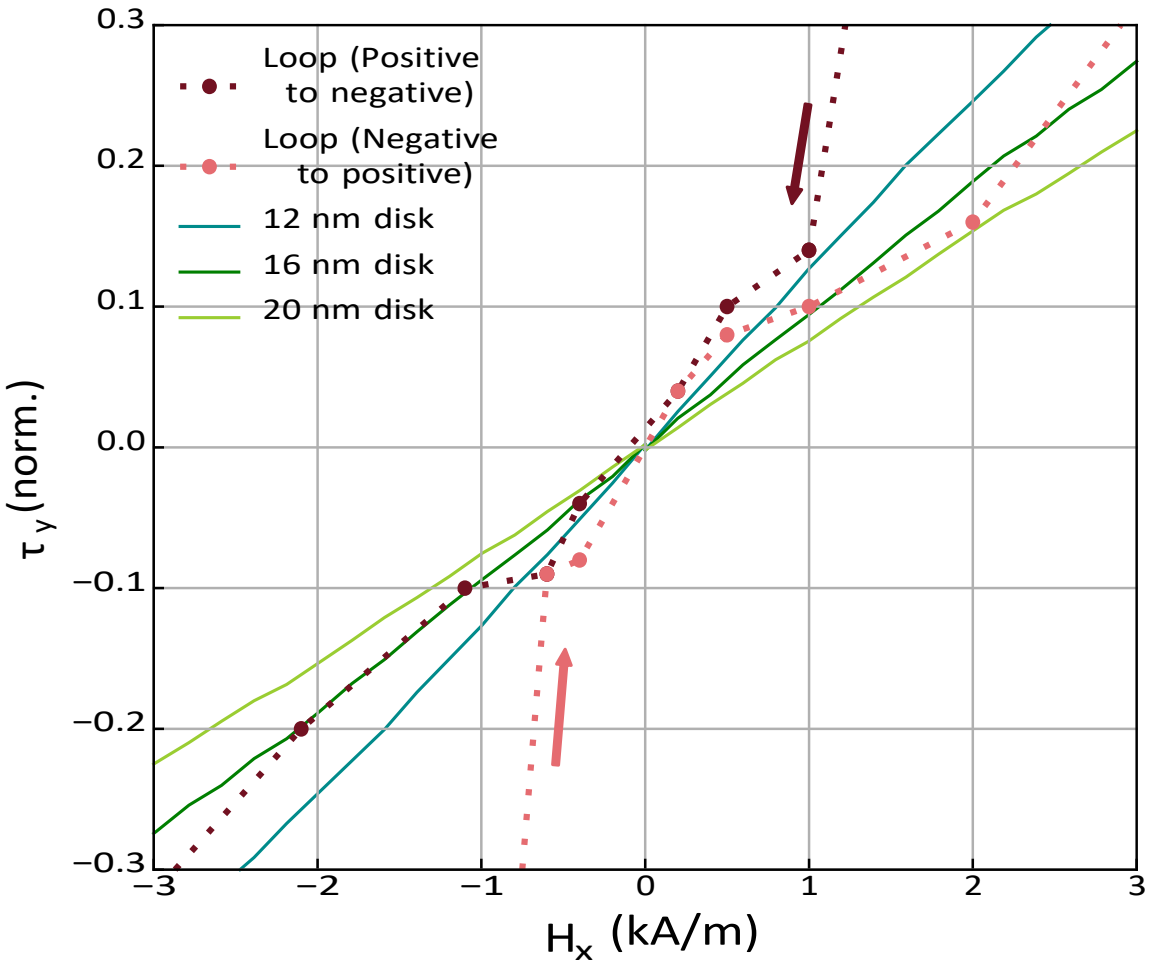

Figure 6.3.2. Normalized y mode torque signal from ambient temperature linear hysteresis loop obtained on 01 Sep, 2021. Sample S2A1A5. The brown point in the positive to negative field sweep, near the brown arrow, and the red point in the negative to positive field sweep, near the red arrow, show where vortex nucleations occurred. The data in the field span from -2 to 2 kA/m is approximately linear. The slope depends on the aspect ratio and thickness of the sample.[327] A fit to the slope of the data in this region gave an estimate of the effective thickness of the ferromagnetic layer. The best fit to the data was obtained with a thickness of 16.1 nm. The simulation program and plot were generated by Michael Dunsmore.

ii) <u>Ferromagnetic saturation magnetization.</u> The slopes of the y mode torque signal in the high positive and high negative field regions of an ambient and a field-cooled linear hysteresis loop were used to determine values for the saturation magnetization of the ferromagnetic layer at ambient and cryogenic temperatures.[332 and [k]] The cause of the slopes is explained in Chapter 2, section 2.3, subsection 2.3.11. The shape anisotropy (dominated by the out-of-plane demagnetization factor, N_Z), the sample shape (determined from the fabrications steps and SEM images), the sample thickness, (determined as described in the previous paragraph), and a measure of the slopes from the recorded data were input parameters to a micromagnetic simulation program (mumax3[292]). The program reproduced the recorded slopes as a function of the input parameters and a test parameter that represented the saturation magnetization. The value of saturation magnetization for which the simulated slopes matched the recorded slopes was taken as an estimate of the true ferromagnetic saturation magnetization. The values obtained from each slope (one for $H_x < 0$ and one for $H_x > 0$) were averaged.

The ambient temperature data were taken from the linear hysteresis loop obtained from sample S2A1A5 on 01 Sep, 2021. The data are shown in figure 6.3.3. At ambient temperature, where anisotropies are very low, the simulations gave a saturation value of M_S = 763 +/- 7 kA/m at a temperature of 295° K.

The cryogenic temperature data were taken from the linear hysteresis loop obtained from sample S2A1A5 on 08 Sep, 2021. The data are shown in figure 6.3.4. At cryogenic temperature the sample had an exchange bias anisotropy. An additional input parameter to account for unidirectional anisotropy was added to the program. The simulations gave M_S = 801 +/- 8 kA/m at a temperature of 68° K. The simulation program and results were generated by Michael Dunsmore.

[k] As in page note [j] above, with help from my supervisor.

iii) <u>Confirmation of exchange bias.</u> The y mode torque signals obtained from linear hysteresis loops at ambient and cryogenic temperatures were used to confirm the presence of exchange bias after field-cooling. The only analysis necessary for making the confirmation was to inspect the plots to verify that a shift of coercive field points had occurred in the field-cooled loops. An estimate for the exchange bias energy per unit area of film was extracted from the observed shift (refer to Chapter 5, section 5.4, subsection 5.4.2, and to figures 5.4.4 to 5.4.6). A value of σ_{ex} ~0.08 J/m^2 was obtained from data recorded on 08 Sep, 2021. The maximum value of exchange bias energy from the samples we tested was 0.11 mJ/m^2. This value was obtained from data collected on 26 Sep, 2019.

The ambient temperature data were obtained from sample S2A1A5 on 01 Sep, 2021. The data are shown in Chapter 5, figure 5.4.4 and again here in figure 6.3.3. The cryogenic temperature data were obtained on 08 and 09 Sep, 2021. The data are shown in Chapter 5, figure 5.4.5, first loop after field-cooling, and figure 5.4.6, second loop after field-cooling. The data are presented again here in figure 6.3.4 which shows the data from the first and second loops on the same plot. Note the decrease in loop shift of the second field-cooled loop compared to that of the first. The reduction in loop shift is consistent with the training effect.

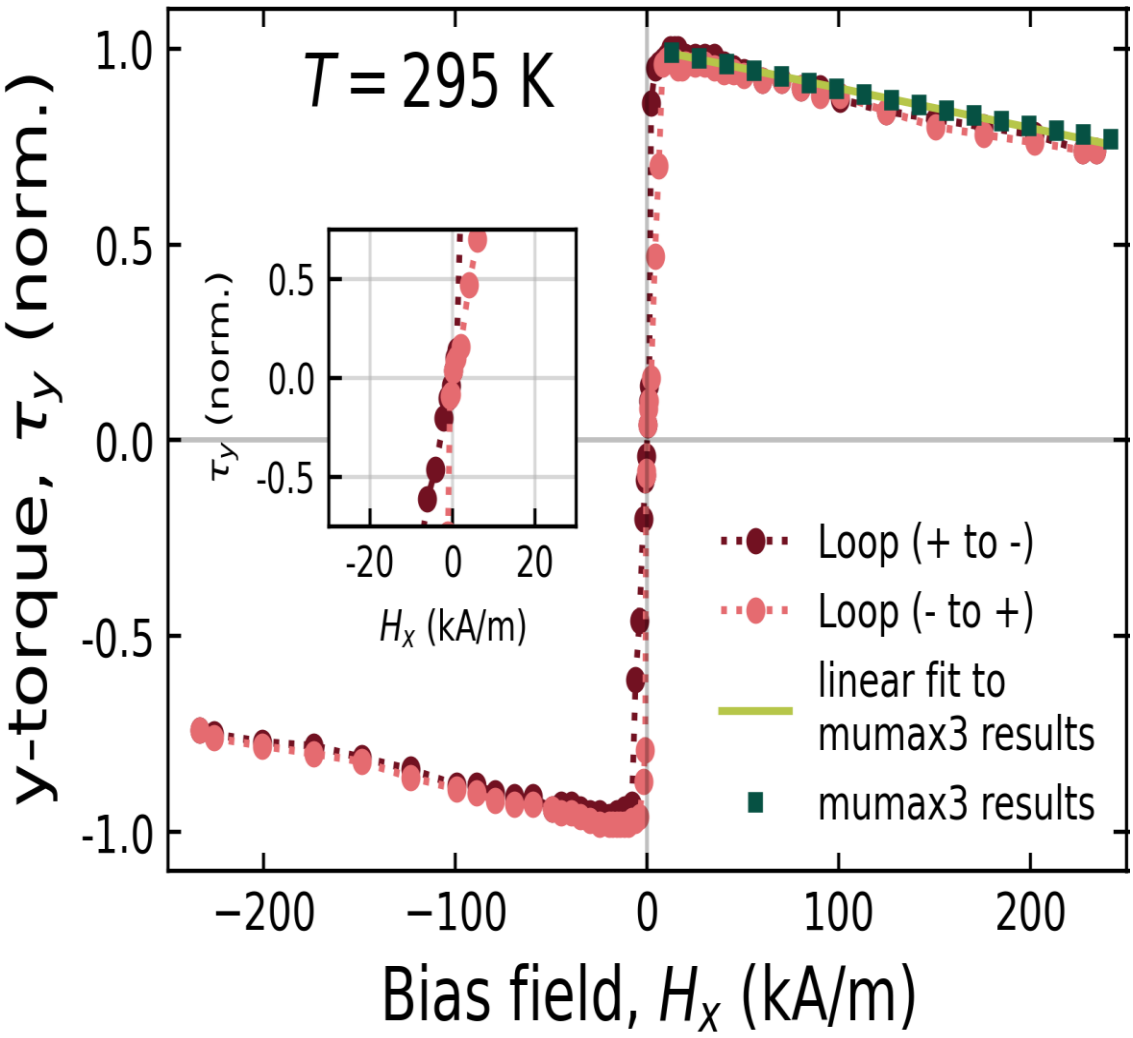

Figure 6.3.3. Normalized y mode torque. Sample S2A1A5. Linear hysteresis loop obtained at ambient temperature on 01 Sep, 2021. These are the same data that are presented in figure 5.4.4. Simulated data were obtained from mumax3[292] for the slopes in both the positive and negative field regions. The simulated data were plotted only for the positive field region. The slopes in these regions were used to extract values for the ferromagnetic saturation magnetization, M_S, which was a fitting parameter for the simulation. The simulations gave M_S = 763 +/- 7 kA/m after averaging the results from both slopes. The inset is plotted over the lower field region. It shows that the zero crossings are at zero field and that there is no shift of the coercive field points (both are zero at zero field). Simulations and plot by Michael Dunsmore, fall 2021.

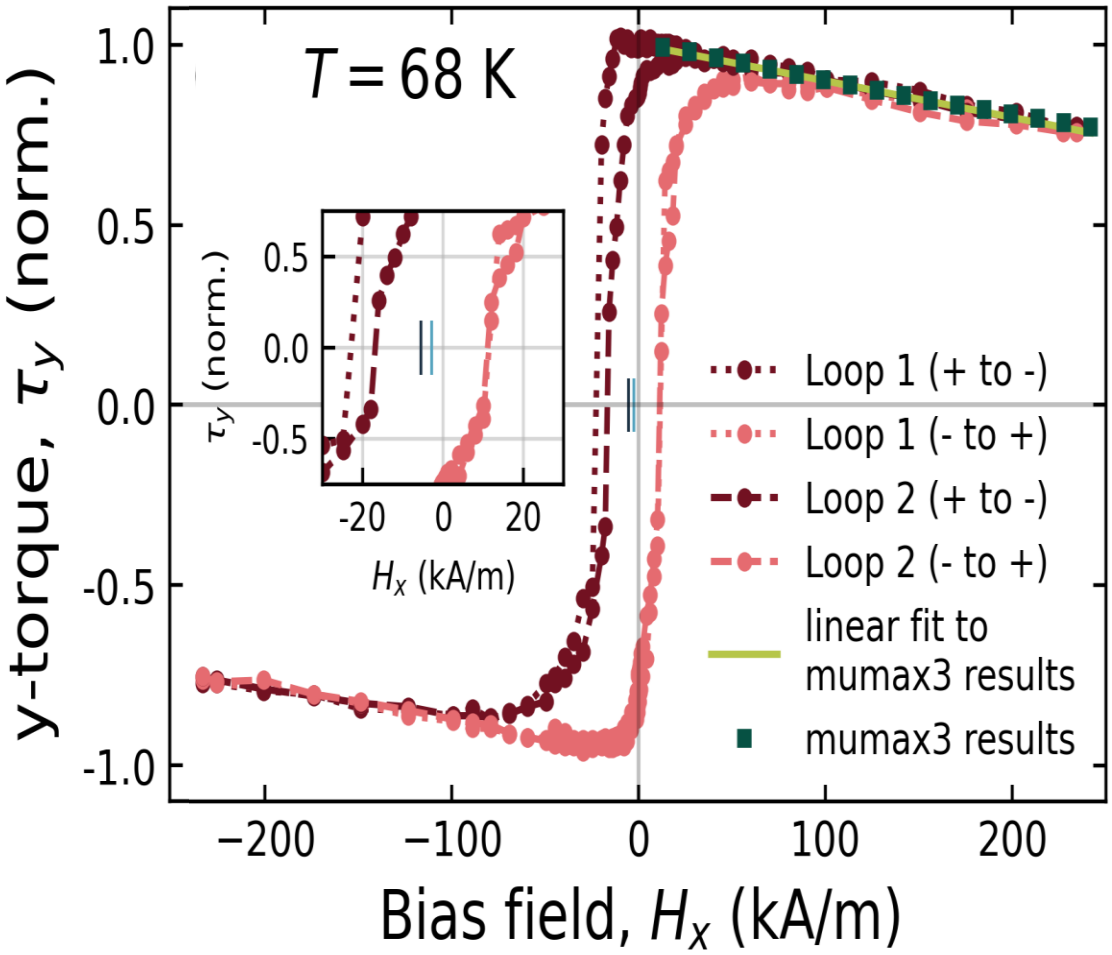

Figure 6.3.4. Normalized y mode torque. Sample S2A1A5. Linear hysteresis loops obtained at 68° K on 08 Sep, 2021, first loop after field-cooling, and 09 Sep, 2021, second loop after field-cooling. These are the same data that are presented in figures 5.4.5 and 5.4.6. Simulated data were obtained from mumax3[292] for the slopes in both the positive and negative field regions. The simulated data were plotted only for the positive field region. The slopes in these regions were used to extract values for the ferromagnetic saturation magnetization, M_S, which was a fitting parameter for the simulation. The simulations gave M_S = 801 +/- 8 kA/m after averaging the results from both slopes. The inset is plotted over the lower field region. It shows a shift in the coercive field points (dark blue line for the first loop and light blue line for the second loop). Simulations and plot by Michael Dunsmore, fall 2021.

iv) Confirmation of saturation. The analysis strategy required that the magnetization of the sample, during rotating hysteresis loops, was at all times saturated. This requirement enabled the use of a macrospin description of the magnetization throughout the entire 360° rotations of the DC bias field.

Refer to: 1) Chapter 5, section 5.4, subsection 5.4.3, and figure 5.4.9, 2) Chapter 2, figure 2.3.5, and 3) Chapter 4, figure 4.4.2 for details regarding the strengths of the DC bias field components during rotation of the DC magnet. The plots in figures 6.3.3 and 6.3.4 show that the magnetization was saturated in the high field portions of linear hysteresis loops, but the linear loops were obtained with the magnet angle at 0° for which the x component of the field reaches strengths of over 200 kA/m when the magnet is near the cryostat. The field strength at the sample decreases during rotation of the magnet away from 0°. The position of the magnet for rotating hysteresis loops gave a maximum field strength of 199.8 kA/m at a field angle of 359.6° and a minimum of 17.7 kA/m at 93.0°. It is possible that the minimum field was too low to achieve saturation.

A method for determining whether or not the magnetization was always saturated during complete rotations of the DC magnet was available.[332 and [l]] The x and y mode torque signals, both of which are in-plane, were obtained during full rotations of the DC magnet. Ambient temperature data from sample S2A1A5 obtained on 11 and 12 Dec, 2020, and cryogenic temperature data, from the same sample, obtained on 19 and 20 Nov, 2020, were used. The data were corrected for the decrease in signal strength in the high field regions (the cause of the decrease is explained in Chapter 2, section 2.3, subsection 2.3.11). The data were then normalized.

The normalized data gave normalized representations of the x and y moments. As a result of the high demagnetization factor for out-of-plane magnetization, the normalized x

[l] As in page notes [j] and [k] above, with help from my supervisor.

and y moments could be combined to give a normalized saturation magnetization without need of consideration for the z component of magnetization (which would have been negligibly small because of high shape anisotropy caused by the high out-of-plane demagnetizing factor). The normalized x and y moments should then combine to give $\sqrt{m_X^2 + m_Y^2} \sim 1$ if the magnetization was in fact saturated. A plot of the data for complete rotations of the magnet could then be checked for adherence to the relation. The data were prepared as described and then plotted. The results are shown in figure 6.3.5 and confirm that a value adequately near 1 was obtained throughout full rotations of the magnet thus confirming saturation at all times during rotating hysteresis loops.

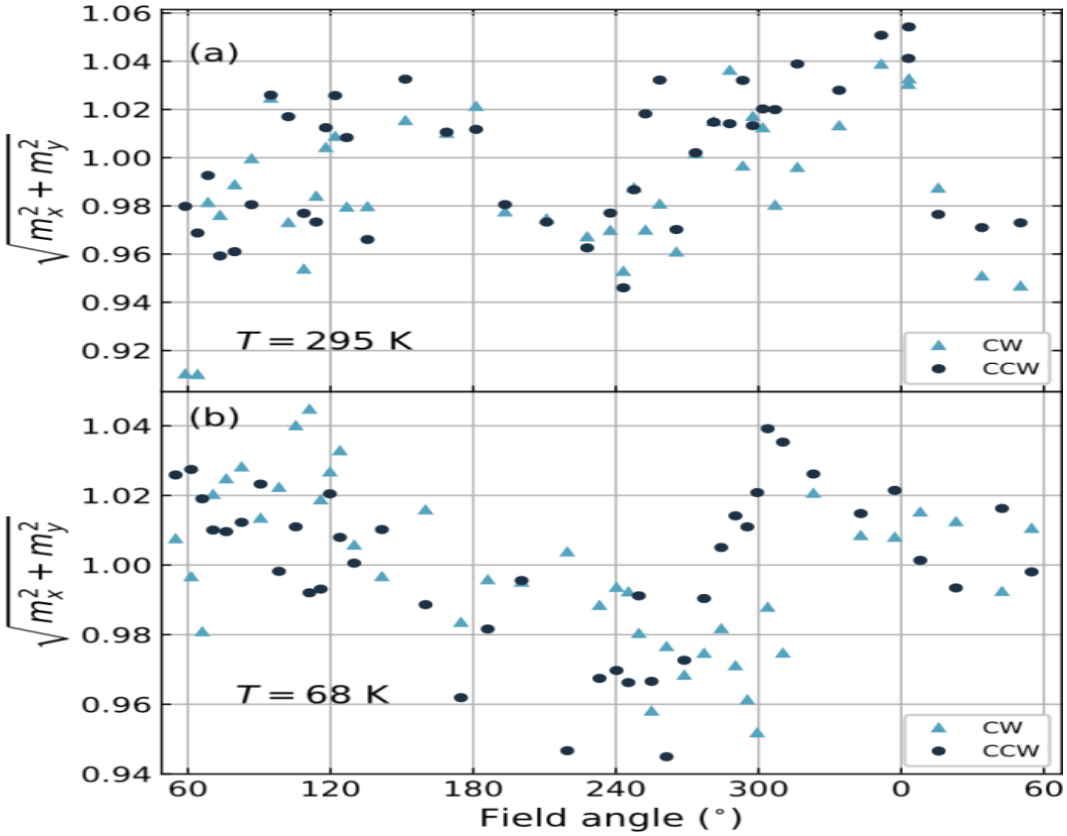

Figure 6.3.5. Confirmation of saturation. Data from sample S2A1A5. Top panel, (a), data from 11 and 12 Dec, 2020, at 295° K. Bottom panel, (b), data from 19 and 20 Nov, 2020, at 68° K. Reduction and plot by my supervisor, Dr. Mark Freeman.

v) Rotating hysteresis loops. The reduced data from rotating hysteresis loops are shown in figure 6.3.6. The ambient temperature data were collected on 11 and 12, Dec, 2020. The field-cooled data were collected on 19 and 20 Nov, 2020. The cooling-field strength was 95.8 kA/m and the cooling-field angle at the sample was 59.7°. Training effects in the field-cooled data were reduced by performing five rotating hysteresis loops before collecting the data.

The raw data from the x and y mode torque signals (in-plane) were reduced to normalized magnetizations using the same method as described in para (iv) above (i.e. the data were corrected for the slopes in the high field regions and were then normalized).

The ambient temperature data are shown in panel (a) of figure 6.3.6. The important feature is that the x and y components of the magnetization show no indications of hysteretic effects. The magnetizations during the clockwise field rotation were the same as during the counterclockwise rotation. The absence of hysteresis implies an absence of anisotropy so that the total magnetization was free to rotate with the applied field. The behaviour was that of permalloy alone. The results are consistent with data from the ambient temperature linear hysteresis loops which also showed an absence of hysteresis.

Panel (b) of figure 6.3.6 shows the field-cooled data. Note the substantial hysteresis in both components of the magnetization. Field-cooling induced an interaction between the permalloy and cobalt oxide layers. The hysteresis is due to anisotropy and interfacial coupling that was not present at ambient temperature. Refer to the anisotropy energy density equation in subsection 6.3.2, para (i). The contributions to the equation are from anisotropy and coupling terms. The anisotropy and coupling constants were determined from simulation which is discussed later in subsection 6.3.3, para (vii).

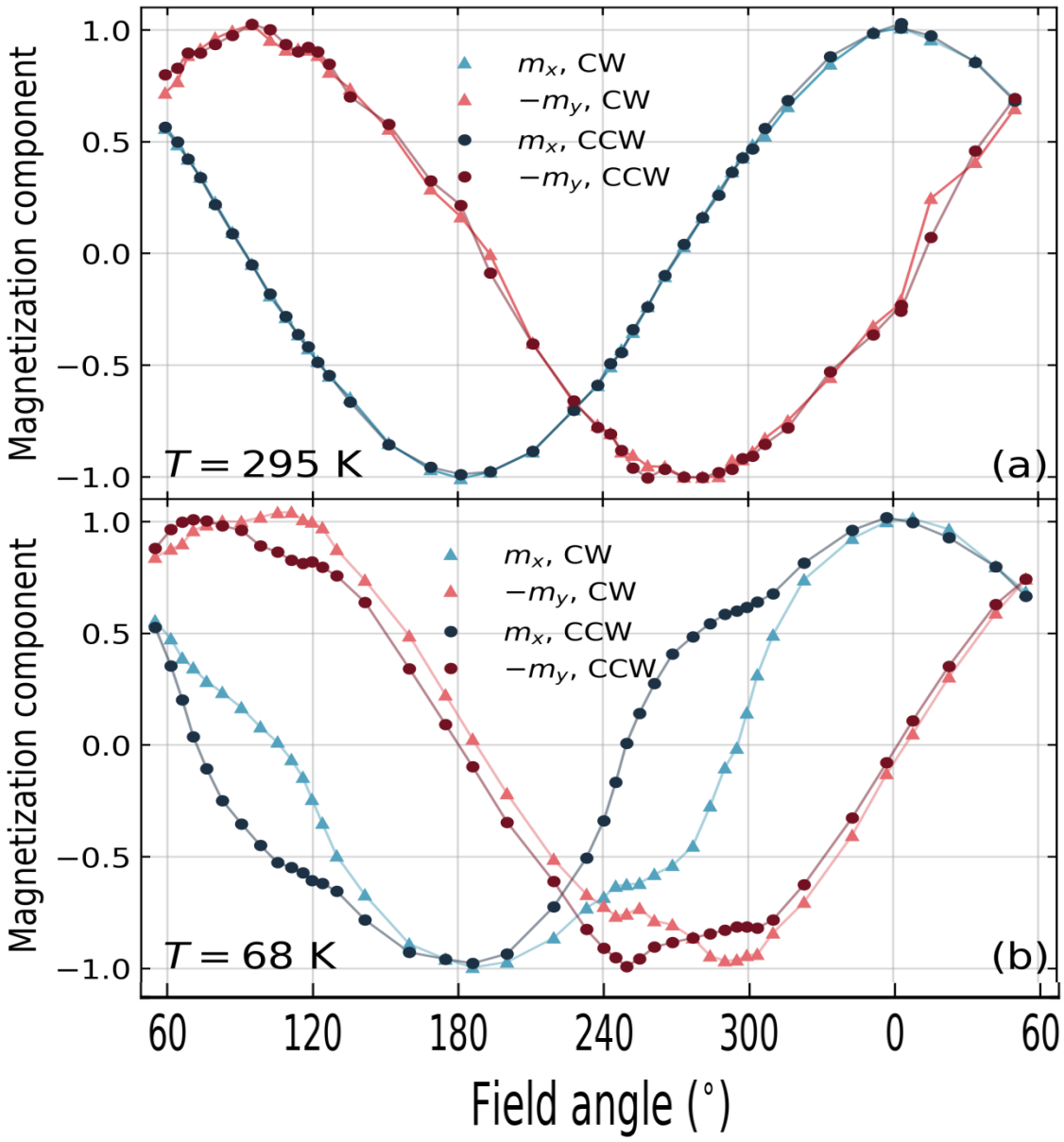

Figure 6.3.6. Normalized x and y magnetization components. Panel (a) shows the components at ambient temperature. Hysteresis is not present since there is little to no anisotropy. The behaviour is that of permalloy alone. The field-cooled data are shown in panel (b). The substantial hysteresis is due to anisotropy and interfacial coupling between the permalloy and cobalt oxide layers that was induced by field-cooling. The plot was generated by Michael Dunsmore.

vi) Out-of-plane torque. The field-cooled data that were obtained from sample S2A1A5 on 18 Nov, 2020, were calibrated using the method described in Chapter 2, section 2.4, Thermomechanical calibration, subsections 2.4.5 to 2.4.7, with further description provided in section S3 of the supplement to our paper that was published in AIP Advances in March of 2022.[1] The calibration procedure produced sensitivity factors for the z mode (out-of-plane) torque signal of 11.1 +/- 0.06 aNm/mV of signal at 295° K and 6.4 +/- 0.4 aNm/mV of signal at 69° K. The calibration program and results were generated by Michael Dunsmore.

The calibrated z mode torque from the field-cooled rotating hysteresis loop is shown in figure 6.3.7 along with the z mode torque obtained at ambient temperature. The ambient temperature data were collected on 12 Dec, 2020. The inset shows the increase of the z mode torque signal, normalized to the value at ambient temperature, as the temperature was decreased. The field angle was fixed for the data in the inset.

The relevant features in figure 6.3.7 are the hysteretic behaviour that results from the anisotropy and interfacial coupling that were induced by field-cooling and the substantial increase of the torque as compared to the torque at ambient temperature. The results are consistent with our other data and provide additional support for the premise that hysteresis in the field-cooled data is the result of effects not present at ambient temperature.

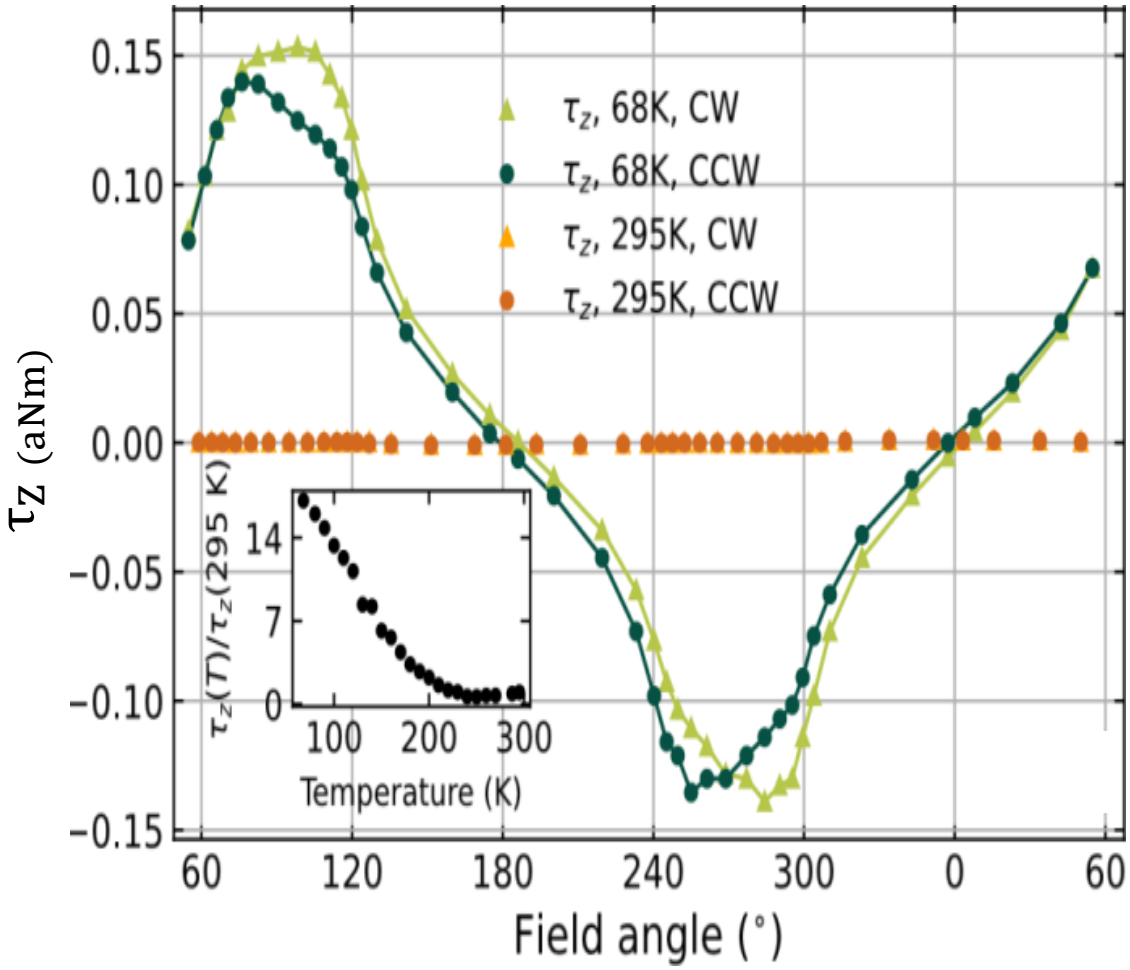

Figure 6.3.7. z mode torque (out-of-plane). Sample S2A1A5. Rotating hysteresis loops at ambient and cryogenic temperatures. The field-cooled loop shows hysteresis consistent with effects due to anisotropy and interfacial coupling induced by field-cooling. The torque at ambient temperature is near zero throughout the rotating hysteresis loop indicating that the effects present at cryogenic temperature are absent at ambient temperature. The plot was generated by Michael Dunsmore.

vii) Simulations.

A) Energy densities.

The terms in the phenomenological energy equation are presented again here for quick reference. Full descriptions of the terms are given in Chapter 2, section 2.1, subsection 2.1.6. The energy densities are,

anisotropy, ε_A,

$$\begin{aligned}\varepsilon_{\mathrm{A}} = & -\mathrm{K_{SF}}\sin^2(\theta)\cos^2(\Phi-\Phi_{\mathrm{SF}}) - \mathrm{K_{EB}}\sin(\theta)\cos(\Phi-\Phi_{\mathrm{EB}}) \\ & - \mathrm{K_{Rot}}\cos(\Delta\Phi_{\mathrm{Rot}} - \Delta\Phi_{\mathrm{m}}),\end{aligned} \tag{2-1}$$

demagnetization, ε_D,

$$\varepsilon_{\mathrm{D}} = \frac{1}{2}\mu_0 \mathrm{M_S^2}\left[\mathrm{N_x}\cos^2(\Phi)\sin^2(\theta) + \mathrm{N_y}\sin^2(\Phi)\sin^2(\theta) + \mathrm{N_z}\cos^2(\theta)\right], \tag{2-2}$$

and Zeeman, ε_Z,

$$\varepsilon_{\mathrm{Z}} = -\mu_{\mathrm{o}}\vec{\mathrm{m}}_{\mathrm{FM}} \cdot \vec{\mathrm{H}}_{\mathrm{ext}}^{\mathrm{DC}} = -\mu_{\mathrm{o}}\mathrm{m_{FM}}\mathrm{H}_{\mathrm{ext}}^{\mathrm{DC}}\cos(\Phi_{\mathrm{DC}} - \Phi_{\mathrm{m}}), \tag{2-3}$$

giving a total energy density, ε_T, of,

$$\varepsilon_T = \varepsilon_A + \varepsilon_D + \varepsilon_Z. \tag{2-4}$$

B) Landau-Lifshitz-Gilbert (LLG) equation.

The anisotropy constants in the phenomenological energy equation were estimated by fitting simulated data to the data obtained from rotating hysteresis loops. The simulated data were generated from macrospin solutions to the LLG equation.

The magnetization of the sample was saturated at all times during rotating hysteresis loops and was thus describable as a single macrospin. Confirmation of saturation was presented in subsection 6.3.3, para (iv). A single macrospin does not require analysis by way of micromagnetic simulation, but, instead, can be analyzed by solving the Landau-Lifshitz-Gilbert (LLG) equation in a suitably prepared, iterative computation, algorithm that provides solutions to a pair of coupled differential equations.

Michael Dunsmore prepared a suitable simulation program. Inputs to the program were test values for the anisotropy constants and axis orientations. The fixed inputs were the saturation magnetization (determined as described in subsection 6.3.3, para (ii), the demagnetization factors (determined by Michael Dunsmore using the forms given by Joseph[286]), and the strengths and orientations of the externally applied DC and AC fields. Simulated data generated by the program were compared to the observed data. Best fits to the data were obtained by suitable refinement of the anisotropy constants and angles.

The form of the LLG equation that was used is,

$$\frac{d\vec{M}}{dt} = -\gamma\vec{M} \times \vec{B}_{eff} + \frac{\alpha}{M_S}\vec{M} \times \frac{d\vec{M}}{dt}, \qquad (6\text{-}1)$$

where $\vec{M}$ is the magnetization, γ is the gyromagnetic ratio (e/m_e for a spin moment), $\vec{B}_{eff}$ is the effective field, α is the Gilbert damping constant, and M_S is the saturation

magnetization. The first term describes precession of the magnetization and the second term introduces damping to the precession thus causing the magnetization to eventually align with the externally applied field.

In a spherical coordinate system, the saturation magnetism is $M_r = M_S$. The effective field, $\vec{B}_{eff}$, can be written as a functional derivative of energy with respect to field giving $\vec{B}_{eff} = \partial\varepsilon_T / \partial\vec{M}$.[333 and [m]]. The LLQ equation can then be written as a pair of coupled differential equations,

$$\frac{d\theta}{dt} = -\frac{\gamma}{\mu_0 M_S(1+\alpha^2)}\left(\frac{1}{\sin(\theta)}\frac{\partial\varepsilon_T}{\partial\Phi} + \alpha\frac{\partial\varepsilon_T}{\partial\theta}\right), \qquad (6\text{-}2)$$

$$\frac{d\Phi}{dt} = \frac{\gamma}{\mu_0 M_S(1+\alpha^2)}\left(\frac{1}{\sin(\theta)}\frac{\partial\varepsilon_T}{\partial\theta} - \frac{\alpha}{\sin^2(\theta)}\frac{\partial\varepsilon_T}{\partial\Phi}\right), \qquad (6\text{-}3)$$

where θ and Φ are the polar and azimuthal angles, respectively, in a standard spherical coordinate system. M_S is the saturation magnetism, γ is the gyromagnetic ratio (e/m_e for a spin moment), α is the Gilbert damping constant and ε_T is the total energy density given by equation (2-4).

Test values for the anisotropy constants and angles, fixed values for the demagnetization factors, the experimentally determined value of M_S, the measured values for the externally applied DC and AC fields and a test value for the damping constant, α, were input parameters to the simulation program. The program used these parameters to form and then differentiate the phenomenological energy equation to obtain the derivatives $\partial\varepsilon_T/\partial\theta$ and $\partial\varepsilon_T/\partial\Phi$.

[m] From notes prepared by my supervisor and also obtainable from Coey, page 56, (ref 333).

The damping term of the LLG equation will dominate over the precession term given sufficient time. The minimum precession frequency was approximately 620 MHz for the minimum applied DC bias field of approximately 17.7 kA/m. The maximum frequency of the applied AC field was approximately 4.2 MHz (much lower than the minimum precession frequency) meaning that damping would have been effectively complete before the AC dither could have caused any appreciable change to the magnetization.

By way of iterative computation and comparison, the simulation program provided solutions for equations (6-2) and (6-3) from which the steady state values of the magnetization directions, θ and Φ, were extracted. The value of the damping constant, α, was 0.001, but a range of values from 0.1 to 1 x 10^{-4} were tested and were found to have negligible affect on the results.

Refer back to the field and orientation diagram in figure 6.3.1. The AC dither fields, H^{AC}, cause a small perturbation to the magnetization, m_{FM}, and its direction, Φ_M, thus generating the term $\Delta\Phi_M$ in equation (2-1) for the anisotropy energy density, ε_A. The effect of the dither field was introduced by obtaining individual solutions with the dither field at zero, maximum, and minimum. For each of these solutions, the torque was calculated using $\vec{\tau} = \mu_o \vec{m} \times \vec{H}_{ext}^{DC}$. The AC torque was then extracted from the slope of the torque vs. field curve.

Solutions were required for each field angle that was used to obtain the rotating hysteresis loops. The program generated simulated magnetization and torque data for comparison and fitting to the recorded data.[n]

[n] The simulation algorithm was devised by Michael Dunsmore. Michael prepared the program, ran the simulations, and produced the fits to the recorded data.

viii) Simulation results.

A) Magnetizations.

Figure 6.3.8, panel (a) is a plot of the x and y components of magnetization obtained from simulation of a rotating hysteresis loop at ambient temperature. At ambient temperature only shape anisotropy would have contributed to the anisotropy energy, so the other anisotropy constants were set to zero. The simulated data show no hysteresis and thus compare well with the recorded data in figure 6.3.6, panel (a).

Simulated data for a field-cooled rotating hysteresis loop were obtained by including unidirectional, uniaxial, and rotatable anisotropies in the anisotropy energy equation. The results are shown in figure 6.3.8, panel (b). The hysteresis in the simulated data compares reasonably well with the hysteresis in the recorded data shown in figure 6.3.6, panel (b).

B) Out-of-plane torque.

Comparison of the simulated and recorded magnetization components showed that the simulation program performed adequately in reproducing the recorded data at both ambient and cryogenic temperatures. With confidence that the program was providing correct results, fits to the field-cooled z mode torque (out-of-plane) were obtained by suitable refinement of the anisotropy constants and angles. The recorded data and results of the fit are shown in figure 6.3.8, panel (c).

The anisotropy constants and angles for the fit were K_{EB} = 0.1 +/- 0.05 kJ/m^3 at an angle of Φ_{EB} = 55 +/- 3° for the unidirectional anisotropy, K_{ROT} = 22 +/- 1 kJ/m^3 at an angle of $\Delta\Phi_{ROT}$ = -5 +/- 3° for the rotatable anisotropy, and K_{SF} = 8.3 +/- 0.3 kJ/m^3 at an angle of Φ_{SF} = -91 +/- 2° for the uniaxial spin-flop coupling term.[o]

[o] Michael Dunsmore obtained the anisotropy constants and angles from his simulation program.

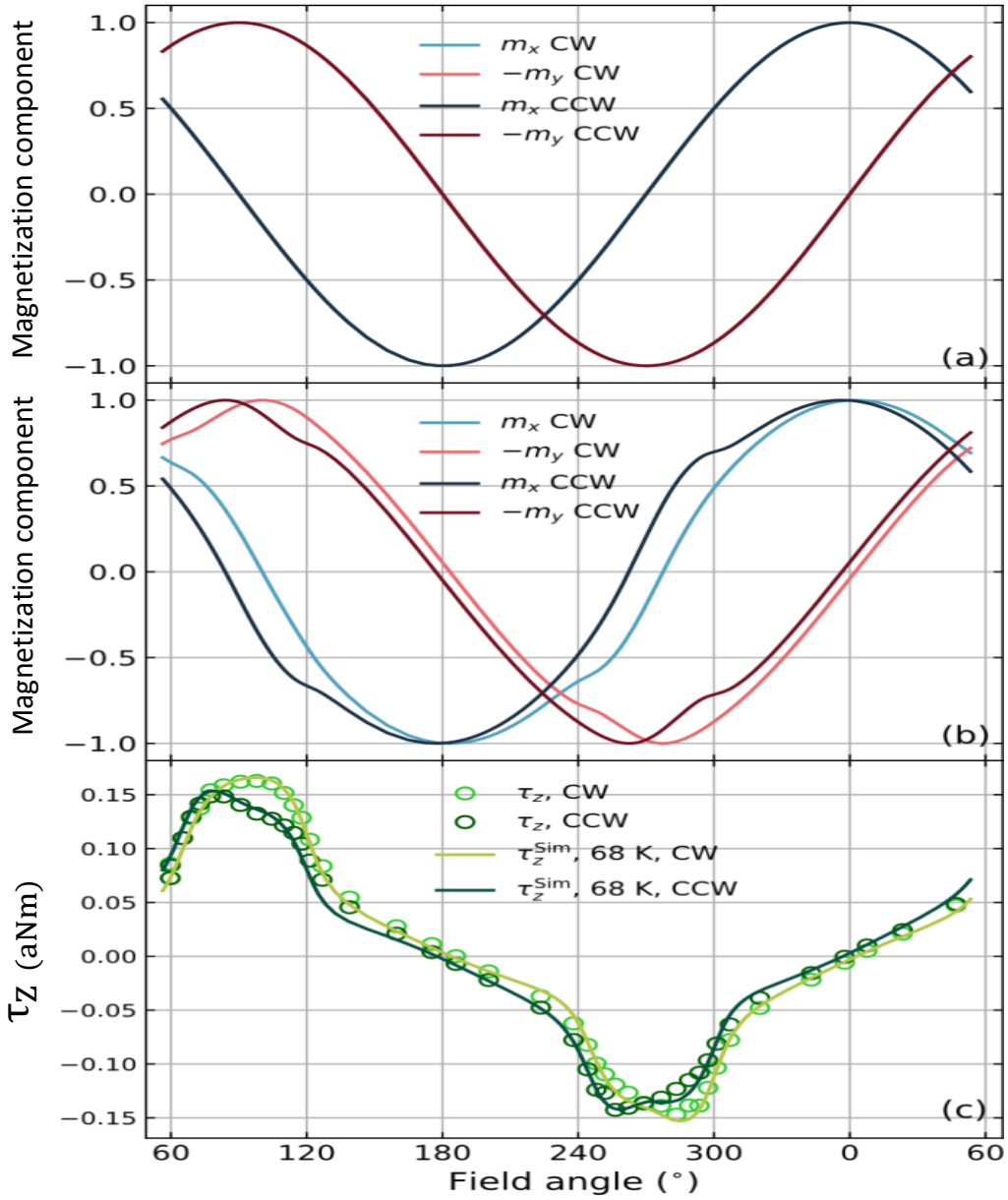

Figure 6.3.8. Rotating hysteresis loops. Panel (a) shows the simulated x and y components of the magnetization at ambient temperature where only shape anisotropy is present. Panel (b) shows the components for field-cooled data where unidirectional, uniaxial, and rotatable anisotropies are active. Compare to figure 6.3.6, panels (a) and (b). Panel (c) shows the recorded and simulated z mode torque (out-of-plane) after field- cooling. The simulated data and plots were generated by Michael Dunsmore.

C) Training effect.

The training effect refers to the progressive reduction in unidirectional anisotropy that occurs in successive field-cooled linear hysteresis loops. A comparison was made of the z mode torque (out-of-plane) from a rotating hysteresis loop obtained immediately after field-cooling (i.e. first loop) to one that was obtained after many loops (eighth loop). The comparison was made by plotting the differences in torque between the first and trained loops. The sample was S2A1A5. The trained (eighth) loop is from data collected on 18 Nov, 2020. Data for the first loop after field-cooling was collected on 13 Dec, 2020.

Figure 6.3.9, panel (a) shows the comparison results obtained from the recorded data. Note that the plot does not show a torque curve, but, instead, shows the difference in torque curves obtained by subtraction of the trained (eighth) loop from the first loop. The plot begins on the left side with the counterclockwise field rotation starting at a field angle of 0° (dark green dots and dark green arrow). The difference is small up to a field angle of approximately 45°, increases rapidly (the magnitude of the difference increases) until the field angle is approximately 75°, and then decreases until the field angle is approximately 110° after which the difference is again small and continues to be so for the rest of the counterclockwise rotation to a field angle of 360°. The difference remained small during the entire clockwise field rotation back to a field angle of 0° (light green dots and light green arrow). The results indicate that substantial training occurred during the first half of the counterclockwise rotation and that training thereafter was negligible (the training occurred during the first 1/4 of the loop).

Figure 6.3.9, panel (b) shows the simulated comparison. The trend from 0° to 180° of the counterclockwise field rotation (solid dark green trace) was obtained with K_{EB} = 1.00 +/- 0.05 kJ/m^3 at an angle of Φ_{EB} = 0° for the unidirectional anisotropy, K_{ROT} = 22.5 +/- 0.3 kJ/m^3 at an angle of $\Delta\Phi_{ROT}$ = -3 +/- 2° for the rotatable anisotropy, and K_{SF} = 7.2 +/- 0.1 kJ/m^3 at an angle of Φ_{SF} = -91 +/- 2° for the uniaxial spin-flop coupling term.

The simulated data captured the trend in the recorded data from 0° to 180° of the counterclockwise field rotation fairly well, but produced other trends from 180° to 360° of the counterclockwise field rotation (dashed dark green trace) that do not appear in the recorded data. This does not indicate failure of the simulation to correctly reproduce the recorded data since the algorithm for the simulation did not include a means for automatically adjusting the input parameters to somehow account for training.

The poor match of the simulated data from 180° to 360° of the counterclockwise field rotation to the recorded data indicate that there must have been some change to one or more of the anisotropy constants during the first part of the rotation from 0° to 180°. To show this, the clockwise field rotation (light green dots and light green arrow) was simulated using different anisotropy constants. K_{EB} was changed from 1.00 +/- 0.05 to 0.45 +/- 0.05 kJ/m^3 with no change to Φ_{EB}, K_{ROT} was kept at 22.5 +/- 0.3 kJ/m^3, but with a change of angle from $\Delta\Phi_{ROT}$ = -3 +/- 2° to +3 +/- 2°, and K_{SF} was changed from 7.2 +/- 0.1 to 7.3 +/ 0.1 kJ/m^3 with no change to Φ_{SF}. The simulation was run for the clockwise rotation with the adjusted parameters and then plotted. The simulated results compared well with the recorded data for the clockwise rotation thus confirming that the anisotropy constants had changed during the first 180° of the counterclockwise field rotation.

If there had been no change to the anisotropy constants then the features in the dashed portion of the simulated data would have appeared in the recorded data. Specifically, it was the reduction in the unidirectional anisotropy constant, K_{EB}, that was responsible for the absence in the recorded data of the features in the simulated data from 180° to 360° of the counterclockwise field rotation. Jenkins discusses metastable states and athermal training as mechanisms responsible for the reduction in K_{EB}.[321]

The simulation showed that training in rotating hysteresis loops occurs early in the first part of the field rotation and before reversal of the magnetization. Training in linear hysteresis loops is observed as a decrease in the shift of one or both of the coercive field

points which occurs during the first magnetization reversal for one coercive field point and during the second magnetization reversal for the second coercive field point. It would seem, then, that linear hysteresis loops do not provide as much information regarding training effects as do rotating hysteresis loops. Linear hysteresis loops mask the early training effects that occur prior to magnetization reversal.

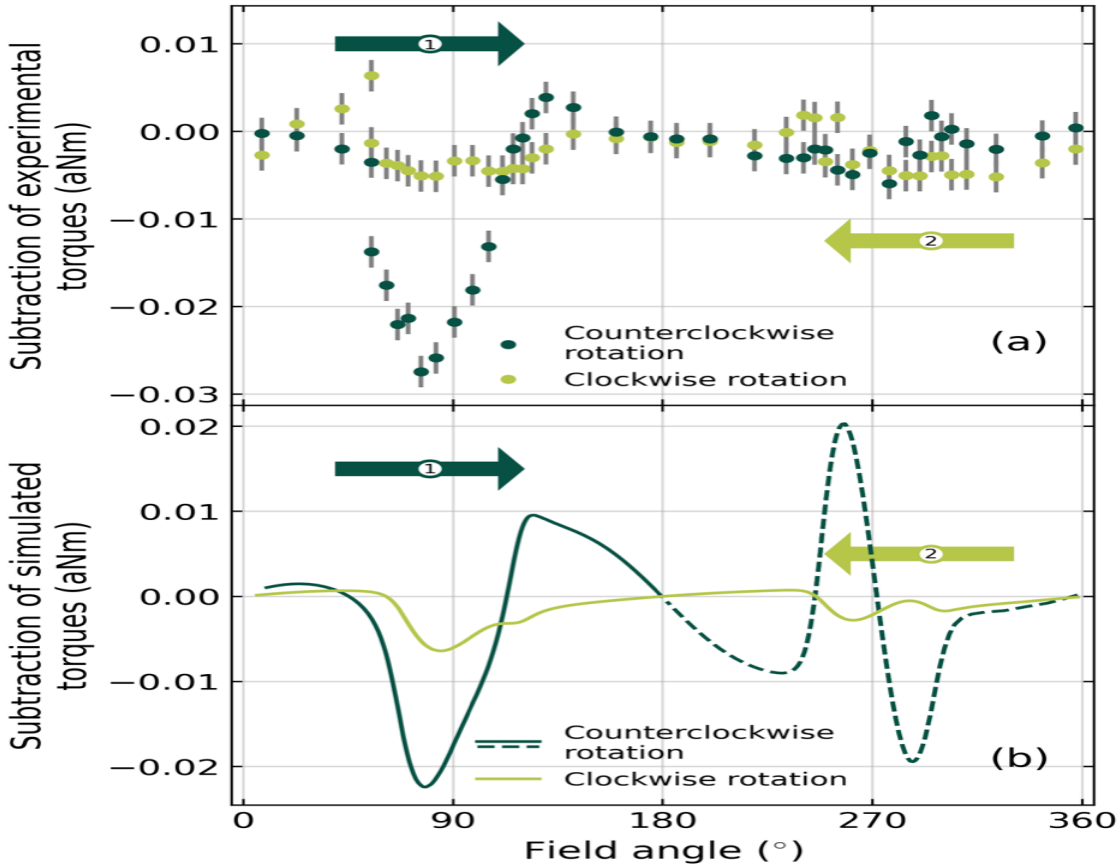

Figure 6.3.9. Training effects in field-cooled rotating hysteresis loops. Sample S2A1A5. Comparison of z mode torque (out-of-plane) obtained from the first loop after field-cooling to the eighth loop after field-cooling. Panel (a) shows the difference between the recorded first and trained loops. Panel (b) shows the simulated results. The dashed portion of the simulation does not appear in the recorded data because the unidirectional anisotropy decreased during the first part of the counterclockwise field rotation from 0° to 180°. The simulations and plots were generated by Michael Dunsmore.

D) Effects of changes to anisotropy constants.

The effects of changes to the anisotropy constants and angles on the simulated data are shown in figures 6.3.10 and 6.3.11. The simulation program was used to generate fits to the recorded data for the z mode torque (out-of-plane). The fits are shown in figures 6.3.7 to 6.3.9.

The anisotropy constants and angles were fitting parameters for the simulation program. Best fits to the data were obtained only after running the simulation program many times while adjusting the fitting parameters between iterations.

The effects of parameter variation on the simulation results were plotted. The program was run with a range of values for a selected fitting parameter while the other parameters were held constant. Changes in the angle between the rotatable anisotropy axis and the magnetization, $\Delta\Phi_{ROT}$, were found to have little effect on the simulation results when the angle was near its best fit value of -5°, so $\Delta\Phi_{ROT}$ was held constant at -5° for all of the parameter tests and a plot of its effect was not generated.[p] The shapes and locations of the peaks and zero crossings were the primary fitting tasks. The plots in figures 6.3.10 to 6.3.11 show how each of the parameters affected the peak locations and zero crossings of the torque curve.

The values of the fitting parameters that were used to generate the final fits to the z mode torque were given in para (viii), subpara (B), above and are given here again for quick reference. The anisotropy constants and angles for the best fit were K_{EB} = 0.1 +/- 0.05 kJ/m^3 at an angle of Φ_{EB} = 55 +/- 3° for the unidirectional anisotropy, K_{ROT} = 22 +/- 1 kJ/m^3 at an angle of $\Delta\Phi_{ROT}$ = -5 +/- 3° for the rotatable anisotropy, and K_{SF} = 8.3 +/- 0.3 kJ/m^3 at an angle of Φ_{SF} = -91 +/- 2° for the uniaxial spin-flop coupling term.

[p] Michael Dunsmore ran the parameter effect tests. He confirmed, on 20 June, 2022, that he had checked the effect of changes in $\Delta\Phi_{ROT}$ and further confirmed that they were negligible.

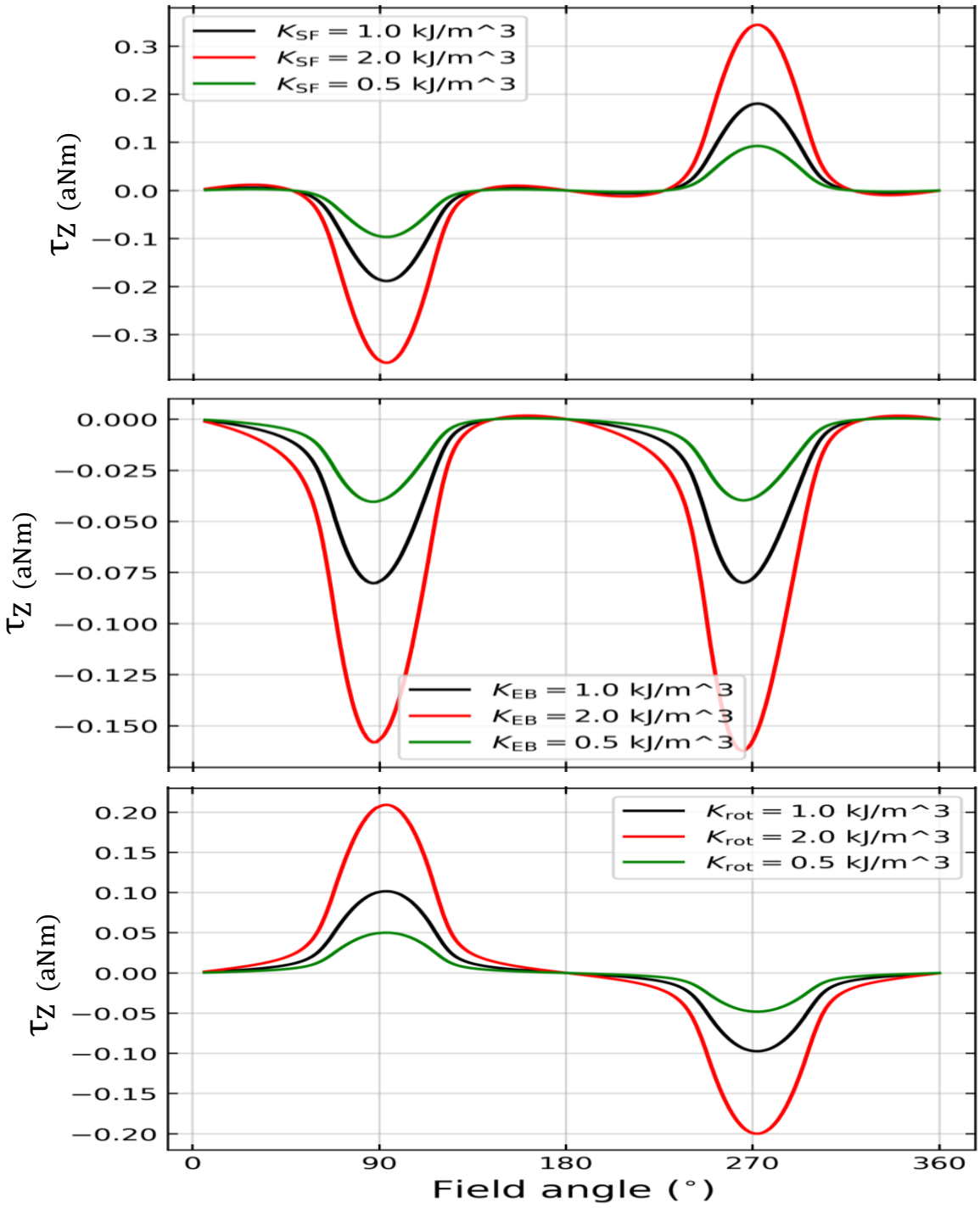

Figure 6.3.10. Effects of K_{EB}, K_{SF}, and K_{ROT} on simulation results for the z mode torque. Data and plots generated by Michael Dunsmore.

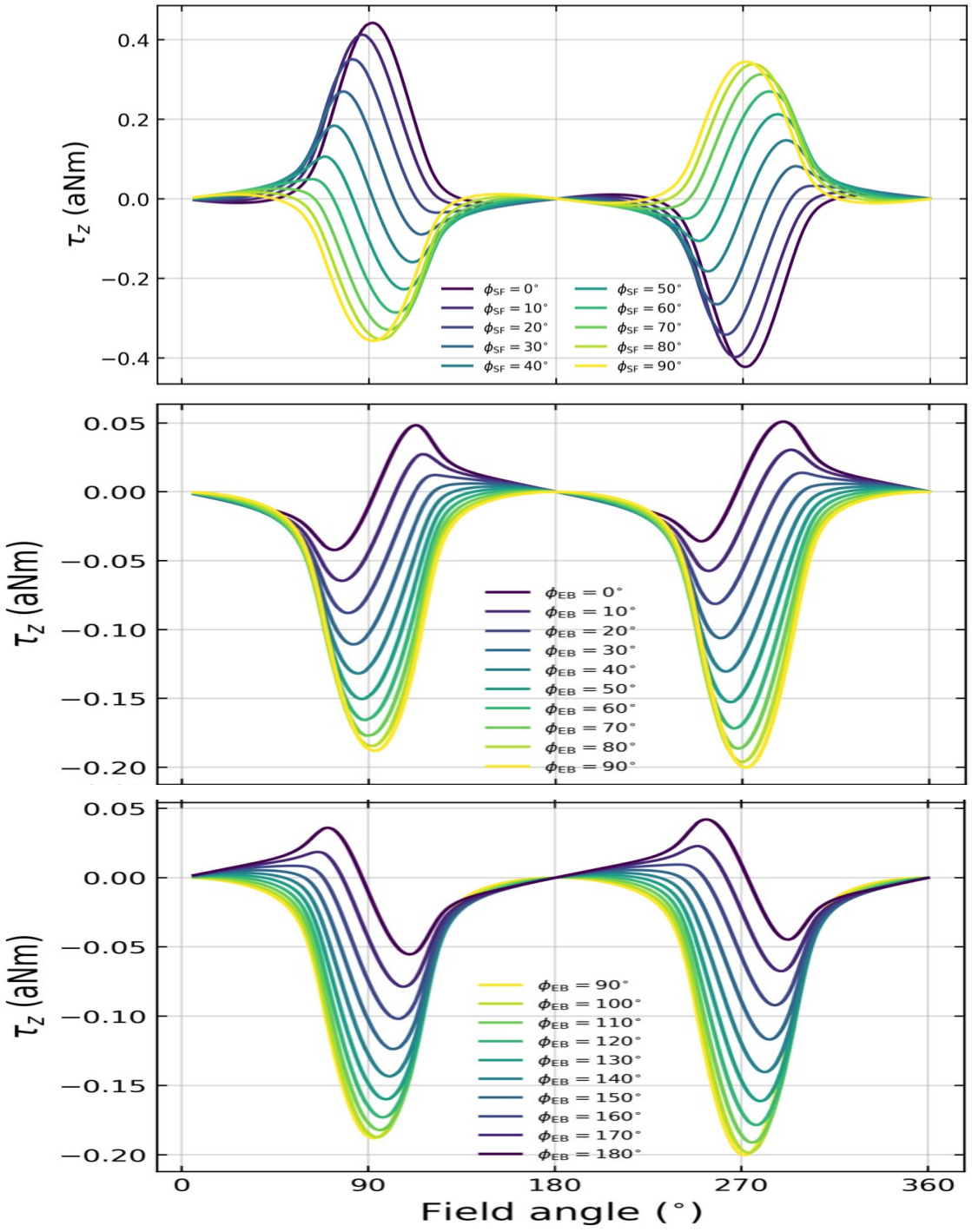

Figure 6.3.11. Effects of Φ_{SF} and Φ_{EB} on simulation results for the z mode torque. Data and plots generated by Michael Dunsmore.

6.4) Discussion.

A) Linear hysteresis loops.

Linear hysteresis loops obtained at ambient temperature confirmed that the behaviour of the thin-film, bilayer, samples was attributable to the ferromagnetic permalloy layer alone with no influence from the antiferromagnetic cobalt oxide layer. The confirmation was arrived at by noting the zero to very low hysteresis and the low field vortex nucleations and annihilations. The features observed in the bilayer samples were compared to those observed in single-layer samples of permalloy that were studied previously by our group. The ambient temperature linear hysteresis loops obtained from the bilayer, exchange bias, sample were essentially the same as those obtained from a single-layer sample of permalloy. This work provided a reliable starting point from which to begin a study of exchange bias and interfacial coupling effects in the bilayer sample.

Field-cooled linear hysteresis loops showed a shift of the coercive field points consistent with the shift observed originally by Meiklejohn and Bean in 1956.[2] The explanation for the shift was given as the introduction of a unidirectional anisotropy upon cooling the sample, in a saturating DC bias field, from a temperature above to below the Néel temperature of the antiferromagnetic layer. The findings from the field-cooled linear hysteresis loops obtained from our bilayer sample were much the same as those reported by Meiklejohn and Bean (and many, many, times afterward by others) so that it was reasonable to conclude that the cause of the shifts observed in our linear hysteresis loops could also be attributed to introduction of a unidirectional anisotropy upon field-cooling.

The data from the high field regions of linear hysteresis loops were used to obtain values of the saturation magnetization at ambient and cryogenic temperatures. The low field data where vortex nucleation and annihilation occurs at ambient temperature was used to obtain an estimate of the effective thickness of the ferromagnetic permalloy layer.

B) Increase of z mode torque.

The z mode torque (out-of-plane) was measured as the temperature was lowered from ambient to 68° K in increments of 10° K while the sample was exposed to a saturating DC bias field. The data showed that the z mode torque increased from a level near the noise floor of the lock-in amplifier to an increasingly higher level as the temperature was lowered. In the absence of in-plane anisotropy, the z mode torque should be zero. Increase of the torque with a decrease in temperature could have occurred only if the effect of lowering the temperature was to cause formation of an anisotropy axis (or axes) that increased in strength as the temperature was lowered further. The data also gave an estimate of the blocking temperature (a temperature, below the Néel temperature, at which the effects of exchange bias are first observable). The increase of torque with a decrease in temperature and the existence of a blocking temperature provided additional confirmation that anisotropies not present at ambient temperature were induced by field-cooling.

C) Rotating hysteresis loops.

To obtain values of anisotropy constants and angles, the data from rotating hysteresis loops were analyzed using a phenomenological energy equation and macrospin solutions to the LLG equation. A prerequisite for the technique was confirmation that the magnetization in the sample was at all times saturated so that a macrospin description of the magnetization could be justified. Confirmation of saturation was determined by examining the x and y (in-plane) components of the magnetization which showed that the magnetization was saturated throughout the full 360° rotations of the DC bias field.

Data from rotating hysteresis loops obtained at ambient temperature showed no hysteresis while the field-cooled rotating loops showed substantial hysteresis. Simulated data obtained from the macrospin solutions showed the same features as the recorded

data. The ambient temperature data were simulated by including only shape anisotropy. The field-cooled data were simulated by introduction of additional terms to account for uniaxial, unidirectional, and rotatable anisotropies. Simulation of the field-cooled data required all of the anisotropy terms to adequately reproduce the recorded data. This means that the features in the field-cooled data could not have been due to a unidirectional exchange bias alone.

D) Training effects.

Comparison of the first rotating hysteresis loop obtained after field-cooling to one obtained after many loops (the eighth loop) showed surprising results that, to our knowledge, have not been reported in the existing literature. Substantial training occurred during the first half of the first field rotation meaning that the shift in linear hysteresis loops does not expose the training, and evolution thereof, that occurs before the first magnetization rotation. This means that there is an opportunity to expand the knowledge regarding the cause(s) of training effects by focusing attention on rotating rather than linear hysteresis loops.

An additional result obtained from comparison of first and trained field-cooled rotating loops, not reported previously herein, was that the values obtained for the unidirectional anisotropy, K_{EB}, before and after training of the rotating loops, were insufficient to account for the entire shift observed in field-cooled linear loops and, thus, the shift in field-cooled linear loops cannot be due to unidirectional anisotropy alone. Also, features in the field-cooled rotating hysteresis loops persisted even after the unidirectional anisotropy had been substantially reduced by training meaning that other interfacial coupling effects were the primary contributors to the features observed in the field-cooled rotating hysteresis loops.

Chapter 7

Conclusions and Future Work.

7.1) Conclusions.

The purpose of the experiment was to investigate exchange bias and interfacial coupling effects in a nanoscale, thin-film, bilayer deposit of permalloy (ferromagnetic) and cobalt oxide (antiferromagnetic). The measurement method was AC torque magnetometry. Resonator samples with deposits of permalloy and cobalt oxide on the resonator paddles were fabricated at the NanoFAB facility located on the University of Alberta main campus.

Investigations began by collecting data from linear hysteresis loops at ambient temperature. The results were compared to those previously obtained from samples that had only a single layer of permalloy. The question being asked was whether or not the bilayer sample had the same behaviour as the single layer sample (permalloy only). If it did, then one could argue that, at ambient temperature, the layer of antiferromagnetic cobalt oxide on the bilayer sample had no effect on sample behaviour. The results of the comparison were that the bilayer sample behaved just as did the sample having only a single layer of permalloy thus confirming that, at ambient temperature, there was no influence from the cobalt oxide layer on the bilayer sample. The cobalt oxide did not introduce any measurable anisotropy, it did not interfere with vortex nucleation and

annihilation, and it did not alter the shape of linear hysteresis loops. With these results, one could continue the investigation by recording the behaviour of the bilayer sample at cryogenic temperature with the knowledge that any change in behaviour would be attributable to temperature related effects.

Linear hysteresis loops were collected after cooling the sample in a DC bias field of sufficient strength to saturate the magnetization. Field-cooling from above to below the Néel temperature of the cobalt oxide should have caused a unidirectional anisotropy axis to form at the interface between the two layers (this is what Meiklejohn and Bean found in 1956,[2] an effect now referred to as exchange bias). Formation of such an axis would cause a linear hysteresis loop to widen and to show a shift of coercive field points as compared to a hysteresis loop obtained at ambient temperature. Our recorded data showed both of these effects. There was no reason to suppose that the cause was any different than what Meiklejohn and Bean proposed since it has been verified many, many, times since 1956. We felt confident that the response of our samples after field-cooling was the result of a unidirectional anisotropy (an exchange bias) combined with, possibly, additional effects due to other interfacial coupling mechanisms.

An additional test to confirm that field-cooling induced an interaction between the permalloy and cobalt oxide layers was conducted. The test was designed to expose any increase in anisotropy that could be attributed directly to temperature induced effects. The z mode torque (out-of-plane) was the ideal candidate for such a test. The sample was exposed to a saturating DC bias field and the z mode torque was measured at temperatures from ambient to 68° K in successively decreasing temperature steps of 10°. The results showed that the torque increased as the temperature was lowered. This was the expected result and it helped to confirm that the sample behaviour was due to temperature induced coupling of the permalloy and cobalt oxide layers.

A value for the exchange bias energy per unit area of sample, σ_{ex}, was extracted from the shifts of linear hysteresis loops. A value of ~0.08 mJ/m^2 was found. The maximum value observed was 0.11 mJ/m^2. The obtained values fit within a range of values for various bilayer combinations given by Coey (0.05 to 0.33 mJ/m^2,[317] but the list did not include permalloy/cobalt oxide). Mitrofanov obtained 0.3 mJ/m^2 for a bilayer sample of permalloy/CoO,[11] but the samples tested were 6 mm x 2 mm (over one million times larger than ours). The point here is that the sample sizes were so different and the magnetization was being examined on such different scales that direct comparison may not be appropriate.

Data from an ambient temperature linear hysteresis loop was used to obtain the effective thickness of the ferromagnetic permalloy layer. The thickness as recorded after deposition was 20 nm, but the data showed that the thickness was 16.1 nm. The reduced thickness (an effective thickness) was less than the deposited thickness due, most likely, to oxidation of the top surface of the permalloy. The deposits were not capped and the samples were several years old by the time the experiment was conducted.

The saturation magnetization, M_S, was determined from linear hysteresis loops obtained at ambient and cryogenic temperature. At 295° K, M_S was found to be 763 +/-7 kA/m. At 68° K, M_S was found to be 801 +/-8 kA/m. Coey gives a value of 830 kA/m for bulk permalloy (presumably at ambient temperature). The results of a study of permalloy thin films by Ounadjela et al. show that M_S varies considerably with film thickness.[334] They report a value of approximately 760 kA/m for 20 nm thickness (presumably at ambient temperature). The values of M_S obtained in the experiment appear to be in reasonable agreement with other reported values given that thickness and composition are determining factors.

Chapter 7. Conclusions and Future Work.

Collection of rotating hysteresis loops at ambient and cryogenic temperatures was the next step. Part of the motivation for continuing in this direction came by way of a comment from Meiklejohn regarding his opinion that the information contained in rotating hysteresis loops is more fundamental to exchange bias than are the shifts observed in linear hysteresis loops.[6]

Data were collected from many rotating hysteresis loops at ambient and cryogenic temperatures. Fits to the data were obtained after first confirming that the magnetization was saturated at all times during the full 360° rotations of the DC bias field. Saturation was required since the proposed method of analysis was based on the premise that, when saturated, the magnetization can be treated as a single macrospin thus not requiring micromagnetic simulation.

Michael Dunsmore of our research group prepared a program that produced fits to the recorded data. The program provided solutions to the Landau-Lifshitz-Gilbert equation. The terms from a phenomenological energy equation were inputs to the program. The energy equation included anisotropy terms and angles to represent the orientations of the anisotropy axes. The fitting algorithm adequately reproduced the recorded data. The recorded data were calibrated in units of torque so that the fit parameters could be used to obtain values for the anisotropy constants and axes angles.

The anisotropy constants and angles for the fits that were obtained were K_{EB} = 0.1 +/- 0.05 kJ/m^3 at an angle of Φ_{EB} = 55 +/- 3° for the unidirectional anisotropy, K_{ROT} = 22 +/- 1 kJ/m^3 at an angle of $\Delta\Phi_{ROT}$ = -5 +/- 3° for the rotatable anisotropy, and K_{SF} = 8.3 +/- 0.3 kJ/m^3 at an angle of Φ_{SF} = -91 +/- 2° for the uniaxial spin-flop coupling term. The anisotropy terms are included in the phenomenological energy equation that was used. The form of the equation is similar to that used by others.[8, 9, 282]

It is difficult to determine if the obtained anisotropy values compare well with those reported elsewhere. The technique used (AC torque magnetometry) and the sample size differ considerably from other methods and sample sizes. The shift that was observed in linear hysteresis loops indicated a unidirectional anisotropy, K_{EB}, less than reported by Mitrofanov,[11] but comparison may not be justified. It is also possible that data from a wafer of samples prepared at one facility will not necessarily compare well with data from another wafer of samples prepared at another facility. Literature review did not provide an answer to this question.

Training effects were investigated by examining the difference between a rotating hysteresis loop obtained immediately after field-cooling and one that was the eighth loop after field-cooling. The results showed that substantial training occurred in the first half rotation of the DC bias field during the first half of the loop and that the rest of the loop showed little to no training. The parameter responsible for the observed training was the unidirectional anisotropy, K_{EB}. Specifically, the data showed that K_{EB} decreased from 1.00 +/- 0.05 to 0.45 +/- 0.05 kJ/m^3 during the first half of the first rotation of the field. Significant results were that unidirectional anisotropy was found to be insufficient to account for, by itself, the shifts observed in field-cooled linear hysteresis loops and that features in field-cooled rotating loops persisted even after the unidirectional anisotropy had been substantially reduced by training.

The highlights of the experiment were that 1) exchange bias and interfacial coupling effects were observed in nanoscale, thin-film, bilayer samples of permalloy and cobalt oxide, 2) solutions to a macrospin representation of the magnetic system provided fits that adequately reproduced the recorded data (micromagnetic simulations were not required), and 3) training effects observed in field-cooled rotating hysteresis loops indicated that unidirectional exchange bias was not sufficient to account for the total shift in field-cooled linear hysteresis loops.

7.2) Future work.

A modification to our apparatus to provide a constant DC bias field for rotating hysteresis loops would be beneficial. The rotating field in the current arrangement is not constant with angle.

It would be useful to determine if the interfacial effects observed in bilayer samples are affected as much by fabrication technique as by any other parameter. Sample specific behaviours make determination of anisotropy constants a difficult, if not impossible, task.

The spin arrangement at the interfaces of bilayer samples is often discussed.[8, 9, 12, 282, 284] Phenomenological energy equations do not adequately represent the spin system at a scale suitable for study of the spin arrangement. X-Ray studies provide useful data regarding spin arrangement.[3, 10, 16]

7.3) Closing comment.

I recall being a young soldier. Many (most) young soldiers, particularly at the Private and Corporal level, react quite negatively when, during exercise debriefs, the officers would always say that “the mission was a success” in spite of the fact that everyone knew that most everything went wrong. It was laughable. It took a long time for me to realize that all of the exercise missions were indeed a success. Did you get out to the field? Did you become more familiar with your weaponry and equipment? Did you increase your knowledge of how to fight and how to survive the elements? Well...I guess that I did. In this way, success was achieved each and every time.

My experiences as a grad student and as a researcher have been at least partly the same as those from when I was a young soldier. Did you get into the lab? Did you get your apparatus working correctly? Did you collect some useful data? Well...yes I did and I am glad and grateful for having been allowed to do so.

References

[1] M.G. Dunsmore, J.A. Thibault, K.R. Fast, V.T.K Sauer, J. E. Losby, Z. Diao, M. Belov, and M.R. Freeman, "Three-axis torque investigation of interfacial exchange coupling in a NiFe/CoO bilayer micromagnetic disk", AIP Advances, **12**, 035142 (2022).

[2] W. H. Meiklejohn and C. P. Bean, "New magnetic anisotropy", Physical Review, **105**, 904–913 (1957).

[3] F. Nolting, A. Scholl, J. Stöhr, J. W. Seo, J. Fompeyrine, H. Siegwart, J.-P. Locquet, S. Anders, J. Lüning, E. Fullerton, *et al.*, "Direct observation of the alignment of ferromagnetic spins by antiferromagnetic spins", Nature, **405**, 767–769 (2000).

[4] E. Jiménez, J. Camarero, J. Sort, J. Nogués, N. Mikuszeit, J. M. García-Martín, A. Hoffmann, B. Dieny, and R. Miranda, "Emergence of noncollinear anisotropies from interfacial magnetic frustration in exchange-bias systems", Physical Review B, **80**, 014415 (2009).

[5] E. Maniv, R. A. Murphy, S. C. Haley, S. Doyle, C. John, A. Maniv, S. K. Ramakrishna, Y.-L. Tang, P. Ercius, R. Ramesh, *et al.*, "Exchange bias due to coupling between coexisting antiferromagnetic and spin-glass orders", Nature Physics, **17**, 525–530 (2021).

[6] W. H. Meiklejohn, "Exchange anisotropy - a review", Journal of Applied Physics, **33**, 1328–1335 (1962).

[7] J. Burgess, A. Fraser, F. F. Sani, D. Vick, B. Hauer, J. Davis, and M. Freeman, "Quantitative magneto-mechanical detection and control of the Barkhausen effect", Science, **339**, 1051–1054 (2013).

[8] M. D. Stiles and R. D. McMichael, "Model for exchange bias in polycrystalline ferromagnet-antiferromagnet bilayers", Physical Review B, **59**, 3722 (1999).

References

[9] O. da Silva, J. de Siqueira, P. Kern, W. Garcia, F. Beck, J. Rigue, and M. Carara, "Magnetic anisotropies and rotational hysteresis in $Ni_{81}Fe_{19}/Fe_{50}Mn_{50}$ films: A study by torque magnetometry and anisotropic magnetoresistance", Journal of Magnetism and Magnetic Materials, **451**, 507–514 (2018).

[10] H. Ohldag, A. Scholl, F. Nolting, E. Arenholz, S. Maat, A.T. Young, M. Carey, and J. Stöhr, "Correlation between exchange bias and pinned interfacial spins", Physical Review Letters, **91**, 017203 (2003).

[11] A. Mitrofanov, G. Chen, A. Kozhanov, and S. Urazhdin, "Exchange bias without directional anisotropy in permalloy/CoO bilayers", Physical Review B, **104**, 144413 (2021).

[12] M. Kiwi, "Exchange bias theory," Journal of Magnetism and Magnetic Materials, **234**, 584–595 (2001).

[13] Ibid., page 585.

[14] Ibid., page 586.

[15] A. Scholl, F. Nolting, J. Stöhr, T. Regan, J. Lüning, J. W. Seo, J.-P. Locquet, J. Fompeyrine, S. Anders, H. Ohldag, and H. A. Padmore, "Exploring the microscopic origin of exchange bias with photoelectron emission microscopy", Journal of Applied Physics, **89**, 7226 (2001).

[16] H. Ohldag, H. Shi, E. Arenholz, J. Stöhr, and D. Lederman, "Parallel versus Antiparallel Interfacial Coupling in Exchange Biased Co/FeF_2", Physical Review Letters, **96**, 027203 (2006).

[17] Web article written, presumably, by one or more of the authors in refs [3], [10], [15], and [16]. (The web article begins with "Here we give a brief review...") The affiliation for authors Ohldag and Stöhr of refs [10], [15], and [16] is the Stanford Synchrotron Radiation Laboratory, Stanford University. The author(s) of the web article were not identified. The publication date was not provided, but it can be no earlier than 2000 and no later than 2020. A list of eleven publications is provided at the end of the web article. Each of them was published in a recognized scientific journal (Physical Review Letters, Science, Nature, and Physical Review B). Six of the publications address exchange bias and interfacial coupling directly. Refs [3], [10], [15], and [16] are included in the list. The page source for the web article is,
https://www ssrl.slac.stanford.edu/stohr/magneticexchange.htm

[18] T. Blachowicz and A. Ehrmann, "Exchange bias in thin films – An update", Coatings, **11**, **122**, 1-21 (2021).

[19] Ibid., page 16.

[20] The sources are my collection of undergraduate and graduate level physics and chemistry textbooks as well as books on general history, general philosophy, philosophy of science, biographical books on Einstein, a book by de Broglie, the Feynman lecture series, dictionaries, and, of course, Wikipedia and other web sources. It seems unlikely that a historical record exists identifying who discovered magnetism and when. (I did not check my Norton Anthology, Dante, either of my books on Che Guevara, or any of my books on the classics, supposing that they were candidates not likely to contain the sought after information).

[21] S. F. Mason, "A History of the Sciences", Collier Books Edition, MacMillan Publishing Company, 1962, page 74.

References

[22] R. A. Serway, “Physics for Scientists and Engineers”, 3rd Edition, Saunders College Publishing, 1992, page 625.

[23] Ibid.

[24] J. M. D. Coey, “Magnetism and Magnetic Materials”, Cambridge University Press, 2013, page 1.

[25] Ibid.

[26] D. C. Giancoli, “General Physics”, Prentice-Hall, Inc., 1984, page 538.

[27] Ibid., Coey, Ref [24], page 1.

[28] Ibid., Mason, Ref [21], page 35.

[29] Ibid., Coey, Ref [24], page 1.

[30] Wikipedia article, “History of the compass”. The page source is, https://en.wikipedia.org/wiki/History_of_the_compass

[31] Ibid., Mason, Ref [21], page 74.

[32] Ibid., Coey, Ref [24], page 1.

[33] Ibid.

[34] Web version of Encyclopedia Britannica. The page source is, https://www.britannica.com/technology/steel/History

[35] Ibid., Coey, Ref [24], page 1.

[36] Ibid.

[37] Ibid.

[38] Ibid., page 2.

[39] Ibid.

[40] Ibid.

[41] Ibid., Mason, Ref [21], page 194.

[42] Ibid.

[43] Ibid.

[44] Ibid., page 195.

[45] Ibid., Coey, Ref [24], page 2.

[46] J. A. Schuster in his contribution to "The Cambridge Descartes Lexicon". The citation for the book is, Nolan, L. (Ed.), (2015), "The Cambridge Descartes Lexicon". Cambridge: Cambridge University Press. doi:10.1017/CB09780511894695.

The comments from Schuster were taken from his published notes, "Drafts for Cambridge Descartes Lexicon." The notes were available on ResearchGate. The page source is https://www.researchgate.net/publication/323533598

[47] Wikipedia article, "Principles of Philosophy". It is only the publication dates that were obtained from the Wikipedia page. The page source is, https://en.wikipedia.org/wiki/Principles_of_Philosophy

[48] Ibid., Coey, Ref [24], page 2.

[49] Wikipedia article, "Horseshoe Magnet". The article says that William Sturgeon invented the horseshoe magnet in 1825, but this appears to be incorrect. The page source is, https://en.wikipedia.org/wiki/Horseshoe_magnet. Coey, page 2, has Bernoulli as inventor of the horseshoe magnet in 1743 and, on page 4, has Sturgeon as inventor of the electromagnet in 1824.

[50] Ibid., Coey, Ref [24], page 2.

[51] Ibid., Giancoli, Ref [26], pages 497 and 498.

[52] Ibid., Mason, Ref [21], page 456. Mason does not use the words *animal electricity*, but, instead, says that Galvani "...thought that this was a biological electrical phenomenon...".

[53] Ibid., Giancoli, Ref [26], page 498.

[54] Ibid., Mason, Ref [21], page 456.

[55] Web version of Encyclopedia Britannica. The page source is, https://www.britannica.com/biography/Franz-Anton-Mesmer

[56] Ibid., Coey, Ref [24], page 3.

[57] Ibid.

[58] Ibid.

[59] Ibid., Mason, Ref [21], page 477.

[60] Ibid.

[61] Ibid.

[62] Ibid., pages 477 and 478.

[63] Ibid., page 478.

[64] Ibid., page 479.

[65] Ibid.

[66] Ibid.

[67] Ibid.

[68] Ibid., Giancoli, Ref [26], footnote at bottom of page 435.

[69] E. Hecht, "Optics", 2nd Edition, Addison-Wesley Publishing Company, Inc. 1988, page 316.

[70] Ibid., Mason, Ref [21], page 481.

[71] Ibid.

[72] Ibid., page 482.

[73] Ibid., page 483.

[74] Ibid., pages 483 and 484.

[75] Ibid., page 484.

[76] Ibid., pages 484 and 485.

[77] J. D. Jackson, Classical Electrodynamics, 2nd Edition, John Wiley & Sons, Inc., 1975, page 2.

[78] Wikipedia Article, "Lorentz Force". The page source is, https://en.wikipedia.org/wiki/Lorentz_Force

[79] Ibid., Coey, Ref [24], page 4.

[80] Ibid.

[81] Ibid.

[82] Ibid.

[83] Allan Green, "150 years of industry & enterprise at Enderby's Wharf". This article was presented by Allan Green in 2004 during the Submarine Telegraphy session at the Fleming Centenary Conference held by University College London. Allan Green was a research fellow at the Porthcurno Telegraph Museum, Cornwall, UK. He is now, apparently, a senior research associate at Science Museum London, Woodley, UK (obtained from LinkedIn). The article was downloaded from, https://atlantic-cable.com/Article/EnderbyAG/index.htm

[84] Ibid., Coey, Ref [24], page 5.

[85] Ibid.

[86] Ibid., Mason, Ref [21], page 550.

[87] Ibid., Giancoli, Ref [26], pages 545, 546, and 782.

[88] R. B. Leighton, “Principles of Modern Physics”, McGraw-Hill Book Company, Inc., 1959, page 70.

[89] Ibid., page 72.

[90] Ibid., Mason, Ref [21], pages 553 and 554.

[91] Ibid., Leighton, Ref [88], page 81.

[92] Ibid., page 254.

[93] D. J. Griffiths, “Introduction to Quantum Mechanics”, 2nd Edition, Pearson Prentice Hall, 2005, page 160.

[94] Ibid., Mason, Ref [21], page 554.

[95] Ibid.

[96] Ibid.

[97] Ibid., Giancoli, Ref [26], page 803.

[98] Ibid., Mason, Ref [21], page 554.

[99] Ibid., Giancoli, Ref [26], page 803.

[100] P. A. Tipler, “Modern Physics”, Worth Publishers, Inc., 1982, page 254.

[101] B. H. Bransden and C. J. Joachain, “Introduction to Quantum Mechanics”, Longman Scientific and Technical, Copublished in the United States with John Wiley & Sons, Inc., 1989, page 37.

[102] Ibid., Tipler, Ref [100], page 254.

[103] Ibid., Bransden and Joachain, Ref [101], pages 37 and 38.

[104] Ibid., Leighton, Ref [88], page 185.

[105] Ibid.

[106] Ibid.

[107] Ibid., Giancoli, Ref [26], page 803.

[108] Ibid., Tipler, Ref [100], page 252.

[109] Ibid., Mason, Ref [21], page 555.

[110] Ibid., page 556.

[111] Ibid.

[112] Ibid.

[113] Ibid.

[114] Ibid., Bransden and Joachain, Ref [101], pages 31 and 51.

[115] Ibid., page 51.

[116] Ibid.

[117] Ibid., Mason, Ref [21], page 557.

[118] Ibid.

[119] Ibid.

[120] Ibid., page 558.

[121] Ibid.

[122] Ibid.

[123] Ibid., Leighton, Ref [88], page 666.

[124] Ibid., Mason, Ref [21], page 557.

[125] Ibid.

[126] Ibid.

[127] Ibid., Coey, Ref [24], page 7.

[128] Ibid., Giancoli, Ref [26], page 574. Giancoli does not give the year. It may be that Curie included the work in his 1895 Doctoral Thesis.

[129] Wikipedia Article, "Nikola Tesla". Used for dates. The page source is, https://en.wikipedia.org/wiki/Nikola_Tesla

Invention of the induction motor by Ferraris instead of by Tesla would seem to be correct. See Ref [130].

[130] Web article for Galileo Ferraris from the Edison Tech Center, Engineering Hall of Fame. The article brings attention to litigation in the early 1900's concerning Ferraris and Tesla. Assignment of intellectual property rights was the matter before the court. The page source is https://edisontechcenter.org/GalileoFerraris.html

[131] J. Larmor, D. Sc. F. R. S. (1897) LX111 "On the theory of the magnetic influence on spectra; and on the radiation from moving ions", The London, Edinburgh, and Dublin Philosophical Magazine and Journal of Science, **44:271**, 503-512. The 1897 paper was originally published in Philosophical Magazine. The reference here is for Series 5 of a set of books containing the papers that were published in Philosophical Magazine. Series 5 covers the period 1876 to 1900. The paper from Larmor is in this book.

[132] Dr. Thomas Meier, "Ferromagnetische resonanz (FMR)". This is an online article. The date on the article is 18 Dec, 2020. The affiliation for Dr. Meier is the Department of Physics, Technical University of Munich. On page 3 of the article, Dr Meier assigns credit for discovery of FMR to Vladimir Arkad'yev (1911). The page source is, https://www.ph.tum.de/academics/org/labs/fopra/docs/userguide-23.en.pdf

[133] A. Aharoni, "Introduction to the Theory of Ferromagnetism", 2nd Edition, Oxford University Press, 2000, page 70. Aharoni has the year as 1925 instead of 1924.

[134] Ibid., Griffiths, Ref [93], page 273. Griffiths does not give the year. The contribution from Thomas is in his paper, L. H. Thomas, "I. The kinematics of an electron with an axis", The London, Edinburgh, and Dublin Philosophical Magazine and Journal of Science, **3:13**, 1 - 22, (1927).

[135] Ibid., Coey, Ref [24], page 5.

[136] N. W. Ashcroft and N. D. Mermin, "Solid State Physics", Brooks/Cole Cengage Learning, 1976, pages 680, 681, and footnote 22 at the bottom of page 681.

[137] A. M. Forrest, "Meissner and Ochsenfeld revisited", European Journal of Physics, **4**, 117 - 120, (1983). Forrest provides a version of the original 1933 paper by Meissner and Ochsenfeld that has been translated from German to English.

[138] Ibid., Coey, Ref [24], page 6.

[139] Wikipedia Article, "Landau - Lifshitz – Gilbert equation". Used for dates only. The page source is https://en.wikipedia.org/wiki/Landau-Lifshitz-Gilbert_equation

[140] Wikipedia Article, "Magnetic resonance imaging". Used for dates only.
The page source is https://en.wikipedia.org/wiki/Magnetic_resonance_imaging

[141] O. W. Richardson, "A Mechanical Effect Accompanying Magnetization", Physical Review (Series 1), **26**, (1908), page 248.

[142] Ibid.

[143] Ibid., pages 251 and 252.

[144] Ibid., page 249.

[145] Ibid., pages 249 and 250.

[146] Ibid., page 250.

[147] Ibid., page 252.

[148] Ibid., Coey, Ref [24], page 64.

[149] Ibid., Richardson, Ref [141], pages 252 and 253.

[150] A. Einstein and W. J. de Haas, "Experimental proof of the existence of Ampère's molecular currents", Koninklijke Nederlandsche Akademie van Wetenschappen Proceedings, **18, iss. 1**, 696 - 711 (1915).

[151] Ibid., pages 706 and 707.

[152] Ibid., page 711.

[153] S. J. Barnett, "Magnetization by rotation", Physical Review, **6**, 239 - 270, (1915).

[154] Ibid., page 269.

[155] J. Q. Stewart, "The moment of momentum accompanying magnetic moment in iron and nickel", Physical Review, **11**, 100-120, (1918).

[156] A. P. Chattock and L. F. Bates, "On the Richardson gyro-magnetic effect", Physical Transactions of the Royal Society of London, Series A, Containing Papers of a Mathematical or Physical Character, **223**, 257-288, (1923).

[157] G. G. Scott, "Review of gyromagnetic ratio experiments", Reviews of Modern Physics, **34**, 102 - 111, (1962).

[158] C. Kittel, "On the gyromagnetic ratio and spectroscopic splitting factor of ferromagnetic substances", Physical Review, **76**, 743 - 748, 1949.

[159] Ibid., Coey, Ref [24], page 65.

[160] Ibid., page 63.

[161] Ibid., page 62.

[162] Ibid., page 24.

[163] Ibid.

[164] Ibid., page 51.

[165] Ibid., Ashcroft and Mermin, Ref [136], page 672.

[166] Ibid., page 673.

[167] Ibid., pages 710 and 711.

[168] Ibid., pages 217 and 218.

[169] Ibid., Leighton, Ref [88], page 377.

[170] Ibid.

[171] Ibid., Ashcroft and Mermin, Ref [136], page 694.

[172] Ibid., page 682.

[173] M. P. Marder, "Condensed Matter Physics", 2nd Edition, John Wiley & Sons, Inc, 2010, page 723.

[174] R. P. Feynman, "The Feynman Lectures On Physics", Addison-Wesley Publishing Company, 1977, Volume II, page 35-1.

[175] Ibid., Coey, Ref [24], page 76.

[176] J. H. Van Vleck, "The theory of electric and magnetic susceptibilities", Oxford at the Clarendon Press, 1932. This is a book. The content referred to is in Section IV, paragraph 24, beginning on page 94.

[177] Ibid., Coey, Ref [24], page 76.

[178] Ibid., Ashcroft and Mermin, Ref [136], footnote 7 at the bottom of page 646.

[179] G. Küestler, "Diamagnetic levitation – Historical milestones", Revue Roumaine des Sciences Techniques, Série Électrotechnique et Énergétique, **52(3)**, 265 - 282, (2007). The referenced comment is on page 266.

[180] Ibid., page 267.

[181] Ibid., pages 267 and 268.

[182] M. Faraday, "Experimental researches in electricity. Twentieth series", Philosophical Transactions of the Royal Society, **136**, 21-40, 1846.

[183] Ibid., Coey, Ref [24], page 11 and footnote 9 at the bottom of page 11.

[184] Ibid., Faraday, Ref [182], page 30, subpara 2288.

[185] Ibid., Mason, Ref [21], page 478.

[186] C. M. Hurd, "Varieties of magnetic order in solids", Contemporary Physics, **23:5**, 469-493, 1982.

[187] Ibid., Coey, Ref [24], page 13.

[188] Ibid., Ashcroft and Mermin, Ref [136], page 3 and footnote 4 at the bottom of page 3.

[189] Ibid., Coey, Ref [24], pages 24 and 63.

[190] B. D. Cullity and C. D. Graham, "Introduction to Magnetic Materials", 2nd Edition, IEEE Press, John Wiley & Sons, Inc., 2009.

[191] Ibid., page 95.

[192] Ibid., Hurd, Ref [186], page 478.

[193] Ibid., Cullity and Graham, Ref [190], page 111.

[194] Ibid., Coey, Ref [24], page 135.

[195] Ibid., Cullity and Graham, Ref [190], page 111.

[196] Ibid., Hurd, Ref [186], page 480.

[197] Ibid., Cullity and Graham, Ref [190], page 146.

[198] Ibid.

[199] Ibid., Coey, Ref [24], page 5.

[200] Ibid., Ashcroft and Mermin, Ref [136]. The content for this paragraph is from the section "Magnetic properties of a two-electron system: Singlet and triplet states" that begins on page 674 and ends on page 681.

[201] Ibid., footnote 15 at the bottom of page 679.

[202] Ibid., footnote 1 at the bottom of page 672.

[203] Ibid., page 673.

[204] Ibid., Coey, Ref [24], pages 103 and 104.

[205] Ibid., page 168.

[206] Ibid., page 174.

[207] Ibid., page 181.

[208] Ibid., page 187.

[209] Ibid., page 514.

[210] Ibid., Cullity and Graham, Ref [190], page 146.

[211] Ibid., page 147.

[212] Ibid.

[213] Ibid., Leighton, Ref [88], page 377.

[214] Ibid.

[215] Ibid.

[216] Ibid., pages 378 and 379.

[217] Ibid., page 379.

[218] Ibid.

[219] Ibid.

[220] C. Kittel, "Introduction to Solid State Physics", 8th Edition, John Wiley & Sons, Inc., 2005, page 167.

[221] Ibid., page 164.

[222] Ibid., Ashcroft and Mermin, Ref [136], page 139.

[223] Ibid.

[224] Ibid., Kittel, Ref [220], pages 180 and 181.

[225] Ibid., Ashcroft and Mermin, Ref [136], footnote 23 at the bottom of page 143.

[226] Ibid., page 562.

[227] Ibid., Leighton, Ref [88], footnote 1 at the bottom of page 380.

[228] H. T. Stokes, “Solid State Physics”, Allyn and Bacon, Inc., 1987, pages 163 to 165.

[229] Ibid., Ashcroft and Mermin, Ref [136], page 563.

[230] Ibid., pages 575 and 576.

[231] Ibid., Leighton, Ref [88], page 387.

[232] Ibid.

[233] Ibid., Ashcroft and Mermin, Ref [136], footnote 29 at the bottom of page 684.

[234] Ibid., Kittel, Ref [220], pages 329 and 330.

[235] Ibid., Ashcroft and Mermin, Ref [136], footnote 29 at the bottom of page 684.

[236] Ibid., Kittel, Ref [220], page 329.

[237] Ibid., Ashcroft and Mermin, Ref [136], footnote 29 at the bottom of page 684.

[238] Ibid. page 673.

[239] Ibid., Coey, Ref [24], pages 94 and 95.

[240] Ibid., page 195.

[241] Ibid., Cullity and Graham, Ref [190], page 151.

[242] Ibid., Coey, Ref [24], page 195.

[243] Ibid., page 197.

[244] Ibid.

[245] Ibid., page 198.

[246] Ibid., Cullity and Graham, Ref [190], page 151.

[247] Ibid., Coey, Ref [24], pages 196 to 198.

[248] Ibid., Cullity and Graham, Ref [190], page 154.

[249] Ibid.

[250] Ibid., page 173.

[251] Ibid., Ashcroft and Mermin, Ref [136], page 681.

[252] Ibid.

[253] Ibid., Cullity and Graham, Ref [190], page 170.

[254] Ibid., page 175.

[255] Ibid.

[256] Ibid.

[257] Ibid., page 177.

[258] Ibid., page 178.

[259] Ibid., page 177.

[260] Ibid.

[261] Ibid., page 178.

[262] Ibid.

[263] Ibid., page 180.

[264] Ibid.

[265] Ibid., Coey, Ref [24], pages 274 to 280.

[266] Ibid., Cullity and Graham, Ref [190], pages 394 to 397.

[267] Ibid.

[268] Ibid., page 397.

[269] Ibid., page 396.

[270] Ibid., pages 450 and 451.

[271] Ibid., page 373.

[272] Ibid., Coey, Ref [24], page 51.

[273] Ibid., page 63.

[274] Ibid., Bransden and Joachain, Ref [101], footnote 1 at the bottom of page 533.

[275] CODATA Recommended Values Of The Fundamental Physical Constants: 2018. CODATA is the "Committee on Data for Science and Technology". The CODATA chart is available from the National Institute of Standards and Technology, NIST SP 961, (May, 2019). The link to the NIST website for the 2019 CODATA chart is, https://physics.nist.gov/cuu/Constants/

[276] Ibid., Griffiths, Ref [93], footnote 11 at the bottom of page 273.

[277] Ibid., Coey, Ref [24], page 51.

[278] Ibid., page 75.

[279] Ibid., page 309.

[280] Ibid., page 67.

[281] Ibid., pages 315 and 316.

[282] N. Müglich, A. Gaul, M. Meyl, A. Ehresmann, G. Götz, G. Reiss, and T. Kuschel, "Time dependent rotatable magnetic anisotropy in polycrystalline exchange-bias systems: Dependence on grain-size distribution," Physical Review B, **94**, 184407 (20116)

[283] Ibid., Dunsmore and Thibault et al., Ref [1], Manuscript, section III, subsection C.

[284] F. Radu, H. Zabel, "Exchange bias effect of ferro-/antiferromagnetic heterostructures". In: Zabel, H., Bader, S. D. (eds) Magnetic Heterostructures. Springer Tracts in Modern Physics, **227**. Springer, Berlin, Heidelberg, 97 - 184, (2008). The content referred to is on pages 106 and 107. (Page 6 of the version on arXiv).

[285] Ibid., Dunsmore and Thibault et al., Ref [1], Supplementary Material, section S6, subsection B.

References

[286] R. I. Joseph, “Ballistic demagnetizing factor in uniformly magnetized cylinders,” Journal of Applied Physics, **37**, 4639–4643 (1966).

[287] G. Rowlands, “On the magnetostatic energy of magnetized needles”, Journal of Magnetism and Magnetic Materials, **118**, 307-314, (1993).

[288] D. A. Goode and G. Rowlands, “The demagnetizing energies of a uniformly magnetized cylinder with an elliptic cross-section”, Journal of Magnetism and Magnetic Materials, **267**, 373-385, (2003).

[289] R. D. McMichael, M. D. Stiles, P. Chen, and W. F. Egelhoff Jr, “Ferromagnetic resonance studies of NiO-coupled thin films of $Ni_{80}Fe_{20}$,” Physical Review B, **58**, 8605 (1998).

[290] J. E. Losby, Z. Diao, F. Fani Sani, D. T. Grandmont, M. Belov, J. A. J. Burgess, W. K. Hiebert, and M. R. Freeman, “Nanomechanical AC susceptometry of an individual mesoscopic ferrimagnet”, Solid State Communications, **198**, 3 - 6, (2014).

[291] K. R. Fast, J. A. Thibault, V. T. K. Sauer, M. G. Dunsmore, A. Kav, J. E. Losby, Z. Diao, E. J. Luber, M. Belov, and M. R. Freeman, “Simultaneous three-axis torque measurements of micromagnetism,” AIP Advances, **11**, 015119 (2021).

[292] A. Vansteenkiste, J. Leliaert, M. Dvornik, M. Helsen, F. Garcia-Sanchez, and B. Van Waeyenberge, “The design and verification of mumax3,” AIP Advances, **4**, 107133 (2014).

[293] “COMSOL Multiphysics (TM), v.5.6, www.comsol.com, COMSOL AB, Stockholm, Sweden.”

[294] M. J. Donahue and D. G. Porter, "OOMMF User's Guide, Version 1.0", Interagency Report **NISTIR 6376**, National Institute of Standards and Technology, Gaithersburg, MD (Sep 1999).

[295] H. Fangohr, M. Albert, M. Franchin, "Nmag micromagnetic simulation tool – software engineering lessons learned", Proceedings of the International Workshop on Software Engineering for Science, 1-7, (2016), arXiv:1601.07392v2 **[cs.SE]**.

[296] R. Bjørk, E. B. Poulsen, K. K. Nielson, and A. R. Insinga, "MagTense: a micromagnetic framework using the analytical demagnetization tensor", Journal of Magnetism and Magnetic Materials, **535**, 168057, (2021).

[297] D. Martien, "Introduction to: AC Susceptibility", The article was written for a company, *Quantum Design*, and is available on their website. The company has offices in the United States, 11578 Sorrento Valley Road, San Diego, California.

[298] Ibid., Cullity and Graham, Ref [190], pages 217 and 218.

The papers in references 299 to 304 are not connected directly to the work conducted for the thesis. They are from the tiltmeter research group that I was a member of from the mid 1980's to early 1990's. I was the group technician. I also collected and managed the tilt data during the extended periods of time that the instruments were installed in the field. Much of the expertise required for the experimental work reported on herein was developed during my time with the tiltmeter group.

[299] J. S. Rogers, C. U. Park, and F. W. Jones, "Test cell results for a mercury-level tiltmeter", Journal of Physics E: Scientific Instruments, **13**, 161-162, (1980).

References

[300] J. S. Rogers, F. W. Jones, and P. Rouleau, "Long-term Gain Changes in Mercury-level Tiltmeters of the Stacey Type", Pure and Applied Geophysics, **125(5)**, 835-843, (1987).

[301] F. W. Jones, J. S. Rogers, P. Rouleau, K. Hutchence, and L. W. Vigrass, "Tilt Measurements in Western Canada", Pure and Applied Geophysics, **125(5)**, 813-834, (1987).

[302] P. Rouleau, J. S. Rogers, et F. W. Jones, "La marée d'inclinaison à Leduc (Alberta), Canada : observation, analyse et interprétation", Canadian Journal of Earth Sciences, **25(10)**, 1649-1659, (1988).

[303] J. S. Rogers, F. W. Jones, M. E. Ertman, and J. Thibault, "Near-surface tilt response to steam injection into a tar sands formation", Canadian Journal of Earth Sciences, **27(10)**, 1312-1315, (1990).

[304] F. W. Jones, F. Pascal, and J. S. Rogers, "Interpretation of the tilt response of two tiltmeters to water injection into a tar sands formation", Canadian Geotechnical Journal, **29(3)**, 516-521, (1992).

[305] "NIST Policy on Metrological Traceability", 2021. The link to the NIST website for the document is https://www.nist.gov/calibrations/traceability

[306] NIST/SEMATECH e-Handbook of Statistical Methods. The Handbook is available from the NIST website, https://www.itl.nist.gov/div898/handbook/,2022. The information regarding standards is in the handbook, section 2.3.1.2, Reference Standards.

[307] H. Nyquist, "Thermal agitation of electrical charge in conductors", Physical Review, **32**, 110 - 113, (1928).

[308] H. B. Callen and T. A. Welton, “Irreversibility and generalized noise”, Physical Review, **83**, 34 - 40, (1951).

[309] A. N. Cleland and M. L. Roukes, “Noise processes in nanomechanical resonators”, Journal of Applied Physics, **92**, 2758 - 2769, (2002). The sentence quoted is at the beginning of Section III on page 2761.

[310] Ibid., Section III, subpara A, first para.

[311] A. N. Cleland, “Foundations of Nanomechanics: From Solid State Theory to Device Applications”, Springer-Verlag Berlin Heidelberg New York, 2003. The content relevant to dissipation in nanomechanical resonators is in Chapter 8, section 8.5, pages 292 to 301.

[312] B. D. Hauer, C. Doolin, K. S. D. Beach, and J. P. Davis, “A general procedure for thermomechanical calibration of nano/micro-mechanical resonators”, Annals of Physics, **339**, 181 - 207, (2013).

[313] J. Losby, J. A. J. Burgess, Z. Diao, D. C. Fortin, W. K. Hiebert and M. R. Freeman, “Thermo-mechanical sensitivity calibration of nanotorsional magnetometers”, Journal of Applied Physics, **111**, 07D305, (2012).

[314] Ibid., Dunsmore and Thibault et al., Ref [1], Supplementary Material, section S3.

[315] R. Prosen, J. Holmen, and B. Gran, “Rotatable anisotropy in thin permalloy films,” Journal of Applied Physics, **32**, S91–S92 (1961).

[316] Ibid., Coey, Ref [24], page 387.

[317] Ibid., Table 8.2 at the top of page 278.

[318] T. Dias, E. Menéndez, H. Liu, C. Van Haesendonck, A. Vantomme, K. Temst, J. E. Schmidt, R. Giulian, and J. Geshev, "Rotatable anisotropy driven training effects in exchange biased Co/CoO films," Journal of Applied Physics, **115**, 243903 (2014).

[319] C. Schlenker, S. Parkin, J. Scott, and K. Howard, "Magnetic disorder in the exchange bias bilayered FeNi-FeMn system," Journal of Magnetism and Magnetic Materials, **54**, 801–802 (1986).

[320] X. Qiu, D. Yang, S. Zhou, R. Chantrell, K. O'Grady, U. Nowak, J. Du, X. Bai, and L. Sun, "Rotation of the pinning direction in the exchange bias training effect in polycrystalline NiFe/FeMn bilayers," Physical Review Letters, **101**, 147207 (2008).

[321] S. Jenkins, R. W. Chantrell, and R. F. Evans, "Atomistic origin of the athermal training effect in granular IrMn/CoFe bilayers," Physical Review B, **103**, 104419 (2021).

[322] Ibid., Coey, Ref [24], pages 250 and 257.

[323] M. Gruyters, "Cobalt oxide/ferromagnet bilayers: Exchange coupling and dominance of the antiferromagnet", Europhysics Letters, **64 (6)**, 803 - 809, (2003).

[324] Ibid., Cullity and Graham, Ref [190], page 397.

[325] Ibid., Radu and Zabel, Ref [284], pages 163 and 164. (Pages 33 and 34 of the version on arXiv).

[326] Ibid., Kiwi, Ref [12], page 586. Kiwi acknowledges the importance of investigating temperature effects, but does not provide any discussion of them.

[327] Ibid., Dunsmore and Thibault et al., Ref [1], Supplementary Material, section S4.

[328] Ibid., Radu and Zabel, Ref [284], pages 152 to 158. (Pages 28 to 31 of the version on arXiv).

[329] Ibid., Coey, Ref [24], page 278.

[330] Ibid., Radu and Zabel, Ref [284], pages 151 and 152. (Page 28 of the version on arXiv).

[331] Ibid., Cullity and Graham, Ref [190], page 152.

[332] Ibid., Dunsmore and Thibault et al., Ref [1], Manuscript, section III, subsection A and Supplement section S5.

[333] Ibid., Coey, Ref [24], page 56.

[334] K. Ounadjela, H. Lefakis, V. Speriosu, C. Hwang, P. Alexopoulos, "Thickness dependence of magnetization and magnetostriction on NiFe and NiFeRh films", Journal de Physique Colloques, **49 (C8)**, C8-1709 - C8-1710, (1988).